Reactive transport modeling of CO2 through cementitious materials under CO2 geological storage conditions

Jiyun Shen

THÈSE

Présentée pour obtenir le grade de

DOCTEUR DE

L'UNIVERSITÉ PARIS–EST

Domaine : Génie Civil

Présentée par :

Jiyun Shen

Sujet de la thèse :

Reactive Transport Modeling of CO_2 through Cementitious Materials under CO_2 Geological Storage Conditions

Modélisation de la prénétration du CO_2 dans les matériaux cimentaires dans le contexte du stockage du CO_2

Mémoire provisoire

Jury :

Dr. Fabrice Brunet	CNRS Paris	Rapporteur
Dr. Kwaikwan WONG	ENTPE France	Rapporteur
Dr. Bruno HUET	Lafarge France	Examinateur
Prof. Aït-Mokhtar KARIM	LEPTIAB France	Examinateur
Dr. Patrick DANGLA	IFSTTAR, U. Paris-Est	Directeur de thèse
Dr. Mickaël THIERY	IFSTTAR, U. Paris-Est	Conseiller d'études

Résumé

Un modèle de transport réactif est proposé pour simuler la réactivité des matériaux à base de ciment en contact avec une saumure saturée en CO_2 et/ou le CO_2 supercritique (CO_2sc) dans les conditions de stockage géologique du CO_2. Un code a été développé pour résoudre simultanément le transport et la chimie par une approche globale couplée, compte tenu de l'effet de la température et de la pression.

La variabilité des propriétés du CO_2sc avec la pression et la température, telles que la solubilité dans l'eau, la densité et la viscosité sont pris en compte. On suppose que tous les processus chimiques sont en équilibre thermodynamique. Les réactions de dissolution et de précipitation de la portlandite (CH) et de calcite ($C\bar{C}$) sont décrites par des lois d'action de masse et des seuils de produit d'activité ioniques. Une cinétique de dissolution de CH est introduite pour faciliter la convergence numérique. La définition d'une variable principale permet de capturer la précipitation et la dissolution des phases solides à base de calcium. Une généralisation de la loi d'action de masse est développée et appliquée aux silicates de calcium hydratés (C-S-H) pour tenir compte de la variation continue (diminution) du rapport Ca/Si au cours de la dissolution des C-S-H. Les variations de porosité et de la microstructure induites par les réactions de précipitation et de dissolution sont également prises en compte.

Le couplage entre le transport et la chimie est modélisé par cinq équations de bilan de masse écrites pour chaque atome (Ca, Si, C, K, Cl), ainsi que par une équation de conservation de la masse totale et celle de la charge électrique. Les lois de Darcy et de Nernst-Planck sont utilisées pour décrire le transport de masse et d'ions. Les propriétés de transport dépendent du degré de saturation et de la porosité.

Le modèle est implémenté dans le code de volumes finis, Bil. Les principes de cette méthode et l'approche de modélisation sont discutés et illustrés sur un exemple simple.

Ce modèle est en mesure de simuler les processus de carbonatation des matériaux à base de ciment, dans des conditions à la fois saturés et insaturés, dans une large plage de concentration de CO_2, de température et de pression. Plusieurs expériences, rapportées dans la littérature, sont simulées en utilisant divers types de conditions aux limites: (i) solutions saturées ou non en CO_2 et carbonate de calcium, (ii) gas supercritique de CO_2. Les prédictions sont comparées avec les observations expérimentales. Certains

phénomènes observés expérimentalement peuvent être également expliqués par le modèle.

Mots-clés:

Carbonatation, CO_2 supercritique, Transports, Ciment, C-S-H, Décalcification, Pression, Température, Stockage du CO_2.

Abstract

A reactive transport model is proposed to simulate the reactivity of cement based material in contact with CO_2-saturated brine and supercritical CO_2 ($scCO_2$) under CO_2 geological storage conditions. This code is developed to solve simultaneously transport and chemistry by a global coupled approach, considering the effect of temperature and pressure.

The variability of $scCO_2$ properties with pressure and temperature, such as solubility in water, density and viscosity are taken into account. It is assumed that all chemical processes are in thermodynamical equilibrium. Dissolution and precipitation reactions for portlandite (CH) and calcite ($C\bar{C}$) are described by mass action laws and threshold of ion activity products in order to account for complete dissolved minerals. A chemical kinetics for the dissolution and precipitation of CH and $C\bar{C}$ is introduced to facilitate numerical convergence. One properly chosen variable is able to capture the precipitation and dissolution of the relevant phase. A generalization of the mass action law is developed and applied to calcium silicate hydrates (C-S-H) to take into account the continuous variation (decrease) of the Ca/Si ratio during the dissolution reaction of C-S-H. The changes in porosity and microstructure induced by the precipitation and dissolution reactions are also taken into account.

Couplings between transport equations and chemical reactions are treated thanks to five mass balance equations written for each atom (Ca, Si, C, K, Cl) as well as one equation for charge balance and one for the total mass. Ion transport is described by using the Nernst-Plank equation as well as advection, while gas and liquid mass flows are governed by advection. Effect of the microstructure and saturation change during carbonation to transport properties is also considered.

The model is implemented within a finite-volume code, Bil. Principles of this method and modeling approach are discussed and illustrated with the help of a simple example.

This model, with all the efforts above, is able to simulate the carbonation processes for cement based materials, at both saturated and unsaturated conditions, in a wide CO_2 concentration, temperature and pressure range. Several sets of experiments, including sandstone-like conditions, limestone-like conditions, supercritical CO_2 boundary and unsaturated conditions reported in the literature are simulated. Good

predictions are provided by the code when compared with experimental observations. Some experimental-observed phenomena are also explained by the model in terms of calcite precipitation front, CH dissolution front, porosity profile, etc.

Keywords:

Carbonation, Supercritical CO_2, Transport, Cement, C-S-H, Decalcification, Pressure, Temperature, CO_2 storage.

Acknowledgements

There are many people who have influenced, guided, and supported me at my time in IFSTTAR. Foremost, I would like to express my sincere gratitude to my advisor Dr. Patrick Dangla, for the continuous support of my Ph.D study and research, for his patience and immense knowledge. His guidance helped me in all the time of research and writing of this thesis. My sincere thanks also goes to my 'conseiller d'études', Dr. Mickaël THIERY, whose motivation and enthusiasm have inspired me deeply.

Besides, I would like to thank the rest of my thesis committee: Prof. Aït-Mokhtar Karim, Dr. Kwaikwan Wong, Dr. Fabrice Brunet and Dr. Bruno Huet for their time, encouragement and insightful comments.

I would also like to thank Olivier Poupard and Bruno Capra of OXAND, for their discussions and financial support for this research project.

I thank my fellow labmates and friends in IFSTTAR and Université Paris-Est: Dr. Aza Azouni, Dr. Teddy Fen-Chong, Louisa Loulou, Rongwei Yang, Haifeng Yuan, Qiang Zeng, Antoine Morandeau, Biyun Wang, Linlin Wang, Zhidong Zhang, Pengyun Hong, Qiong Wang, Jucai Dong, Yiguo Wang, Shuo Wang, Kun Li, Zheng He, Yan Liu, Lianhua He, etc., for all the help, discussions and most of all, their accompany during the past 3 years.

Last but not the least, I would like to thank my parents Anbiao Shen and Xiaochun Wang, for their opinions on conducting research and getting a Ph.D, their understanding and supporting throughout my life.

.

Contents

List of Figures

List of Tables

Chapter 1

Introduction

1.1 Background

Anthropogenic emissions of greenhouse gases, such as carbon dioxide (CO_2), have caused world-wide concerning during the recent years. Atmospheric CO_2 concentration was close to 280±5 μmol/mol from 1000 to 1800 AD (Fig. 1.1), and exceeded 350 μmol/mol in the last century (Keeling et al., 2011; Tans, 2012), while currently, it has increased to a level of 390 μmol/mol (Fig. 1.2). It is believed that the growing amount of greenhouse gases could contribute to the global warming by trapping energy from the sun in the earth's atmosphere. Carbon dioxide capture and storage (CCS), a process consisting of the capture of the CO_2 at large point sources and long-term isolation from the atmosphere, is considered as a promising option in the portfolio of mitigation actions for stabilization of atmospheric CO_2 concentration.

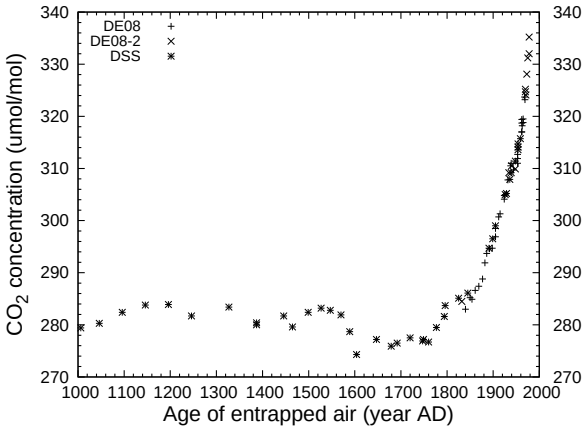

Figure 1.1: Atmospheric carbon dioxide concentration during the past 1000 years, based on the Antarctic ice cores Law Dome DE08, DE08-2 and DSS (data from (Etheridge et al., 1998, 1996)).

Carbon dioxide capture and storage consists in 3 steps, first, the separation of CO_2 from industrial and

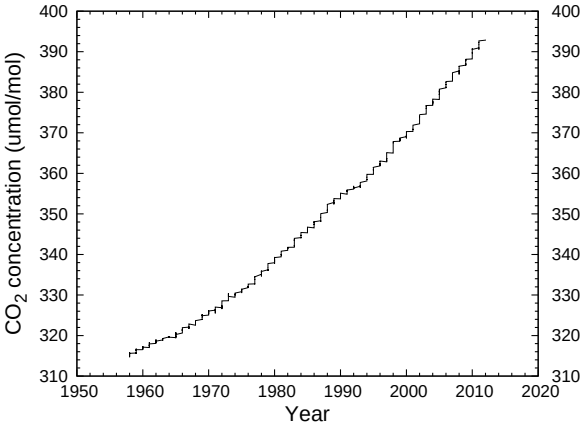

Figure 1.2: Atmospheric carbon dioxide concentration in recent years based on direct measurement (data from (Tans, 2012)).

energy-related sources (cement plants, power plants, industrial boilers, etc.), second, the transport of CO_2 to a storage location, and last, the injection and long-term storage of CO_2 in deep geological reservoirs.

According to (Metz, 2005), CO_2 could be captured from large point sources, including large fossil fuel or biomass energy facilities, major CO_2 emitting industries, natural gas production, synthetic fuel plants and fossil fuel-based hydrogen production plants (see Table 1.1).

Table 1.1: CO_2 point sources with emissions of more than 0.1 million tonnes of CO_2 per year and their corresponding annual emissions, data from (Metz, 2005)

Process	**Number of sources**	**Emissions($MtCO_2yr^{-1}$)**
Fossil fuels		
Power	4,942	10,539
Cement production	1,175	932
Refineries	638	798
Iron and steel industry	269	646
Petrochemical industry	470	379
Oil and gas processing	Not available	50
Other sources	90	33
Biomass		
Bioethanol and bioenergy	303	91
Total	**7,887**	**13,466**

The captured CO_2 is compressed and transported to storage points, and then injected into geological formations so as to be isolated from the atmosphere. CO_2 geological storage has the potential of storing more than 10,000 Gt of CO_2, see Table 1.2. However, long term storage of CO_2 involves risks of leakage of CO_2 through the oil well cement-based material. In order to predict the CO_2 leakage, it is essential to understand the CO_2 transfers, as well as the chemical reactions at stake (carbonation mechanism) which take place within the materials exposed to CO_2 under geological storage conditions.

1.2 CO_2 geological sequestration

CO_2 geological sequestration, involves injecting CO_2, generally in supercritical form, directly into underground geological formations. Potential geological sequestration sites include three types: deep unmineable coal seams, deep saline aquifers, and depleted oil and gas fields. The estimated potential storage capacity for each storage options is summarized in Table 1.2.

Table 1.2: Storage capacity for different geological storage options, data from (Metz, 2005)

Reservoir type	**Lower estimate of storage capacity ($GtCO_2$)**	**Upper estimate of storage capacity ($GtCO_2$)**
Oil and gas fields	675[a]	900[a]
Unminable coal seams	3-15	200
Deep saline formations	1,000	possibly 10,000

[a] These values are calculated based on the oil and gas fields already disvovered.

Unmineable coal seams can be used to store CO_2 because the CO_2 molecules attach to the surface of coal. The CO_2 storage in coal beds could also enhance coal bed methane recovery (ECBM), since coal has a larger affinity for CO_2 than for methane. When CO_2 is injected, the previously absorbed methane is released. Saline formation has the largest potential storage capacity, due to their abundant volume and common occurrence. Petroleum companies have been injecting CO_2 into oil reservoirs since the late 1960s to enhance oil recovery (EOR). The same type of equipment and technology could be used for CO_2 sequestration. Another advantage of storage CO_2 in oil/gas reservoir is that the geology of the reservoirs is generally well understood and the cost could be partly offset by the additional oil recovered.

The option of storing CO_2 in coal beds is still in demonstration phase, while there are already several CO_2 storage projects under way in deep saline aquifers and depleted oil/gas fields. Some of the projects in progress are listed in Table 1.3.

Table 1.3: CO_2 storage projects in progress, data from (Metz, 2005)

Project name	**Country**	**Injection start (year)**	**Injection rate (tCO_2 day^{-1})**	**Total storage (tCO_2)**	**Reservoir type**
Weyburn	Canada	2000	3,000-5,000	20,000,000	EOR
In Salah	Algeria	2004	3,000-4,000	17,000,000	Gas field
Sleipner	Norway	1996	3,000	20,000,000	Saline formation
Frio	U.S.A	2004	177	1600	Saline formation
Fenn Big Valley	Canada	1998	50	200	ECBM
Qinshui Basin	China	2003	30	150	ECBM
Yubari	Japan	2004	10	200	ECBM

1.3 CO_2 leakage

Intergovernmental Panel on Climate Change (IPCC) estimated that 99% CO_2 could be retained in the storage site over 1,000 years, if the reservoir is well-selected, designed and managed (Metz, 2005). The liability of potential leak is one of the largest barriers to large-scale CCS. During long-term storage, abandoned oil or gas wells, as well as the CO_2 injection pipe, may act as conduits for CO_2 to return to the atmosphere (Gasda et al., 2004; Duguid and Scherer, 2010). There are several possible leakage pathways, as indicated in Fig. 1.3. The CO_2 may migrate through the cement well plug or the primary cement between well casing and formation rock. Other migration pathways include interfaces between rock and cement, between cement and well casing, and between casing and cement plug.

The leakage of CO_2 will reduce the efficiency of CO_2 storage. It could also cause some environment problem and even pose risk to the human life. In December 2008 a modest release of CO_2 from a pipeline under a bridge in Berkel en Rodenrijs resulted in the deaths of some ducks sheltering there. In 1986 a natural leakage of CO_2 took place at Lake Nyos in Cameroon resulted from a volcanic event and asphyxiated 1,700 people (Pentland, 2008). The natural CO_2 release near Mammoth Mountain in California after several small earthquakes caused large amount of tree-killing and one human fatality as well (Farrar et al., 1995; Hill, 2000).

Both the cement plug and the primary cement may degrade during time, since the injected CO_2 lowers the pH value of the underground water. The degradation could increase the permeability of cement, it could also enlarge the annuli between cement-rock or cement-casing. This process will raise the possibility of CO_2 leakage. Thus, the cement behavior, *i.e.* the carbonation and leaching effect, is a key requirement to the prediction of CO_2 transport and the assessment of leakage risk.

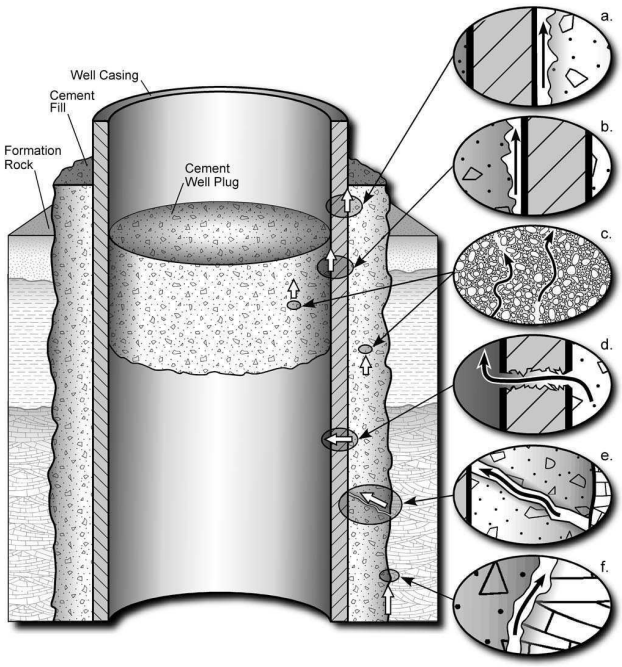

Figure 1.3: Potential leakage pathways through an abandoned well. a) Between casing and cement; b)between cement plug and casing; c) through the cement pore space as a result of cement degradation; d) through casing as a result of corrosion; e) through fractures in cement; and f) between cement and rock. (Gasda et al., 2004)

1.4 Summary of reseach work about carbonation of cement based materials

In deep geological formations, assuming a 20 ℃ surface temperature and a gradient of 30 ℃ per kilometer, the temperature could reach 50 ℃ and the pressure could be more than 10 MPa at the depth of 1 km. Under these conditions, the CO_2 is in supercritical state ($scCO_2$), with the density like that of a liquid and the viscosity like a gas. Since $scCO_2$ and water are not miscible and can dissolve into each other, they form a two-phase system composed of a $scCO_2$ rich phase (wet $scCO_2$) and a water rich phase (CO_2-saturated aqueous solution). Therefore the cement could be exposed to either a CO_2-saturated aqueous solution or wet $scCO_2$, or even both. Carbonic acid will form when CO_2 is dissolved in water. The acid will attack the cement and calcium carbonate will be generated. The precipitated calcium carbonate could also dissolve in some cases, leaving a high porous silica gel (Duguid and Scherer, 2010). In other cases, the calcium carbonate will not dissolve and protect the inner side of the cement from further degradation (Duguid and Scherer, 2010; Kutchko et al., 2008).

Research work conducted in this field includes laboratory and in-situ studies as well as numerical modeling.

Duguid et al. (Duguid and Scherer, 2010) conducted a series of experiments to examine the effects

of flowing carbonated brine on well cementitious materials. They used CO_2 saturated brine in a batch reactor and simulated both sandstone (*i.e.*, boundary conditions not saturated with calcite) and limestone reservoir conditions (*i.e.*, boundary conditions saturated with calcite). Class H cement pastes were exposed to different test conditions simulating sandstone-like conditions: $T = 20$ or 50 ℃ and pH $= 2.4$ or 3.7. All the cylindrical samples under sandstone-like conditions were degraded over the course of the experiment. Five different regions were observed: an orange ring followed by brown, white, light gray rings and a dark gray core. The orange and brown zones were fully degraded, with little calcium left comparing to the unreacted core. The white ring showed an increase in calcium, corresponding to the presence of the carbonation front. In the light gray ring, portlandite was partially dissolved, reflecting the presence of a dissolution front. The dark gray core was the unreacted zone. The author also noted that the formation of the white and calcium carbonate-rich layer had a protective effect and slowed down the reaction rate. Under limestone-like conditions, no evident attack was observed. Duguid et al. also did also some proposals to predict the degradation of *in situ* an oil-well cement in contact with sandstone (Duguid, 2009). The authors believed that the formation of the calcite-rich layer would largely hinder the carbonation penetration. With a rough estimation, it will take 30,000 to 700,000 years to degrade 25 mm of a cement paste in a sandstone reservoir.

Rimmelé et al. (Rimmelé et al., 2008) exposed cement samples to both CO_2-saturated brine and wet $scCO_2$, under pressure and temperature similar to downhole conditions. The porosity distribution at different states was monitored by SEM-BSE image analysis. The observed penetration kinetics of the carbonation front, as well as carbonation patterns, were similar between the samples exposed to $scCO_2$ and CO_2-saturated water. A slightly faster penetration kinetics of the carbonation front was measured for the one exposed to $scCO_2$.

Fabbri et al. (Fabbri et al., 2009) used same set-up as in (Rimmelé et al., 2008) and exposed both initially saturated and initially dried cement samples to $scCO_2$, different types of carbonation features were achieved. For the initially saturated samples (wet samples), annular carbonation with a sharp carbonation front was observed, while for the initially dried samples (dry samples), homogeneous carbonation took place.

Carey et al. (Carey et al., 2007) studied cement samples taken from a well after 30 years of CO_2 exposure. The reservoir was located at about 2100 m depth, and had a temperature and pressure of 54 ℃ and 18 MPa. The observations demonstrated that CO_2 migrated along both the casing-cement and cement-shale interfaces. The carbonation depth was 0.1-0.3 cm thick within the cementitious matrix adjacent to the casing while 0.1-1 cm thick within the cementitious matrix in contact with the shale. They reconstructed the cross-section of the wellbore environment which included casing, cement, and shale caprock. A dark rind

(0.1-0.3 cm thickness) occurred between the casing and the cement, which consisted of calcite, aragonite, and halite. An orange-colored alteration zone of the cement (0.1-1 cm) occurred adjacent to the shale, which was heavily carbonated cement and contained three polymorphs of $CaCO_3$ (calcite, aragonite, and vaterite), halite, and a substantial amorphous component. Between the shale and the cement there was a texturally complex region which the authors had informally named the shale-fragmentzone (SFZ). This consisted of a mixture of shale fragments, carbonated cement, and pure carbonates. The interface between the cement and orange zone was characterized by a narrow (<1 mm), dark gray deposit of layered amorphous silica, silica-carbonate, and carbonates. This interface was denser than the gray cement or orange zone as shown in X-ray tomographic images. This interface was more or less like the carbonation front observed in lab experiments. The analyzed cement pastes located at 3-4 m above the reservoir contact, as a result, the in-situ results showed much slower and less heavily carbonation compared with experimental results of (Duguid and Scherer, 2010; Rimmelé et al., 2008), etc., in which cement samples were exposed to $scCO_2$ or CO_2-saturated water directly. They also made some numerical simulations in their study.

Kutchko et al. (Kutchko et al., 2008) exposed samples made of class H cement to $scCO_2$ and to CO_2 saturated brine at 50 ℃ and 30.3 MPa for 1 year. Results for cement in contact with $scCO_2$ was similar to that in contact with atmospheric CO_2 with a strong effect of the clogging of the microstructure able to hinder the CO_2 penetration, while the one exposed to CO_2 saturated brine was typical of acid attack on cement-based materials with a significant leaching effect (both of hydration compounds and calcium carbonate). With the data collected during 1 year, they estimated a penetration depth range of around 1.00 mm for CO_2 saturated brine and 1.68 mm for the $scCO_2$ after 30 years, which is consistent with the observations in (Carey et al., 2007).

Bachu and Bennion (Bachu and Bennion, 2009) tested the permeability change of good-quality cement samples subjected to 90 days of flow with CO_2 saturated brine, at 15 MPa and 65 ℃. Cement permeability dropped rapidly and remained almost constant thereafter, most likely as a result of CO_2 exsolution due to the pressure drop along the flow path. They believe that these processes are likely to occur in the field if the cement is of good quality to begin with, which is in contrast to some laboratory experimental results. Other test results in this study suggested that the presence of cracks and/or gaps would lead to a significant increase in effective permeability.

Brandvoll et al. (Brandvoll et al., 2009) tested both batch and flow conditions and presented some initial results. Since they used brine water, carbonation front was limited in 200 μm for batch conditions (until 42 days). For flow conditions, the reacted zone did not exceed 200 μm, but the experiments lasted only 12 days.

Regnault et al. (Regnault et al., 2009) tested the reaction rates of portlandite with supercritical CO_2.

The initial carbonation rates were presented in their paper, CO_2-vapor-only experiments (without water) showed the formation of a passivation layer of calcite while with the presence of water, full carbonation took place.

Garcia-Gonzalez et al. (García-González et al., 2008) analyzed the effects of supercritical carbon dioxide on the carbonation of Portland cement pastes, with different mineral additions. A set of powdered samples of different cement pastes was exposed to laboratory atmosphere for 200 days, and was examined as well. After a few hours of $scCO_2$ treatment, the Portlandite was partially carbonated and the Ca/Si ratio of C-S-H (calcium silicate hydrates) reduced. The precipitated calcite covered the Portlandite surface and inhibited further carbonation. Low-temperature N_2 adsorption-desorption analysis (BET method) and Hg intrusion porosimetry (MIP method) were used for microstructure analysis. The results showed a decrease of macropore volume and an increase of fine pore volume. Permeability was largely reduced, K_w (water permeability coefficient) changed from 4×10^{-7} ms^{-1} for the raw mortar to 2×10^{-10} ms^{-1} for the supercritical carbonated sample. A pH drop of pore water from 12.5 to 8.5 was also observed.

William Carey et al. (William Carey et al., 2010) also published some experimental simulation results. In this study, they investigated the casing-cement microannulus through core-flood experiments. The experiments were conducted at 40 ℃ and 14 MPa pore pressure for 394 h. A 1:1 mixture of supercritical CO_2 and 30,000 ppm NaCl-rich brine flowed through 10cm of limestone before flowing through the 6 cm length cement-casing wellbore system with a 5 cm diameter. The Portland cement was carbonated to depths of 50-250 μm by a diffusion-dominated process. There was very little evidence for mass loss or erosion of the Portland cement. The experimental results were applied to field observations of carbonated wellbore cement by (Carey et al., 2007) and (Crow et al., 2010) to show that carbonation of the field samples was not accompanied by significant CO_2-brine flow at the casing-cement interface. These experiments also reinforced other studies that indicated rates of Portland cement deterioration were slow.

Existing models mainly focus on the transport and reactions within cement-based materials exposed to CO_2-saturated brine. Carey et al. (Carey and Lichtner, 2007) have presented numerical simulations which are consistent with in-situ observations if the modeling parameters are adjusted. An interesting reactive transport modeling has been proposed and discussed in details in the work of (Huet et al., 2010). The authors have intended to simulate the conditions of CO_2-saturated water which were tested in Duguid's experiments (Duguid and Scherer, 2010). In the recently published work of (Huet et al., 2011), experimental works of cement pastes exposed to CO_2-saturated brine, from (Duguid and Scherer, 2010; Rimmelé et al., 2008; Kutchko et al., 2008) were simulated and compared briefly. Huet et al. concluded that the reactivity is either controlled by Ca/CO_2 diffusion, or stops because of calcium carbonate caused clogging. Despite these simulation works, comparisons between experimental works and numerical simulations are far from

being abundant in the literature. Indeed published modeling works mainly deal with the saturated condition, *i.e.*, CO_2-saturated brine. Since in the case of CO_2 geological storage conditions, cement-based materials could also be exposed to $scCO_2$, a model should work with both conditions: wet/dry $scCO_2$ and CO_2-saturated water conditions.

1.5 Research objectives

The purpose of this work is to study the CO_2 transport properties as well as the behavior of cement paste exposed to $scCO_2$ or CO_2-saturated water, and build up a reactive transport model. This model should take into account several aspects listed below:

1. Thermodynamic properties of the CO_2-H_2O mixture.
2. Dissolution and precipitation reactions of portlandite (CH) and calcite ($C\bar{C}$).
3. The continuous variation (decrease) of the Ca/Si ratio during the dissolution reaction of C-S-H.
4. Thermodynamical equilibriums in chemical reactions.
5. The changes in porosity and microstructure induced by the precipitation and dissolution reactions.
6. Multiphase transport (liquid/gas phase).
7. Couplings between transport equations and chemical reactions.
8. Temperature and pressure effects to the thermodynamical equilibrium and transport.

The model is implemented within a finite-volume code Bil (http://perso.lcpc.fr/dangla.patrick/bil). The key parameters implemented in this numerical code will be detailed and discussed. Simulations will be conducted, including CO_2-saturated water conditions from (Duguid and Scherer, 2010), $scCO_2$ conditions presented in (Rimmelé et al., 2008; Fabbri et al., 2009; Kutchko et al., 2008). Some simulation results dealing with carbonation and porosity profiles will be pointed out and compared with experimental results taken from the previous references. With well studied parameters, this code can provide good prediction and is able to explicate the different observations for experimental works in literatures. However, due to the lack of some essential data (*e.g.*, initial solid contents, initial porosity), some experimental works (*e.g.* (Kutchko et al., 2008)) are difficult to precisely simulate. Anyway, the major purpose of this work is to illustrate carbonation mechanisms rather than make perfectly precise simulations (which is actually impossible).

1.6 Outline of the thesis

The following chapter, Chapter 2, presents thermodynamical properties of the CO_2-H_2O mixture. The state equations of pure carbon dioxide and CO_2-H_2O mixture are introduced. The calculation method of CO_2 density, the CO_2 and H_2O fugacity coefficients, are described in detail, and the parameters needed are presented. In the last part of this chapter, mutual solubilities of CO_2 and H_2O are calculated and presented under different temperatures and pressures.

Chapter 3 discusses the carbonation of cement based materials. Major chemical reactions taking place during carbonation are introduced first. The carbonation of portlandite (CH) and C-S-H are then described separately. Dissolution and precipitation reactions for CH and calcite ($C\bar{C}$) are described by mass action laws and threshold of ion activity products in order to account for complete dissolved minerals. A chemical kinetics for the dissolution and precipitation of CH and $C\bar{C}$ is introduced to facilitate numerical convergence. An innovative general idea for the C-S-H is introduced here, which is able to explain the continuous decalcification and facilitate the numerical modeling. Porosity changes induced by the precipitation-dissolution of the various solid compounds are accounted for by the balance of volume. In the end the carbonation of one simple element is presented to illustrate the evolution of the solid volume assemblage.

Chapter 4 introduces the reactive transport modeling. First the field equations for five element (Ca,C,Si,Cl,K) as well as charge and total mass are presented. Followed by the transport parameters of liquid phase and gas phase, including dynamic liquid/gas viscosity, intrinsic and relative liquid/gas permeability of cement, etc. Transport of aqueous species are introduced in the end.

Numerical procedures are discussed in Chapter 5. Principle of the finite volume method is illustrated by a simple transport example. The dissolution and precipitation of CH and C-S-H as well as the kinetics, are also described. One properly chosen variable is able to capture the precipitation and dissolution of the relevant phase. In the end a simple sample is used to illustrate the couplings of transport and chemical reactions.

In Chapter 6, experiments of cement samples exposed to CO_2-saturated brine (Duguid and Scherer, 2010) are simulated and discussed. Simulations are conducted under different conditions, *e.g.*, sandstone-like conditions, high temperature conditions and limestone-like conditions. Simulation results are compared with experimental observations. The effects of CO_2 concentration, temperature and ion activity product of $C\bar{C}$ at the boundary, are analyzed as well.

Chapter 7 deals with cement samples exposed to $scCO_2$. Simulations of experimental work from (Rimmelé et al., 2008) are conducted first to validate the model. Several parameters (porosity, CO_2 dissolution and water evaporation kinetics at the boundary, alkali) will be analyzed. Then the different observations between experimental works (Rimmelé et al., 2008; Duguid and Scherer, 2010; Fabbri et al.,

2009; Kutchko et al., 2008) will be explained by comparing with each other.

Conclusion, summarizes the work of this thesis and propose some future improvement.

Chapter 2

Thermodynamical properties of the CO_2-H_2O mixture

2.1 Introduction

The carbonation of cement-based materials is a chemical reaction between the dissolved CO_2 in the aqueous pore solution and the cement hydrates. Therefore the solubility of the supercritical CO_2 gas is firstly required. Fig. 2.1 illustrates the $P-T$ phase diagram of CO_2. The critical point is 31.1 ℃ and 7.39 MPa. Beyond this point, CO_2 is in supercritical state, with the density like that of a liquid and the viscosity like a gas.

The depth of CO_2 storage varies from 800 m to several kilometers for physical and economical reasons (Metz, 2005). In these formations, the specific pressure and temperature should be taken into account. Assuming a 20 ℃ surface temperature and a gradient of 30 ℃ per kilometer, the temperature will be 50 ℃ at the depth of 1 km, and 80 ℃ at 2 km. Consider an hydrostatic gradient of 100 bars km^{-1}, the pressure will be 101 bars at 1 km and 201 bars at 2 km. In these $P-T$ conditions, CO_2 is a supercritical fluid. Together with underground water, they form a two-phase system composed of a $scCO_2$ rich phase (wet $scCO_2$) and a water rich phase (CO_2-saturated aqueous solution).

The thermodynamic of CO_2-H_2O mixtures will be studied in this chapter. We have followed (Spycher et al., 2003) and (Marini, 2007) to calculate the mutual solubility of CO_2 and H_2O in the temperature range of 12-110 ℃ and at a gas pressure up to 600 bars, further details could be found in their work.

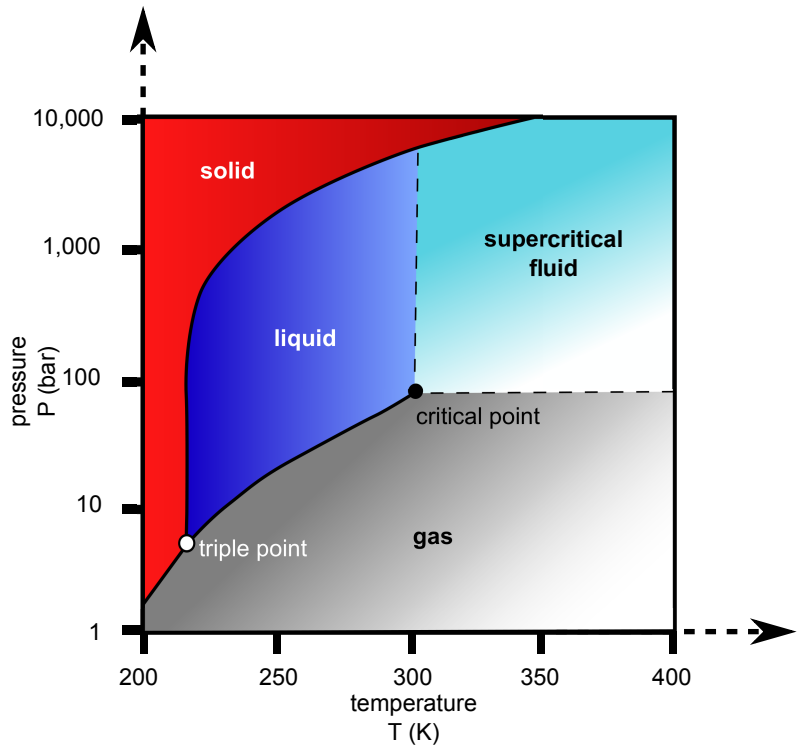

Figure 2.1: Carbon dioxide pressure-temperature phase diagram.

2.2 The state equation of carbon dioxide

For a pure gas, the simplest equation of state (EOS) is the ideal gas law. For 1 mole of an ideal gas, there is a relation between the P-T-V, written as

$$P_G = \frac{RT}{V_G} \tag{2.1}$$

where P_G and V_G represent the gas pressure and molar volume, R = 8.31451 J mol^{-1} K^{-1} is the gas constant. Since it does not consider the volume of molecules and the interaction between them, the ideal gas law is not suitable for describing the P-T-V relationship of real gas, especially at high pressures. These effects are incorporated in the van der Waals equation (Marini, 2007), by introducing two adjustable parameters, written as

$$P_G = \frac{RT}{V_G - b} - \frac{a}{V_G^2} \tag{2.2}$$

where parameter a is the correction for intermolecular attractions while b is for the volume of the molecules. One of the derived EOS from the van der Waals equation proposed by Redlich et al. (Redlich and Kwong, 1949) is commonly used today, in the form of

$$P_G = \frac{RT}{V_G - b} - \frac{a}{T^{0.5} V_G (V_G + b)} \tag{2.3}$$

The Redlich-Kwong EOS also has two parameters, which could be obtained by fitting experimental data, or alternatively from the P-T-V data at the critical point (Marini, 2007). Spycher et al. (Spycher et al., 2003) has fitted the a,b values with experimental results, and proposed to use $b = 27.80 \pm 0.01$ cm^3/mol and $a = 7.54 \times 10^7 - 4.13 \times 10^4 \times T$ (K) with the unit of bar cm^6 K$^{0.5}$ mol^{-2} for pure CO_2, which work in the temperature range of 12 to 107 ℃ and pressure range from 1-600 bars.

The molar volume of CO_2 could be calculated by solving Eq. (2.3). Then the CO_2 density ρ_{CO_2} is calculated by Eq. (2.4) and plotted in Fig. 2.2. The compression factor $Z(P_G) = P_G V_G / RT$ of the Redlich-Kwong's model is plotted in the Fig. 2.3.

$$\rho_{CO_2} = \frac{M_{CO_2}}{V_G} \tag{2.4}$$

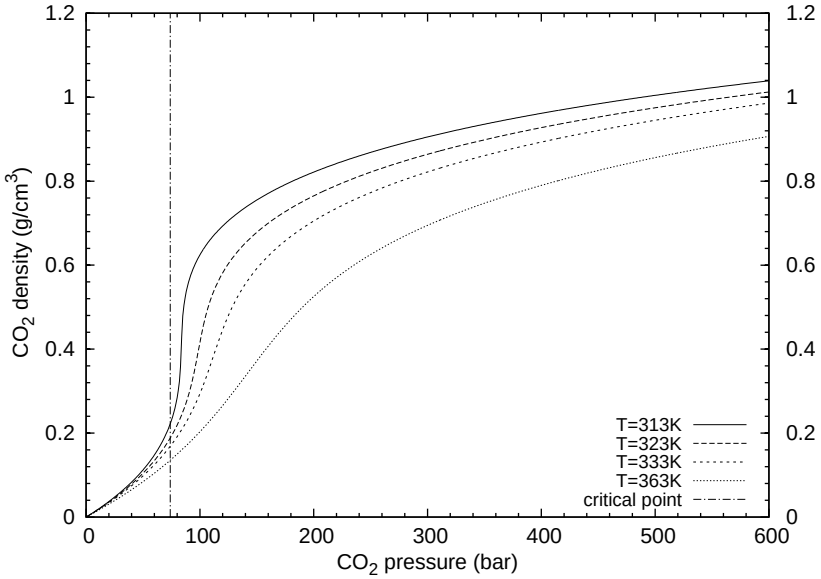

Figure 2.2: CO_2 density at different temperatures calculated with Redlich-Kwong EOS, with parameters a and b fitted by (Spycher et al., 2003).

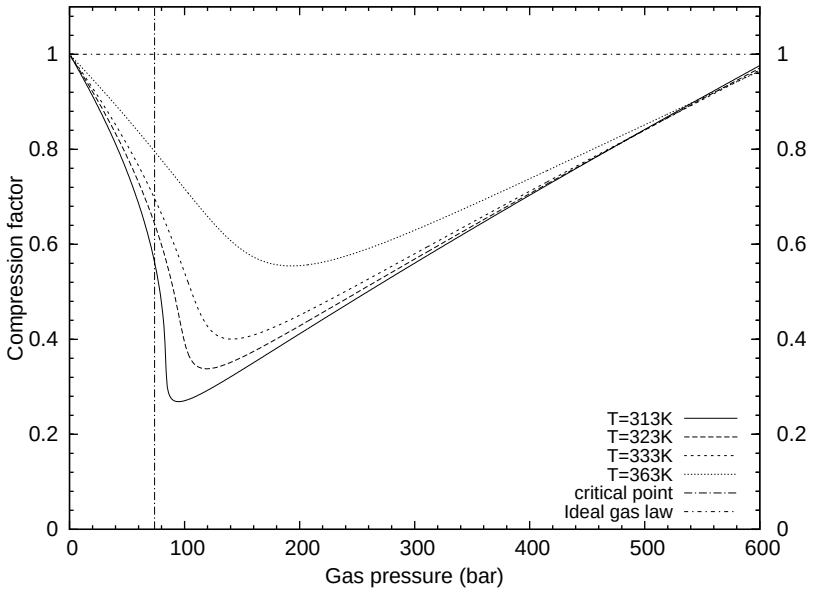

Figure 2.3: CO_2 compression factor at different temperatures calculated with Redlich-Kwong EOS, with parameters a and b fitted by (Spycher et al., 2003).

2.3 The state equation of CO_2-H_2O mixture

The CO_2-rich phase is a binary mixture of CO_2 and H_2O. For the mixture, the parameters a and b can be calculated by the following mixing rules (Prausnitz et al., 1998),

$$a_{mix} = y_{CO_2}^2 a_{CO_2} + 2y_{H_2O}y_{CO_2}a_{H_2O-CO_2} + y_{H_2O}^2 a_{H_2O} \tag{2.5}$$

and

$$b_{mix} = y_{CO_2}b_{CO_2} + y_{H_2O}b_{H_2O} \tag{2.6}$$

where y_i denotes the mole fraction of each component. Due to the rather small H_2O mole fraction in the gas mixture, it is reasonable to assume a zero value for y_{H_2O}, *i.e.*, infinity H_2O dilution in CO_2-rich phase (Marini, 2007; Spycher et al., 2003). Then the a_{mix} and b_{mix} are equivalent as given in last section. The fugacity coefficients of CO_2 and H_2O in CO_2-rich phase, ϕ_{CO_2} and ϕ_{H_2O}, could be calculated by (Spycher et al., 2003):

$$\begin{aligned}\ln(\phi_{CO_2}) = &\ln\left(\frac{V_G}{V_G - b_{CO_2}}\right) + \frac{b_{CO_2}}{V_G - b_{CO_2}} - \frac{2a_{CO_2}}{RT^{1.5}b_{CO_2}}\ln\left(\frac{V_G + b_{CO_2}}{V_G}\right) \\ &+ \frac{a_{CO_2}b_{CO_2}}{RT^{1.5}b_{CO_2}^2}\left[\ln\left(\frac{V_G + b}{V_G}\right) - \frac{b_{CO_2}}{V_G + b_{CO_2}}\right] - \ln Z\end{aligned} \tag{2.7}$$

and

$$\ln(\phi_{H_2O}) = \ln\left(\frac{V_G}{V_G - b_{CO_2}}\right) + \frac{b_{H_2O}}{V_G - b_{CO_2}} - \frac{2a_{H_2O-CO_2}}{RT^{1.5}b_{CO_2}} \ln\left(\frac{V_G + b_{CO_2}}{V_G}\right) + \frac{a_{CO_2}b_{H_2O}}{RT^{1.5}b_{CO_2}^2}\left[\ln\left(\frac{V_G + b_{CO_2}}{V_G}\right) - \frac{b_{CO_2}}{V_G + b_{CO_2}}\right] - \ln Z, \tag{2.8}$$

where V_G stands for the molar volume of the gas mixture and Z is the compression factor. With the assumption of infinite H_2O dilution, ϕ_{CO_2} is the same as that of pure CO_2. Other parameters needed for the calculation are listed in Table 2.1. The calculated fugacity coefficients at different temperatures are plotted in Fig. 2.4 and Fig. 2.5. With these values, we are able to calculate the mutual solubilities of CO_2 and H_2O, which will be dealt with in next section.

Table 2.1: Parameters used for Eqs. (2.7, 2.8)

Parameters	**Value**	**Unites**
a_{CO_2}	$7.54 \times 10^7 - 4.13 \times 10^4 \times T\ (K)$ (fitted T range: 283-380 K)	bar cm^6 $K^{0.5}$ mol^{-2}
b_{CO_2}	27.80 ($\pm$0.01)	cm^3/mol
b_{H_2O}	18.18 ($\pm$1.05)	cm^3/mol
$a_{H_2O-CO_2}$	7.89×10^7 ($\pm 0.08 \times 10^7$)	bar cm^6 $K^{0.5}$ mol^{-2}

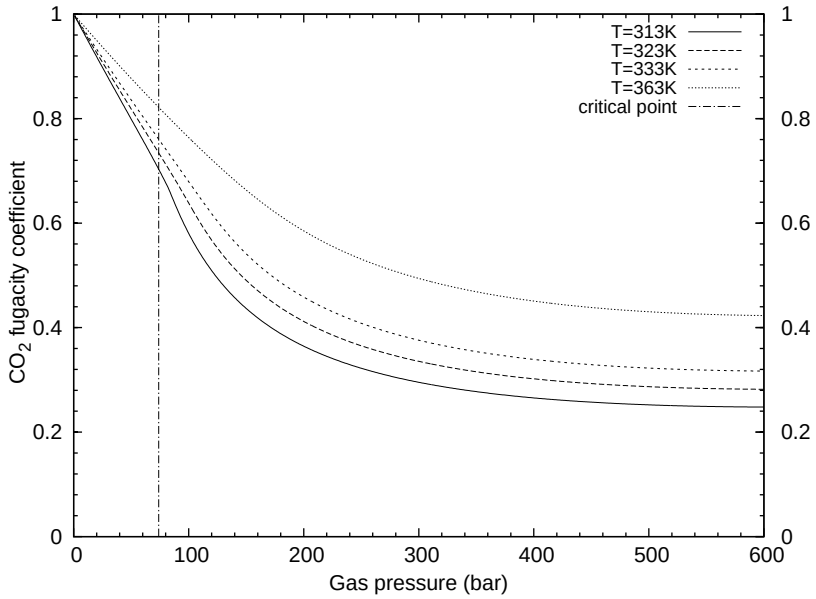

Figure 2.4: CO_2 fugacity coefficients in CO_2-rich phase at different temperatures, calculated with Redlich-Kwong EOS, with parameters suggested by (Spycher et al., 2003).

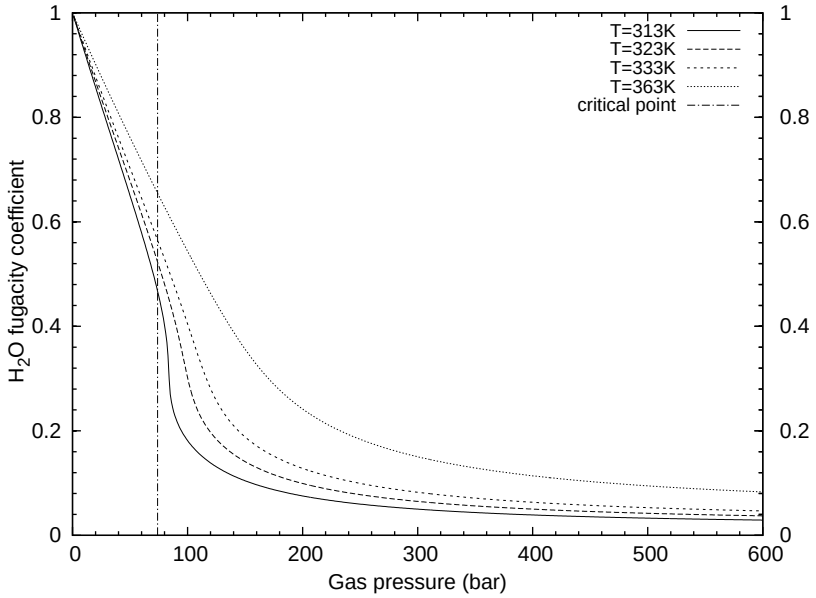

Figure 2.5: H_2O fugacity coefficients in CO_2-rich phase at different temperatures, calculated with Redlich-Kwong EOS, with parameters suggested by (Spycher et al., 2003).

2.4 Mutual solubilities of CO_2 and H_2O

Here we follow the work of (Spycher et al., 2003) to calculate the mutual solubilities of CO_2 and H_2O. Thermodynamical equilibrium requires equality of the chemical potentials in both phases. These equalities can be expressed at given T, P as:

$$K_{\mathrm{H_2O},T,P} = \frac{f_{\mathrm{H_2O}_{(g)}}}{a_{\mathrm{H_2O}_{(l)}}} \tag{2.9}$$

and

$$K_{\mathrm{CO_2},T,P} = \frac{f_{\mathrm{CO_2}_{(g)}}}{a_{\mathrm{CO_2}_{(aq)}}} \tag{2.10}$$

where f and a are fugacities of gas components and activities of aqueous components. As a first approximation, we discard the effect of activity, therefore the activity of CO_2 in aqueous solution is approximated to its solubility, *i.e.*, $\mathrm{a_{CO_2}}_{(aq)} \cong \mathrm{S_{CO_2}}$, where $\mathrm{S_{CO_2}}$ is the solubility of CO_2. We also assume a unit activity for water ($\mathrm{a_{H_2O}}_{(l)} = 1$). Thus, Eqs. (2.9) and (2.10) can be rewritten as:

$$K_{\mathrm{H_2O},T,P} \cong f_{\mathrm{H_2O}_{(g)}} \tag{2.11}$$

and

$$K_{\mathrm{CO_2},T,P} = \frac{f_{\mathrm{CO_2}_{(g)}}}{S_{\mathrm{CO_2}}} \tag{2.12}$$

For gas mixture, the fugacity equals to the product of fugacity coefficient and the gas pressure, as below:

$$f_i = \phi_i \cdot y_i \cdot P_G, \tag{2.13}$$

where f_i, ϕ_i, and y_i are the fugacity, fugacity coefficient and mole fraction of component i in the gas phase, respectively, and P_G is the total gas pressure. Substituting Eq. (2.13) in Eqs. (2.11) and (2.12) then yields:

$$f_{\mathrm{H_2O}_{(g)}} = \phi_{\mathrm{H_2O}} \cdot y_{\mathrm{H_2O}} \cdot P_G = K_{\mathrm{H_2O},T,P} \tag{2.14}$$

and

$$f_{\mathrm{CO_2}_{(g)}} = \phi_{\mathrm{CO_2}} \cdot y_{\mathrm{CO_2}} \cdot P_G = K_{\mathrm{CO_2},T,P} \cdot S_{\mathrm{CO_2}} \tag{2.15}$$

At certain temperature and pressure, fugacity coefficients ϕ_i can be calculated by Eqs. (2.7) and (2.8). As long as we know the value of $K_{\mathrm{CO_2},T,P}$ and $K_{\mathrm{H_2O},T,P}$, we can calculate $S_{\mathrm{CO_2}}$ and $y_{\mathrm{H_2O}}$ by solving Eqs. (2.14) and (2.15). Equilibrium constants K at liquid pressure P_L and T are calculated by:

$$K_{\mathrm{H_2O},T,P} = K_{\mathrm{H_2O},T,P^0} \exp\left(\frac{(P_L - P^0)\overline{V}_{\mathrm{H_2O}}}{RT}\right) \tag{2.16}$$

and

$$K_{\mathrm{CO_2},T,P} = K_{\mathrm{CO_2},T,P^0} \exp\left(\frac{(P_L - P^0)\overline{V}_{\mathrm{CO_2}}}{RT}\right) \tag{2.17}$$

where $\overline{V}_i$ is the average partial molar volume of i in the standard state. Here we use $\overline{V}_{\mathrm{H_2O}} = 18.1$ cm^3/mol, $\overline{V}_{\mathrm{CO_2}} = 32.6$ cm^3/mol as in the work of (Spycher et al., 2003). P^0 is a reference pressure taken as 1 bar for $T < 100$ ^{o}C and water saturation pressure for $T > 100$ ^{o}C. K_{T,P^0} is fitted with parameters in Table 2.2, in the form of:

$$logK_{T,P^0} = a + bT + cT^2 + dT^3, \tag{2.18}$$

with temperature in ℃.

Table 2.2: Parameters used for Eq. 2.18

Species	**a**	**b**	**c**	**d**
H_2O (10-110 ℃)	-2.209	3.097×10^{-2}	-1.098×10^{-4}	2.048×10^{-7}
$CO_{2(g/sc)}$ (12-110 ℃)	1.189	1.304×10^{-2}	-5.446×10^{-5}	0

Substituting Eqs. (2.16) and (2.17) into Eqs. (2.14) and (2.15) leads to:

$$y_{\mathrm{H_2O}} = \frac{K_{\mathrm{H_2O},T,P^0}}{\phi_{\mathrm{H_2O}} P_G} exp\left(\frac{(P_L - P^0)\overline{V}_{\mathrm{H_2O}}}{RT}\right) \tag{2.19}$$

and

$$S_{CO_2} = (1 - y_{H_2O}) \frac{\phi_{CO_2} P_G}{K_{CO_2,T,P^0}} exp(-\frac{(P_L - P^0)\overline{V}_{CO_2}}{RT}), \tag{2.20}$$

The calculated CO_2 solubility at $P_L = P_G$ is shown in Fig. 2.6 and the mole fraction of H_2O in wet CO_2 (y_{H_2O}) is shown in Fig. 2.7. Spycher et al. compared the calculated results with collected experimental results (Spycher et al., 2003), the model can reproduced mutual solubilities of CO_2 from 12 to 110 ^{o}C and H_2O from 15 to 100 ^{o}C within a few percent of published experimental values up to 600 bars.

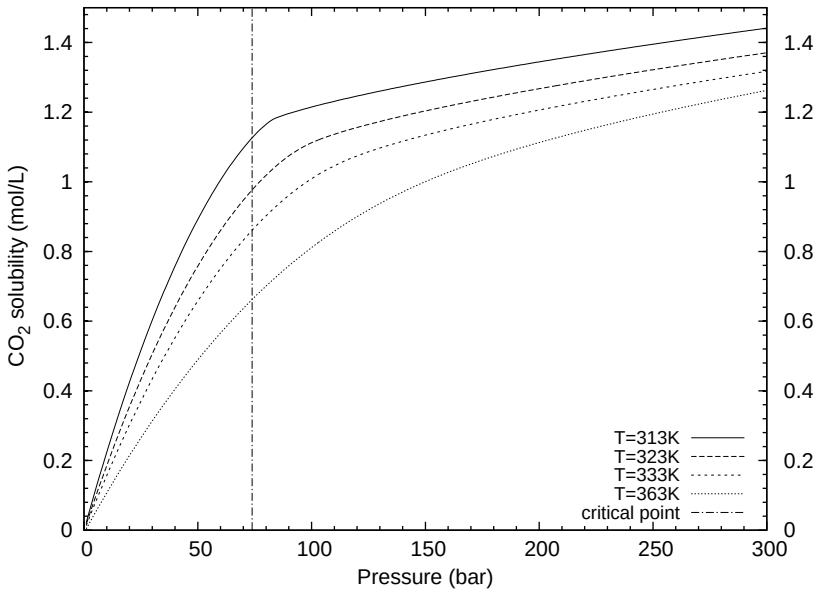

Figure 2.6: CO_2 solubility in water at different temperatures (Spycher et al., 2003).

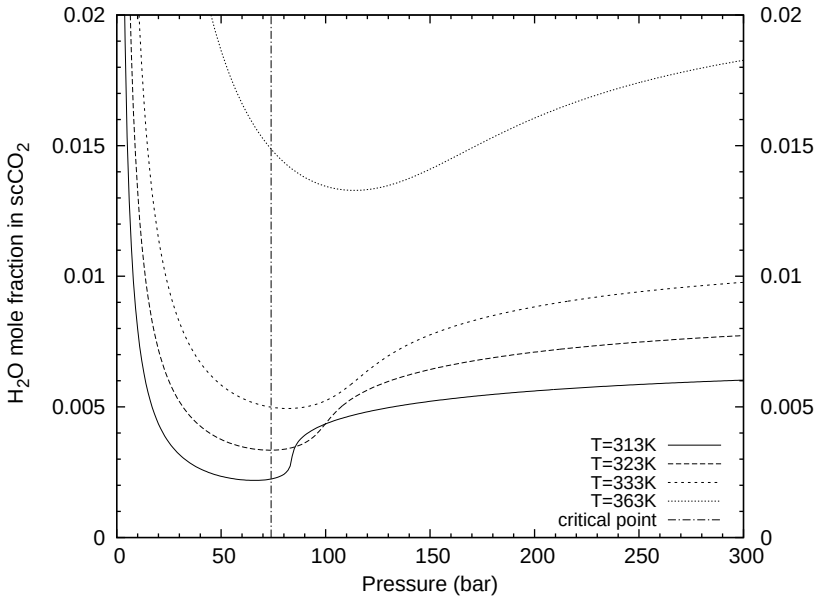

Figure 2.7: H_2O mole fraction in wet CO_2 at different temperatures (Spycher et al., 2003).

Chapter 3

Carbonation of cement-based materials

3.1 Introduction

When put in contact with cement-based materials, CO_2 will dissolve into the pore solution. The dissolved CO_2, denoted as CO_2^0 hereafter, will acidify the pore solution resulting in a series of homogeneous chemical reactions. When the CO_2 concentration gets high enough ($\geq 3 \times 10^{-15}$ mol/L at 298 K), portlandite (CH) will start to dissolve and calcium carbonate will form. When the CO_2 concentration gets higher, calcium silicate hydrate (C-S-H) carbonates and generates calcium carbonate ($C\bar{C}$) [1]. During this carbonation process, the microstructure of material also changes. When portlandite dissolves, the porosity will first increase, and it will then decrease as the calcite forms, which has a higher molar volume than CH. The decalcification of C-S-H could also contribute to a porosity increase or drop, due to the volume difference between C-S-H and the precipitated calcium carbonate and formed silica gel whose hydration degree is very variable (Antoine Morandeau, 2012; Thiéry et al., 2011, 2012). The formed calcite could dissolve under peculiar boundary conditions and cause an increase in porosity.

Reactive modeling of the hydration and carbonation of cementitious materials have been well developed during the past twenty years. Lothenbath et al. (Lothenbach and Winnefeld, 2006) developed a thermodynamic model to calculate the aqueous composition and the assemblage of the solid phases during the hydration of OPC at temperature of 20 ℃. In (Lothenbach et al., 2008) they extended the temperature range from 0 to 60 ℃. Chemical equilibriums in the pore solution and the formation of solid components including C-S-H are modeled and discussed in their work. Thoenen and Kulik built up a chemical thermody-

1. We will use the cement chemistry notation throughout the paper : C = CaO, S = SiO_2, H = H_2O, $\bar{C}$ = CO_2.

namic data base (Thoenen and Kulik, 2003) which provides the chemical equilibrium constants at different temperatures which are the same as those used in the present research. Thiery (Thiery, 2006) studied atmospheric carbonation of cementitious materials with experiments and developed a reactive transport model. Kinetics of the dissolution of CH is included in this model. Morandeau (Morandeau, 2009) further developed this model by introducing alkali and considering C-S-H as a solid solution with four members (silica gel, tobermorite I and II, jennite).

Comparing with the carbonation of portlandite, the carbonation of C-S-H is more complicated since it does not have any specific crystalline form. Many research works have examined the structure and stoichiometry of C-S-H (Chen et al., 2004; Greenberg and Chang, 1965; Kalousek, 1952; Soler, 2007; Fujii and Kondo, 1981).

In this chapter, the carbonation reactions of cement-based materials will be discussed. Chemical reactions taking place during carbonation are introduced in the first section. The effects of the chemical activity are disregarded as a first approximation (a unit activity coefficient is assumed throughout the paper). The carbonation of CH and C-S-H are then described separately. An innovative description of the C-S-H dissolution is introduced. The proposed approach provides a way to explain the continuous decalcification of the C-S-H during carbonation and facilitate the numerical modeling. Porosity change induced by the precipitation-dissolution of the various solid compounds is considered in the following section. In the last section, a simple carbonation example without transport is present to illustrate the evolution of the solid volume assemblage.

3.2 Chemical reactions

The chemical equilibrium considered in the pore solution are listed in Table 3.1. In this table and throughout this work, we use a superscript ^{0} in the chemical formula of any element (*e.g.* in CO_2^0) as a convention to denote the dissolved form of this element. Mass action laws are considered for these reactions. Note that, in addition to these ions, alkali K^+/Na^+ and chloride ion Cl^- are included in the model. In this work, we assume infinite dilution approximation for aqueous species. The activity of each aqueous species is thus equal to the molar concentration expressed in mol/L, and that of each solid component equals to 1 (CH and $C\bar{C}$) except for the different poles of C-S-H. This hypothesis may be criticized since the concentrations of the aqueous species could become too high in some situation like for unsaturated conditions when the concentration of the aqueous species increases. An improved model considering the effects of the chemical activity could be developed in a future work.

Table 3.1 provides equilibrium constants at 298 K. The temperature dependence of these constants can

Table 3.1: Homogeneous chemical reactions and equilibrium constants at 298 K, data from (Thoenen and Kulik, 2003). ρ_i prepresents the concentration of each species.

Aqueous reactions			log K	Mass action law
H_2O	$\rightleftharpoons$	$H^+ + OH^-$	-14	$\rho_{H^+}=K_{H_2O}/\rho_{OH^-}$
$CO_2^0 + H_2O$	$\rightleftharpoons$	$HCO_3^- + H^+$	-6.353	$\rho_{HCO_3^-}=K_{CO_2^0}\rho_{CO_2^0}/\rho_{H^+}$
HCO_3^-	$\rightleftharpoons$	$CO_3^{2-} + H^+$	-10.33	$\rho_{CO_3^{2-}}=K_{HCO_3^-}\rho_{HCO_3^-}/\rho_{H^+}$
$CaCO_3^0$	$\rightleftharpoons$	$Ca^{2+} + CO_3^{2-}$	-3.223	$\rho_{CaCO_3^0}=\rho_{CO_3^{2-}}\rho_{Ca^{2+}}/K_{CaCO_3^0}$
$CaOH^+$	$\rightleftharpoons$	$Ca^{2+} + OH^-$	-1.224	$\rho_{CaOH^+}=\rho_{OH^-}\rho_{Ca^{2+}}/K_{CaOH^+}$
$CaHCO_3^+$	$\rightleftharpoons$	$Ca^{2+} + HCO_3^-$	-1.105	$\rho_{CaHCO_3^+}=\rho_{HCO_3^-}\rho_{Ca^{2+}}/K_{CaHCO_3^+}$
$H_4SiO_4^0$	$\rightleftharpoons$	$H_3SiO_4^- + H^+$	-9.812	$\rho_{H_3SiO_4^-}=\rho_{H_4SiO_4^0}K_{H_4SiO_4^0}/\rho_{H^+}$
$H_3SiO_4^-$	$\rightleftharpoons$	$H_2SiO_4^{2-} + H^+$	-13.33	$\rho_{H_2SiO_4^{2-}}=\rho_{H_3SiO_4^-}K_{H_3SiO_4^-}/\rho_{H^+}$
$CaH_2SiO_4^0$	$\rightleftharpoons$	$Ca^{2+} + H_2SiO_4^{2-}$	-4.6	$\rho_{CaH_2SiO_4^0}=\rho_{H_2SiO_4^{2-}}\rho_{Ca^{2+}}/K_{CaH_2SiO_4^0}$
$CaH_3SiO_4^+$	$\rightleftharpoons$	$Ca^{2+} + H_3SiO_4^-$	-1.2	$\rho_{CaH_3SiO_4^+}=\rho_{H_3SiO_4^-}\rho_{Ca^{2+}}/K_{CaH_3SiO_4^+}$

be taken into account through the following analytical expression:

$$\log K(T) = A + BT + C/T + D \log T + E/T^2 \tag{3.1}$$

where T is the temperature in K, and values for parameters A to E can be found in (Thoenen and Kulik, 2003). Chemical equilibrium constants calculated with Eq. (3.1) at different temperatures are listed in Appendix A.

From Table 3.1 the concentration of all the aqueous species can be determined by knowing ρ_{OH^-}, $\rho_{CO_2^0}$, $\rho_{Ca^{2+}}$ and $\rho_{H_4SiO_4^0}$ which can be seen as main variables. Each molecule, i, has a fixed valence number, z_i, hence carrying a constant charge. Since electroneutrality must be held in the medium and assuming that the solid phase is not charged, we have

$$\sum_i z_i \rho_i = 0 \tag{3.2}$$

If $\rho_{CO_2^0}$, $\rho_{Ca^{2+}}$ and $\rho_{H_4SiO_4^0}$ are known, Eq. (3.2) can be solved to get the value of ρ_{OH^-}, it is then possible to calculate the concentration of all the other aqueous species.

We assume that only CH and C-S-H react with the dissolved CO_2 to form $C\bar{C}$. The carbonation mechanism can be synthesized by considering three basic dissolution reactions:

$$CH \rightleftharpoons Ca^{2+} + 2OH^- \tag{3.3}$$

$$C\bar{C} \rightleftharpoons Ca^{2+} + CO_3^{2-} \tag{3.4}$$

$$C_xS_yH_z \rightleftharpoons xCa^{2+} + 2xOH^- + yH_4SiO_4^0 + (z - x - 2y)H_2O \tag{3.5}$$

These basic dissolution reactions can be considered either at thermodynamical equilibrium or not, depend-

ing on the concentration of the dissolved CO_2. First let us consider the carbonation of CH. That of C-S-H will be considered in the following section.

3.3 Carbonation of Portlandite (CH)

Let's consider the chemical equilibriums listed in Table 3.1. For CO_2 dissolution, we have three chemical equilibriums:

$$K_{H_2O} = \rho_{H^+}\rho_{OH^-}, \tag{3.6}$$

and

$$K_{CO_2^0} = \frac{\rho_{HCO_3^-}\rho_{H^+}}{\rho_{CO_2^0}} \tag{3.7}$$

and

$$K_{HCO_3^-} = \frac{\rho_{CO_3^{2-}}\rho_{H^+}}{\rho_{HCO_3^-}} \tag{3.8}$$

where ρ_i is the concentration of dissolved aqueous species, *e.g.* $\rho_{CO_2^0}$ is the dissolved CO_2 concentration (*i.e.*, $\rho_{CO_2^0} = S_{CO_2}$ in presence of supercritical gas). Combining Eqs. (3.6) to (3.8), we can express $\rho_{CO_3^{2-}}$ by:

$$\rho_{CO_3^{2-}} = \frac{K_{CO_2^0}K_{HCO_3^-}}{K_{H_2O}^2}\rho_{CO_2^0}\rho_{OH^-}^2 \tag{3.9}$$

The presence of CH and $C\bar{C}$ is characterized by a threshold value of the activity products. It means that the activity product of CH and $C\bar{C}$ cannot be above the solubility constant of CH and $C\bar{C}$, respectively.

$$Q_{CH} = \rho_{Ca^{2+}}\rho_{OH^-}^2 \quad \leq \quad K_{CH} \tag{3.10}$$

$$Q_{C\bar{C}} = \rho_{Ca^{2+}}\rho_{CO_3^{2-}} \quad \leq \quad K_{C\bar{C}} \tag{3.11}$$

where $pK_{CH} = 5.2$ and $pK_{C\bar{C}} = 8.5$ at 298 K, values at other temperatures can be found in Appendix A. Together with Eq. (3.9), we easily derive:

$$Q_{C\bar{C}} = \frac{K_{CO_2^0}K_{HCO_3^-}}{K_{H_2O}^2}\rho_{CO_2^0}\rho_{OH^-}^2\rho_{Ca^{2+}} = Q_{CH}\frac{K_{CO_2^0}K_{HCO_3^-}}{K_{H_2O}^2}\rho_{CO_2^0}. \tag{3.12}$$

Setting

$$\rho_{CO_2^0}^{CH} = \frac{K_{C\bar{C}}K_{H_2O}^2}{K_{CH}K_{CO_2^0}K_{HCO_3^-}} \approx 3.10^{-15} \text{ mol/L at 298 K} \tag{3.13}$$

then Eq. (3.12) can be rewritten as:

$$\frac{Q_{C\bar{C}}}{K_{C\bar{C}}} = \frac{Q_{CH}}{K_{CH}} \frac{\rho_{CO_2^0}}{\rho_{CO_2^0}^{CH}} \tag{3.14}$$

Therefore $C\bar{C}$ is not stable for $\rho_{CO_2^0} < \rho_{CO_2^0}^{CH}$ (since $Q_{C\bar{C}}$ is necessarily lower than $K_{C\bar{C}}$) while CH is not stable for $\rho_{CO_2^0} > \rho_{CO_2^0}^{CH}$. The stability domains are summarized in the Fig. 3.1.

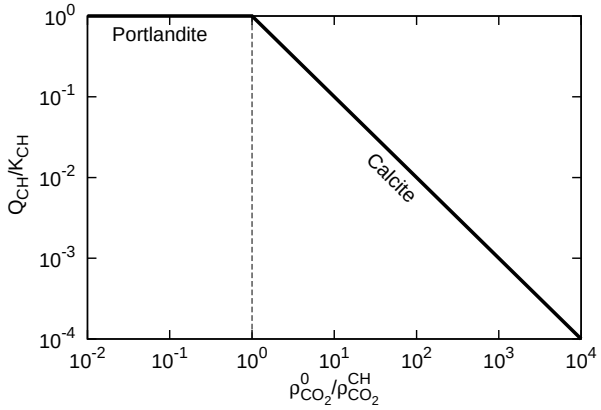

Figure 3.1: Stability domains of portlandite and calcium carbonate.

Before carbonation, *i.e.*, for $\rho_{CO_2^0} < \rho_{CO_2^0}^{CH}$, portlandite is stable. When CO_2 concentration gets higher and exceeds $\rho_{CO_2^0}^{CH}$, portlandite is not stable anymore and starts to dissolve. A kinetic law for this dissolution process is introduced to facilitate numerical convergence. Therefore a simple law for the rate of decrease of CH molar content can be formulated by using a characteristic time, τ_{CH}, as follows

$$\frac{dn_{CH}}{dt} = -\frac{n_{CH}}{\tau_{CH}} \ln\left(\frac{\rho_{CO_2^0}}{\rho_{CO_2^0}^{CH}}\right) = -\frac{n_{CH}}{\tau_{CH}} \frac{(\mu_{CO_2^0(real)} - \mu_{CO_2^0(eq)})}{RT} \tag{3.15}$$

Even if this kinetic law has a numerical purpose, Eq. (3.15) has also a theoretical meaning since the driving force of the kinetics is written as proportional to the difference of chemical potentials (Gibb's potential) of CO_2 between the real state (not at equilibrium) and the equilibrium state.

Due to the high CO_2 concentration used in this study, this characteristic time is chosen in practice as small as possible to oblige the reaction to be as close as possible to equilibrium. The dissolved calcium ion will precipitate into $C\bar{C}$ with the almost same rate. It is also worth noting that the reduction in accessibility when $C\bar{C}$ forms, observed in atmospheric carbonation, is not taken into account. In atmospheric conditions, the material is partially saturated (quite dry), thus the precipitation of $C\bar{C}$ occurs around CH crystals. In this study we mainly work on saturated samples (or very close to full saturation after carbonation), thus we assume $C\bar{C}$ precipitation is homogeneous within the porosity. For lower CO_2 concentration, such as found in atmospheric carbonation, a more physical kinetic law, as found in (Thiery, 2006), should be used.

3.4 Carbonation of calcium silicate hydrates (C-S-H)

C-S-H is a very complex hydration product which contributes to the strength of cement-based materials. Many research works have examined the structure and stoichiometry of C-S-H (Chen et al., 2004; Greenberg and Chang, 1965; Kalousek, 1952; Soler, 2007; Fujii and Kondo, 1981). The dashes in the notation ¨C-S-H¨ indicate that no specific composition is implied. The C/S ratio (molar and in mass) is generally used to characterize the C-S-H. In this work C/S will note the ratio of the molar content between CaO and SiO_2 involved in C-S-H. It is known that the C/S ratio of C-S-H is variable. It is about 1.7 from fresh hydrated Portland cement and tends to become lower during the dissolution process. Modeling the dissolution of the C-S-H (Eq. (3.5)) is an important requirement to understand the process of carbonation of cement-based materials. To reach that purpose we have to model the thermodynamical properties of C-S-H, *e.g.*, the C/S ratio, the water to silica ratio, the molar volume, etc. Literature provides several kind of modeling, starting from the use of empirical or semi-empirical models (Glynn and Reardon, 1990; Koenigsberger et al., 1992) and evolving to solid solution models (Kulik and Kersten, 2001). We will start with a non-continuous discrete model then come to a solid solution model. In the end of this section, a new approach will be proposed to account for the continuous change of the stoichiometric coefficients of C-S-H during decalcification due to carbonation.

3.4.1 A brief introduction of discrete and solid solution models

The carbonation of C-S-H results from two basic dissociation reactions (3.5) and (3.4). There are different types of C-S-H, *e.g.* jennite with C/S ratio of approximately 1.7, tobermorite with C/S ratio of approximately 0.83 and amorphous silica gel with C/S ratio of 0. Table 3.2 lists different forms of C-S-H and their thermodynamical properties proposed by (Lothenbach et al., 2008).

Table 3.2: Different C-S-H type proposed by (Lothenbach et al., 2008).

C-S-H type	C/S	(x,y,z)	$\log K$
Amorphous silica gel	0	(0,1,0)	-2.713
Tobermorite	0.83	(0.83,1,1.3)	-12.19
Jennite	1.67	(1.67,1,2.1)	-17.36

To describe the dissolution of C-S-H, we can use the same approach as the one adopted for the CH dissolution (see Eq. (3.5) and Section 3.3),

$$\frac{Q_{\mathrm{C}_x\mathrm{S}_y\mathrm{H}_z}}{K_{\mathrm{C}_x\mathrm{S}_y\mathrm{H}_z}} = \frac{(K_{\mathrm{CH}})^x (K_{\mathrm{SH}_t})^y}{K_{\mathrm{C}_x\mathrm{S}_y\mathrm{H}_z}} \left(\frac{Q_{\mathrm{CH}}}{K_{\mathrm{CH}}}\right)^x \left(\frac{Q_{\mathrm{SH}_t}}{K_{\mathrm{SH}_t}}\right)^y \tag{3.16}$$

where $Q_{\mathrm{SH}_t} = \rho_{\mathrm{H_4SiO_4^0}}$ is the activity product of amorphous silica. From Eq. (3.16), we can deduce the

stability domains for the amorphous silica SH_t and the different types of C-S-H. Taking jennite as example (see Table 3.2), the equilibrium equation for jennite and amorphous silica is in the following form:

$$\frac{Q_{\text{Jen}}}{K_{\text{Jen}}} = \frac{(K_{\text{CH}})^{1.67}(K_{\text{SH}_t})}{K_{\text{Jen}}} \left(\frac{Q_{\text{CH}}}{K_{\text{CH}}}\right)^{1.67} \left(\frac{Q_{\text{SH}_t}}{K_{\text{SH}_t}}\right) \tag{3.17}$$

The stability domains are shown in Fig. 3.2. At the critical point (dashed line in the plot), $\log(\text{Q}_{\text{CH}}/\text{K}_{\text{CH}}) = -3.57$. Combing with Eq. (3.14) we can get the threshold CO_2 concentration $\rho_{\text{CO}_2}^{\text{SH}_t\text{-Jen}} \approx 10^{-11}$ mol/L.

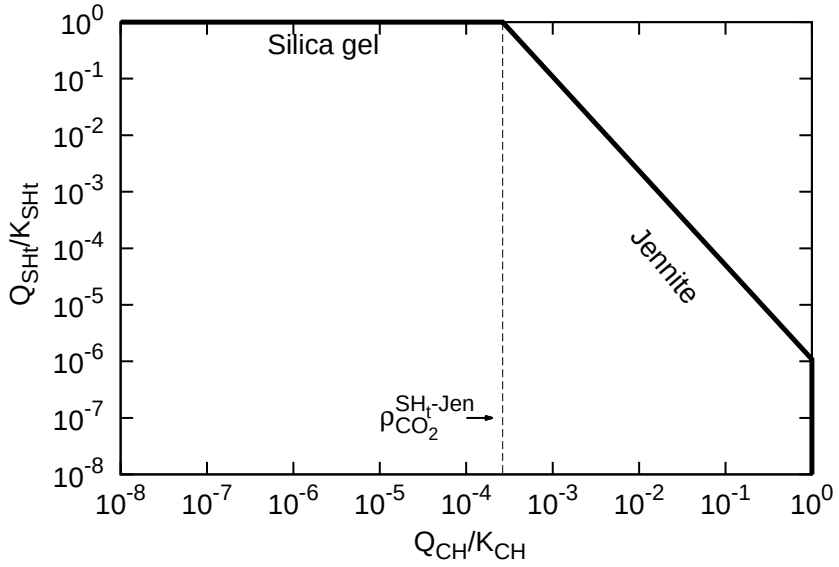

Figure 3.2: Stability domains of jennite and amorphous silica gel.

Similarly we can calculate the stability domains with the system of jennite-tobermorite-silica gel, as shown in Fig. 3.3. The threshold CO_2 concentration for tobermorite $\rho_{\text{CO}_2}^{\text{Tob}} \approx 4.76 \times 10^{-9}$ mol/L and for jennite $\rho_{\text{CO}_2}^{\text{Jen}} \approx 3 \times 10^{-14}$ mol/L. When the CO_2 concentration is lower than $\rho_{\text{CO}_2}^{\text{Jen}}$, jennite is stable, when it lays between $\rho_{\text{CO}_2}^{\text{Jen}}$ and $\rho_{\text{CO}_2}^{\text{Tob}}$, tobermorite is stable, and when CO_2 concentration exceeds $\rho_{\text{CO}_2}^{\text{Tob}}$, amorphous silica gel is stable.

Rather than the discrete model discussed above, a solid solution method which considers different solid poles in equilibrium, is more appropriate to describe the continuous decalcification of C-S-H. Let's consider a solid solution composed of N end-members, M_i respectively ($i = 1, ..., N$). In the framework of the solid solution theory, a reaction between the end-members (poles) to form a solid solution can be written as:

$$\sum_{i=1}^{N} n_i \text{M}_i \rightleftharpoons (M_1)_{n_1}(M_2)_{n_2}...(M_N)_{n_N} \tag{3.18}$$

Each end-member is assumed to be in thermodynamical equilibrium with the aqueous solution. The

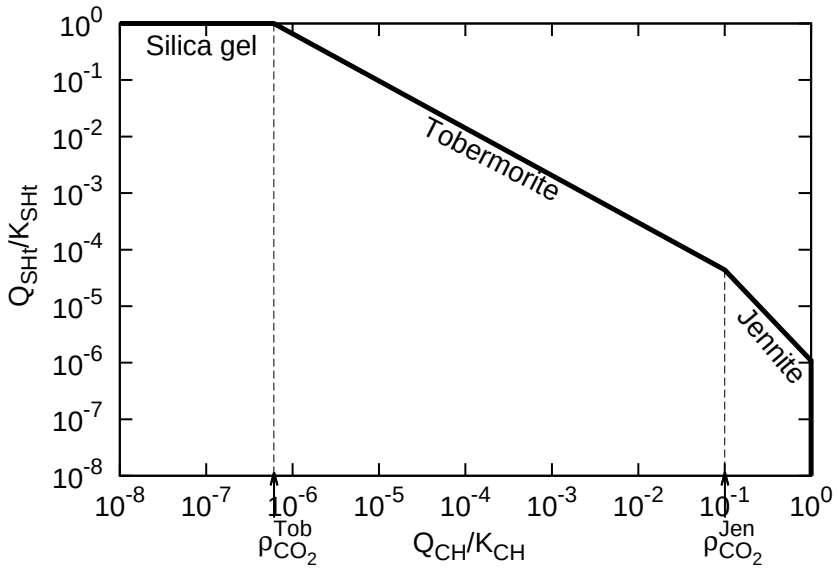

Figure 3.3: Stability domains of jennite, tobermorite and amorphous silica gel.

chemical potential of the end-member i in the solid solution is given by

$$\mu_i = \mu_i^0 + RT \ln a_i \tag{3.19}$$

where μ_i^0 is the chemical potential of the pure end-member. The equilibrium between the end-member i and the aqueous solution results in

$$K_i = \frac{Q_i}{a_i} \tag{3.20}$$

where

$$a_i = \lambda_i X_i \tag{3.21}$$

In Eqs. (3.20) and (3.21), K_i denotes the equilibrium constant, Q_i is the activity product, a_i is the chemical activity, X_i is the mole fraction of the component i within the solid solution and λ_i is the activity coefficient. For a pure end-member, a_i equals to 1, while in the framework of solid solution, a_i follows Eq. (3.21). Thus, for each end-member, the equilibrium between a solid solution and an aqueous solution can be written as

$$\frac{Q_i}{K_i} = \lambda_i X_i \tag{3.22}$$

For an ideal solid solution, the chemical activity a_i equals to the mole fraction X_i, i.e., λ_i=1. While in the non-ideal solid solution, this two values are different. To represent accurately the C-S-H as a solid solution,

the end-members and the stoichiometry coefficients should be carefully chosen. Several possible values are reported in the literature. (Atkinson et al., 1989) used two non-ideal solid solutions to describe the behavior of C-S-H, based on experimental data from (Greenberg and Chang, 1965). For C/S≤0.8, end-members were chosen as S - nC·S·mH (amorphous silica - "tobermorite") and for C/S>0.8, end-members were chosen as nC·S·mH - CH ("tobermorite" - portlandite), where n = 0.833 and m = 0.917. For C/S≥1.8, equilibrium with portlandite is added. (Börjesson et al., 1997) used an non-ideal solid solution of CH - CaH_2SiO_4 for 1<C/S≤1.43, based on data from (Kalousek, 1952). (Rahman et al., 1999) proposed a similar model as (Börjesson et al., 1997), within the C/S range from 1. to 1.5. (Kersten, 1996) proposed a non-ideal binary solid solution CH - $CaHSiO_{3.5}$·H2O based on the experimental data from (Greenberg and Chang, 1965) and (Fujii and Kondo, 1981). (Kulik and Kersten, 2001) described the solubility of C-S-H with a system of two ideal solid solutions: C-S-H-(I): S - tobermorite and C-S-H-(II): tobermorite - jennite. The experimental data of (Greenberg and Chang, 1965) was used to calibrate the model, and the applicable range of C/S ratio is between 0 to 1.7. (Carey and Lichtner, 2006) proposed a non-ideal binary solid solution (S - CH) calibrated with the experimental data from (Chen et al., 2004).

All these models above are able to reproduce the experimental results within the dispersion of experimental data (Soler, 2007). Therefore it is hard to say which one is better. However, the models proposed by (Atkinson et al., 1989), (Kersten, 1996), (Kulik and Kersten, 2001) and (Carey and Lichtner, 2006) are applicable over a wider range of C/S ratio than those of others.

The model of (Kulik and Kersten, 2001) introduced the temperature dependence of equilibrium constant K, from 0 to 50 ℃. They also provided the molar values of the end-members, which is useful for calculating porosity changes. (Lothenbach and Winnefeld, 2006; Lothenbach et al., 2008) used the model of (Kulik and Kersten, 2001) to simulate the hydration of an ordinary portlandite cement (OPC). They have refitted the equilibrium constants proposed by (Kulik and Kersten, 2001). In (Lothenbach et al., 2008) they extended the variable temperature range to 0-100 ℃ for the dissolution of C-S-H. However, they also mentioned that the solubility of jennite and tobermorite doesn't change so much according to temperature.

Here we use an ideal solid solution with four poles, similar as that proposed by (Kulik and Kersten, 2001) with thermodynamical data from (Lothenbach and Winnefeld, 2006). The chemical equilibrium constant of amorphous silica gel dissolution, is considered as temperature-dependent (see Appendix A), while the temperature dependences of jennite and tobermorite dissolution are neglected. The stoichiometric and equilibrium constants for the different poles are listed in Table 3.3.

Combing Eq. (3.16) and (3.22), for each pole, we get

$$\lambda_i X_i = \frac{Q_i}{K_i} = \frac{(K_{\mathrm{CH}})^{x_i}(K_{\mathrm{SH}_t})^{y_i}}{K_{\mathrm{C}_{x_i}\mathrm{S}_{y_i}\mathrm{H}_{z_i}}}\left(\frac{Q_{\mathrm{CH}}}{K_{\mathrm{CH}}}\right)^{x_i}\left(\frac{Q_{\mathrm{SH}_t}}{K_{\mathrm{SH}_t}}\right)^{y_i} \tag{3.23}$$

Table 3.3: Poles of a solid solution of C-S-H

C-S-H (pole)	(x,y,z)	$\log K$ [1]
Amorphous Silica	(0,1,0)	-2.713
Tobermorite I	(2,2.4,4)	-28.26
Tobermorite II	(1.5,1.8,3)	-21.19
Jennite	(1.5,0.9,2.4)	-15.62

[1] data from (Lothenbach and Winnefeld, 2006)

With the hypothesis of ideal solid solution, $\lambda_i = 1$ and $\sum X_i = 1$, therefore we have following equation

$$\sum A_i (q_{\mathrm{CH}})^{x_i} (q_{\mathrm{S}})^{y_i} = 1 \tag{3.24}$$

with

$$A_i = \frac{(K_{\mathrm{CH}})^{x_i} (K_{\mathrm{SH}_t})^{y_i}}{K_{\mathrm{C}_{x_i}\mathrm{S}_{y_i}\mathrm{H}_{z_i}}},\ q_{\mathrm{CH}} = \frac{Q_{\mathrm{CH}}}{K_{\mathrm{CH}}},\ q_{\mathrm{S}} = \frac{Q_{\mathrm{SH}_t}}{K_{\mathrm{SH}_t}} \tag{3.25}$$

Eq. (3.24) indicates that q_{S} is a function of q_{CH}, $q_{\mathrm{S}}(q_{\mathrm{CH}})$, that we can solve. Thus, the mole fraction of each end-member can be calculated by Eq. (3.23) as a function of q_{CH}. The C/S ratio can be attained as a function of q_{CH}, as well, by using Eq. (3.26)

$$\mathrm{C/S} = \frac{\sum X_i x_i}{\sum X_i y_i} = \chi(q_{\mathrm{CH}}) \tag{3.26}$$

The calculated mole fraction for each pole and the C/S ratio as a function of q_{CH} are illustrated in Fig. 3.4. We can see that for q_{CH}=1, which means CH is in equilibrium with the aqueous solution, the C-S-H is in the form of jennite. When q_{CH} decreases, C-S-H will first decalcify to the form of tobermorite, and finally to amorphous silica gel. Thus, C/S ratio drops continuously as q_{CH} decreases.

3.4.2 Proposal of a new model of C-S-H decalcification

We propose here a more general description of the solubility of C-S-H which encompasses the solid solution model previously described. The C/S ratio is considered here as a variable of the model. Defining a unit mole content of C-S-H as a unit mole content of Si (*i.e.* $y = 1$), the dissociation reaction of an infinitesimal small amount of C-S-H can be written formally as

$$\mathrm{C}_x\mathrm{S}_1\mathrm{H}_z \rightleftharpoons x\mathrm{Ca}^{2+} + 2x\mathrm{OH}^- + \mathrm{H}_4\mathrm{SiO}_4^0 + (z - x - 2)\mathrm{H}_2\mathrm{O} \tag{3.27}$$

where x stands for the current C/S ratio and z for the H/S (water to Si) ratio. As defined implicitly, molar quantities related to C-S-H will be defined, in the followings, per unit mole of Si. Accordingly the molar Gibbs energy of C-S-H, $g(x, z)$, depends only on x and z (in addition to the pressure and the temperature

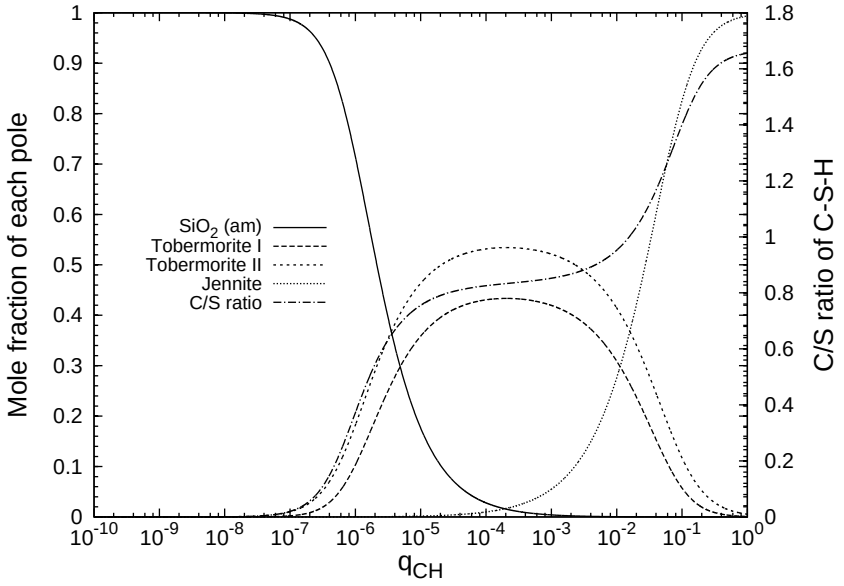

Figure 3.4: Mole fraction of different poles and C/S evolution *vs.* q_{CH}.

that are not explicitly mentioned for sake of simplicity). Furthermore, we will assume, later on, that z is only a function of x : $z(x)$. Therefore the molar Gibbs energy of C-S-H is written as $g(x)$. During the dissociation of an infinitesimal small amount moles of dn C-S-H, the Gibbs free energy G can only decrease spontaneously

$$dG = -\mu_{\mathrm{Ca^{2+}}} d(nx) - \mu_{\mathrm{OH^-}} d(2nx) - \mu_{\mathrm{H_4SiO_4^0}} dn - \mu_{\mathrm{H_2O}} d(n(z-x-2)) + d(ng(x)) \leq 0 \tag{3.28}$$

where μ_i are the chemical potentials of each species. At equilibrium G is minimum and therefore, noting $z' = dz/dx$, we have

$$\left(-x(\mu_{\mathrm{Ca^{2+}}} + 2\mu_{\mathrm{OH^-}}) - \mu_{\mathrm{H_4SiO_4^0}} - (z-x-2)\mu_{\mathrm{H_2O}} + g(x)\right) dn \quad + \tag{3.29}$$

$$\left(-\mu_{\mathrm{Ca^{2+}}} - 2\mu_{\mathrm{OH^-}} - (z'-1)\mu_{\mathrm{H_2O}} + \frac{\partial g}{\partial x}\right) n dx \quad = \quad 0 \tag{3.30}$$

for arbitrary increment dn and C-S-H mole content n. Since the chemical potentials cannot depend on n, we must conclude that

$$\mathcal{A} = x(\mu_{\mathrm{Ca^{2+}}} + 2\mu_{\mathrm{OH^-}}) + \mu_{\mathrm{H_4SiO_4^0}} + (z-x-2)\mu_{\mathrm{H_2O}} - g(x) \quad = \quad 0 \tag{3.31}$$

$$\frac{\partial \mathcal{A}}{\partial x} = (\mu_{\mathrm{Ca^{2+}}} + 2\mu_{\mathrm{OH^-}}) + (z'-1)\mu_{\mathrm{H_2O}} - \frac{\partial g}{\partial x} \quad = \quad 0 \tag{3.32}$$

Eq. (3.31) states that the chemical affinity of reaction (3.27) $\mathcal{A}$ vanishes at equilibrium. Eq. (3.32) states that this chemical affinity must remain to zero, or equivalently, that equilibrium must hold during the decalcification of the C-S-H. Indeed classical expression for the chemical potential entails

$$\mu_{Ca^{2+}} + 2\mu_{OH^-} = \mu^0_{CH} + RT \ln \frac{Q_{CH}}{K_{CH}} \tag{3.33}$$

$$\mu_{H_4SiO_4^0} + (t-2)\mu_{H_2O} = \mu^0_{SH_t} + RT \ln \frac{Q_{SH_t}}{K_{SH_t}} \tag{3.34}$$

where $t = z(0)$ is the hydration level of the amorphous silica, SH_t, obtained after a complete decalcification of the C-S-H. K_{CH} and K_{SH_t} are the equilibrium constants for the dissolution of portlandite and amorphous silica. Combining Eqs. (3.31) - (3.34) will then provide two new equations in the form of (3.35) and (3.36):

$$x \ln\left(\frac{Q_{CH}}{K_{CH}}\right) + \ln\left(\frac{Q_{SH_t}}{K_{SH_t}}\right) = \ln a(x) \tag{3.35}$$

$$\ln\left(\frac{Q_{CH}}{K_{CH}}\right) = \frac{\partial \ln a}{\partial x} \tag{3.36}$$

where we defined $RT \ln a(x) = g(x) - x\mu^0_{CH} - \mu^0_{SH_t} - (z-t-x)\mu_{H_2O}$. Note that $\ln a(0) = 0$ since we have to meet the molar Gibbs energy of the amorphous silica in the form $g(0) = \mu^0_{SH_t}$. Hence, from Eq. (3.36) we have:

$$\int_0^x \ln\left(\frac{Q_{CH}}{K_{CH}}\right) dx = \ln a(x) \tag{3.37}$$

then Eq. (3.35) can be rewritten as:

$$\ln\left(\frac{Q_{SH_t}}{K_{SH_t}}\right) = \ln a(x) - x\frac{\partial \ln a}{\partial x} = -\int_0^x x\frac{\partial^2 \ln a}{\partial x^2} dx \tag{3.38}$$

Eq. (3.37) shows that x and $\frac{Q_{CH}}{K_{CH}}$ are related through a constitutive-like equation of the form

$$x = \chi(\frac{Q_{CH}}{K_{CH}}) \tag{3.39}$$

From Eq. (3.38) and (3.39), we infer that there is a relation between $\frac{Q_{SH_t}}{K_{SH_t}}$ and $\frac{Q_{CH}}{K_{CH}}$ in the form

$$\ln\left(\frac{Q_{SH_t}}{K_{SH_t}}\right) = -\int_0^{\frac{Q_{CH}}{K_{CH}}} \frac{\chi(q)}{q} dq \tag{3.40}$$

resulting in a typical pattern shown in Fig. 3.5.

It is noteworthy that this theory encompasses the solid solution model involving any number of poles with coefficient (x_i,y_i,z_i). Indeed, the solid solution theory shows that $X_i = A_i q^{x_i}(F)^{y_i}$, where $F(q) =$

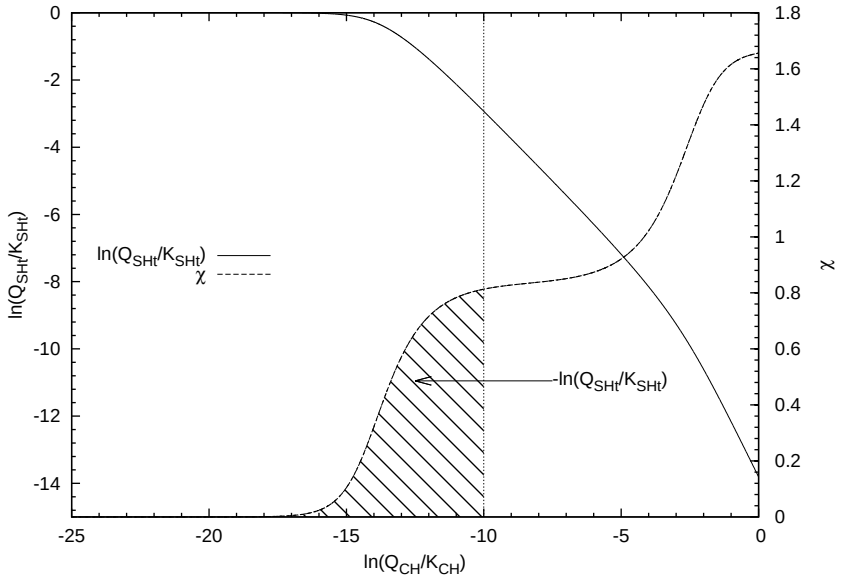

Figure 3.5: A typical pattern of the relationship between $\frac{Q_{\mathrm{SH}_t}}{K_{\mathrm{SH}_t}}$ and $\frac{Q_{\mathrm{CH}}}{K_{\mathrm{CH}}}$.

$\frac{Q_{\mathrm{SH}_t}}{K_{\mathrm{SH}_t}}$. It is then easy to show that the average stoichiometric coefficients are given by $x = X(q)$ and $y = Y(q)$ with

$$X(q) = \sum_i (x_i A_i q^{x_i} F^{y_i}) \tag{3.41}$$

$$Y(q) = \sum_i (y_i A_i q^{x_i} F^{y_i}) \tag{3.42}$$

Since the solid fraction has to satisfy $\sum X_i = 1$, namely

$$1 = \sum_i (A_i q^{x_i} F^{y_i}) \tag{3.43}$$

Hence deriving this last equation with respect to q leads to

$$\frac{F'}{F} = -\frac{X/Y}{q} \tag{3.44}$$

which is akin to Eq. (3.40). Eq. (3.40) is a generalization of the mass action law for C-S-H with variable C/S ratio. To confirm this relationship we used the result of an experiment conducted by Greenberg and Chang (Greenberg and Chang, 1965). In these experiments the solubilities of reaction mixtures of calcium oxide, silica and water were investigated (0.805 g of SiO_2 was poured in 100 ml of water with varying

additions of CaO). The calcium ion concentration, the silicic acid concentration (H_4SiO_4 + $H_3SiO_4^-$ + $H_2SiO_4^{2-}$) and the *p*H were measured. They are reported in Fig. 3.6. In Fig. 3.7 we plot the fraction $\frac{Q_{SH_t}}{K_{SH_t}}$ obtained on one hand, from Eq. (3.40), and on the other hand, from the direct use of the Greenberg's results. To perform this latter calculation, the ion activity product of silica gel, Q_{SH_t}, is approximated by the concentration of the monosilicic acid $H_4SiO_4^0$. The solubility constant, K_{SH_t}, is 1.93 mM. The comparison between the model (3.40) and the experiments is fairly good.

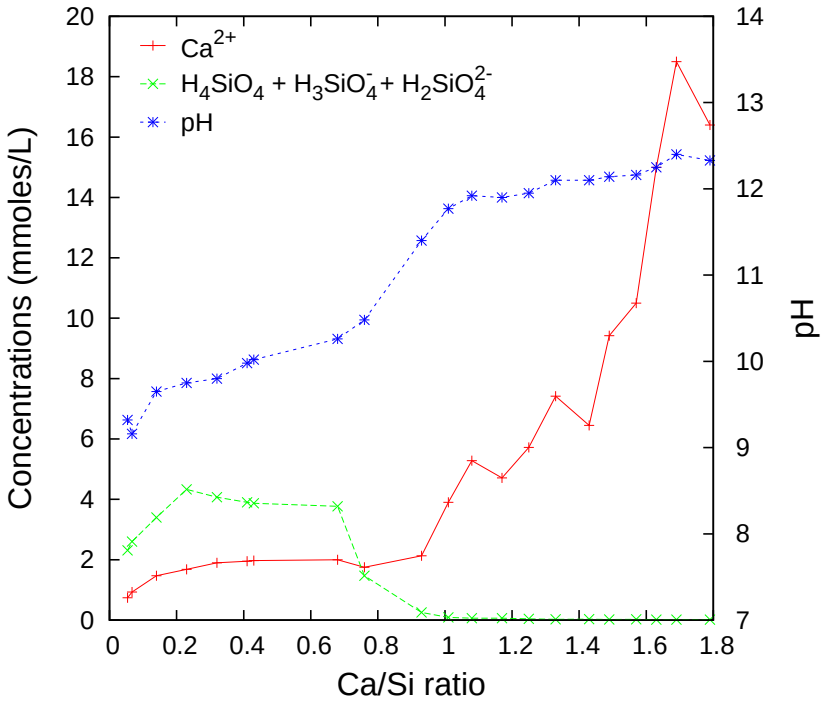

Figure 3.6: Composition of a calcium-silicon solution in equilibrium with its solid phase *vs*. C/S ratio. Results reported from (Greenberg and Chang, 1965).

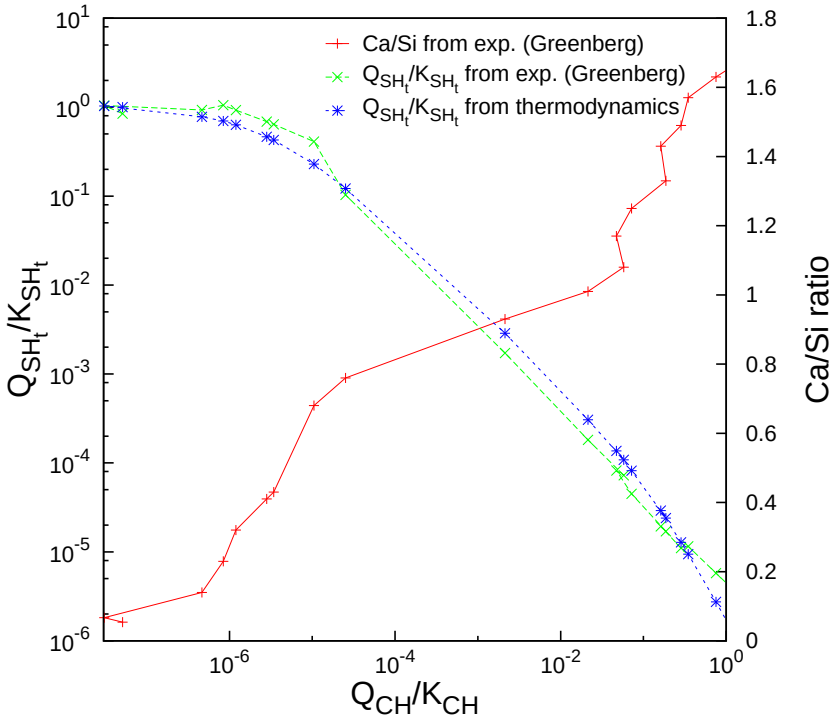

Figure 3.7: The fraction $\frac{Q_{\mathrm{SH}_t}}{K_{\mathrm{SH}_t}}$ computed with Eq. (3.40) is compared to the direct use of the Greenberg's experiment.

3.5 Porosity changes

The change in porosity, $\phi - \phi_0$, induced by the precipitation-dissolution of the various solid compounds can be easily accounted for by a simple balance of volume.

$$\begin{aligned}\phi - \phi_0 = &- V_{\mathrm{CH}}(n_{\mathrm{CH}} - n^0_{\mathrm{CH}}) - V_{\mathrm{C\bar{C}}}(n_{\mathrm{C\bar{C}}} - n^0_{\mathrm{C\bar{C}}}) \\ &- V_{\text{C-S-H}} n_{\mathrm{Si}} + V^0_{\text{C-S-H}} n^0_{\mathrm{Si}}\end{aligned} \tag{3.45}$$

In Eq. (3.45), V_i is the molar volume of the solid compound i (L/mol), n_i and n_i^0 are the current and initial solid content of i (mol/L). We used $V_{\mathrm{CH}} = 33$ cm^3/mol for the molar volume of portlandite and $V_{\mathrm{C\bar{C}}} = 37$ cm^3/mol for the molar volume of calcite.

However there is a lack of data regarding the molar volume of C-S-H. It is theoretically a function of the C/S ratio, x, and the Water/Si ratio, z, as seen previously ($V_{\text{C-S-H}}$ is the partial derivative of g with respect to the pressure). The molar volume of $C_{1.7}SH_{1.4}$ is approximately 64.5 cm^3/mol, that of $C_{1.7}SH_{2.1}$ is 78.8 cm^3/mol and that of $C_{1.7}SH_4$ is 113.6 cm^3/mol (Chen et al., 2004). On the other hand that of amorphous silica un-hydrated (*i.e.* $t = 0$), is approximately 29 cm^3/mol (Lothenbach et al., 2008). Therefore, in absence of knowledge, we use a linear function for $V_{\text{C-S-H}}(x)$ and $z(x)$: $V_{\text{C-S-H}}(x) = x/x_0 V^0_{\text{C-S-H}} + (1 - x/x_0)V_{\mathrm{SH}_t}$, $z(x) = x/x_0 z^0_{\text{C-S-H}} + (1 - x/x_0)t$ with $x_0 = 1.7$, $V_{\mathrm{SH}_t} = 29$ cm^3/mol, $V^0_{\text{C-S-H}} = 78$ cm^3/mol, $z^0_{\text{C-S-H}} = 2.1$ and $t = 0$. The calculated $V_{\text{C-S-H}}(x)$ and $z(x)$ as function of x is shown in Fig. 3.8.

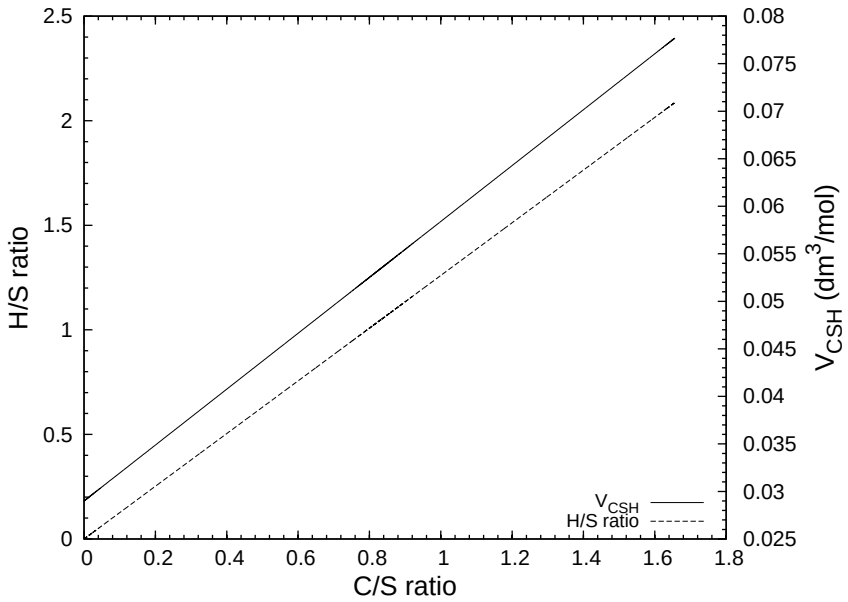

Figure 3.8: $V_{\text{C-S-H}}$ and H/S ratio z as function of C/S ratio x.

3.6 Illustration of the evolution of the solid volume assemblage

To illustrate the evolution of the solid volume assemblage, the carbonation of a homogeneous representative volume element (RVE) of cement paste is presented. The cement paste contains initially 5.16 mol/L of portlandite (CH) and 3.9 mol/L of jennite (*i.e.* $C_{1.7}SH_{2.1}$), the same value of a well hydrated Class H cement with water/cement ratio (W/C) of 0.38 (Huet et al., 2010). Porosity is chosen as 40%, the same as predicted in (Huet et al., 2010). Temperature is set to 25°C. A small value (here about 1×10^{-16} mol/L) is affected to the initial aqueous CO_2 concentration in the pore solution of the material, to avoid the dissolution of the portlandite, and this value increases to 0.049 mol/L (the approximate solubility of atmospheric CO_2 at 25°C) in 72000 s. There is no mass transport at the boundary due to diffusion. In the simulation we use the model given by Eq. (3.40). A fit of the experimental curve obtained by (Greenberg and Chang, 1965) is used for the C/S ratio of C-S-H, see Fig. 3.9.

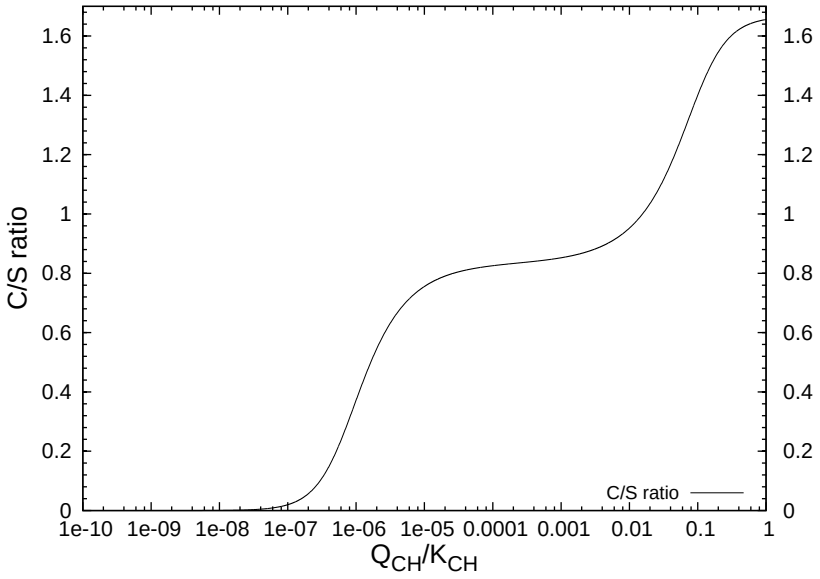

Figure 3.9: C/S ratio *vs.* $\frac{Q_{\mathrm{CH}}}{K_{\mathrm{CH}}}$ used in this work, fitted from the experimental curve obtained by (Greenberg and Chang, 1965).

Aqueous CO_2 concentration and pH value versus time is presented in Fig. 3.10. The initial pH value is 12.4 and drops to 5.8 when CO_2 concentration reaches 0.049 mol/L.

Solid volume assembling (*i.e.* $n_i V_i$) for CH, $C\bar{C}$, and C-S-H is shown in Fig. 3.11. Portlandite content starts to decrease when CO_2 concentration reaches 3 10^{-15} mol/L, and is fully dissolved quickly. Carbonation of C-S-H starts at the same time. The C/S ratio of C-S-H decreases gradually when CO_2 concentration increases. The C/S ratio drops to 0 when CO_2 concentration reaches to 1.2 10^{-6} mol/L. Porosity decreases from 0.4 to 0.379 when portlandite is fully dissolved, when C-S-H is fully carbonated, porosity drops to

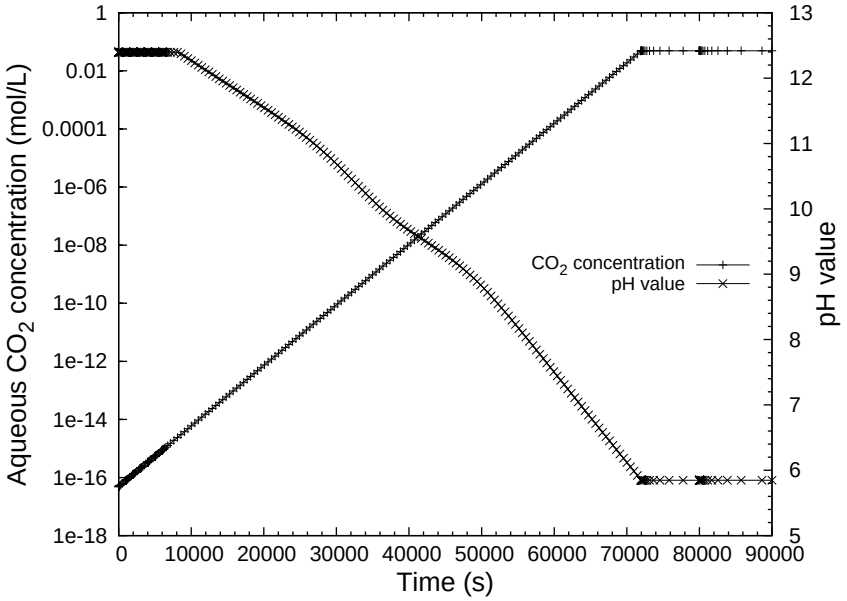

Figure 3.10: CO_2 concentration and pH value versus time in the cement.

0.33. The carbonation of both portlandite and C-S-H will make the porosity decrease, since the generated calcite and amorphous silica occupy more space than the dissolved hydration products. In this case, due to the absence of transport, the dissolution of the generated calcite does not occur. The leaching effect, as well as the dissolution of calcite due to boundary condition, will be illustrated and discussed in the following chapters.

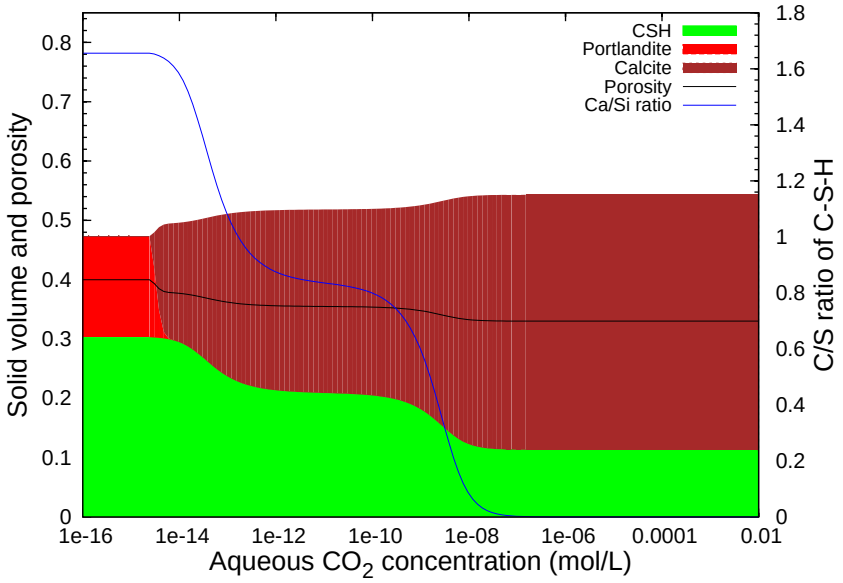

Figure 3.11: Evolution of the solid volume assemblage *vs.* CO_2 concentration in the case of a class H cement paste (W/C=0.38).

3.7 Conclusion

This chapter deals with the carbonation reactions taking place in cement-based materials. We consider homogeneous chemical reactions in the pore solution. The equilibrium constants for each reaction taking place in aqueous solution are considered as temperature-dependent. It is assumed that all chemical processes are in thermodynamical equilibrium except for some of them (dissolution reactions) for which a kinetics is introduced for numerical reasons.

Dissolution and precipitation reactions for CH and $C\bar{C}$ are described by mass action laws and threshold of ion activity products to identify the stability of the solid phases. Temperature dependence for the chemical equilibrium has also been taken into account here. A chemical kinetics for the dissolution of CH is introduced to facilitate numerical convergence. In this study, the characteristic time of CH dissolution is chosen as small as possible during simulation to achieve a quick dissolution, due to the high CO_2 concentration encountered. In the following chapters we generally use 2000 s for scCO2 boundary condition and 400000 s for low CO_2 concentration (in case of atmospheric CO_2 pressure). A future work could include a more physical kinetic law, *e.g.*, provided by (Thiery, 2006) which considers the reduction in accessibility when $C\bar{C}$ forms.

Discrete and solid solution methods for C-S-H dissolution have been introduced. Temperature dependence of amorphous silica gel dissolution is considered, while that of jennite and tobermorite is neglected since it is reported that the solubility product of them does not change so much according to temperature.

Comparing with discrete method, the solid solution method is more appropriate to describe the continuous decalcification of C-S-H. A generalization of the mass action law is proposed to C-S-H. This theory encompasses the solid solution model involving any number of poles of coefficient (x_i,y_i,z_i), and is clearly easier to implement in a transport-reaction modeling. Thus in the following chapters, we will use only this general approach for the description of C-S-H carbonation, rather than the discrete or solid solution methods.

The changes in porosity induced by the precipitation and dissolution reactions have also been taken into account, in a simple way, and illustrated in the case of homogeneous carbonation of a representative volume element. Without transport, the carbonation of both portlandite and C-S-H is responsible for a porosity reduction. It's hard to compare the porosity change with experiment results in this chapter since in most experiments the porosity distribution after carbonation is heterogeneous. One homogeneous carbonation experiment has been conducted by (Fabbri et al., 2009) with scCO2, which will be discussed in chapter 7. They measured an homogeneous porosity drop from 0.41 to 0.26, about 0.15, while our prediction is about 0.07 here. This difference could come from the fact that we only consider CH and C-S-H as carbonatable hydration products, but could also comes from the molar volume we chose for C-S-H. The reported molar volume and H/S ratio of C-S-H vary a lot from different literatures. In our work we use values provided by (Lothenbach et al., 2008). Values provided by other authors, *e.g.*, $V_{\mathrm{SH}_t} = 43$ cm^3/mol and $t = 2$ proposed by (Antoine Morandeau, 2012; Thiéry et al., 2011, 2012) could explain better the porosity change after carbonation. A serious study of these values will be worthwhile in a future work.

Chapter 4

Reactive transport modeling

4.1 Introduction

The system is not only controlled by the chemical equilibrium but also by the transport of different species. The advection of $scCO_2$, the diffusion of aqueous CO_2 permit carbonation taking place deep into the cement-based material, and the change of porosity as the result of carbonation could further enhance or limit the transport speed. The coupling of transport and chemical equilibrium together should be clear in order to describe the physical-chemical phenomena taking place in the cementitious materials.

In this study, we deal with an unsaturated porous material with two immiscible fluid phases: a gas phase consisting in wet supercritical CO_2 (supercritical CO_2 with dissolved water) and a liquid phase consisting in the interstitial solution. Transport phenomena taking place in these two phases will be explained in this chapter. First, the field equations governing the coupling between transport and chemistry are presented. In the following section the capillary pressure and the saturation of the two-phase system are introduced. Then the transport parameters of gas and liquid phase as well as aqueous species are presented in detail. Advection of gas and liquid phases are considered. For the dissolved aqueous species, electro-diffusion (Nernst-Plank equation) and the advection are taken into account.

4.2 Field equations

4.2.1 Atom mass balance equation

The coupling between transport and chemical reactions is treated thanks to a set of mass balance equations. The first subset of equations consists in mass balance equations applied to atoms such as carbon (C), calcium (Ca), silicon (Si), potassium (K) and chlorine (Cl). For each atom (A = C, Ca, Si, K, Cl) we

have

$$\frac{\partial n_{\mathrm{A}}}{\partial t} = -\mathrm{div}\ \underline{w_{\mathrm{A}}} \tag{4.1}$$

where n_{A} stands for the total molar content of element A per unit volume of porous medium. There are 3 contributions to n_{A} associated to the liquid, gas, and solid phases : $n_{\mathrm{A}} = \phi S_L \rho_{\mathrm{A}}^{\mathrm{L}} + \phi S_G \rho_{\mathrm{A}}^{\mathrm{G}} + n_{\mathrm{A}}^{\mathrm{S}}$.

For example, let us consider the carbon element A = C. The carbon concentration in the liquid phase is

$$\rho_{\mathrm{C}}^{\mathrm{L}} = \rho_{CO_2^0} + \rho_{HCO_3^-} + \rho_{CO_3^{2-}} + \rho_{CaHCO_3^+} + \rho_{CaCO_3^0} \tag{4.2}$$

where the ρ_i are linked by mass action laws and equilibrium constants listed in the Table 3.1. The carbon concentration in the gas phase is

$$\rho_{\mathrm{C}}^{\mathrm{G}} = (1 - y_{H_2O})/V_{\mathrm{G}} \tag{4.3}$$

where y_{H_2O} is given by Eq. (2.19) and V_{G} is the molar volume of the gas mixture given by Eq. (2.3). The carbon solid content is the mole content of the calcium carbonate : $n_{\mathrm{C}}^{\mathrm{S}} = n_{C\bar{C}}$. Obviously the total molar flow of A, $\underline{w_{\mathrm{A}}}$, can be decomposed in the same manner as n_{A}.

4.2.2 Conservation of total mass

Instead of writing mass balance equation for elements H and O, we preferred to write a total mass balance and a charge balance. The first one reads

$$\frac{\partial m}{\partial t} = -\mathrm{div}\ \underline{w} \tag{4.4}$$

In Eq. (4.4) m stands for the total mass. There are 3 contributions to m : $m = \phi S_L \rho_{\mathrm{L}} + \phi S_G \rho_{\mathrm{G}} + m_{\mathrm{S}}$. Similarly there are 2 contributions to the total mass flow, $\underline{w}$, : $\underline{w} = \rho_{\mathrm{L}} \underline{v_{\mathrm{L}}} + \rho_{\mathrm{G}} \underline{v_{\mathrm{G}}}$. These liquid and gas mass flows are given by a generalized Darcy's law in Section 4.4 and 4.5.

4.2.3 Charge balance

It is known that there is a balance of charge for each chemical reaction (there is no source of charge in the chemical reaction). As a consequence we have a global charge balance equation of the form

$$\mathrm{div}\ \underline{i} = 0 \tag{4.5}$$

where $\underline{i}$ stands for the ionic current reading

$$\underline{i} = \sum_i z_i \underline{w_i} \tag{4.6}$$

where the summation applies on the set of electrolyte ions. The ionic flow $\underline{w_i}$ is given by a Nernst-Planck Eq. (4.16). In this law, each ion has its own diffusion coefficient according to its size (see Section 4.6).

Eqs. (4.1, 4.4 and 4.5) are the set of the field equations governing the coupling between transport and chemistry.

4.3 Capillary pressure and saturation of two-phase system

In the porous material, due to the interfacial tension between gas and liquid phase, there is a difference of pressure across the interface between two phases. This pressure difference, called as capillary pressure, is defined as: $P_C = P_G - P_L$. The capillary pressure plays a key role in the determination of the saturation in porous material.

The liquid water saturation, S_L is measured for isothermal conditions at room temperature (T=23 ℃) as a function of relative humidity HR by different authors (Baroghel-Bouny, 2007; Thiery, 2006) with general form proposed by van Genuchten(van Genuchten, 1980).

$$S_L = [1 + (-\alpha \ln(\mathrm{HR}))^{\frac{1}{1-\beta}}]^{-\beta} \tag{4.7}$$

The values α and β have been assessed for desorption or adsorption with a least squares fit. For cement paste C45 (see Fig. 4.1), $\alpha = 5.72$ and $\beta = 0.444$, parameters for different cement paste are listed in Table 4.1.

Capillary pressure is related to relative humidity through the Kelvin's law:

$$P_C = -\frac{RT \ln(\mathrm{HR})}{V_{\mathrm{H_2O}}} \tag{4.8}$$

The relationship between capillary pressure and saturation can be obtained by Eq. (4.7) and (4.8).

$$P_C = -\frac{\rho_{\mathrm{w}} RT}{\alpha M_{\mathrm{w}}} (S_L^{-1/\beta} - 1)^{1-\beta} \tag{4.9}$$

Fig. 4.2 is an example of the relationship between liquid water saturation S_L and capillary pressure P_C for cement type CN calculated by Eq. (4.9).

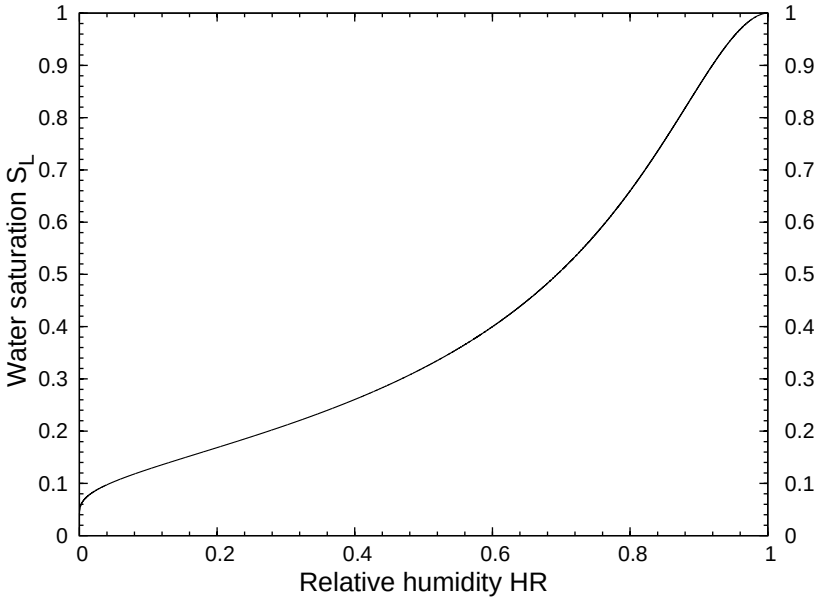

Figure 4.1: The relationship between liquid water saturation S_L and relative humidity HR for cement type CN calculated by Eq. (4.7).

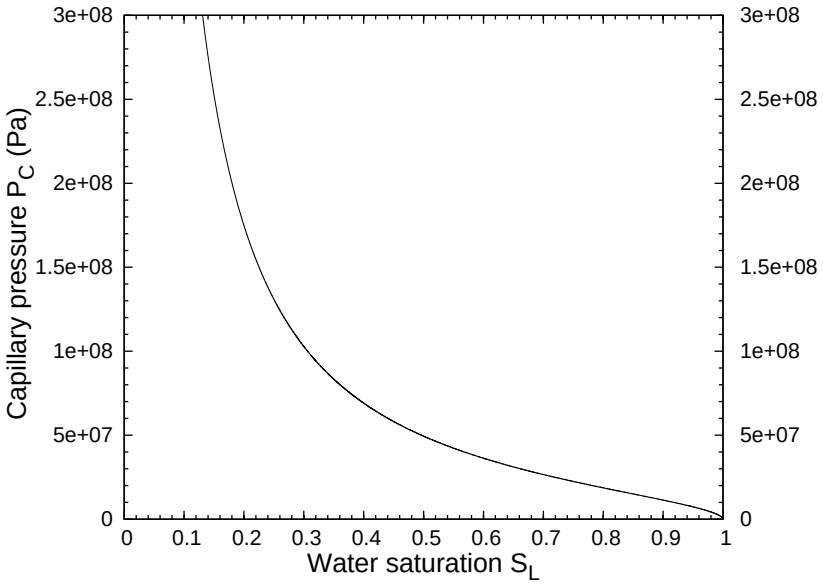

Figure 4.2: The relationship between liquid water saturation S_L and capillary pressure P_C for cement type CN calculated by Eq. (4.9).

Table 4.1: Fitted parameters α and β for different materials

Material reference	**C45 ∼ CN**	**CO**	**CH**
Water-to-cement ratio (W/C)	0.45	0.35	0.20
Water-to-binder ratio (W/B)	0.45	0.35	0.18
Silica fume to cement ratio (SF/C)			0.1
α	5.72	3.61	1.41
β	0.444	0.461	0.513

4.4 Transport of the liquid phase

The transport of liquid in unsaturated media is controlled by the extended Darcy's law. This law characterizes the viscous flow of an incompressible fluid driven by liquid pressure gradient, thus, the advection of liquid phase, $\underline{v_{\mathrm{L}}}$, is written as follows:

$$\underline{v_{\mathrm{L}}} = -\frac{K_l}{\mu_{\mathrm{L}}} k_{rl}(S_L)\underline{\nabla P_{\mathrm{L}}} \tag{4.10}$$

where μ_{L}, P_{L} denote the dynamic viscosity of liquid and the liquid pressure, respectively. K_l is the intrinsic permeability of cement based materials for water. The relative permeability, k_{rl}, depends on the pore network, the characteristics of the fluid, as well as the saturation degree in the cement pores.

4.4.1 Dynamic viscosity of liquid

The dynamic viscosity of liquid, μ_{L}, is related with temperature, liquid pressure and the dissolved aqueous components. For pure water at one atmosphere with temperature between 20 to 100^{o}C, there is an empirical relationship between viscosity and temperature proposed in (Weast et al., 1988), written as:

$$\log_{10} \frac{\mu_{L(T)}}{\mu_{L(20)}} = \frac{1.3272(20-T) - 0.001053(T-20)^2}{T+105} \tag{4.11}$$

where $\mu_{L(T)}$ is the dynamic water viscosity at temperature T (in ^{o}C), with the unit of mPa·s, $\mu_{L(20)}$ is water viscosity at 20^{o}C, equals to 1.002 mPa·s. The calculated profile of water dynamic viscosity as a function of temperature is shown in Fig. 4.3. Pressure dependence is not considered here since water viscosity change little with pressure. The influence of dissolved aqueous components is also neglected here, which could be introduced in the future work.

4.4.2 Intrinsic permeability

The intrinsic permeability, K, which is a characteristic of the cement, is related with the microstructure of the porous material (pore sizes, connectivity...). Thus this value is not constant during carbonation. In the work of (van Genuchten, 1980), K is considered as a function of porosity, based on Kozeny-Carman equation:

$$K = K^0 (\frac{\phi}{\phi_0})^3 (\frac{1-\phi_0}{1-\phi})^2 \tag{4.12}$$

where K^0 is the intrinsic permeability before carbonation, with the porosity ϕ_0. This equation considers the influence of the porosity change during carbonation, when ϕ=ϕ_0, K equals to K^0, when ϕ<ϕ_0, K is smaller

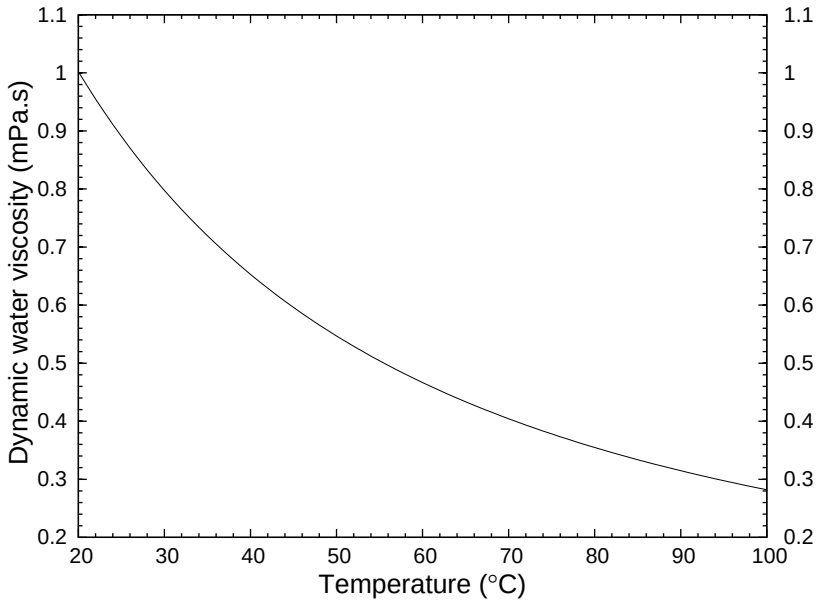

Figure 4.3: Dynamic water viscosity as a function of temperature at one atmosphere, following (Weast et al., 1988).

than K^0, reflecting the clogging of the pores. The evolution of the pore size distribution, corresponding with the disappearance of micro-crystals of CH and C-S-H and the generation of $C\bar{C}$ and SH_t, is not taken into account here.

Theoretically, intrinsic permeability for liquid and gas should be the same since the intrinsic permeability is a characteristic of the solid. While in the experiment a difference of several orders of magnitude between these two values is observed and discussed by different authors (Baroghel-Bouny, 2007; Fabbri et al., 2009; Thiery et al., 2008). In our work we use different intrinsic permeability for liquid and gas phase to better fit experiment observations, i.e., K_l for liquid and K_g for wet CO_2.

4.4.3 Relative permeability to liquid

Few experimental results exist concerning the relative permeability of cement-based materials to gas and even less to liquid. Nevertheless, analytical expressions can be derived using Mualem's model (van Genuchten, 1980):

$$k_{rl}(S_L) = \sqrt{S_L}(1 - (1 - S_L^{1/\beta})^{\beta})^2 \tag{4.13}$$

where β is the same value as in Eq. (4.7). A curve of k_{rl} vs. S_L could be generated by Eq. (4.13), which is illustrated Fig. 4.4.

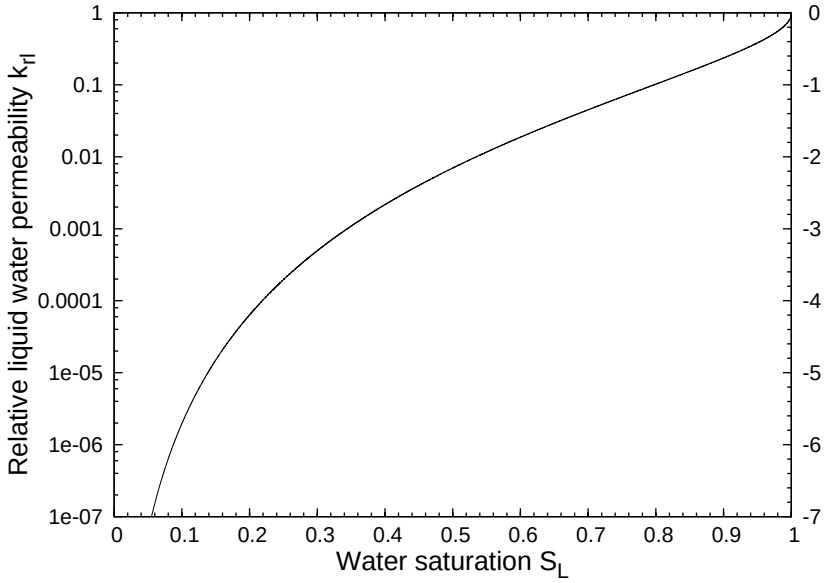

Figure 4.4: The relationship between liquid water saturation S_L and relative liquid water permeability k_{rl} for cement type CN calculated by Eq. (4.13).

4.5 Transport of gas phase

The transport of gas phase is similar to the liquid transport. The transport equation is written as:

$$\underline{v_{\mathrm{G}}} = -\frac{K_g}{\mu_{\mathrm{G}}} k_{rg}(S_L)\underline{\nabla P_{\mathrm{G}}} \tag{4.14}$$

where μ_{G} is the dynamic viscosity of CO_2, K_g is the intrinsic permeability of cement for gas and k_{rg} is the relative permeability to gas, responding to saturation S_L.

4.5.1 Dynamic viscosity of gas

Here we consider dynamic viscosity of gas equals to that of pure CO_2, due to the small mole fraction of H_2O in wet CO_2 phase. In our work we follow the work of (Fenghour et al., 1998) to calculate μ_{G}. Details can be found in Appendix B. The calculated viscosity of CO_2 at different temperature is shown in Fig. 4.5.

4.5.2 Relative permeability to gas

For the relative permeability to gas, the result derived in (Parker et al., 1987) and (Luckner et al., 1989) is used:

$$k_{rg}(S_L) = \sqrt{1 - S_L}(1 - S_L^{1/\beta})^{2\beta} \tag{4.15}$$

A curve of k_{rg} vs. S_L could be generated using expression (4.15), see Fig. 4.6.

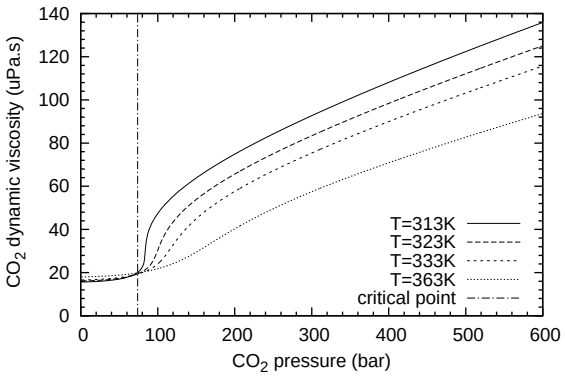

Figure 4.5: CO_2 viscosity at different temperature.

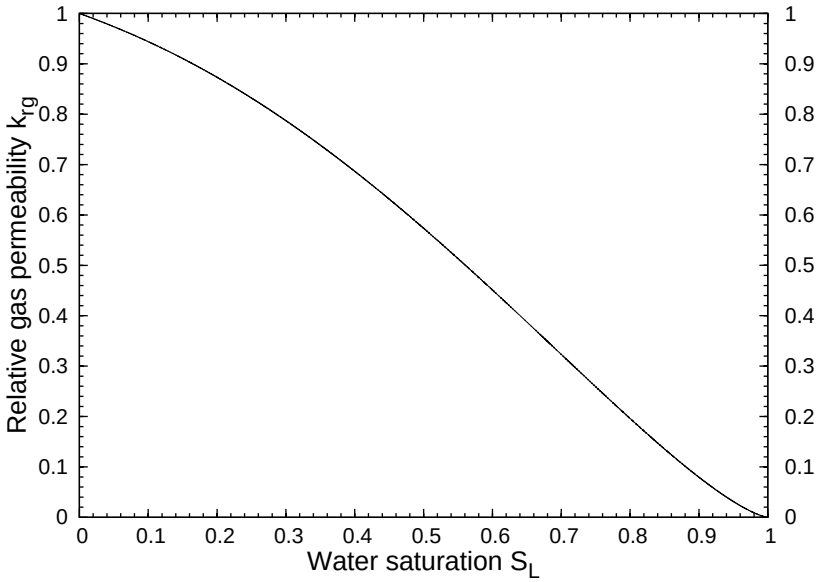

Figure 4.6: The relationship between liquid water saturation S_L and relative liquid water permeability k_{rg} for cement type CN calculated by Eq. (4.13).

4.6 Transport of aqueous species

Concerning the transport equations, we consider the electro-diffusion (Nernst-Plank equation) and the advection of each aqueous species, as indicated in Eq. (4.16).

$$\underline{w_i} = -D_i \left(\underline{\nabla \rho_i} + \rho_i \frac{F z_i}{RT} \underline{\nabla \psi} \right) + \rho_i \underline{v_{\mathrm{L}}} \tag{4.16}$$

In the equation, F is the Faraday's constant (96485 C mol^{-1}), R is the gas constant (8.31 J mol^{-1} K^{-1}), T is the absolute temperature in K, while z_i and ρ_i stand for the ionic valence and the concentration, $\underline{v_{\mathrm{L}}}$ is the advection of liquid phase, discussed in Section 4.4. The first term refers to the diffusion effect due to the concentration gradient (in agreement with the Fick's law), and the second part accounts for the electric effect. The effective diffusion coefficient D_i (dm^2 s^{-1}) of each species i is calculated taking into account the porosity changes as well as the degree of saturation. For a saturated cement paste, (Tognazzi and Ollivier, 1998; Mainguy et al., 2000) proposed an empirical relationship between the effective diffusion coefficient and the porosity of sound materials. For ϕ<0.92, we have:

$$D_i = \frac{D_i^0}{D_{Ca^{2+}}^0} \times 2.35\ 10^{-11} e^{9.95\phi} = D_i^0 \times 2.9\ 10^{-4} e^{9.95\phi} \tag{4.17}$$

D_i^0 is the diffusion coefficient of species i in pure water, which can be achieved either from experimental measurement or by Stokes-Einstein equation in the form as below:

$$D_i^0 = \frac{k_B T}{6\pi \mu_L r} \tag{4.18}$$

where k_B=1.3806488 10^{-23} J/K is Boltzmann's constant, T is absolute temperature in K, μ_L is liquid water viscosity and r is the radius of the aqueous species. The collected diffusion coefficients of different aqueous species at T=298 K is listed in Table 4.2. Note that the diffusion coefficients of Na^+ and K^+ are quite similar, it is thus acceptable to assimilate these two species.

For unsaturated material the diffusion coefficient depends on the saturation degree through an additional coefficient $\tau^*(S_L)$. As proposed by (Bažant and Najjar, 1972) and used by (Bary and Sellier, 2004) in their modeling of the carbonation of unsaturated concrete, this coefficient takes the form:

$$\tau^*(S_L) = \frac{1}{1 + 625(1 - S_L)^4} \tag{4.19}$$

Thus, we can express D_i as:

$$D_i = D_i^0 \times 2.9\ 10^{-4} e^{9.95\phi} \tau^*(S_L) \tag{4.20}$$

Table 4.2: Diffusion coefficients of different aqueous species at T=298 K

Species	Value (dm^2/s)	Reference
$D^0_{OH^-}$	$5.273\ 10^{-7}$	(Weast et al., 1988)
$D^0_{H^+}$	$9.311\ 10^{-7}$	(Weast et al., 1988)
$D^0_{CO_{2(aq)}}$	$1.91\ 10^{-7}$	(Weast et al., 1988)
$D^0_{HCO_3^-}$	$1.185\ 10^{-7}$	(Weast et al., 1988)
$D^0_{CO_3^{2-}}$	$9.55\ 10^{-8}$	r=$2.25\ 10^{-10}$ m
$D^0_{Ca^{2+}}$	$7.92\ 10^{-8}$	(Thiery, 2006)
$D^0_{CaHCO_3^+}$	$1.07\ 10^{-7}$	r=$2.\ 10^{-10}$ m
$D^0_{H_4SiO_4^0}$	$1.07\ 10^{-7}$	r=$2.\ 10^{-10}$ m
$D^0_{H_3SiO_4^-}$	$1.07\ 10^{-7}$	r=$2.\ 10^{-10}$ m
$D^0_{H_2SiO_4^{2-}}$	$1.07\ 10^{-7}$	r=$2.\ 10^{-10}$ m
$D^0_{CaH_2SiO_4^0}$	$1.07\ 10^{-7}$	r=$2.\ 10^{-10}$ m
$D^0_{CaH_3SiO_4^+}$	$1.07\ 10^{-7}$	r=$2.\ 10^{-10}$ m
$D^0_{CaCO_{3(aq)}}$	$1.43\ 10^{-7}$	r=$1.5\ 10^{-10}$ m
$D^0_{CaOH^+}$	$1.07\ 10^{-7}$	r=$2.\ 10^{-10}$ m
$D^0_{K^+}$	$1.957\ 10^{-7}$	(Weast et al., 1988)
$D^0_{Cl^-}$	$2.032\ 10^{-7}$	(Weast et al., 1988)
$D^0_{Na^+}$	$1.334\ 10^{-7}$	(Weast et al., 1988)

4.7 Conclusion

The relationship between capillary pressure P_C and liquid saturation degree S_L, the transport of gas and liquid phase as well as aqueous species are introduced in this chapter. The temperature and pressure influence for the viscosity of liquid and gas are considered. Diffusion coefficients are also regarded as a function of temperature thanks to the Stokes-Einstein equation. All these efforts make the simulation of two-phase transport at high temperature and pressure possible. However. temperature dependence is neglected in the relative permeabilities-saturation curve and the saturation-capillary pressure curve, due to the lack of experimental data, further experimental studies could be done to get more precise values at high temperature conditions.

Chapter 5

Numerical procedures

5.1 Introduction

The model aims at simulating the behavior of saturated or unsaturated cement-based materials in contact with CO_2-saturated brine or $scCO_2$, dry or wet. The major solid components including CH and C-S-H are initially assessed (by direct measurements *e.g.* TGA, XRD or by using simple analytical models (Thiery, 2006)). For saturated cement-based materials, when exposed to CO_2-saturated brine or supercritical CO_2, CO_2 will transport into the pore solution by diffusion. For unsaturated cement-based materials exposed to $scCO_2$, CO_2 will enter the material by advection. When the CO_2 concentration gets high enough ($\approx 3 \times 10^{-15}$ mol/L), CH and C-S-H will start to carbonate. The porosity will decrease when CH carbonates, since the molar volume of generated $C\bar{C}$ is greater than that of CH. The decalcification of C-S-H could also contribute to a porosity drop, due to the volume difference between C-S-H and the precipitated calcium carbonate (Thiery, 2006). The transport of calcium between regions with different carbonation degree could also be responsible for a porosity increase in the CH dissolution region, and a porosity decrease in the calcite accumulation region. The formed calcite could dissolve under peculiar boundary conditions and cause an increase in porosity. The porosity decrease will hinder CO_2 transport in the pores of the materials, thus slowing down the carbonation speed. The porosity increase has the opposite effect. Free water will be released during CH and C-S-H carbonation, which will increase the saturation degree of unsaturated material. The porosity reduction will increase the saturation degree as well. An increase of saturation degree in the pores will reduce the CO_2 advection speed and accelerate the aqueous CO_2 diffusion, altogether it will reduce the CO_2 speed, since advection in gas phase is orders of magnitude faster than diffusion in aqueous phase.

The model is implemented within the modeling platform, Bil, based on the finite element and finite

volume methods (http://perso.lcpc.fr/dangla.patrick/bil/). Bil is written in C language and can run on Linux-based OS. This platform is developed for 1D, 2D and 3D problems. It doesn't include mesh generator for 2D and 3D problems or post-possessing treatment of outputs. However, it can read mesh files created by the open-source software like Gmsh (Geuzaine and Remacle, 2009). The output files created by Bil can easily be used by some plotting programs such as Gnuplot (Racine, 2006).

Comparing with other reactive transport codes (Xu et al., 2008; Steefel, 2001; Prevost, 2007; Lichtner, 2001), *etc.*, the originality of this work is to solve the couplings between the chemical reactions and the transport equations in one step. Compared to other numerical simulations of the carbonation of cement-based materials under CO_2 sequestration conditions, *e.g.*, (Huet et al., 2010) who used Dynaflow^{TM} (Prevost, 2007), (Carey and Lichtner, 2007) who used FLOTRAN (Lichtner, 2001), or (Huet et al., 2011) who used both, this model considers the multiple flow of liquid and gas phase, and introduces temperature dependence for both transport and chemical reactions, while the other two are limited to saturated conditions at room temperature. It is worth-noting that even under saturated conditions, this code has the advantage of using different diffusion coefficient for each aqueous species (also did in (Carey and Lichtner, 2007)), thanks to the Nernst-Plank equation employed in the code. This is essential since the change in composition of cement-based material is generally diffusion controlled under saturated conditions. Furthermore, in this study, one properly chosen variable is able to capture the precipitation and dissolution of the relevant phase.

Numerical procedures for the couplings of transport equations and chemical reactions are introduced in this chapter. Principle of the finite volume method is illustrated with a simple transport example. The dissolution and precipitation of solid components, calculation of aqueous species, as well as the kinetics of solid dissolution, are described. Finally, a simple carbonation example (a well hydrated class H cement paste exposed to CO_2 saturated brine), is used to illustrate the couplings of transport and chemical reactions.

5.2 Principle of finite volume method

The finite volume method is a method for solving partial differential equations in the form of algebraic equations. Similar to the finite difference method or finite element method, values are calculated at the nodes of a mesh. "Finite volume" refers to the small volume surrounding each node point of a mesh. In the finite volume method, volume integrals in a partial differential equation that contains a divergence term are converted to surface integrals, using the divergence theorem. These terms are then evaluated as fluxes at the surfaces of each finite volume. This method is widely used in computational fluid dynamics packages. The general description of the method could be found in (Eymard et al., 2000; Toro, 2009; LeVeque, 2002).

Here we illustrate the principle of the finite volume method with a 1D flow problem. The conservation

of mass can be written as follows:

$$\frac{\partial \rho(x,t)}{\partial t} = -\frac{\partial}{\partial x} w(x,t) \tag{5.1}$$

where $\rho(x,t)$ represents the state variable and $w(x,t) = w(\rho(x,t))$ represents the flow of ρ.

We note Ω the computation 1D domain which is discretized by a finite number of sub-domains p_i with a length L_i called control volumes, following the terminology of finite volume method. Their centers are those points where the discrete unknowns ρ have been localized, see Fig. (5.1). The boundary conditions are imposed at the control volume located at each end. The time discretization is noted with an exponent n. The time step Δt defines the time n+1 by: t^{n+1}=$t^n + \Delta t$.

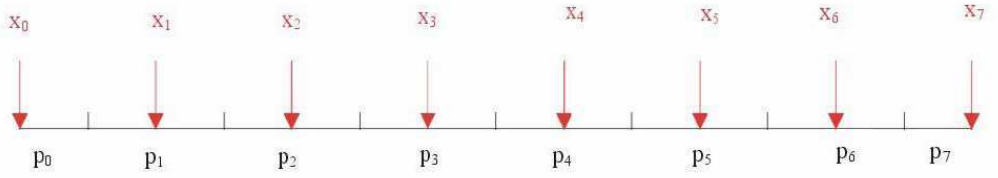

Figure 5.1: 1D spatial discretization of finite volumes.

Spatial integration of the mass balance Eq. (5.1) is performed on each sub-domain p_i. The time derivative is approximated by means of an implicit Euler scheme:

$$AL_i \frac{\rho(x_i, t^{n+1}) - \rho(x_i, t^n)}{\Delta t} = A(w_{i-1,i} - w_{i,i+1}) \tag{5.2}$$

where A is the section of the specimen.

The term $A(w_{i-1,i} - w_{i,i+1})$ corresponds to the integration of the divergence term in the control volume p_i in the mass balance Eq. (5.1). $A(w_{i,i+1})$ is an approximation of $\int_{\partial p_i p_{i+1}} w(x,t^n) dA$ for each sub-domain p_i and its direct neighboring domain p_{i+1} containing a common boundary $\partial p_i p_{i+1}$.

5.3 Modeling dissolution and precipitation of solid components

5.3.1 Principle of modeling the dissolution and precipitation of solid components

In Chapter 3, we have seen that any solid component can dissolve completely as leaving its stability domain. For the dissolution of any solid components (except for the end-members of solid solution), *i.e.* CH or C$\bar{\text{C}}$, at stable state, we have a system of inequality in the following form:

$$n_i \geq 0,\ \log\left(\frac{Q_i}{K_i}\right) \leq 0,\ n_i \log\left(\frac{Q_i}{K_i}\right) = 0 \tag{5.3}$$

where n_i is the content of solid component (mol/L), Q_i and K_i are the ion activity product and the equilibrium constant of the dissolution reaction. Therefore we can introduce a variable as:

$$\zeta_i = \frac{n_i}{n_i^0} + \log\left(\frac{Q_i}{K_i}\right) \tag{5.4}$$

Then we are able to represent both n_i and $\log\left(\frac{Q_i}{K_i}\right)$ as a function of ζ_i:

$$\frac{n_i}{n_i^0} = \zeta_i^+,\ \log\left(\frac{Q_i}{K_i}\right) = \zeta_i^- \tag{5.5}$$

where ζ_i^+ is the positive part of ζ_i and ζ_i^- is the negative part.

5.3.2 Dissolution/Precipitation of CH and C$\bar{\text{C}}$

Now let's recall the equilibrium relation between CH and C$\bar{\text{C}}$ (see Section 3.3):

$$\frac{Q_{\text{C}\bar{\text{C}}}}{K_{\text{C}\bar{\text{C}}}} = \frac{Q_{\text{CH}}}{K_{\text{CH}}} \frac{\rho_{\text{CO}_2^0}}{\rho_{\text{CO}_2^0}^{\text{CH}}} \tag{5.6}$$

In the domain where only CH is stable ($\frac{Q_{\text{CH}}}{K_{\text{CH}}} = 1$), it comes

$$n_{\text{CH}} \geq 0,\ \rho_{\text{CO}_2^0} < \rho_{\text{CO}_2^0}^{\text{CH}},\ \frac{Q_{\text{C}\bar{\text{C}}}}{K_{\text{C}\bar{\text{C}}}} < 1 \tag{5.7}$$

and in the domain where only C$\bar{\text{C}}$ is stable ($\frac{Q_{\text{C}\bar{\text{C}}}}{K_{\text{C}\bar{\text{C}}}} = 1$), it comes

$$n_{\text{C}\bar{\text{C}}} \geq 0,\ \rho_{\text{CO}_2^0} > \rho_{\text{CO}_2^0}^{\text{CH}},\ \frac{Q_{\text{CH}}}{K_{\text{CH}}} < 1 \tag{5.8}$$

and in the domain where both CH and C$\bar{\text{C}}$ are stable ($\frac{Q_{\text{CH}}}{K_{\text{CH}}} = \frac{Q_{\text{C}\bar{\text{C}}}}{K_{\text{C}\bar{\text{C}}}} = 1$), it comes

$$n_{\text{CH}} \geq 0,\ n_{\text{C}\bar{\text{C}}} \geq 0,\ \rho_{\text{CO}_2^0} = \rho_{\text{CO}_2^0}^{\text{CH}} \tag{5.9}$$

Thus, it is possible to model the dissolution of both CH and C$\bar{\text{C}}$ with one variable ζ_{Ca}, defined as:

$$\zeta_{\text{Ca}} = \frac{n_{\text{CH}} + n_{\text{C}\bar{\text{C}}}}{n_{\text{Ca}}^0} + \log[\max(\frac{Q_{\text{CH}}}{K_{\text{CH}}}, \frac{Q_{\text{C}\bar{\text{C}}}}{K_{\text{C}\bar{\text{C}}}})] \tag{5.10}$$

where n^0_{Ca} is the initial CH content. If $\rho_{\mathrm{CO}_2^0} \leq \rho^{\mathrm{CH}}_{\mathrm{CO}_2^0}$, $\mathrm{C\bar{C}}$ is not stable, and we get

$$\zeta_{\mathrm{Ca}} = \frac{n_{\mathrm{CH}} + n_{\mathrm{C\bar{C}}}}{n^0_{\mathrm{Ca}}} + \log\left(\frac{Q_{\mathrm{CH}}}{K_{\mathrm{CH}}}\right) \tag{5.11}$$

If $\rho_{\mathrm{CO}_2^0} \geq \rho^{\mathrm{CH}}_{\mathrm{CO}_2^0}$, CH is not stable, and thus

$$\zeta_{\mathrm{Ca}} = \frac{n_{\mathrm{CH}} + n_{\mathrm{C\bar{C}}}}{n^0_{\mathrm{Ca}}} + \log\left(\frac{Q_{\mathrm{C\bar{C}}}}{K_{\mathrm{C\bar{C}}}}\right) \tag{5.12}$$

5.3.3 Dissolution/Precipitation of C-S-H

We can also model the dissolution of C-S-H with one variable ζ_{Si}, defined as:

$$\zeta_{\mathrm{Si}} = \frac{n_{\mathrm{Si}}}{n^0_{\mathrm{Si}}} + \log\left(\frac{Q_{\mathrm{SH_t}}}{Q_{\mathrm{SH_t(eq)}}}\right) \tag{5.13}$$

where n_{Si} is the molar content of C-S-H in the form of $\mathrm{C}_x\mathrm{S}_1\mathrm{H}_z$, n^0_{Si} is the initial molar content of C-S-H, $Q_{\mathrm{SH_t}}$ is the ion activity product of the dissociation reaction of $\mathrm{SH_t}$, $Q_{\mathrm{SH_t(eq)}}$ is the ion activity product of $\mathrm{SH_t}$ calculated with Eq. (5.14) discussed in Section 3.4:

$$\ln\left(\frac{Q_{\mathrm{SH}_t\mathrm{(eq)}}}{K_{\mathrm{SH}_t}}\right) = -\int_0^{\frac{Q_{\mathrm{CH}}}{K_{\mathrm{CH}}}} \frac{\chi(q)}{q} dq \tag{5.14}$$

ζ^+_{Si} represents the molar content of Si in solid phase. When $\zeta_{\mathrm{Si}}>0$, $Q_{\mathrm{SH_t}}=Q_{\mathrm{SH_t(eq)}}$, which means, in equilibrium with C-S-H solid, $Q_{\mathrm{SH_t}}$ is a function of only $\frac{Q_{\mathrm{CH}}}{K_{\mathrm{CH}}}$. When $\zeta_{\mathrm{Si}}<0$, there is no C-S-H solid, in this case, $Q_{\mathrm{SH_t}}$ can be attained by ζ^-_{Si} and $\frac{Q_{\mathrm{CH}}}{K_{\mathrm{CH}}}$.

5.4 Kinetics

As indicated in Chapter 3, a simple kinetic law is employed for the dissolution of CH, written as:

$$\frac{dn_{\mathrm{CH}}}{dt} = -\frac{n_{\mathrm{CH}}}{\tau_{\mathrm{CH}}} \ln\left(\frac{\rho_{\mathrm{CO}_2^0}}{\rho^{\mathrm{CH}}_{\mathrm{CO}_2^0}}\right) \tag{5.15}$$

thus we can calculate n_{CH} and $n_{\mathrm{C\bar{C}}}$ with

$$n^{t+dt}_{\mathrm{CH}} = n^t_{\mathrm{CH}} + dn_{\mathrm{CH}} \tag{5.16}$$

and

$$n^{t+dt}_{\mathrm{C\bar{C}}} = \zeta^+_{\mathrm{Ca}} n^0_{\mathrm{Ca}} - n^{t+dt}_{\mathrm{CH}} \tag{5.17}$$

where ζ_{Ca}^{+} is the positive part of variable ζ_{Ca}.

5.5 Governing equations *vs* primary variables

Governing equations *vs* primary variables in the model are listed in Table 5.1.

Table 5.1: Governing equations and primary variables in the model

Governing Equations	Primary Variables
Carbon (C)	Gas pressure P_G or CO_2 concentration $\rho_{CO_2^0}$
Calcium (Ca)	ζ_{Ca}
Silicon (Si)	ζ_{Si}
Sodium/Potassium	Concentration ρ_{K^+}
Chlorine (Cl)	Concentration ρ_{Cl^-}
Total mass	Liquid pressure P_L
Charge	Electric potential ψ

As discussed in Section 3.2, the concentration of all aqueous species except ρ_{K^+}, ρ_{Cl^-} can be calculated, as long as $\rho_{CO_2^0}$, $\rho_{Ca^{2+}}$, and $\rho_{H_4SiO_4^0}$ are known. In this study, ρ_{K^+} and ρ_{Cl^-} are considered as primary variables. Secondary variables such as $\rho_{CO_2^0}$, $\rho_{Ca^{2+}}$, and $\rho_{H_4SiO_4^0}$ can be attained through primary variables (P_L,P_G,ζ_{Ca},ζ_{Si}), with the following equations:

$$\rho_{CO_2^0} = (1 - y_{H_2O})\frac{\phi_{CO_2} P_G}{K_{CO_2,T,P^0}} \exp(-\frac{(P_L - P^0)\overline{V}_{CO_2}}{RT}) \text{ (see Section 2.4)} \tag{5.18}$$

and

$$\rho_{Ca^{2+}} = \frac{Q_{C\bar{C}}}{\rho_{CO_3^{2-}}} = \frac{10^{\zeta_{\mathrm{Ca}}^{-}} \min(z_{CO_2}, 1) K_{C\bar{C}}}{\rho_{CO_3^{2-}}} \text{ (see Eq. (5.10))} \tag{5.19}$$

where z_{CO_2}=$\frac{\rho_{CO_2^0}}{\rho_{CO_2^0}^{CH}}$,

and

$$\rho_{H_4SiO_4^0} = Q_{SH_t} = 10^{\zeta_{\mathrm{Si}}^{-}} Q_{SH_{t(eq)}} \text{ (see Eq. (5.13))} \tag{5.20}$$

where $Q_{SH_{t(eq)}}$ is defined in Eq. (5.14).

5.6 An example of simulation

Here we employ a simple carbonation example to illustrate the couplings between transport and chemical reactions. We consider a cement paste cylinder with diameter of 0.75 cm, divided into 50 nodes. The cement paste contains initially 5.16 mol/L of portlandite (CH) and 3.9 mol/L of jennite (*i.e.*, $C_{1.7}SH_{2.1}$) with porosity of 40%, the same as well hydrated class H cement we used in Chapter 3. Temperature is set to 25 ℃. The material is initially saturated with water, and exposed to aqueous CO_2 solution. Aqueous

CO_2 concentration at the material surface increases from a low value (about 10^{-16} mol/L) to 0.049 mol/L (the approximate solubility of atmospheric CO_2 at 25 ℃) in 7200 s to simulate a loading period of 2 hours. The characteristic time τ_{CH} equals to 4.5 days, due to a low CO_2 concentration. No alkali is added here. At the sample surface, the ion activity product of calcite is set as constant and equals to $10^{-20} \times K_{C\bar{C}}$ to enable the leaching of calcium (simulating a boundary condition of pure water saturated with CO_2), by setting ζ_{Ca} = -20. We do not consider the leaching of silicon due to the very small solubility of C-S-H in low pH conditions. Thus the ion activity product of Q_{SH_t} equals to K_{SH_t} at the surface. Boundary and initial conditions are summarized in Table 5.2.

Table 5.2: Boundary and initial conditions in simulation

Boundary conditions			**Initial conditions**
Balance Equation	BC left	BC right	
Carbon (C)	no flow	flow allowed ($\rho_{CO_2^0}$ = 0.049 mol/L)	$\rho_{CO_2^0} = 10^{-16}$ mol/L
Calcium (Ca)	no flow	flow allowed (leaching of Ca: ζ_{Ca}=-20)	ζ_{Ca}=1
Silicon (Si)	no flow	no flow	ζ_{Si}=1
Sodium/Potassium	no flow	no flow	ρ_K^+=0
Chlorine (Cl)	no flow	no flow	ρ_{Cl}^-=0
Total mass	no flow	flow allowed (P_L=10^5 Pa)	P_L=10^5 Pa
Charge	no current	ψ=0	ψ=0

Aqueous CO_2 concentration and pH value profiles from 0 to 30 days are presented in Figs. 5.2 and 5.3. CO_2 penetrates into the material during exposure. As a result, pH decreases from 12.4 in the uncarbonated region to 3.8 at the surface.

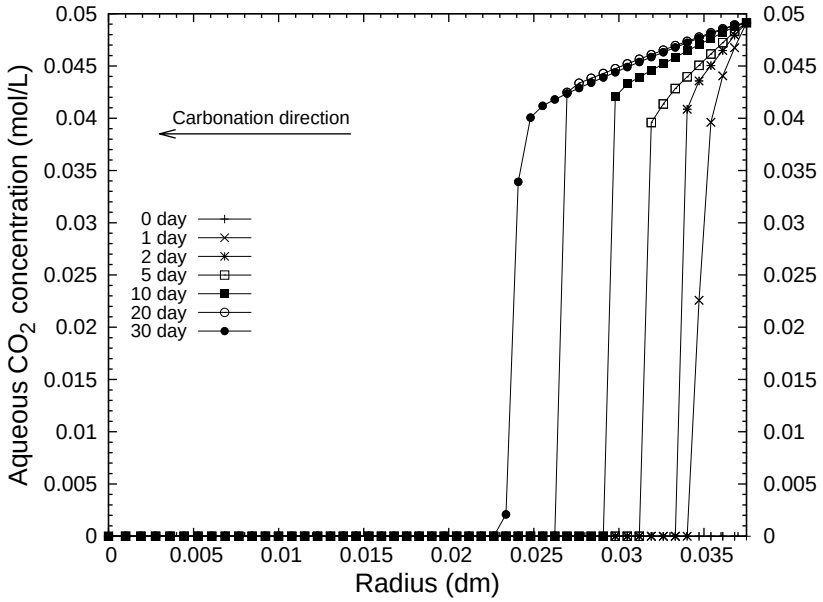

Figure 5.2: Aqueous CO_2 concentration profiles from 0 day to 30 days.

When aqueous CO_2 concentration increases, both CH and C-S-H will react with CO_2. Looking at the

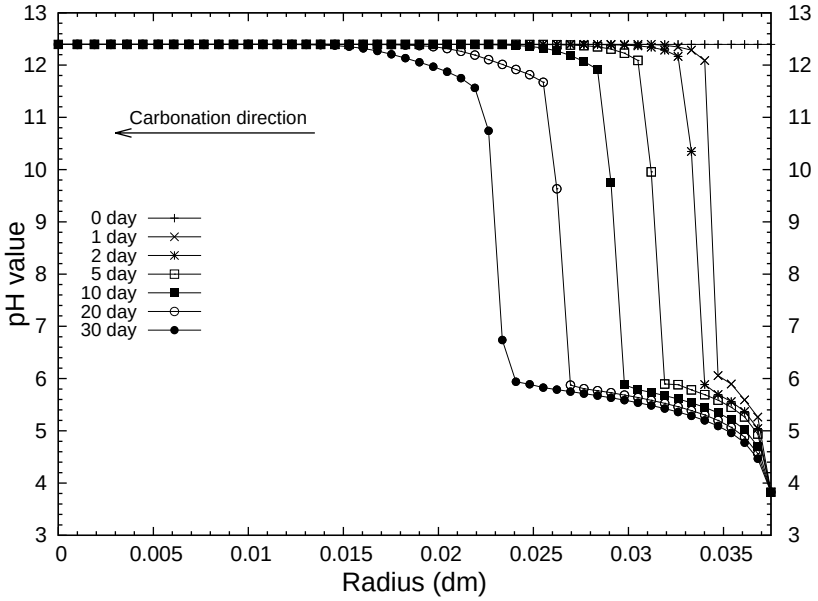

Figure 5.3: pH value profiles from 0 day to 30 days.

solid profiles after 5 days of exposure (see Fig. 5.4), different fronts and regions can be observed. First let's define some fronts. At point A, CH starts to dissolve, we define it as the **CH dissolution front**. At point B, the C/S ratio of C-S-H starts to decrease, we define it as the **C-S-H decalcification front**. Point C is defined as the **calcite precipitation front**, where calcite starts to form. We define point D as the **front of decalcified C-S-H** where C/S ratio of C-S-H drops to 0. And Point E is defined as the **front of dissolved calcite** where the formed calcite is totally dissolved at this point. Now we are able to distinguish different regions by means of these fronts. Between the core of the sample and the CH dissolution front (point A), the solid phase remains uncarbonated. This is the **uncarbonated region**. We call the region between the CH dissolution front (point A) and the calcite precipitation front (point C) as the **CH dissolution region** where CH is dissolved without calcite precipitation. C/S ratio decreases gradually from the C-S-H decalcification front (point B) to the front of decalcified C-S-H (point D), the region between them is defined as the **C-S-H decalcification region**. The region between the calcite precipitation front (point C) and the front of dissolved calcite (point E), is labeled as a **region of calcite accumulation**. From the front of dissolved calcite (point E) to the material surface, all the solid components have been dissolved except amorphous silica gel. Thus denote this region as a **fully degraded region**. The porosity profile is also plotted in Fig. 5.4. From the CH dissolution front (point A) to the calcite precipitation front (point C), the porosity increases from 0.4 to 0.5 due to CH dissolution as well as C-S-H decalcification. It decreases then sharply to 0.25 in the calcite accumulation region given that calcite precipitates. In the fully degraded region, porosity increases to 0.78 since there is only amorphous silica gel left.

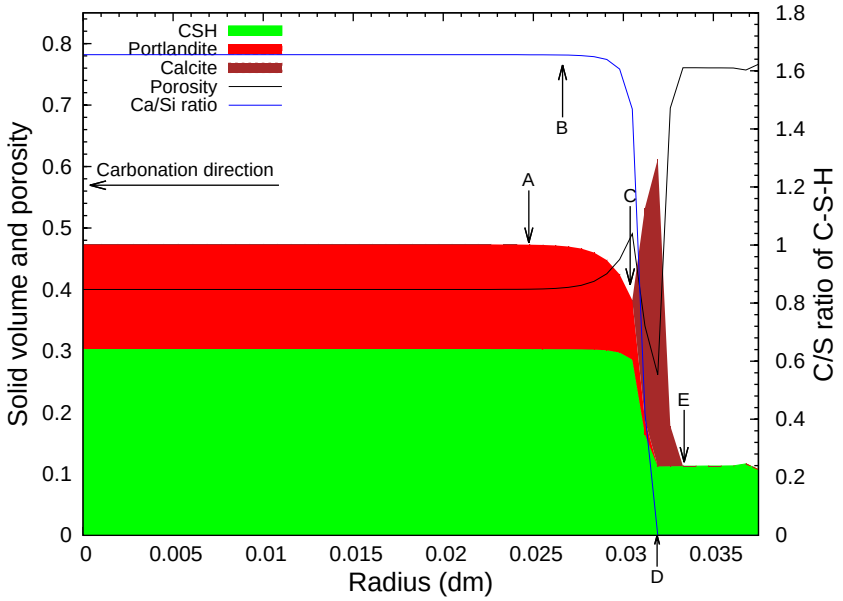

Figure 5.4: Solid profiles after 5 days exposure.

As discussed before, content of CH and C$\bar{\text{C}}$ can be attained by ζ_{Ca} and z_{CO_2}=$\frac{\rho^0_{\text{CO}_2}}{\rho^{\text{CH}}_{\text{CO}_2}}$ (see Eq. (5.15) to (5.17)). ζ_{Ca^+} represents the total molar content of CH and C$\bar{\text{C}}$, and z_{CO_2} defines the stable domain of each solid component. ζ_{Ca}, $\log(z_{\text{CO}_2})$ and CH, C$\bar{\text{C}}$ content profiles after 5 days exposure are plotted in Fig. 5.5. In the uncarbonated region (between the core of the sample and the CH dissolution front point A), z_{CO_2} =1, CH is stable, the content remains the same value as initial. In the CH dissolution region (between point A and C), z_{CO_2} >1, CH is not stable and starts to dissolve, as a result, ζ_{Ca} decreases from 1 at point A to about 0.6 at point C. From the calcite precipitation front of point C, calcite forms and ζ_{Ca} reaches a peak value of 2.6 in the region of calcite accumulation. At the front of dissolved calcite point E, both CH and C$\bar{\text{C}}$ are fully dissolved, thus ζ_{Ca} decreases to 0. In the fully degraded region, there is no CH nor C$\bar{\text{C}}$ and ζ_{Ca} remains negative.

From Fig. 5.5 we can also find that there is a leaching effect of calcium element near the surface. This is related with the diffusion of several aqueous components, among which the diffusion of Ca^{2+} ion is predominant since the concentration of other components related with calcium element, *e.g.* $CaHCO_3^+$ and $CaOH^+$ are several orders of magnitude smaller (see Fig. 5.6). The total calcium flow w_{Ca} and ζ_{Ca} after 5 days of exposure, are plotted in Fig. 5.7. There is clearly a flow of calcium from the vicinity of the front of dissolved calcite (point E) to the surface, this is responsible to the leaching of calcium. There is also a transport of calcium, from the CH dissolution front (point A) to the calcite precipitation front (point C), while this flow of calcium almost vanishes in the region of calcite accumulation.

Similarly, all the information of C-S-H can be attained by ζ_{Si} and q_{CH}=$\frac{Q_{\text{CH}}}{K_{\text{CH}}}$. ζ_{Si^+} represents the molar content of C-S-H, and q_{CH} controls the molar volume, C/S and H/S ratio of C-S-H. ζ_{Si} and q_{CH} profiles

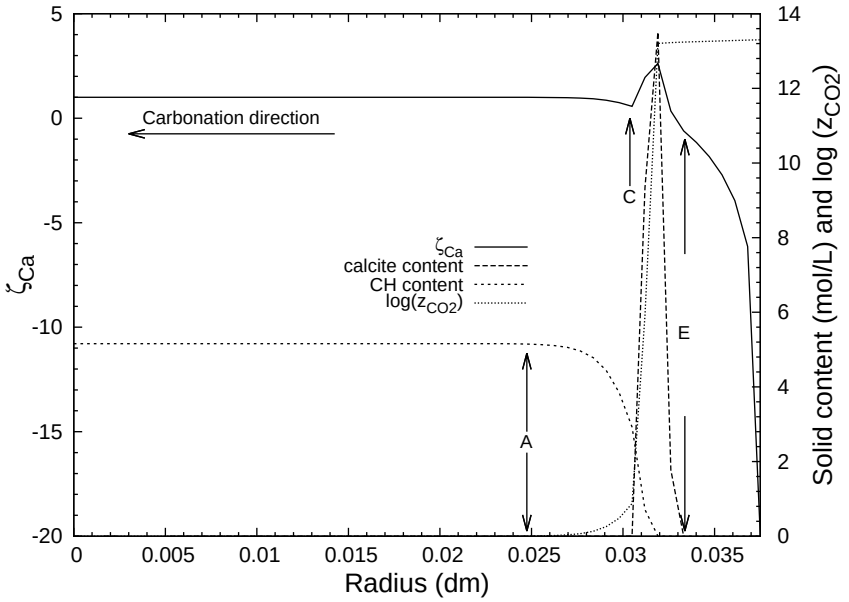

Figure 5.5: ζ_{Ca}, CH,C$\bar{\mathrm{C}}$ content and $z_{\mathrm{CO_2}}$ profiles after 5 days exposure.

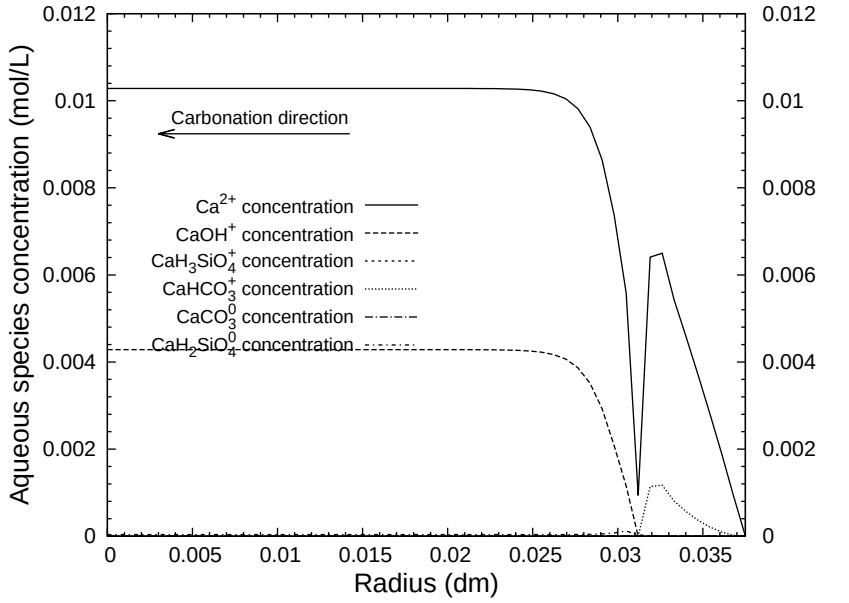

Figure 5.6: Concentration of aqueous species related with calcium transport after 5 days exposure.

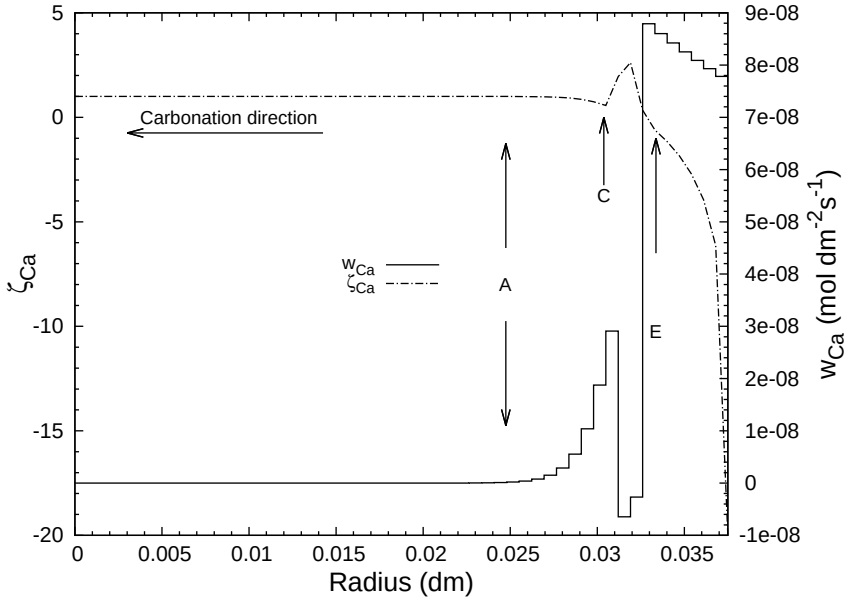

Figure 5.7: ζ_{Ca} and calcium flow after 5 days exposure.

after 5 days exposure are plotted in Fig. 5.8. The decalcification of C-S-H starts at the C-S-H decalcification front point B, as $\log(q_{\mathrm{CH}})$ becomes negative at this point. In the C-S-H decalcification region (between the C-S-H decalcification front point B and the front of decalcified C-S-H point D), the C/S ratio drops from 1.7 to 0 and the H/S ratio drops from 2.1 to 0, as plotted in Fig. 5.9. The molar volume $V_{\text{C-S-H}}$ decreases from 0.078 to 0.029 dm^3/mol, as illustrated in Fig. 5.10.

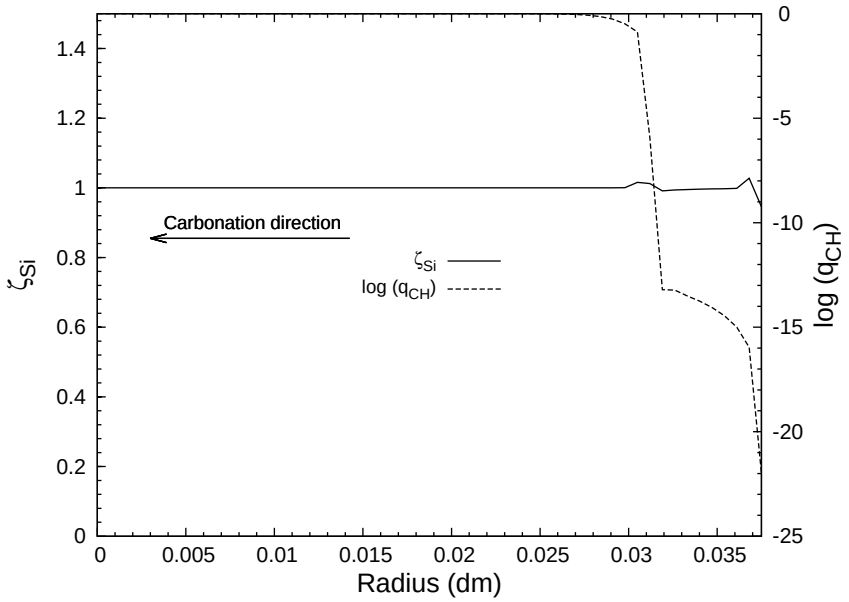

Figure 5.8: ζ_{Si} and $\log(q_{\mathrm{CH}})$ profiles after 5 days exposure.

$H_4SiO_4^0$ and $H_3SiO_4^-$ are the predominant form of silicon transport in this case (see Fig. 5.11). The

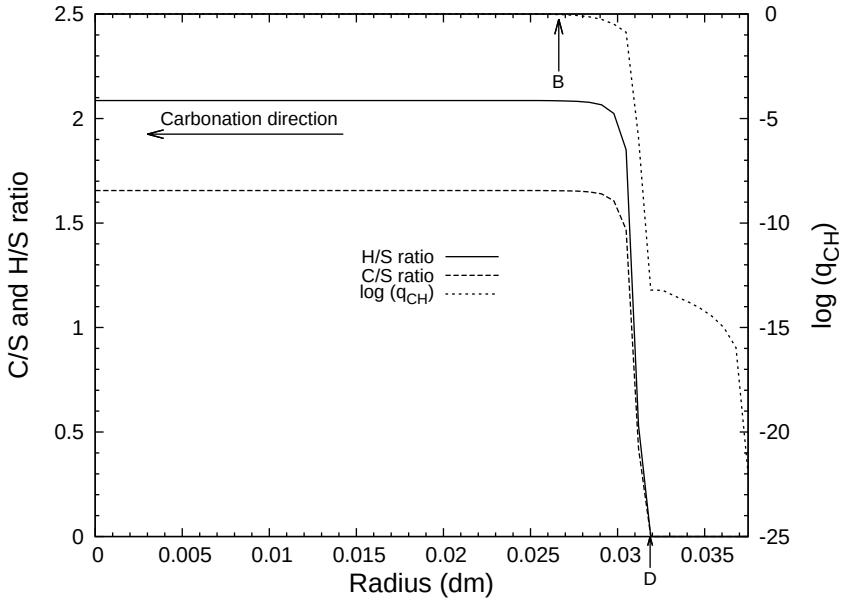

Figure 5.9: C/S ratio, H/S ratio and $\log(q_{\mathrm{CH}})$ profiles after 5 days exposure.

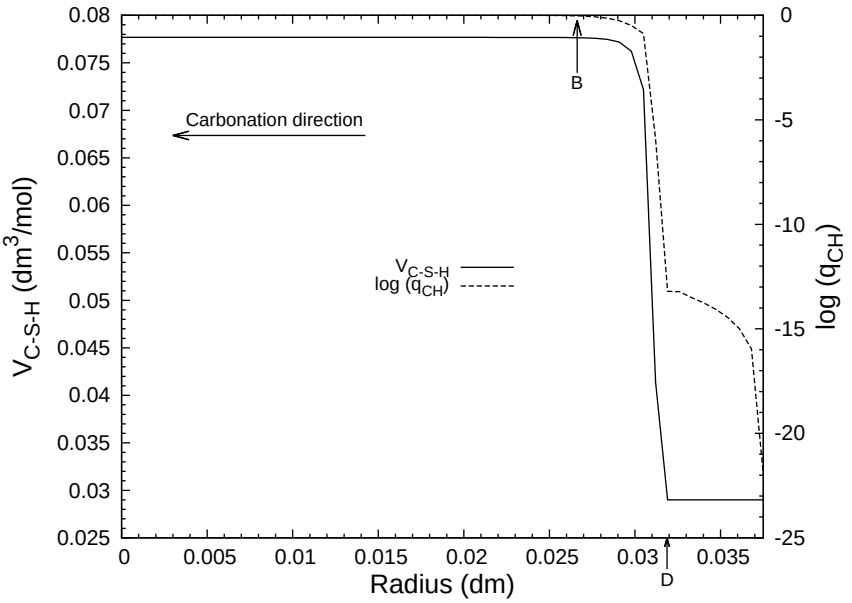

Figure 5.10: $V_{\text{C-S-H}}$ and $\log(q_{\mathrm{CH}})$ profiles after 5 days exposure.

flow of silicon is much smaller than that of calcium, thus the profile of ζ_{Si} doesn't change much after carbonation, see Fig. 5.12.

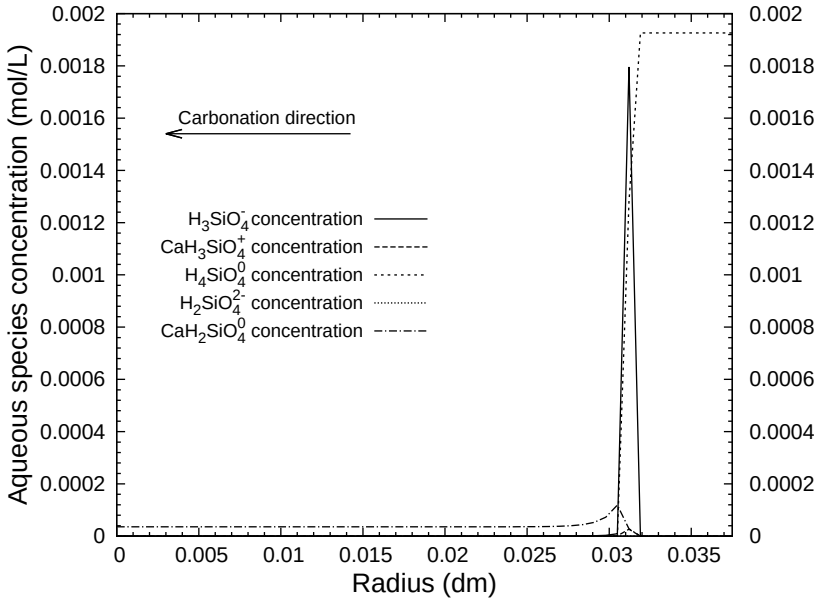

Figure 5.11: Concentration of aqueous species related with silicon transport after 5 days exposure.

The total mass flow w_m, total mass m and solid mass m_S are plotted in Fig. 5.13. In the CH dissolution region, the material losses mass (see m_S) while in the region of calcite accumulation, the material gains mass. In the fully degraded region, solid mass decreases from 1100 g/L to 220 g/L since there is only amorphous silica gel left. In this study, for the solid, we consider only the mass of CH, $C\bar{C}$ and C-S-H, the solid mass is smaller than experimental measurements since we neglect the mass of materials which do not react with CO_2.

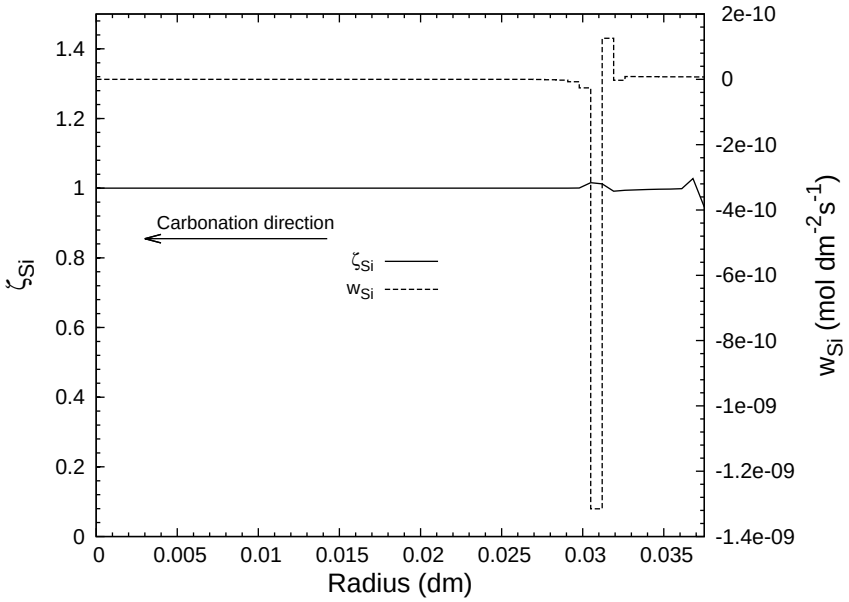

Figure 5.12: ζ_{Si} and silicon flow after 5 days exposure.

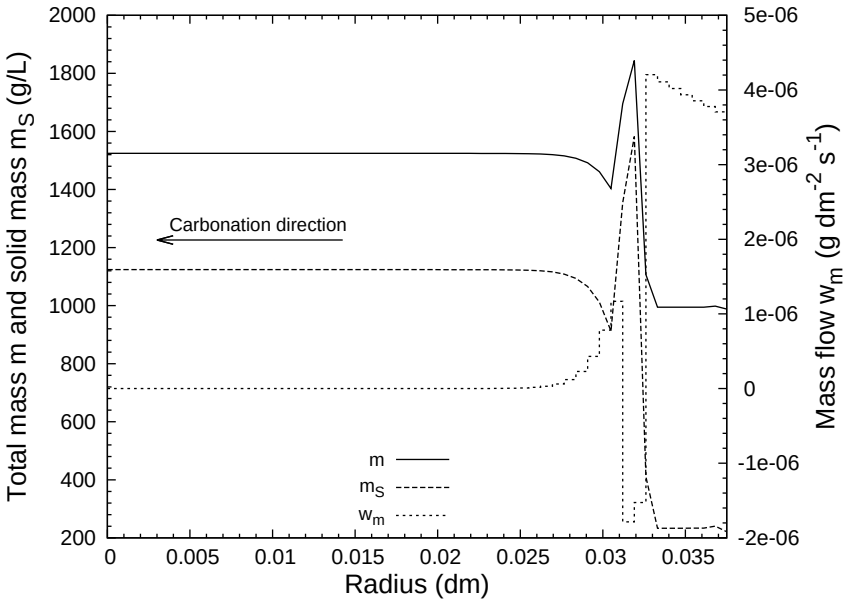

Figure 5.13: Mass flow, total mass and solid mass after 5 days exposure.

5.7 Conclusion

In this chapter, the numerical procedures for the couplings between transport and reaction equations have been introduced. The principle of the finite volume method, the way to take into account the dissolution and precipitation of solid components, as well as the kinetics effects, have been presented. An example of simulation under saturated condition has been presented. Several fronts, *e.g.* the CH dissolution front, the calcite precipitation front, the C-S-H decalcification front, have been identified, and different zones of carbonation have been distinguished. The predominant aqueous species responsible to calcium and silicon transport have been revealed. The diffusion of Ca^{2+} ion as a result of concentration gradient causes the leaching of calcium as well as the calcium transport between different zones. The diffusion of $H_4SiO_4^0$ and $H_3SiO_4^-$ is responsible for the silicon transport, though the amount is very limited comparing with the calcium transport. This model is not only able to deal with saturated conditions but also able to work with unsaturated conditions, as it will be presented in the following chapters.

Chapter 6

Simulation in the case of CO_2 saturated brine boundary conditions

6.1 Introduction

Experimental works on cement reactivity in the context of CO_2 geological storage have been conducted by different research groups, *e.g.*, (i) saturated class H Portland cement exposed to CO_2 saturated brine at atmospheric pressure in a flowing system (Duguid, 2009; Duguid et al., 2005; Duguid and Scherer, 2010) and modeling (Huet et al., 2010); (ii) saturated class H Portland cement exposed to $scCO_2$ or CO_2 saturated brine, at pressure and temperature similar with downhole conditions (Kutchko et al., 2007, 2008); (iii) saturated or unsaturated class G Portland cement exposed to $scCO_2$ or CO_2 saturated brine at pressure and temperature similar with downhole conditions (Rimmelé et al., 2008; Fabbri et al., 2009); (iv) combined effect of CO_2 and H_2S on well cement (Jacquemet et al., 2005, 2007); (v) analysis of cement samples from a well after 30 years of CO_2 exposure (Carey et al., 2007), and modeling (Carey and Lichtner, 2007).

These published experimental results differ from each other, due to different initial and boundary conditions (in terms of CO_2 concentration, temperature, etc.), cement compositions and microstructures. The developed reactive transport model should be able to explain the consistency between these results. In this chapter, we will work with saturated cement paste exposed to CO_2 saturated brine. Simulations for cement paste exposed to $scCO_2$ boundary conditions will be discussed in Chapter 7.

Duguid et al. (Duguid and Scherer, 2010) conducted a series of experiments to examine the effects of flowing carbonated brine on well cementitious materials. In this experiment, the author exposed cylindrical class H cement paste samples (7.5 mm in diameter, W/C=0.38, cured in 0.5 M NaCl for 12 months at either 20 ℃ or 50 ℃) to a flowing CO_2 saturated brine in atmospheric conditions (20 ℃, 1 atm, pure bubbling

of CO_2) for 30 days. In one set of experiments, the brine was saturated with respect to calcite before being put in contact with the cement paste, thus simulating limestone reservoir conditions. In the other set, the brine was not saturated with calcite standing for sandstone-like reservoir conditions. The author also performed the same experiment at a temperature of 50 ℃, and used HCl to study the effect of a low *p*H value environment. Reacted cement paste samples were examined with X-ray diffraction (XRD) and electron probe microanalyzer (EPMA) analysis. Different layers were observed during experiment, among which a layer rich in calcium carbonate was believed to play a key role in the rate of change in composition of cement paste. All the cylindrical samples under sandstone-like conditions were degraded over the course of the experiment. Under limestone-like conditions, no evident attack was observed. The development of different layers versus time was recorded which provides the possibility to verify our model.

Rimmelé et al. (Rimmelé et al., 2008) exposed class G cement paste samples (12.5 mm in diameter, W/C=0.44, cured for 72 h at 207 bars and 90 ℃ in pure water prior to the experiments) to both CO_2-saturated brine and wet $scCO_2$, under pressure and temperature similar to downhole conditions. The porosity distribution at different states was monitored by scanning electron microscopy (SEM) and back-scattered electron (BSE) image analysis. The observed penetration kinetics of the carbonation front, as well as carbonation patterns, were similar between the samples exposed to $scCO_2$ and CO_2 saturated water. A slightly faster penetration kinetics of the carbonation front was measured for the one exposed to $scCO_2$.

Kutchko et al. (Kutchko et al., 2008) exposed cement paste samples made of class H cement (12 mm in diameter, W/C=0.38, cured for 28 days at 303 bars and 50 ℃ in 1% NaCl solution prior to the experiments) to $scCO_2$ and CO_2 saturated brine at 50 ℃ and 30.3 MPa for 1 year. Results for cement samples in contact with $scCO_2$ were similar to that in contact with atmospheric CO_2, with a strong effect of clogging of the microstructure able to hinder the CO_2 penetration, while the one exposed to CO_2 saturated brine was typical of acid attack on cement-based materials with a significant leaching effect (both of hydration compounds and calcium carbonate). With the data collected during 1 year, they estimated a penetration depth range of around 1.00 mm for CO_2 saturated brine and 1.68 mm for $scCO_2$ after 30 years.

Similar successive rings were observed which developed in all these sets of experiments in the case of cement paste exposed to CO_2 saturated brine. The measured kinetics of the penetration of the total reacted zone, differ from each other, by several orders of magnitude: $\sim$ 0.066 mm/day in (Duguid and Scherer, 2010), $\sim$ 0.23 mm/day in (Rimmelé et al., 2008) and $\sim$ 0.004 mm/day in (Kutchko et al., 2008). For cement paste exposed to CO_2 saturated brine, it is believed that, the reactivity is either controlled by Ca or CO_2 diffusion, depending on the kind of boundary conditions, or the CO_2 penetration stops because of the clogging effect due to calcium carbonate formation (Huet et al., 2011). In order to understand the difference between the experimental results, different parameters, *e.g.*, CO_2 concentration in the external

solution, temperature, types of aqueous species in the external solution, should be analyzed separately. In this chapter, calculations are led to simulate experimental works (Duguid and Scherer, 2010) which have examined the behavior of cement paste exposed to a high CO_2 concentration brine under conditions similar to CO_2 storage formations. The sensitivity to CO_2 concentration, temperature and other parameters will also be analyzed.

6.2 Sandstone-like conditions

Duguid and Scherer (Duguid and Scherer, 2010) observed five different regions: an orange ring followed by brown, white, light gray rings and a dark gray core (see Fig. 6.1). The orange and brown zones were fully degraded, with little calcium left comparing to the unreacted core. The white ring showed an increase in calcium, corresponding to the presence of the carbonation front. This layer can be dissolved gradually after its formation. The authors also noted that the formation of this layer had a protective effect and slowed down the reaction rate. It seems that it is the dissolution of this layer and diffusion through the fully degraded layers which control the rate of degradation of the cement paste. In the light gray ring, portlandite was partially dissolved, reflecting the presence of a dissolution front. The dark gray core was the unreacted zone.

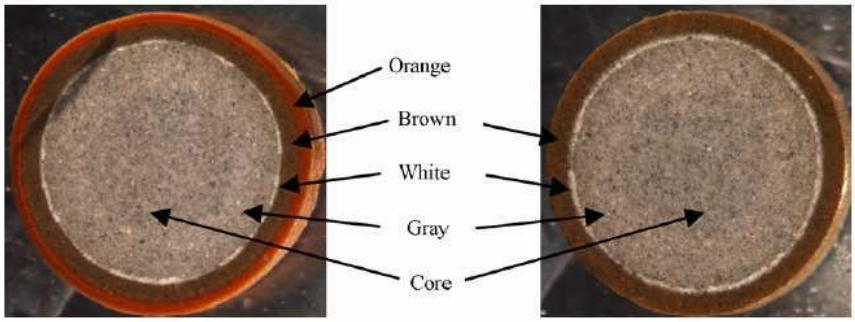

Figure 6.1: Different reaction zones for samples exposed to brine with pH = 2.4 (left) and 3.7 (right), at 323 K, from (Duguid and Scherer, 2010).

Huet et al. (Huet et al., 2010) built up a reactive transport model and simulated this set of experiments. These simulation results are also presented and compared with our results.

To simulate Duguid's experiments, we consider a cement paste cylinder with the same diameter, divided into 50 nodes. The initial CO_2 concentration in the pore solution of the material is small enough to avoid the dissolution of the portlandite (here equals to 1×10^{-16} mol/L), while at the boundary this concentration is fixed at 0.056 mol/L (the approximate solubility of CO_2 in a 0.58 M NaCl brine at 20 °C (Huet et al., 2010)). The cement paste contains initially 5.16 mol/L of portlandite (CH) and 3.9 mol/L of C-S-H considered as

$C_{1.7}SH_{2.1}$ here to have the same stoichiometry as jennite. The initial porosity accessible to water is 40%. Since the cement paste samples were cured in a 0.5 M NaCl solution for 12 months before exposure to carbonic acid, and the leaching solution contained 0.5 M NaCl as well in experiment (Duguid and Scherer, 2010), 0.5 M NaCl was added in the simulated pore solution as well as in the external solution (here we combine the K^+ and Na^+ as one ion for a sake of simplicity. This is not annoying since these two ions have almost the same diffusion coefficient). Concerning sandstone-like conditions, we set the activity product of calcite as constant and equal to $10^{-20} \times K_{C\bar{C}}$ to avoid any precipitation of calcite at this boundary (by setting ζ_{Ca} = -20). Boundary and initial conditions are summarized in Table 6.1.

Table 6.1: Boundary and initial conditions in simulation under sandstone-like conditions at 293 K

Boundary Conditions (BC)			**Initial Conditions**
Balance Equation	BC left	BC right	
Carbon (C)	no flow	flow allowed ($\rho_{CO_2^0}$ = 0.056 mol/L)	$\rho_{CO_2^0} = 10^{-16}$ mol/L
Calcium (Ca)	no flow	flow allowed (leaching of Ca: ζ_{Ca} = -20)	$\zeta_{Ca} = 1$
Silicon (Si)	no flow	no flow	$\zeta_{Si} = 1$
Sodium/Potassium	no flow	flow allowed (ρ_{K^+} = 0.5 mol/L)	ρ_{K^+} = 0.5 mol/L
Chlorine (Cl)	no flow	flow allowed (ρ_{Cl^-} = 0.5 mol/L)	ρ_{Cl^-} = 0.5 mol/L
Total mass	no flow	flow allowed ($P_L = 10^5$ Pa)	$P_L = 10^5$ Pa
Charge	no current	$\psi = 0$	$\psi = 0$

Our simulation results are presented hereafter. The CO_2 concentration at the boundary is about 0.056 mol/L (see Fig. 6.2a). The profile of pH value is illustrated in Fig. 6.2b. In the uncarbonated region, the calculated pH value is around 12.4, the same as Huet's results. At the boundary, it's around 3.6, almost the same value as the external brine (pH= 3.7) measured in the experiment (Duguid and Scherer, 2010).

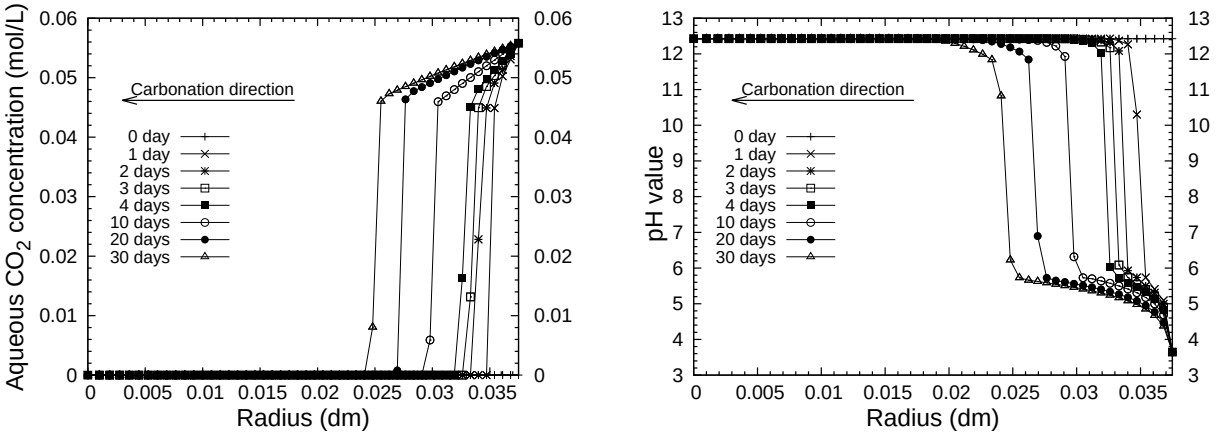

(a) Aqueous CO_2 concentration (b) pH value

Figure 6.2: The calculated aqueous CO_2 concentration and pH value profiles from 1 day to 30 days under sandstone-like conditions at 293 K. (a) Aqueous CO_2 concentration. (b) pH value.

The profiles of solid volume compounds (*i.e.*, $V_i n_i$), as well as porosity profiles, from 10 days to 30

days, are plotted in Fig. 6.3 to 6.5. Successive zones, from the boundary to the core, are observed. At the boundary, a leaching effect is illustrated since there is neither calcite nor portlandite, and the C/S ratio of C-S-H is zero (blue line in the plot which means C-S-H is in the form of silica gel). The porosity has increased to 0.78. This region, as a fully degraded one, corresponds to the brown layer in Fig. 6.1. Following this layer, a calcite-rich region is observed, where calcite accumulates and the porosity hugely drops. This layer corresponds to the white ring in Fig. 6.1, and is defined as a region of calcite accumulation. Calcite is generated in the inner side of this layer and is dissolved at the outside due to the leaching effect observed at the boundary condition. Thus the fronts of calcite precipitation and dissolved calcite move from the boundary to the center of the sample with time. The C-S-H decalcification region, where C/S ratio drops gradually from around 1.67 to zero, illustrates the continuous decalcification of C-S-H during carbonation. A CH dissolution region is observed between the CH dissolution front and the calcite precipitation front, which corresponds to the gray layer in Fig. 6.1. The predicted profiles are quite similar to the simulations of (Huet et al., 2010) carried out for the same configuration and cementitious system (see Fig. 6.6).

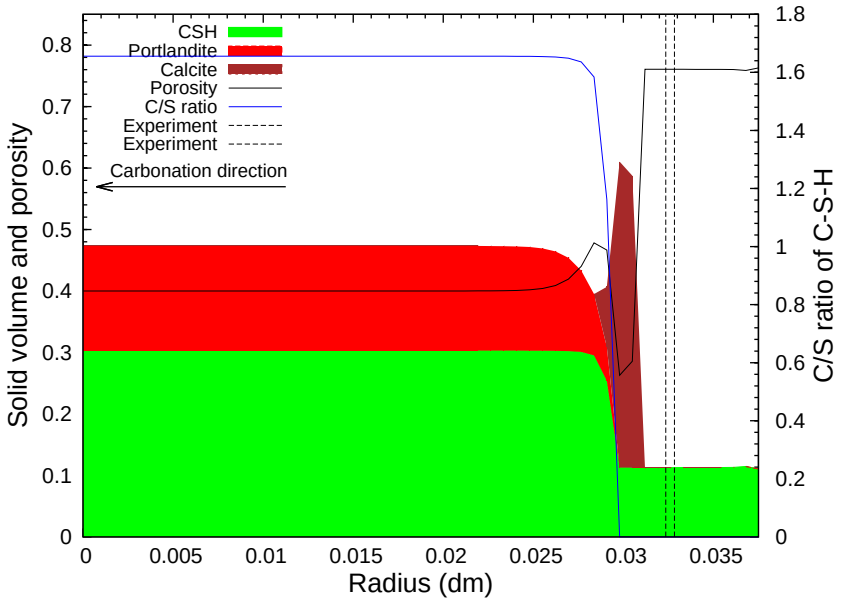

Figure 6.3: Profiles of solid volume compounds after 10 days of exposure under sandstone-like conditions at 293 K (vertical dash lines show the region of calcite accumulation assessed by (Duguid and Scherer, 2010)).

In Fig. 6.7 we compare the predicted position of the region of calcite accumulation (the white layer observed in experiment (Duguid and Scherer, 2010)) with experimental observation, since this layer is easy to identify in both experiments and numerical calculations. In Fig. 6.7, the "penetration kinetics" means the distance between the inner side of this specified layer and the sample surface. We slightly overestimate the kinetics of advancement in the first few days, but after 15 days the simulation results are very close to the experimental observations (Duguid and Scherer, 2010). In the experiment, the inner side of the white

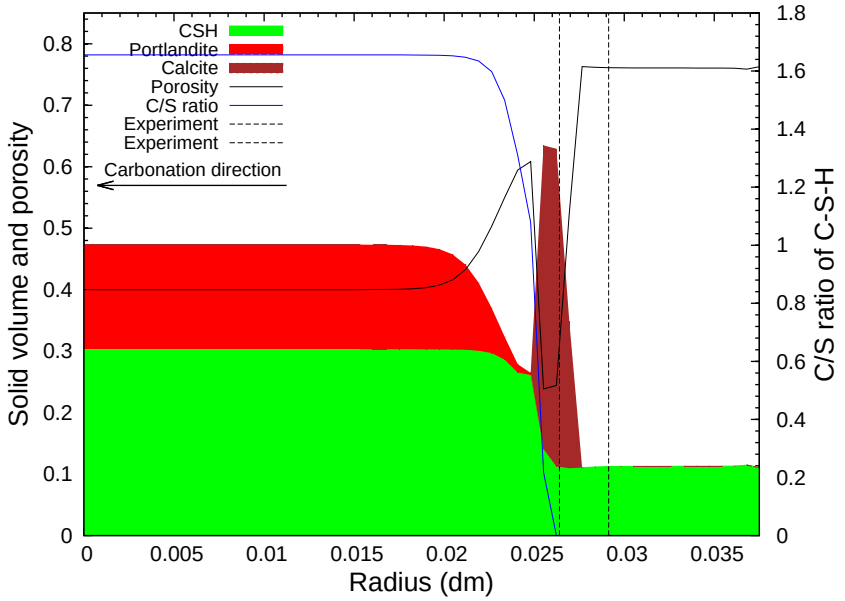

Figure 6.4: Profiles of solid volume compounds after 25 days of exposure under sandstone-like conditions at 293 K (vertical dash lines show the region of calcite accumulation assessed by (Duguid and Scherer, 2010)).

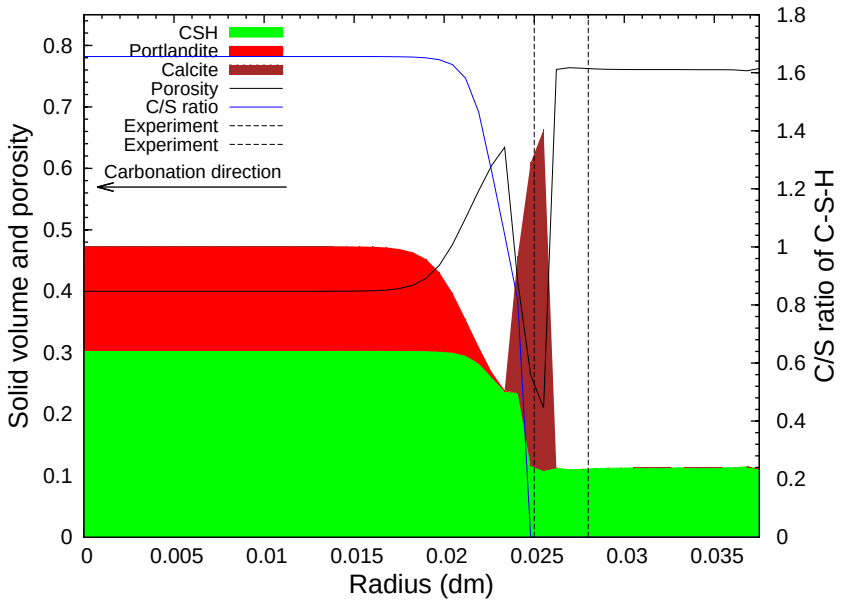

Figure 6.5: Profiles of solid volume compounds after 30 days of exposure under sandstone-like conditions at 293 K (vertical dash lines show the region of calcite accumulation assessed by (Duguid and Scherer, 2010)).

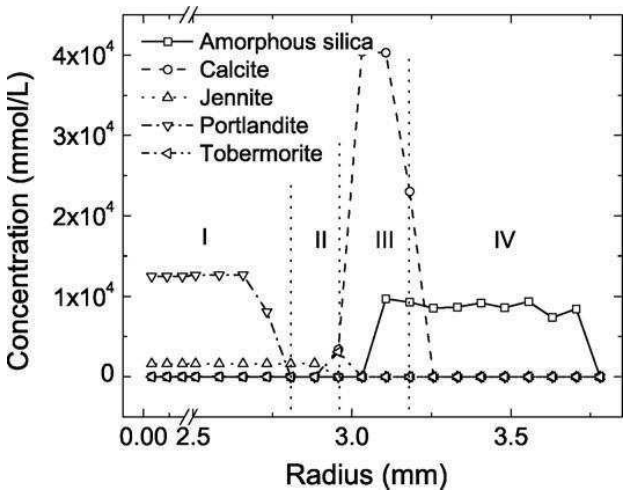

Figure 6.6: Calculated solid content profiles after a 30-day exposure time under sandstone-like conditions at 293 K (Huet et al., 2010).

layer has moved around 1.25 mm into the cement after a 30-day exposure period (vertical dash lines in Fig. 6.5). This is in good agreement with our predictions.

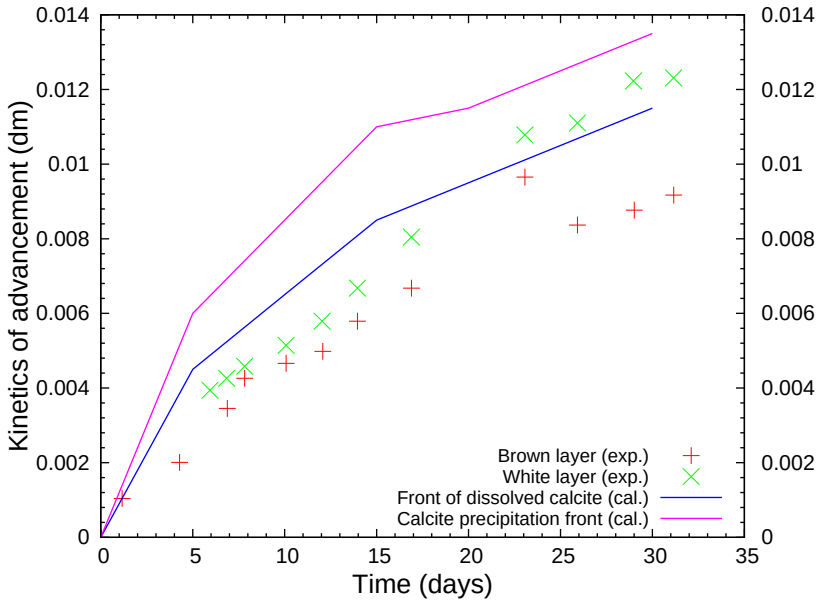

Figure 6.7: Comparison between our simulations and experiments from (Duguid and Scherer, 2010) of the penetration kinetics of the region of calcite accumulation versus time under sandstone-like conditions at 293 K. The calcite precipitation front in our simulation corresponds to the inner side of the white layer observed in the experiments, and the front of dissolved calcite in simulation refers to the inner side of the brown layer observed in the experiments.

6.3 High temperature conditions

Temperature has a complex effect on the change in composition of cement-based materials. On one hand, at higher temperature, the diffusion velocity of the aqueous species increases, which will enhance the change in composition of the cement paste. On the other hand, CO_2 solubility decreases as temperature increases, which will slow down the carbonation speed. Furthermore, the kinetics of dissolution and precipitation of solid compounds are accelerated and the chemical equilibrium of aqueous species, are affected by temperature changes.

Duguid and Scherer performed the same experiment at both 20 ℃ and 50 ℃ under sandstone-like conditions (Duguid and Scherer, 2010). Higher speed of change in composition was observed at 50 ℃. Here we simulate the same experiment at 50 ℃. The initial and boundary conditions are listed in Table 6.2. At 50 ℃ and atmospheric CO_2 pressure, CO_2 concentration is about 0.028 mol/L (see Fig. 6.8a). The calculated pH value at the boundary is about 4.6 (see Fig. 6.9a), higher than that at 20 ℃ where pH= 3.6 (see Fig. 6.9b). Duguid and Scherer didn't mention any difference of CO_2 concentration and pH value between 50 ℃ and 20 ℃ in their experiments.

The same ring pattern as that obtained at 20 ℃ is predicted (see Figs. 6.10). The penetration kinetics of the region of calcite accumulation is illustrated in Fig. 6.12 (lines calculated with 0.028 M CO_2). A faster penetration kinetics of the region of calcite accumulation is predicted compared to that at 20 ℃.

Table 6.2: Boundary and initial conditions in simulation under sandstone-like conditions at 323 K

Boundary Conditions			**Initial Conditions**
Balance Equation	BC left	BC right	
Carbon (C)	no flow	flow allowed ($\rho_{CO_2^0} = 0.028$ or 0.056 mol/L)	$\rho_{CO_2^0} = 10^{-16}$ mol/L
Calcium (Ca)	no flow	flow allowed (leaching of Ca: ζ_{Ca} = -20)	$\zeta_{Ca} = 1$
Silicon (Si)	no flow	no flow	$\zeta_{Si} = 1$
Sodium/Potassium	no flow	$\rho_{K^+} = 0.5$ mol/L	$\rho_{K^+} = 0.5$ mol/L
Chlorine (Cl)	no flow	$\rho_{Cl^-} = 0.5$ mol/L	$\rho_{Cl^-} = 0.5$ mol/L
Total mass	no flow	flow allowed ($P_L = 10^5$ or 2.8×10^5 Pa)	$P_L = 10^5$ or 2.8×10^5 Pa
Charge	no current	$\psi = 0$	$\psi = 0$

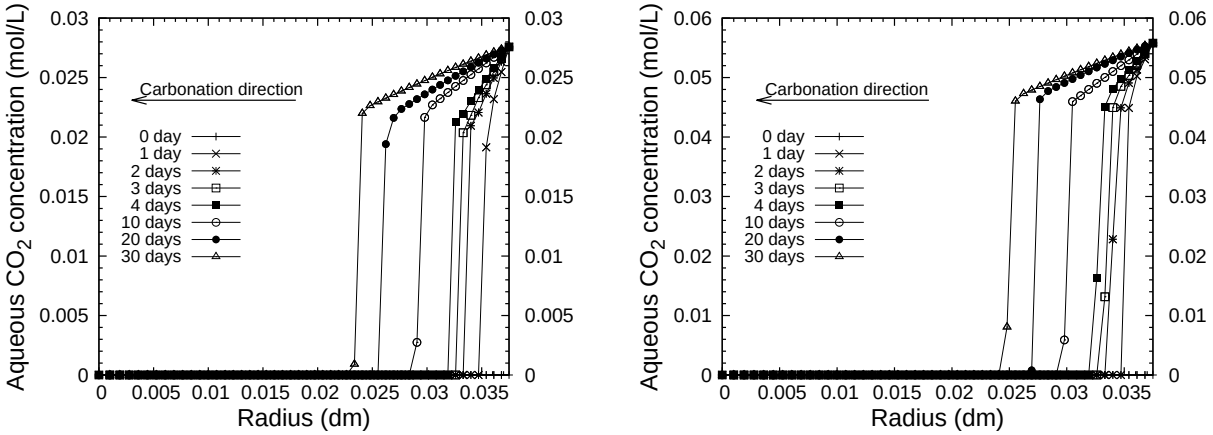

(a) At 323 K with $\rho_{CO_2^0} = 0.028$ M (b) At 293 K with $\rho_{CO_2^0} = 0.056$ M

Figure 6.8: The calculated aqueous CO_2 concentration profiles from 1 day to 30 days under sandstone-like conditions at 323 and 293 K. (a) At 323 K with $\rho_{CO_2^0} = 0.028$ M. (b) At 293 K with $\rho_{CO_2^0} = 0.056$ M.

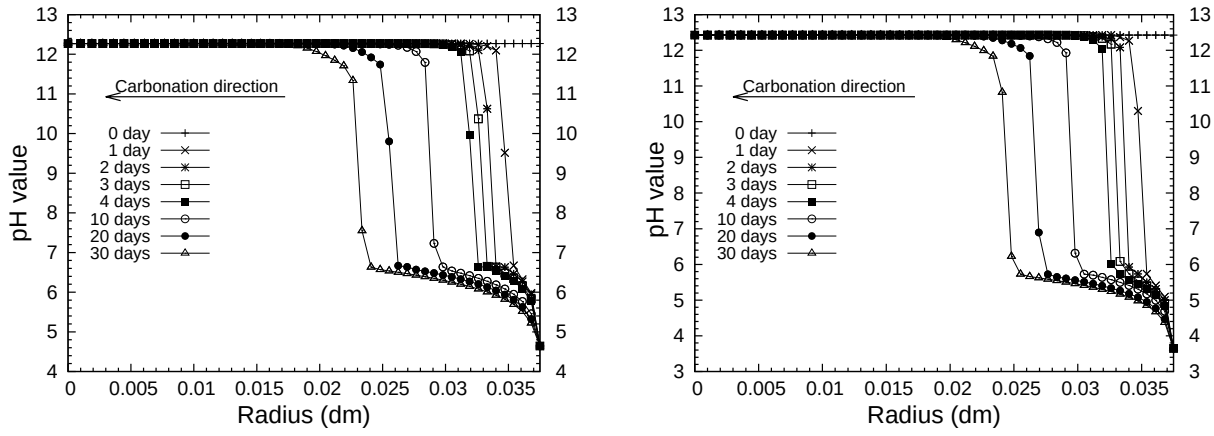

(a) At 323 K with $\rho_{CO_2^0} = 0.028$ M (b) At 293 K with $\rho_{CO_2^0} = 0.056$ M

Figure 6.9: The calculated pH value profiles from 1 day to 30 days under sandstone-like conditions at 323 and 293 K. (a) At 323 K with $\rho_{CO_2^0} = 0.028$ M. (b) At 293 K with $\rho_{CO_2^0} = 0.056$ M.

Comparing with experimental observation, the predicted kinetics of evolution is in good agreement with the experiments during the first 15 days but a little underestimation is observed in the following days. In our simulations, the difference between 20 ℃ and 50 ℃ is not as huge as the one observed in the experiments. However, in the experiments, the author did not mention the concentration difference of CO_2 under different temperatures, if we use the same value of CO_2 concentration as the one used at 20 ℃ (0.056 M) and conduct the simulation at 50 ℃ with $P_L = 2.\ 8{\times}10^5$ Pa (here we increase the liquid pressure due to the fact that 0.056 M is the solubility of CO_2 under $2.8{\times}10^5$ Pa at 50 ℃), the same ring pattern as in the experiments is obtained (see Fig. 6.11) and the predicted evolution kinetics of the region of calcite accumulation is quite close to the experimental observations (see lines calculated with 0.056 M CO_2 in Fig. 6.12).

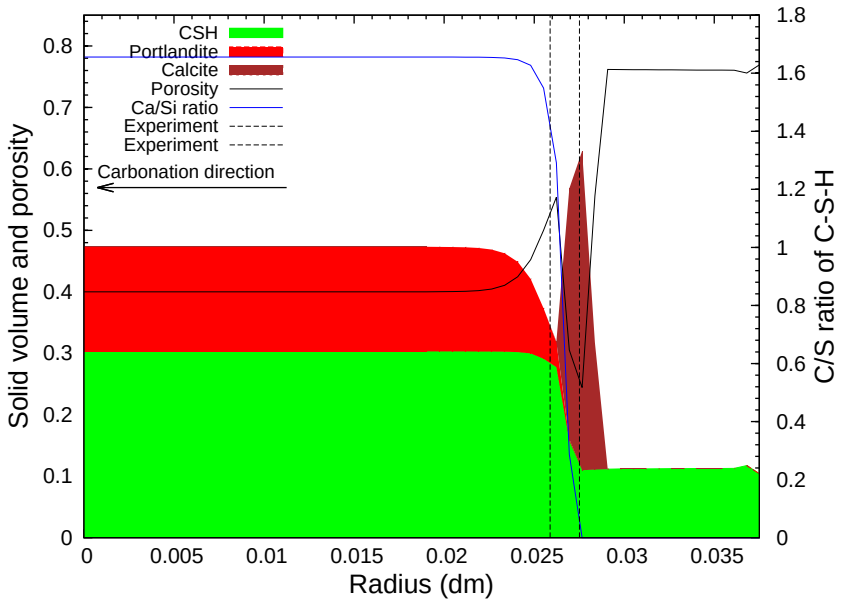

Figure 6.10: Profiles of solid volume compounds after 15 days of exposure under sandstone-like conditions at 323 K with $\rho_{CO_2^0} = 0.028$ M (vertical dash lines show the region of calcite accumulation assessed by (Duguid and Scherer, 2010)).

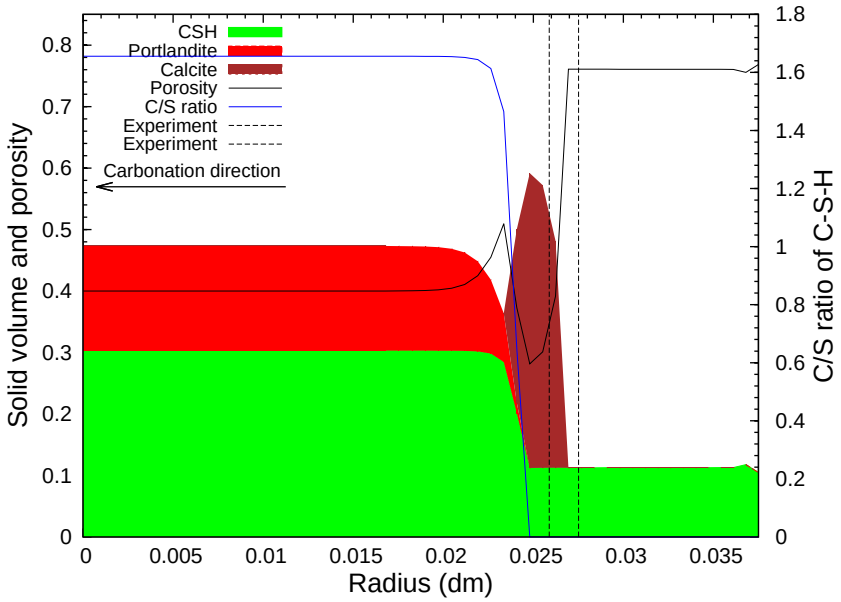

Figure 6.11: Profiles of solid volume compounds after 15 days of exposure under sandstone-like conditions at 323 K with $\rho^0_{CO_2} = 0.056$ M (vertical dash lines show the region of calcite accumulation assessed by (Duguid and Scherer, 2010)).

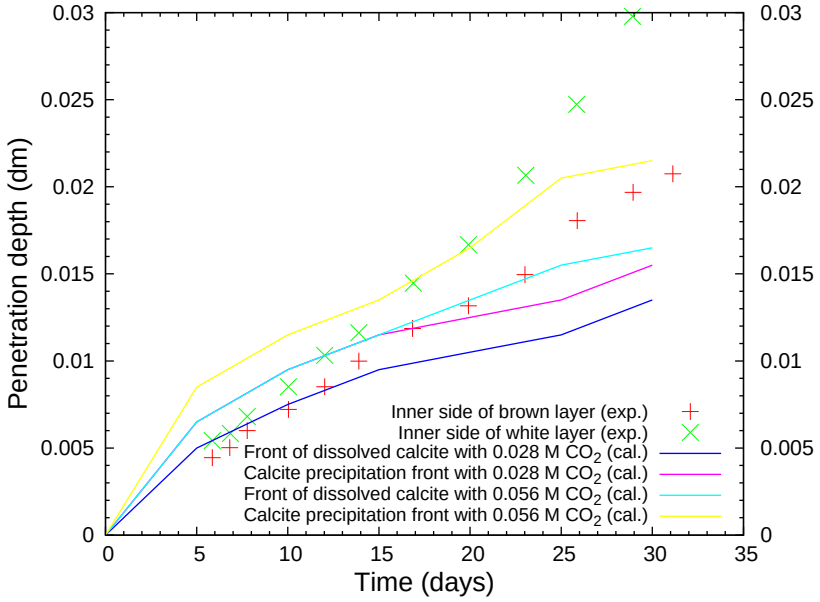

Figure 6.12: Comparison between our simulations and experiments from (Duguid and Scherer, 2010) of the penetration kinetics of the region of calcite accumulation under sandstone-like conditions at 323 K. The calcite precipitation front in our simulation corresponds to the inner side of the white layer observed in the experiments, and the front of dissolved calcite in simulation refers to the inner side of the brown layer observed in the experiments.

6.4 Limestone-like conditions

In one set of experiments, Duguid et al. saturated the brine with respect to calcite before putting in contact with the cement paste, thus simulating limestone reservoir conditions at 50 ℃ (323 K). In this section we simulate this set of experiments. Concerning the limestone reservoir condition, we set the activity product of calcite $Q_{C\bar{C}}$ as constant at the interface between the cement paste and the CO_2-saturated brine and equal to the equilibrium constant $K_{C\bar{C}}$ (by setting $\zeta_{Ca} = 0$), so that at the boundary the pore solution is always saturated with calcite. The calculation is conducted at 50 ℃. Boundary and initial conditions are summarized in Table 7.5.

Table 6.3: Boundary and initial conditions in simulation under limestone-like conditions at 323 K

Boundary Conditions			**Initial Conditions**
Balance Equation	BC left	BC right	
Carbon (C)	no flow	flow allowed ($\rho_{CO_2^0} = 0.028$ mol/L)	$\rho_{CO_2^0} = 10^{-16}$ mol/L
Calcium (Ca)	no flow	$\zeta_{Ca} = 0$	$\zeta_{Ca} = 1$
Silicon (Si)	no flow	no flow	$\zeta_{Si} = 1$
Sodium/Potassium	no flow	flow allowed ($\rho_{K^+} = 0.5$ mol/L)	$\rho_{K^+} = 0.5$ mol/L
Chlorine (Cl)	no flow	flow allowed ($\rho_{Cl^-} = 0.5$ mol/L)	$\rho_{Cl^-} = 0.5$ mol/L
Total mass	no flow	flow allowed ($P_L = 10^5$ Pa)	$P_L = 10^5$ Pa
Charge	no current	$\psi = 0$	$\psi = 0$

The calculated pH value at the boundary is about 6.6 (see Fig. 6.13b), higher than that under sandstone-like conditions at the same temperature (see Fig. 6.13a). The difference comes from the existence of $C\bar{C}$ at the boundary in this situation.

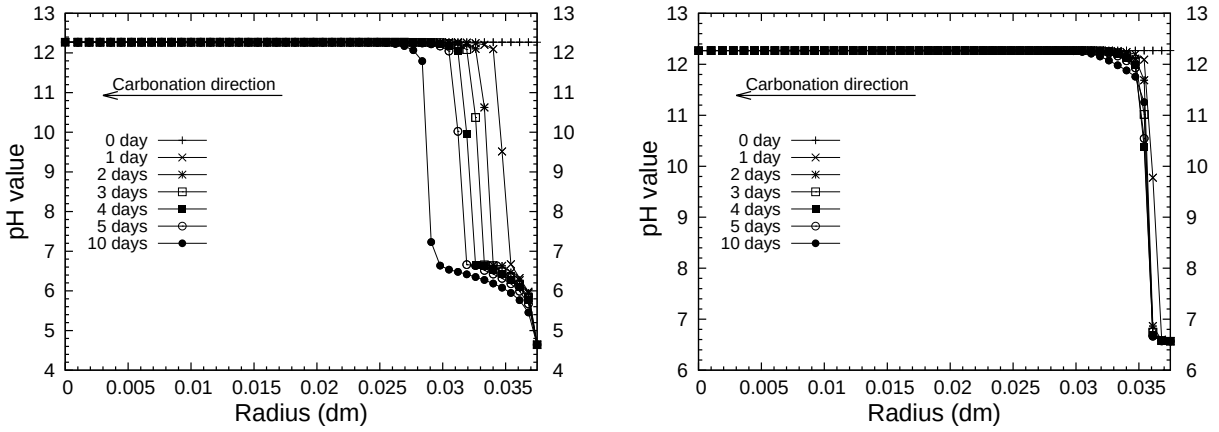

(a) Under sandstone-like conditions

(b) Under limestone-like conditions

Figure 6.13: The calculated pH value profiles at 323 K with $\rho_{CO_2^0} = 0.028$ M. (a) Under sandstone-like conditions. (b) Under limestone-like conditions.

Unlike sandstone-conditions, the samples exposed to calcium-saturated brine showed no apparent damage in this set of experiment (Duguid and Scherer, 2010). One light-colored ring appeared within the first

day and the depth was constant with an average value of 0.58±0.22 mm (vertical dash lines in Figs. 6.14 to 6.18) during the 26 days of exposure. Duguid et al. did not really explain the meaning of this behavior, *i.e.*, under sandstone-like conditions the samples showed rapid acid attack while under limestone-like conditions almost no acid attack took place. With the help of this numerical model, we can provide a relevant explanation. Our simulations show a full clogging (porosity drops to 0) at the point $r = 0.035$ dm after about 10 days of exposure (Fig. 6.18). Actually, the generated calcite can't be dissolved since the external brine is already saturated with calcite. This layer protects the inner part of the sample from leaching of calcite and hinders further carbonation. Accordingly, the carbonation is restricted at the sample surface and the degraded layer depth rapidly stabilizes.

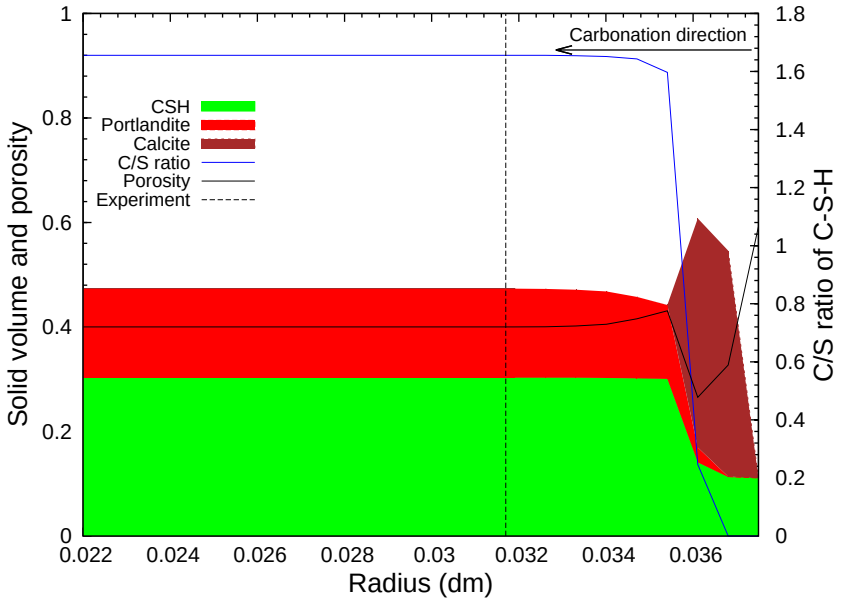

Figure 6.14: Profiles of solid volume compounds after 1 day of exposure under limestone-like conditions at 323 K (vertical dash line shows depth of the reacted region assessed by (Duguid and Scherer, 2010)).

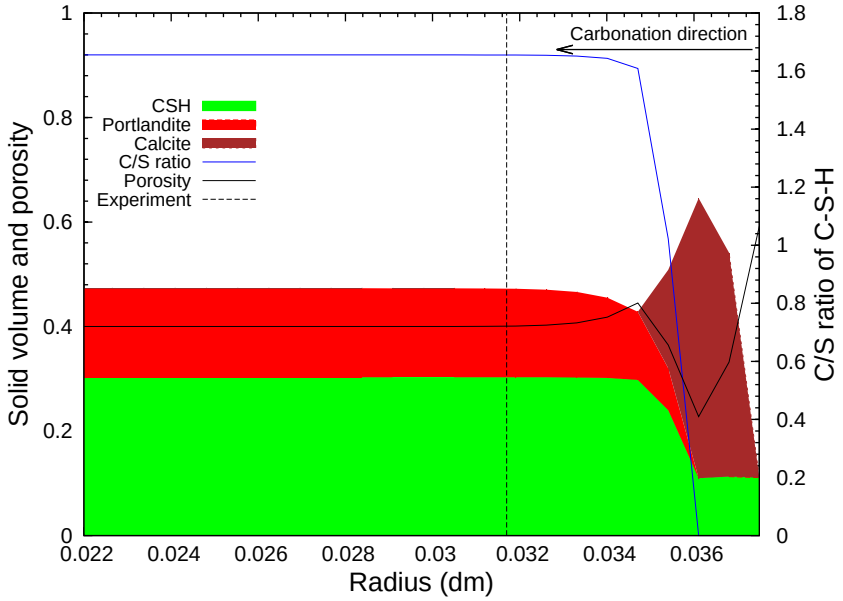

Figure 6.15: Profiles of solid volume compounds after 2 days of exposure under limestone-like conditions at 323 K (vertical dash line shows depth of the reacted region assessed by (Duguid and Scherer, 2010)).

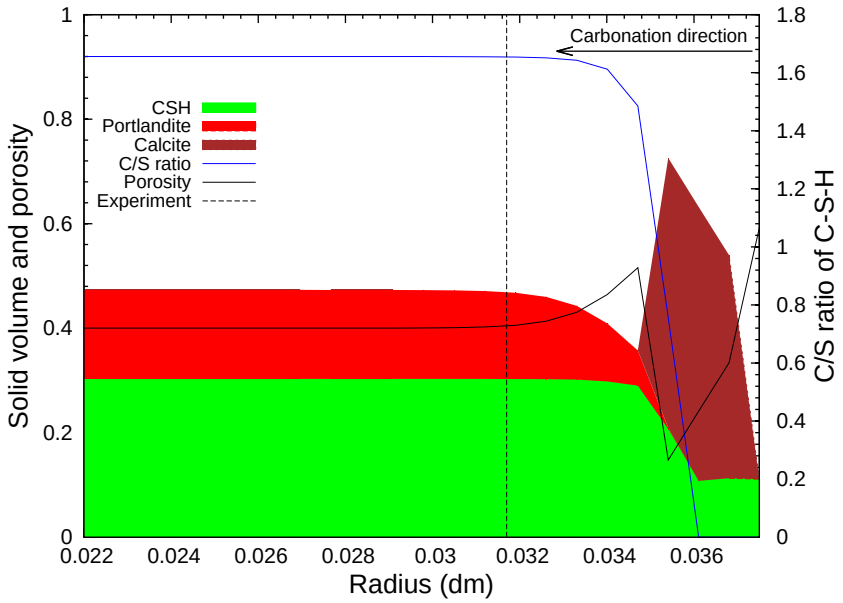

Figure 6.16: Profiles of solid volume compounds after 4 days of exposure under limestone-like conditions at 323 K (vertical dash line shows depth of the reacted region assessed by (Duguid and Scherer, 2010)).

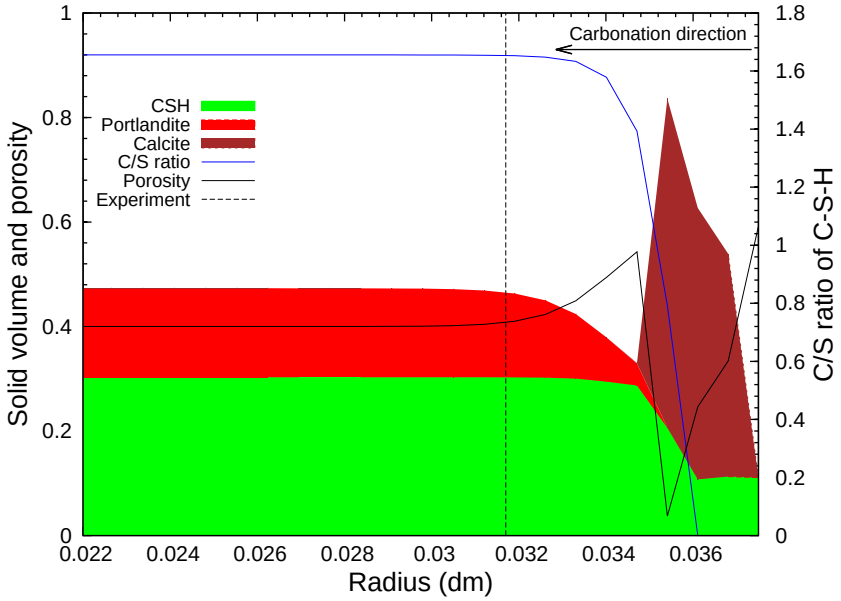

Figure 6.17: Profiles of solid volume compounds after 5 days of exposure under limestone-like conditions at 323 K (vertical dash line shows depth of the reacted region assessed by (Duguid and Scherer, 2010)).

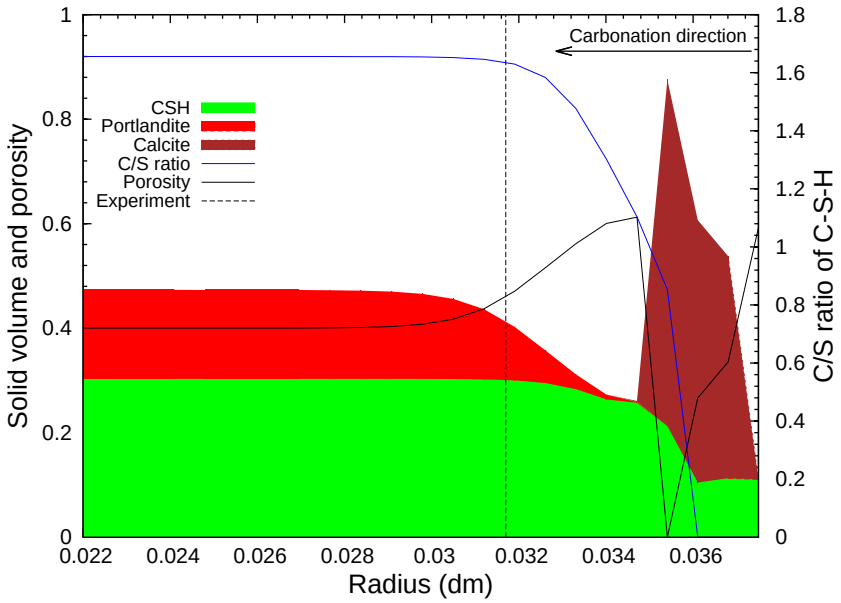

Figure 6.18: Profiles of solid volume compounds after 10 days of exposure under limestone-like conditions at 323 K (vertical dash line shows depth of the reacted region assessed by (Duguid and Scherer, 2010)).

6.5 Sensitivity analysis

In this section, the sensitivity of several parameters, *i.e.*, temperature, CO_2 concentration and activity product of $C\bar{C}$ at the boundary, will be analyzed. For the simulations in this section, a cylinder sample with a radius of 5 mm divided into 50 nodes is used, rather than 3.75 mm used in simulated experiments of (Duguid and Scherer, 2010). The initial CH and C-S-H contents are the same as the previous values for sandstone-like conditions.

6.5.1 Study of CO_2 concentration

In Duguid's experiments (Duguid and Scherer, 2010), the dissolved CO_2 concentration is rather small (around 0.056 M) comparing with the value at downhole conditions. Here we conduct numerical simulations with different CO_2 concentrations at the boundary to propose a sensitivity analysis of this parameter. Simulations are conducted with different CO_2 concentrations at the surface ($\rho_{CO_2^0} = 0.028, 0.185, 1.12$ M), consistent with different liquid pressures (1 bar, 10 bars, 100 bars, respectively). The initial and boundary conditions are listed in Table 6.4. The sandstone-like boundary conditions are maintained. All simulations are run at 50 ℃ (323 K).

Table 6.4: Boundary and initial conditions in simulations for the study of CO_2 concentration at 323 K

Boundary Conditions			**Initial Conditions**
Balance Equation	BC left	BC right	
Carbon (C)	no flow	flow allowed ($\rho_{CO_2^0} = 0.028, 0.185, 1.12$ M)	$\rho_{CO_2^0} = 10^{-16}$ mol/L
Calcium (Ca)	no flow	flow allowed (leaching of Ca: ζ_{Ca} = -20)	$\zeta_{Ca} = 1$
Silicon (Si)	no flow	no flow	$\zeta_{Si} = 1$
Sodium/Potassium	no flow	flow allowed ($\rho_{K^+} = 0.5$ mol/L)	$\rho_{K^+} = 0.5$ mol/L
Chlorine (Cl)	no flow	flow allowed ($\rho_{Cl^-} = 0.5$ mol/L)	$\rho_{Cl^-} = 0.5$ mol/L
Total mass	no flow	flow allowed (P_L = 1, 10, 100 bars)	P_L = 1, 10, 100 bars
Charge	no current	$\psi = 0$	$\psi = 0$

*p*H value profiles during carbonation are illustrated in Fig. 6.19. The *p*H value is 12.4 in the unreacted region, and decreases to 4.6 with $\rho_{CO_2^0} = 0.028$ M, 4.2 with with $\rho_{CO_2^0} = 0.185$ M and 3.9 with with $\rho_{CO_2^0}$ = 1.12 M at the boundary.

As discussed before, calcium flux mainly comes from the Ca^{2+} diffusion. Ca^{2+} concentration profiles are presented in Fig. 6.20. There is a concentration gradient (positive) of Ca^{2+} between the front of dissolved calcite and the sample surface, thus a diffusion of Ca^{2+} towards the surface will cause a leaching effect. Between the CH dissolution front and the calcite precipitation front, a drop of Ca^{2+} concentration (positive concentration gradient) is observed, the Ca^{2+} concentration profiles are quite similar in this region regardless CO_2 concentration. This pattern is responsible for $C\bar{C}$ accumulation and the drop of

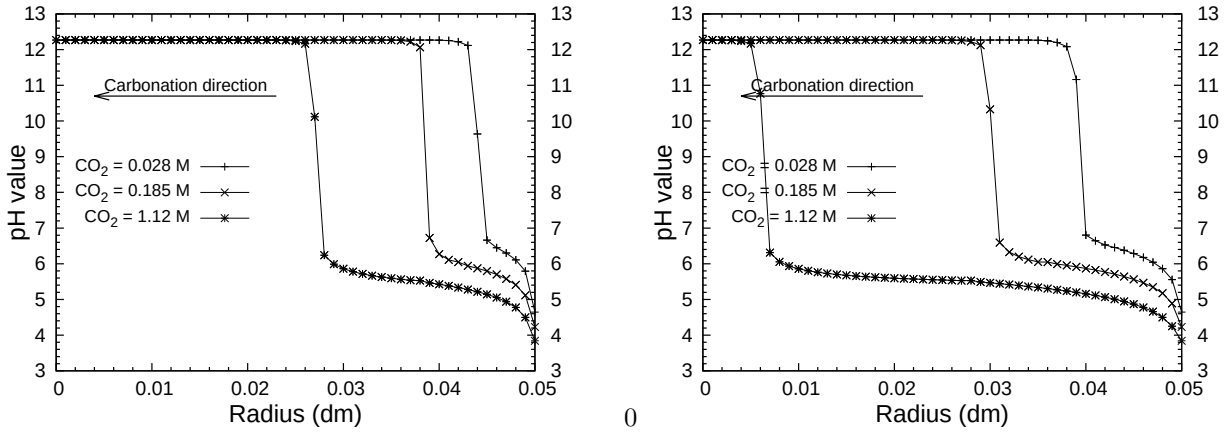

(a) After 5 days of exposure

0

(b) After 15 days of exposure

Figure 6.19: The calculated pH value profiles under sandstone-like conditions at 323 K with different CO_2 concentrations. (a) After 5 days of exposure. (b) After 15 days of exposure.

porosity near the calcite precipitation front, as well as the porosity increase in the CH dissolution region. There is a negative Ca^{2+} gradient between the calcite precipitation front and the front of dissolved calcite, which means the calcium for calcite precipitation comes from both the CH dissolution in the region of CH dissolution and the calcite dissolution in the region of calcite accumulation. The total flux of calcium is illustrated in Fig. 6.21.

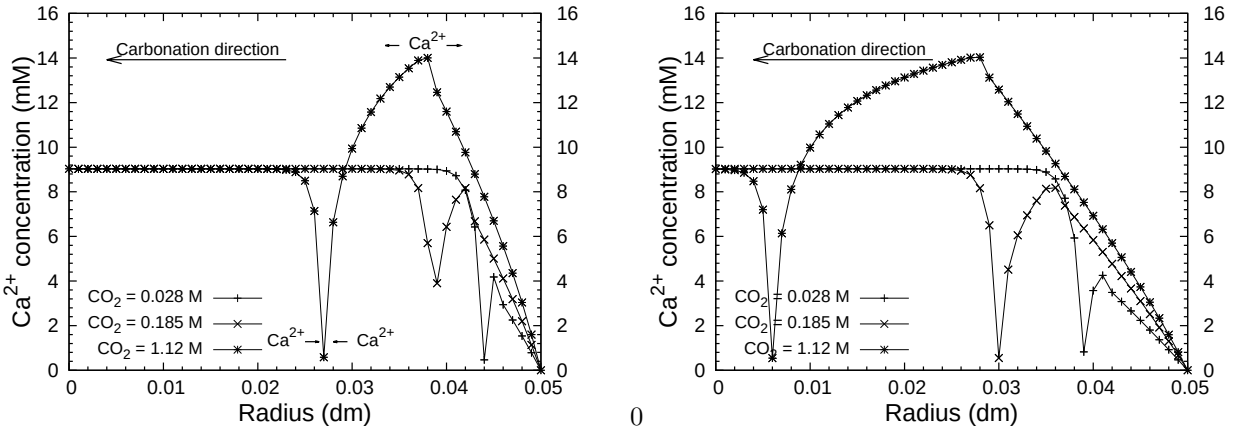

(a) After 5 days of exposure

0

(b) After 15 days of exposure

Figure 6.20: The calculated Ca^{2+} concentration profiles under sandstone-like conditions at 323 K with different CO_2 concentrations. (a) After 5 days of exposure. (b) After 15 days of exposure.

Since there is no gas phase in this simulation, the flux of carbon is contributed mainly by the diffusion of dissolved CO_2 and that of HCO_3^-. In the region of calcite accumulation, the concentration gradients of both aqueous CO_2 and HCO_3^- are negative (see Figs. 6.22 and 6.23). Thus carbon transfers from the front of dissolved calcite to the calcite precipitation front. In the fully degraded region (between the front

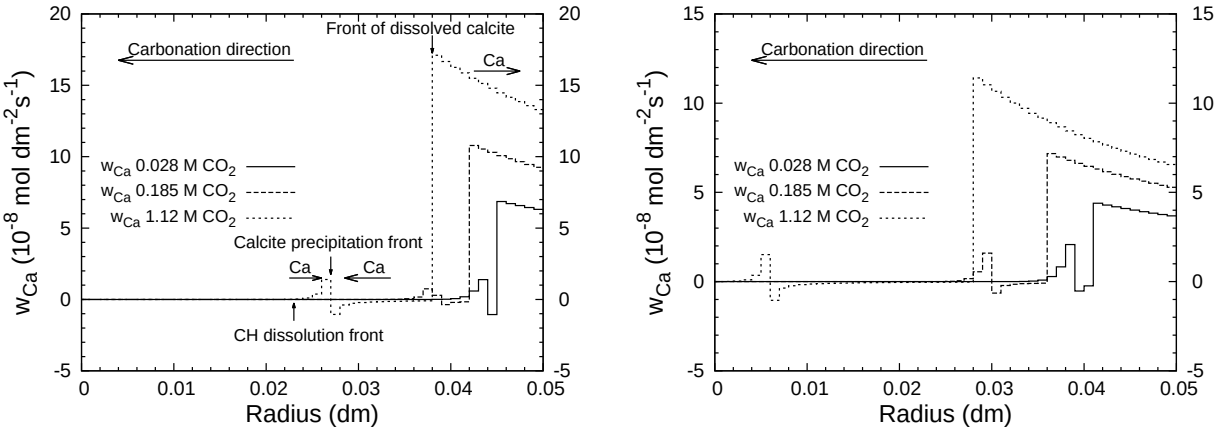

(a) After 5 days of exposure

(b) After 15 days of exposure

Figure 6.21: The calculated flow of calcium (w_{Ca}) under sandstone-like conditions at 323 K with different CO_2 concentrations. (a) After 5 days of exposure. (b) After 15 days of exposure.

of dissolved calcite and the sample surface), concentration gradient of aqueous CO_2 is negative, and that of HCO_3^- is positive. As a result, carbon flux in this region is initially negative and tends to 0 or even positive (see Fig. 6.24). Comparing the carbon flux in these two regions, we can conclude that the major source of of carbon for calcite precipitation is the carbon released from the calcite dissolution front, rather than the external CO_2. Actually part of the carbon released from the calcite dissolution front can diffuse to the external environment in some case (see w_C with 1.12 M CO_2 in Fig. 6.24b).

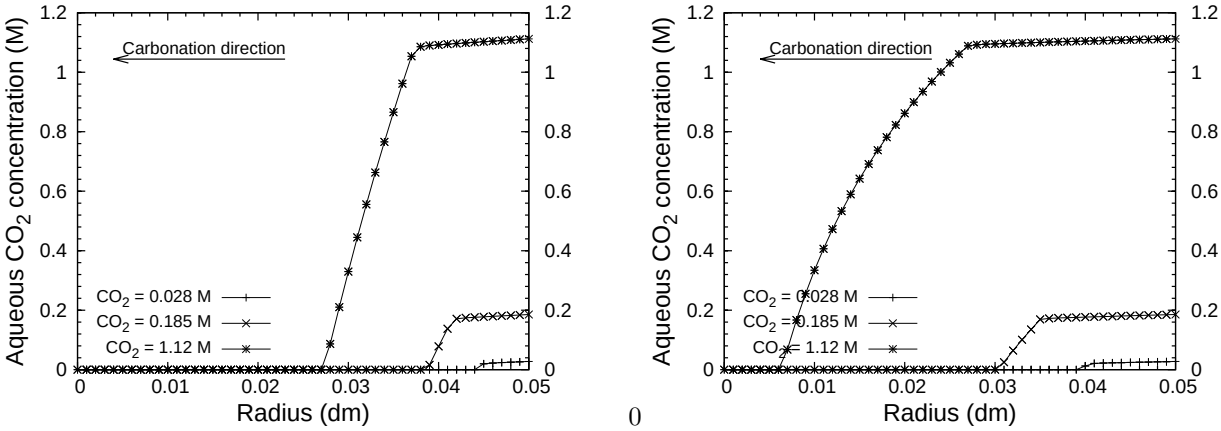

(a) After 5 days of exposure

(b) After 15 days of exposure

Figure 6.22: The calculated aqueous CO_2 concentration profiles under sandstone-like conditions at 323 K with different CO_2 concentrations. (a) After 5 days of exposure. (b) After 15 days of exposure.

Figs. 6.25-6.27 provide solid and porosity profiles after 15 days of exposure with different CO_2 concentrations. Similar successive layers are observed in all conditions. A higher CO_2 concentration causes a faster acid attack. We can also find that the porosity increase in the CH dissolution region gets less obvious

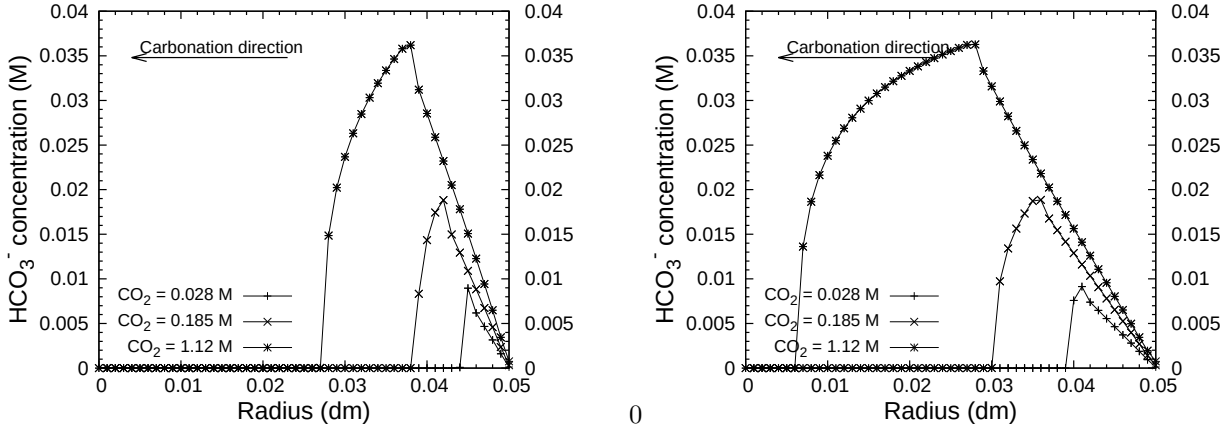

(a) After 5 days of exposure (b) After 15 days of exposure

Figure 6.23: The calculated HCO_3^- concentration profiles under sandstone-like conditions at 323 K with different CO_2 concentrations. (a) After 5 days of exposure. (b) After 15 days of exposure.

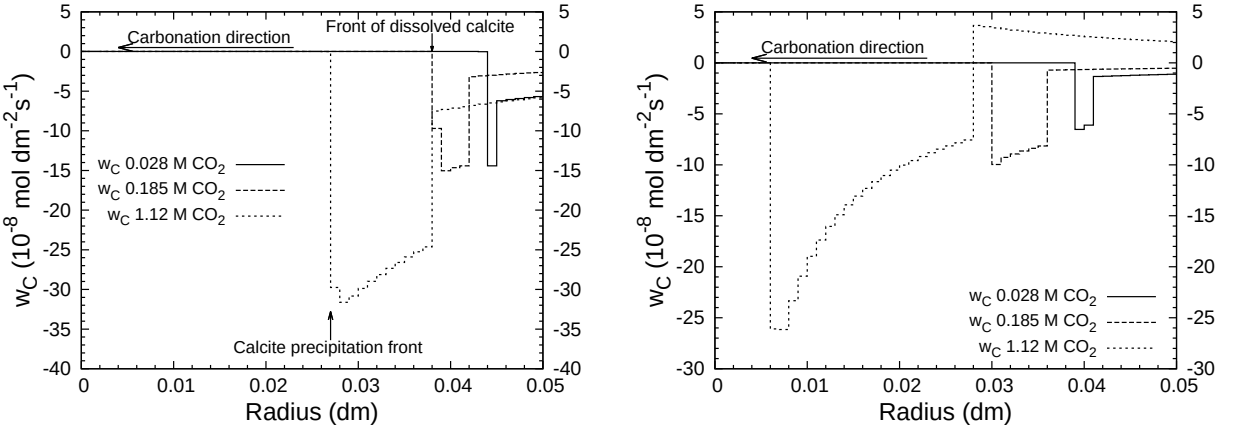

(a) After 5 days of exposure (b) After 15 days of exposure

Figure 6.24: The calculated flow of carbon (w_C) under sandstone-like conditions at 323 K with different CO_2 concentrations. (a) After 5 days of exposure. (b) After 15 days of exposure.

with higher CO_2 concentration, which means this specified pattern caused by calcium transport from CH dissolution front to the calcite precipitation front can be neglected at high CO_2 concentration conditions.

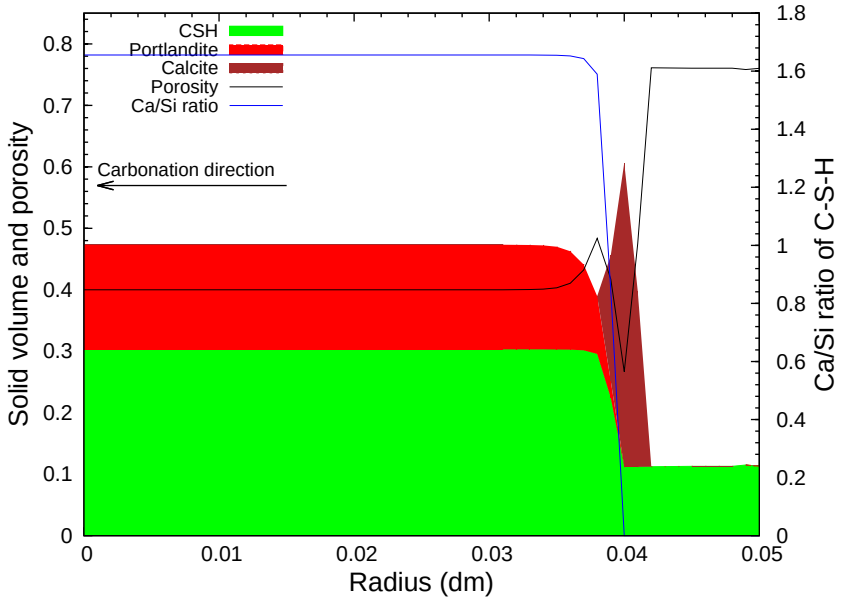

Figure 6.25: Profiles of solid volume compounds after 15 days of exposure under sandstone-like conditions at 323 K with $\rho_{CO_2^0} = 0.028$ M (equivalent to CO_2 concentration at $T = 323$ K, $P = 1$ bar).

Since the major part of carbon and calcium for calcite precipitation is from the cement rather than the external environment (see Fig. 6.26), the calcite precipitation is actually a self-perpetuating phenomenon. The feature which needs to be highlighted is the meaning of the width of the region of calcite accumulation (see Fig. 6.28). A higher CO_2 concentration engenders a wider region of calcite accumulation. We can find that the width of this region grows with time, especially for the situation with $\rho_{CO_2^0} = 1.12$ M. The amount of precipitated calcite is controlled by the flux of carbon element at the calcite precipitation front, and that of dissolved calcite is controlled by calcium flux at the front of the dissolved calcite. If the CO_2 concentration increases, the transport of carbon element at the calcite precipitation front (mainly due to CO_2 diffusion) is enhanced, the transport of calcium at the front of the dissolved calcite (mainly by Ca^{2+} diffusion) seems less affected by CO_2 concentration (see Figs. 6.21 and 6.24). It is thus expected that the region of calcite accumulation becomes broader with higher CO_2 concentration. The width of this region also reflects the total amount of precipitated carbon element in the cement, as long as there is carbon flux from the external environment to the cement, this region get wider. The radius of this region also has an impact. In the simulation with 1.12 M CO_2, after 15 days there is leaching of carbon (see Fig. 6.24b), the width of the calcite accumulation region still gets wider as the radius of this region decreases.

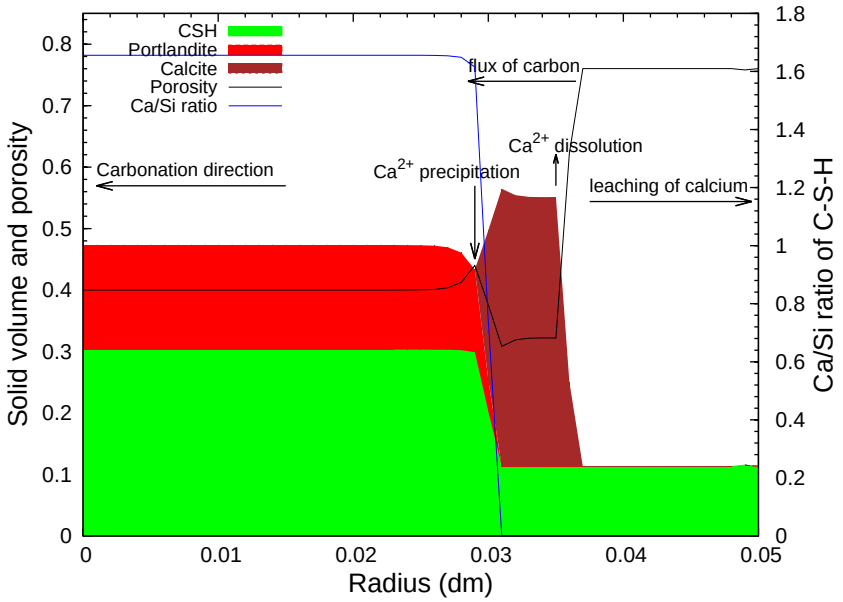

Figure 6.26: Profiles of solid volume compounds after 15 days of exposure under sandstone-like conditions at 323 K with $\rho_{CO_2^0} = 0.185$ M (equivalent to CO_2 concentration at $T = 323$ K, $P = 10$ bar).

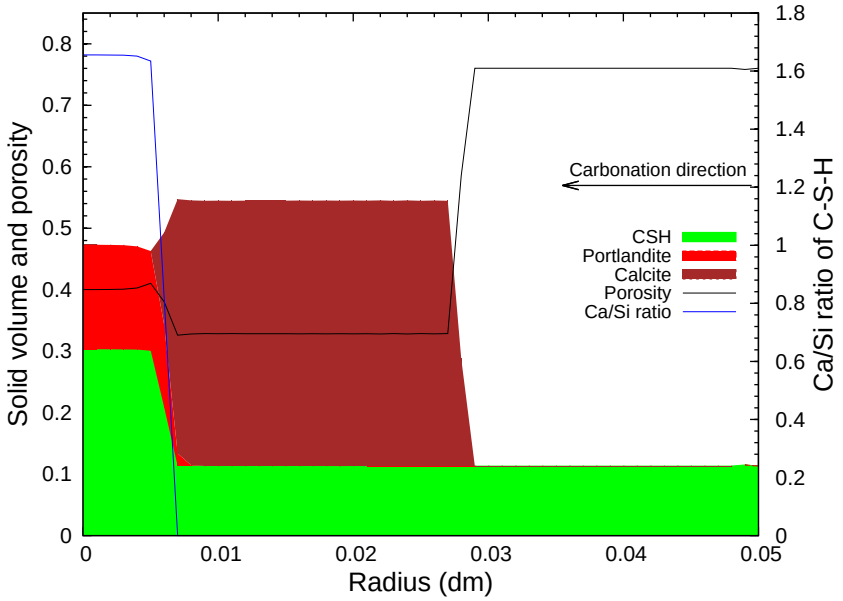

Figure 6.27: Profiles of solid volume compounds after 15 days of exposure under sandstone-like conditions at 323 K with $\rho_{CO_2^0} = 1.12$ M (equivalent to CO_2 concentration at $T = 323$ K, $P = 100$ bar).

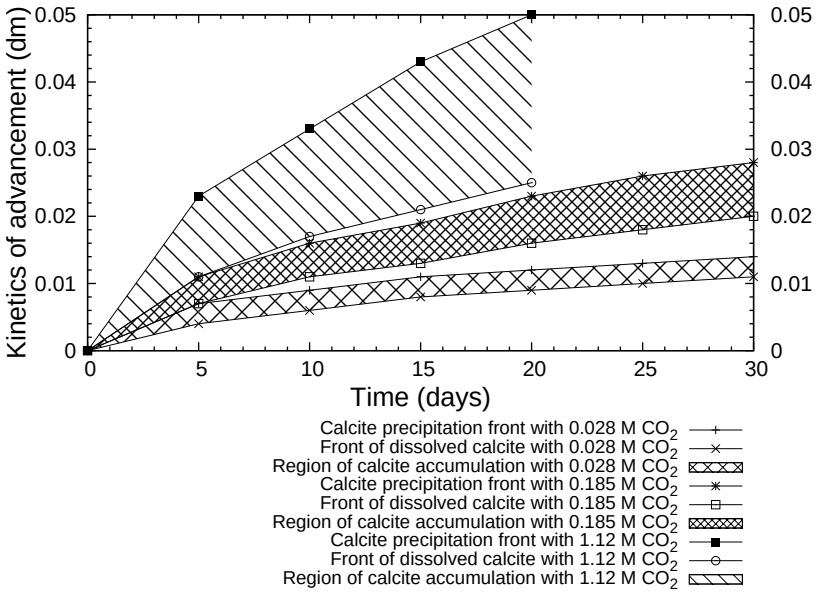

Figure 6.28: Kinetics of penetration of the region of calcite accumulation under sandstone-like conditions at 323 K with different CO_2 concentrations.

6.5.2 Study of temperature effect

Here a set of simulations with same CO_2 concentration at the boundary (0.056 M) at different temperatures (293 K, 323 K and 363 K) are presented to analyze the temperature effect. The initial and boundary conditions are listed in Table 6.5. The sandstone-like boundary conditions are maintained.

Table 6.5: Boundary and initial conditions in simulations for the study of temperature effect

Boundary Conditions			**Initial Conditions**
Balance Equation	BC left	BC right	
Carbon (C)	no flow	flow allowed ($\rho_{CO_2^0} = 0.056$ M)	$\rho_{CO_2^0} = 10^{-16}$ mol/L
Calcium (Ca)	no flow	flow allowed (leaching of Ca: ζ_{Ca} = -20)	$\zeta_{Ca} = 1$
Silicon (Si)	no flow	no flow	$\zeta_{Si} = 1$
Sodium/Potassium	no flow	flow allowed ($\rho_{K^+} = 0.5$ mol/L)	$\rho_{K^+} = 0.5$ mol/L
Chlorine (Cl)	no flow	flow allowed ($\rho_{Cl^-} = 0.5$ mol/L)	$\rho_{Cl^-} = 0.5$ mol/L
Total mass	no flow	flow allowed (P_L = 1, 2.8 and 5.2 bar)	P_L = 1, 2.8 and 5.2 bar
Charge	no current	$\psi = 0$	$\psi = 0$

Chemical equilibrium is affected by temperature and this effect is considered in our code. As a result, we can find that different pH values at the boundary are predicted though the CO_2 concentration is the same, about 3.6 at 293 K, 4.5 at 323 K and 5.4 at 363 K (see Fig. 6.29). Similarly, different Ca^{2+} concentration profiles are predicted. At higher temperature, the Ca^{2+} concentration is lower (see Fig. 6.30).

Figs. 6.31-6.33 provide solid and porosity profiles after a 15-day exposure duration at different temperatures. Similar successive layers are observed in all conditions, which means though chemical equilibrium is related with temperature, carbonation patterns are similar under different temperatures. The influence

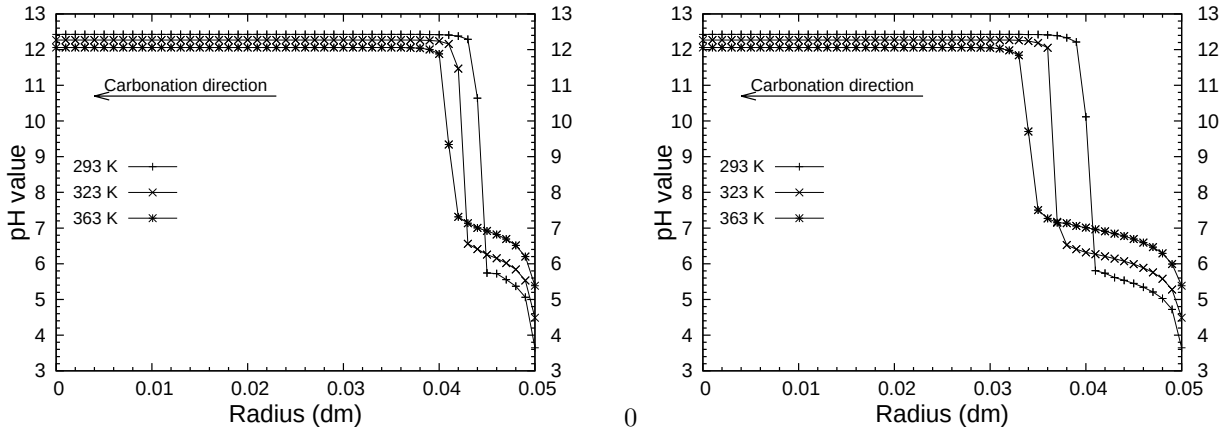

(a) After 5 days of exposure

(b) After 15 days of exposure

Figure 6.29: The calculated pH value profiles under sandstone-like conditions at different temperature with $\rho_{CO_2^0} = 0.056$ M. (a) After 5 days of exposure. (b) After 15 days of exposure.

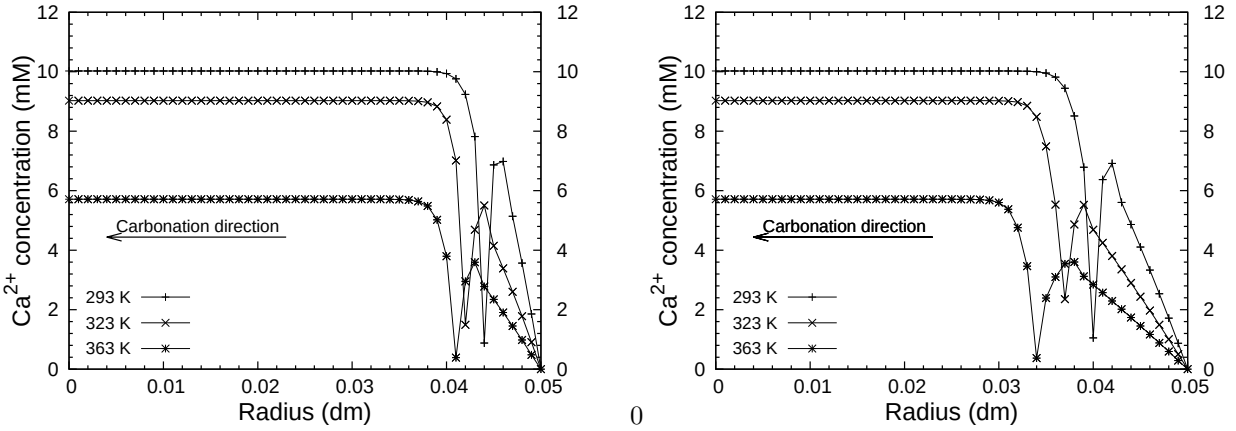

(a) After 5 days of exposure

(b) After 15 days of exposure

Figure 6.30: The calculated Ca^{2+} concentration profiles under sandstone-like conditions at different temperature with $\rho_{CO_2^0} = 0.056$ M. (a) After 5 days of exposure. (b) After 15 days of exposure.

of temperature is mainly reflected in the carbonation kinetics. Diffusion coefficients of aqueous species are very sensitive to temperature (see Eq. (4.18)), as a result faster kinetics of penetration of each layer is observed at higher temperature.

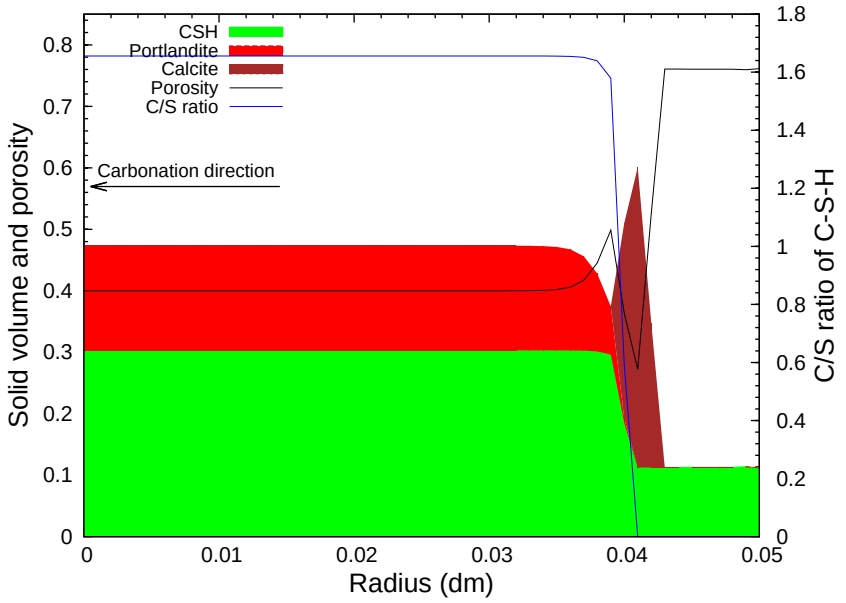

Figure 6.31: Profiles of solid volume compounds after 15 days of exposure under sandstone-like conditions at 293 K with $\rho_{CO_2^0} = 0.056$ M with sample radius of 0.05 dm.

6.5.3 Study of activity product of $C\bar{C}$ at the boundary

Duguid's work has shown that the carbonation pattern drastically depends on whether or not the leaching brine is saturated with $C\bar{C}$. This boundary condition is controlled by the activity product of $C\bar{C}$ at the boundary. Here we analyze the effect of this boundary condition with a set of simulations. Cement paste is exposed to 0.185 M CO_2 at $T = 323$ K, $P_L = 10$ bars with different value of $Q_{C\bar{C}}$ ($Q_{C\bar{C}} = 1, 0.5, 0.1, 0.01, 10^{-20} \times K_{C\bar{C}}$). The initial and boundary conditions are listed in Table 6.6.

Table 6.6: Boundary and initial conditions in simulation for the study of the activity product of $C\bar{C}$ at the boundary

Boundary Conditions			**Initial Conditions**
Balance Equation	BC left	BC right	
Carbon (C)	no flow	flow allowed ($\rho_{CO_2^0} = 0.185$ M)	$\rho_{CO_2^0} = 10^{-16}$ mol/L
Calcium (Ca)	no flow	ζ_{Ca} = 0,-0.3,-1,-2,-20	$\zeta_{Ca} = 1$
Silicon (Si)	no flow	no flow	$\zeta_{Si} = 1$
Sodium/Potassium	no flow	$\rho_{K^+} = 0.5$ mol/L	$\rho_{K^+} = 0.5$ mol/L
Chlorine (Cl)	no flow	$\rho_{Cl^-} = 0.5$ mol/L	$\rho_{Cl^-} = 0.5$ mol/L
Total mass	no flow	flow allowed ($P_L = 10^6$ Pa)	$P_L = 10^6$ Pa
Charge	no current	$\psi = 0$	$\psi = 0$

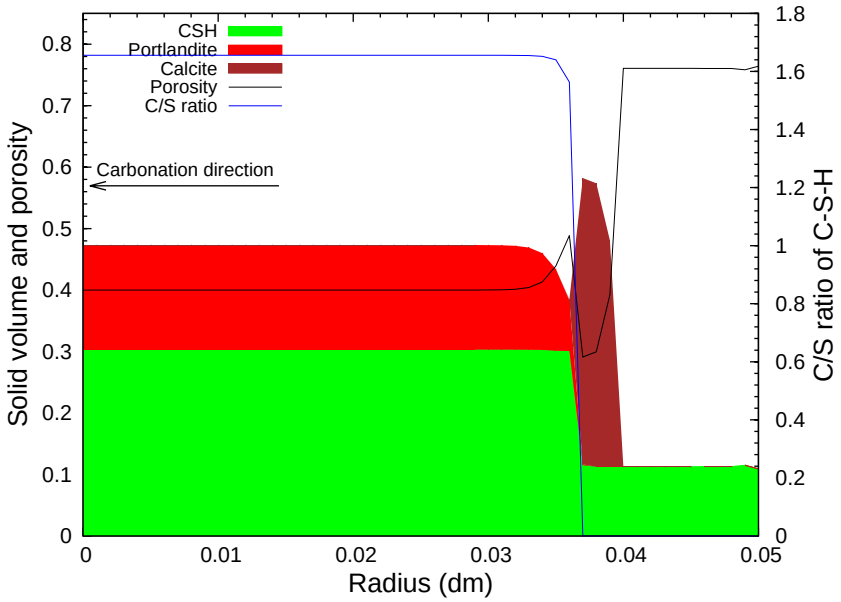

Figure 6.32: Profiles of solid volume compounds after 15 days of exposure under sandstone-like conditions at 323 K with $\rho_{CO_2^0} = 0.056$ M with sample radius of 0.05 dm.

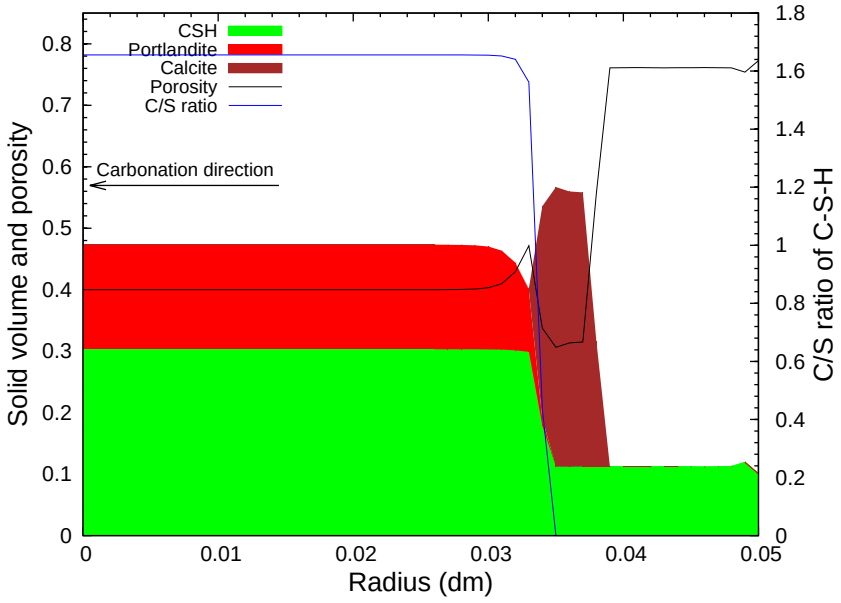

Figure 6.33: Profiles of solid volume compounds after 15 days of exposure under sandstone-like conditions at 363 K with $\rho_{CO_2^0} = 0.056$ M with sample radius of 0.05 dm.

When $Q_{C\bar{C}} = K_{C\bar{C}}$ (see Fig. 6.34), the precipitated $C\bar{C}$ can not dissolve at the sample surface, thus the fully degraded region (where there is only amorphous silica left) is not observed. With $Q_{C\bar{C}}$ smaller than $K_{C\bar{C}}$, $C\bar{C}$ can dissolve at the surface (see Figs. 6.35 to 6.38), thus the kinetics of penetration of each reacted region is faster than in the case of $Q_{C\bar{C}} = K_{C\bar{C}}$, due to the large porosity of the fully degraded region at the surface. We can also find that with smaller $Q_{C\bar{C}}$, faster evolution kinetics of the fully degraded region is observed.

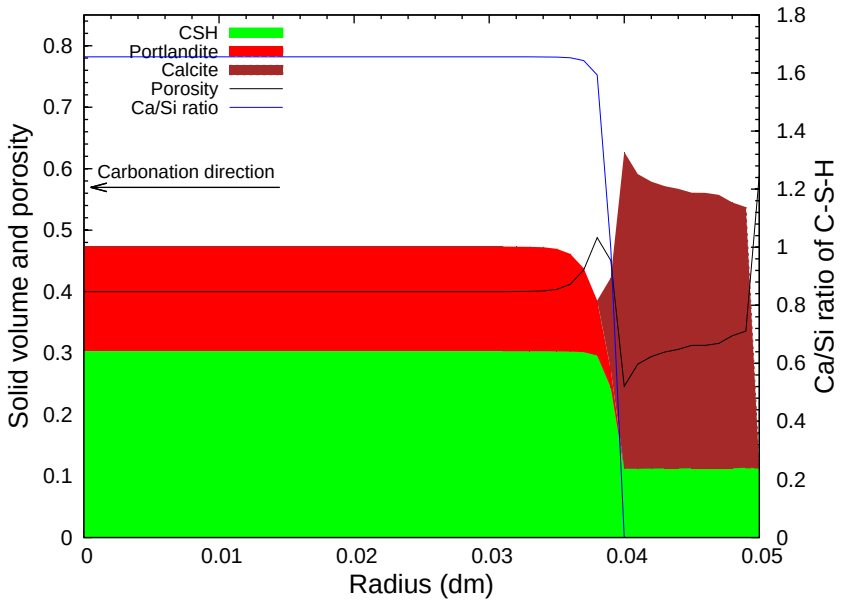

Figure 6.34: Profiles of solid volume compounds after 15 days of exposure with 0.185 M CO_2 at $T = 323$ K, $P = 10$ bar, with $Q_{C\bar{C}} = K_{C\bar{C}}$ at the boundary.

$Q_{C\bar{C}}$ controls the leaching of calcium, which can be inferred from the Ca^{2+} concentration profile (see Fig. 6.39). Ca^{2+} concentration at the boundary is related with the $Q_{C\bar{C}}$ value, about 8.4 mM when $Q_{C\bar{C}} = K_{C\bar{C}}$, and tends to 0 when $Q_{C\bar{C}}$ decreases. When $Q_{C\bar{C}} = K_{C\bar{C}}$, the Ca^{2+} concentration at the sample surface is higher than that of the inner part, so there is no leaching of Ca^{2+} ion in this case. When $Q_{C\bar{C}}$ is smaller than $K_{C\bar{C}}$ at the boundary, there is a concentration gradient of Ca^{2+}, thus a diffusion of Ca^{2+} towards the surface will cause a leaching effect. It is obvious that with lower Ca^{2+} concentration at the surface, the faster the leaching is observed. The Ca^{2+} concentration profiles are quite similar, except in the fully degraded region, which explains that few difference of phase assemblage is observed as soon as $Q_{C\bar{C}} < K_{C\bar{C}}$. Between the CH dissolution front and the calcite precipitation front, a drop of Ca^{2+} concentration is observed regardless the $Q_{C\bar{C}}$ value. This pattern is responsible for $C\bar{C}$ accumulation and the drop of porosity near the calcite precipitation front. The large amount of $C\bar{C}$ precipitation and the drop in porosity which could induce the clogging effect are not only related to CH and C-S-H carbonation but also the transport of the calcium (see mechanisms in Section 6.5.1). Other ions, *i.e.*, $CaHCO_3^+$, $CaOH^+$,

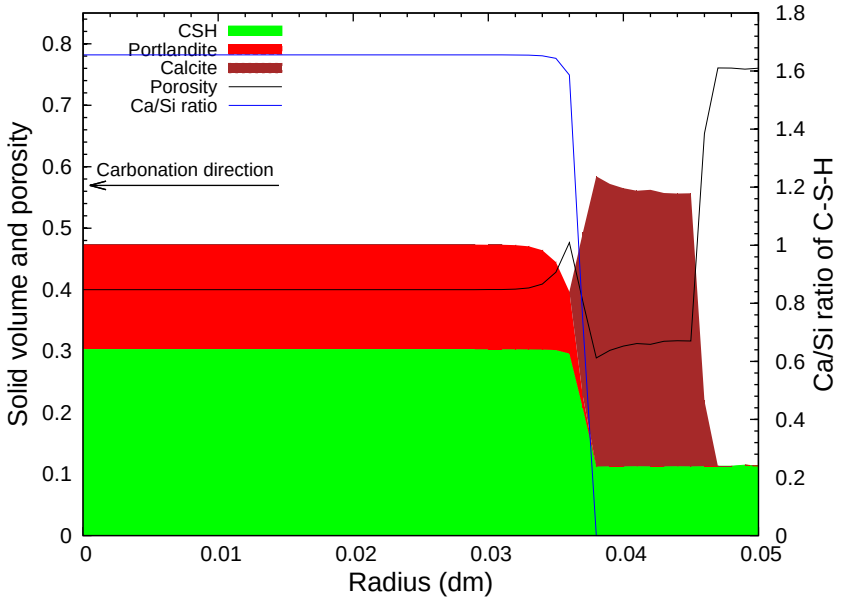

Figure 6.35: Profiles of solid volume compounds after 15 days of exposure with 0.185 M CO_2 at $T = 323$ K, $P = 10$ bar, with $Q_{C\bar{C}} = 0.5\ K_{C\bar{C}}$ at the boundary.

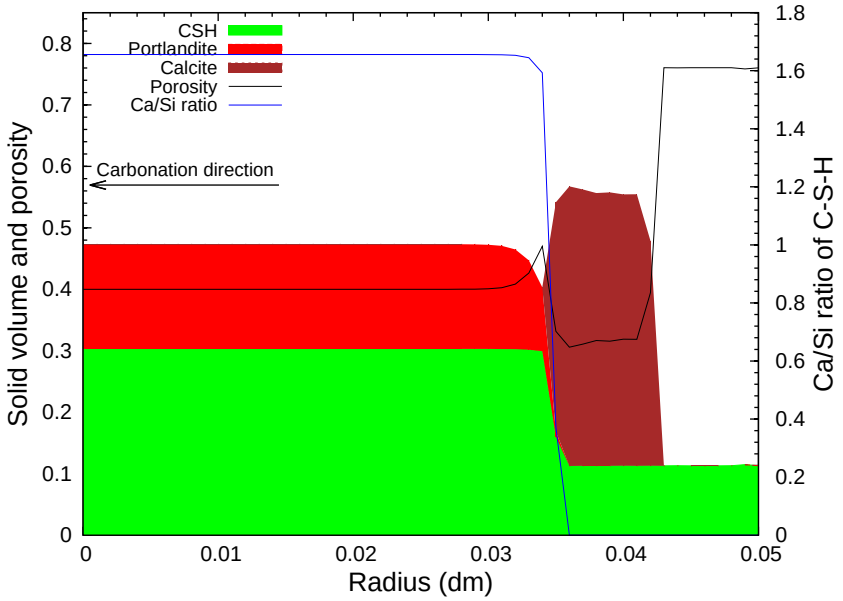

Figure 6.36: Profiles of solid volume compounds after 15 days of exposure with 0.185 M CO_2 at $T = 323$ K, $P = 10$ bar, with $Q_{C\bar{C}} = 0.1\ K_{C\bar{C}}$ at the boundary.

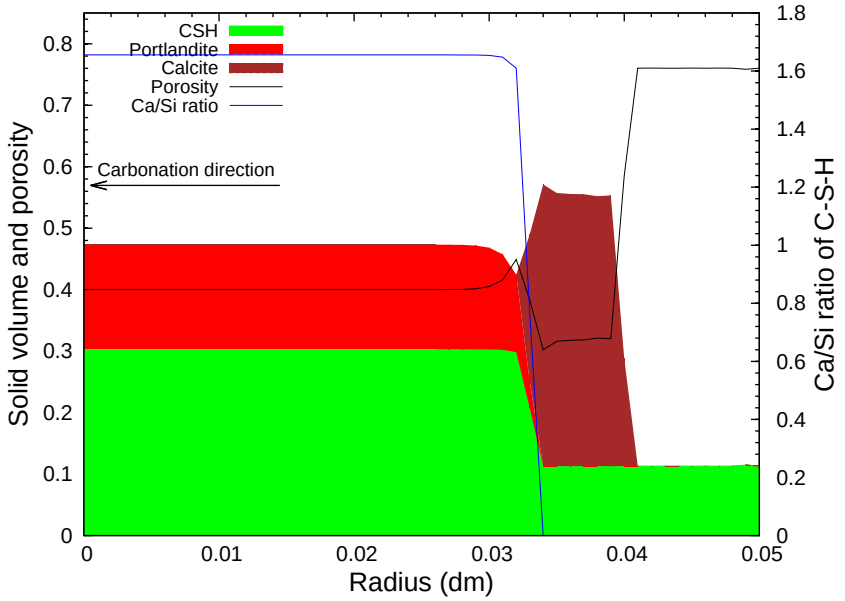

Figure 6.37: Profiles of solid volume compounds after 15 days of exposure with 0.185 M CO_2 at $T = 323$ K, $P = 10$ bar, with $Q_{C\bar{C}} = 0.01\ K_{C\bar{C}}$ at the boundary.

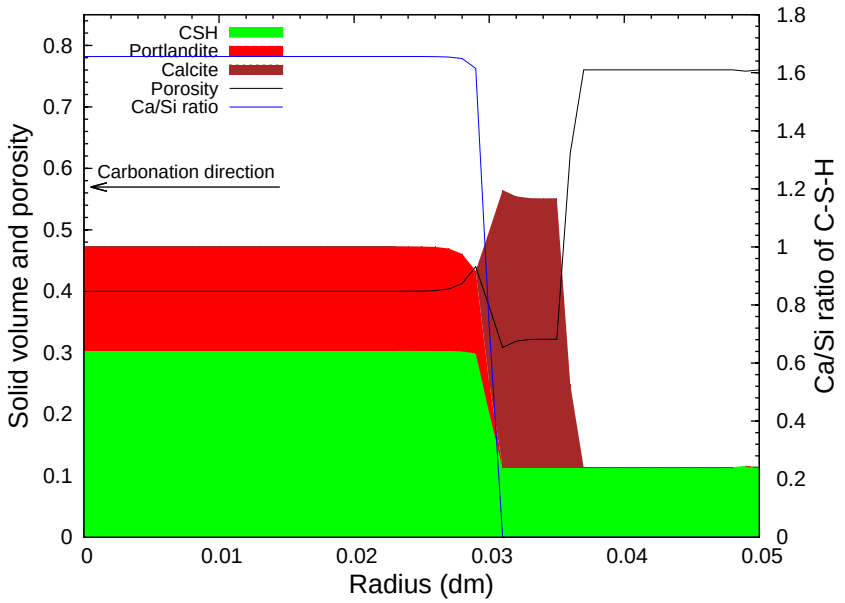

Figure 6.38: Profiles of solid volume compounds after 15 days of exposure with 0.185 M CO_2 at $T = 323$ K, $P = 10$ bar, with $Q_{C\bar{C}} = 10^{-20}\ K_{C\bar{C}}$ at the boundary.

etc., can also contribute to the leaching of calcium element, but with values several orders of magnitude smaller, as discussed in Chapter 5.

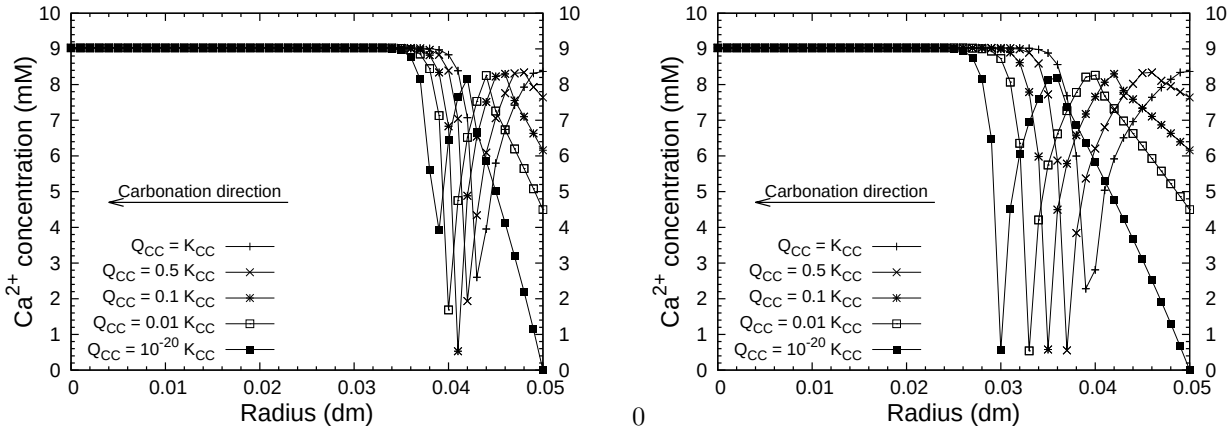

(a) After 5 days of exposure

(b) After 15 days of exposure

Figure 6.39: The calculated Ca^{2+} concentration profiles with different $Q_{C\bar{C}}$ values at the boundary, with $\rho_{CO_2^0} = 0.185$ M and $T = 323$ K. (a) After 5 days of exposure. (b) After 15 days of exposure.

6.6 Conclusion

In this chapter, calculations are led to simulate experimental works of (Duguid and Scherer, 2010). Under sandstone-like boundary conditions, successive zones, *i.e.*, from the boundary to the core, the fully degraded region, the region of calcite accumulation, the C-S-H decalcification region, the CH dissolution region and the uncarbonated region, have been observed in simulation. Higher evolution kinetics of carbonation penetration have been predicted at 50 ℃ than at 20 ℃ under sandstone-like boundary conditions. Under limestone-like conditions, clogging effect due to calcite accumulation has been observed at the surface, and the reaction is restricted at the surface.

Temperature, CO_2 concentration and activity product of $C\bar{C}$ at the boundary, have also been analyzed. Higher CO_2 concentration accelerates penetration kinetics of each layer, due to a larger amount of CO_2 penetrating into the cement paste. The width of the calcite accumulation region grows with time (especially at high CO_2 concentration conditions), due to the fact that the carbon flow at the calcite precipitation front is always greater than the calcium flow at the front of dissolved calcite in our simulations. The width of this region also depends on the CO_2 concentration at the boundary, higher CO_2 concentration will engender a wider region. Higher temperature will enhance the diffusion of aqueous species, thus induces faster penetration kinetics of each reacted layer, with the same CO_2 concentration at the boundary. It is worthwhile noting that CO_2 solubility also depends on the temperature given that at the same pressure, CO_2 concentration decreases when temperature increases. Activity product of $C\bar{C}$ at the boundary is also

an important parameter. With $Q_{C\bar{C}} = K_{C\bar{C}}$, leaching of calcium is not possible, thus the fully degraded region is not predicted. When $Q_{C\bar{C}}$ is smaller than $K_{C\bar{C}}$, all the successive regions, *i.e.*, the fully degraded region, the region of calcite accumulation, the C-S-H decalcification region, the CH dissolution region and the uncarbonated region, have been observed, as for sandstone-like conditions. Faster penetration kinetics of the fully degraded region has been observed with smaller value of $Q_{C\bar{C}}$ at the boundary.

Chapter 7

Simulation and discussion of the experiments with downhole conditions

7.1 Introduction

Experimental works analyzing cement paste behaviors in downhole conditions were conducted by several authors.

Rimmelé et al. (Rimmelé et al., 2008) exposed class G cement paste samples (12.5 mm in diameter, W/C=0.44, cured for 72 h at 207 bars and 90 ℃ in pure water prior to the experiments) to both CO_2-saturated water and $scCO_2$ during varying periods from half a day to six months, under pressure and temperature similar to downhole conditions. The porosity distribution at different ages was monitored by SEM-BSE image analysis. Similar carbonation patterns were observed while the samples exposed to $scCO_2$ showed slightly faster carbonation kinetics.

Fabbri et al. (Fabbri et al., 2009) used the same set-up as in (Rimmelé et al., 2008) and exposed both initially saturated and initially dried cement samples to $scCO_2$. Annular carbonation with a sharp carbonation front was observed for wet samples while homogeneous carbonation took place for dried samples.

Kutchko et al. (Kutchko et al., 2007, 2008) conducted similar experiments as in (Rimmelé et al., 2008). Clogging of pores was observed and a carbonation kinetics about 100 times slower than that in (Rimmelé et al., 2008) was measured.

It is surprising that significant different carbonation patterns/kinetics were observed by these authors,

though their test conditions were not so different. For the numerical simulation, one major challenge is to explain the differences between these experiments. Since the test conditions (temperature, pressure, cement type, boundary conditions, etc.) varied from each other, it is necessary to find out the key parameters which could explain the differences. In this chapter, first we will simulate the experiment of (Rimmelé et al., 2008), several parameters (molar volume of amorphous silica gel, CO_2 dissolution and water evaporation kinetics at the boundary, alkali) will be further investigated. Then simulations for other experimental works will be conducted and compared with the simulation of (Rimmelé et al., 2008), to explain the differences observed in experiments.

7.2 Simulation of experiments in (Rimmelé et al., 2008)

In order to examine the behavior of cement-based materials under pressure and temperature similar to downhole conditions, Rimmelé et al. (Rimmelé et al., 2008) used a specially designed set-up able to provide high CO_2 pressure and high temperature (see Fig. 7.1). This system ensured an infinite supply of CO_2 by maintaining a constant pressure. The water was not renewed during exposure. CO_2 was initially in gas phase and then in supercritical phase when pressure exceeds the critical point (7.39 Mpa). At any time during exposure, CO_2 was wet due to the existence of water in the bottom of the container. With this set-up, cement samples could be exposed to either $scCO_2$ (samples 1-6 in Fig. 7.1), or to CO_2-saturated water (samples 10-15 in Fig. 7.1).

A 1D radial geometry, with two different materials, is used to simulate this set of experiments (see Fig. 7.2). For $r < 6.25$ mm, the material is cement paste. For 6.25 mm $< r <$ 10 mm, it's the water or $scCO_2$ surrounding the cement paste, with neither portlandite nor C-S-H, and porosity of 1. Transfer properties in this region correspond to the porosity ($\phi = 1$) and saturation degree ($S_L = 1$ or 0). The values of $r_{\text{cem}} = 6.25$ mm and $r_{\text{water}} = 10$ mm are chosen to obtain the same water to sample volume ratio as in experiment ($V_{\text{water}}/V_{\text{sample}} = 1.5$ in (Rimmelé et al., 2008)). In the surrounding water, there is no dissolved Ca^{2+} initially, since pure water was used in experiment. Leaching of calcium could occur, until the surrounding water gets saturated with calcite. The water to sample volume ratio determines how much formed calcite could be dissolved, a higher value leads to more calcite dissolution. CO_2 to sample volume ratio ($V_{COO}/V_{\text{sample}}$) doesn't have any effect since the surrounding CO_2 layer is homogeneous and gas pressure is kept constant in this region, thus arbitrary value of r_{CO_2} can be chosen. In this set of simulations we just choose the same value than r_{water}.

Boundary and initial conditions, as well as other parameters used in simulations, are summarized in Table 7.1. Temperature is set to 363 K. The intrinsic liquid permeability before carbonation is 2×10^{-19} m^2, same as that of cement paste C45 (Thiery, 2006). In (Fabbri et al., 2009), the measured intrinsic gas

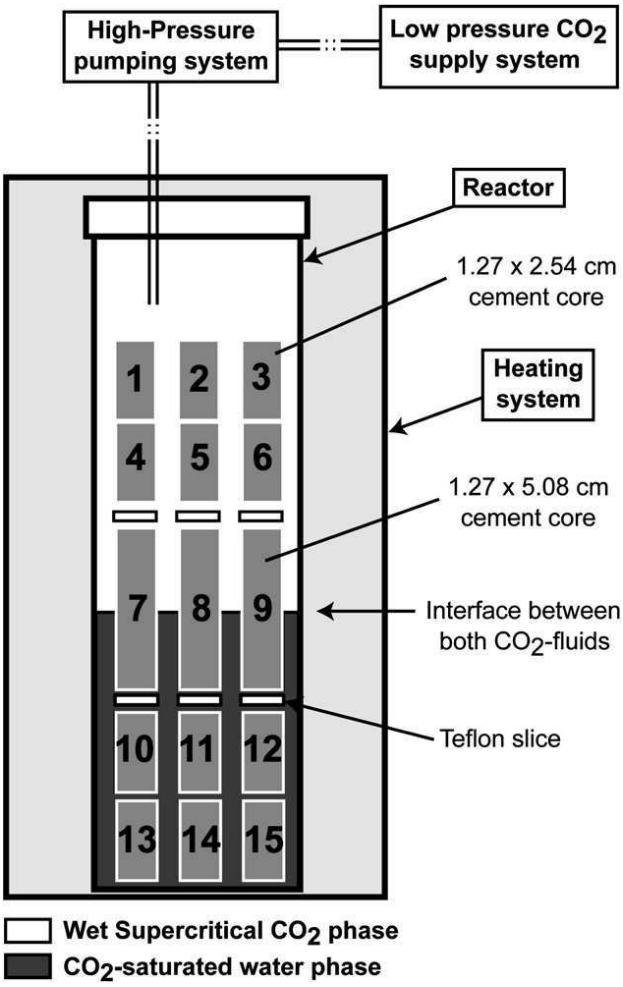

Figure 7.1: Experimental set up of (Rimmelé et al., 2008).

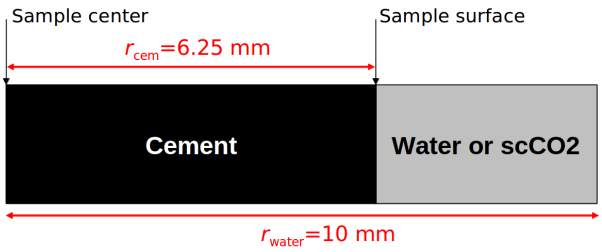

Figure 7.2: Geometry for simulating the work of (Rimmelé et al., 2008).

permeability was 7 times higher than that to liquid, to be consistent with experiment, we use 14×10^{-19} m^2 for the intrinsic gas permeability before carbonation.

Table 7.1: Boundary and initial conditions, as well as other parameters used in simulations of the samples exposed to wet CO_2 and CO_2-saturated water.

Properties of cement paste		
Temperature	Initial CH content	Initial C-S-H content
363 K	5.16 mol/L	3.9 mol/L
Initial porosity	Intrinsic liquid permeability	Intrinsic gas permeability
0.33	$K_l = 2 \times 10^{-19}$ m^2	$K_g = 14 \times 10^{-19}$ m^2
Cement paste (r < 6.25 mm)		
Boundary conditions		**Initial conditions**
Balance Equation	BC left	
Carbon (C)	no flow	$P_G = 10^{-10}$ Pa
Calcium (Ca)	no flow	$\zeta_{Ca} = 1$
Silicon (Si)	no flow	$\zeta_{Si} = 1$
Sodium/Potassium	no flow	$\rho_{K^+} = 0$ mol/L
Chlorine (Cl)	no flow	$\rho_{Cl^-} = 0$ mol/L
Total mass	no flow	$P_L = 10^5$ Pa
Charge	no current	$\psi = 0$
Surrounding CO_2 (6.25 mm < r < 10 mm)		
Boundary conditions		**Initial conditions**
Balance Equation	BC right	
Carbon (C)	$P_{G(2h)} = 280$ bars	$P_G = 10^{-10}$ Pa
Calcium (Ca)	$\zeta_{Ca} = 0$	$\zeta_{Ca} = 0$
Silicon (Si)	$\zeta_{Si} = 0$	$\zeta_{Si} = 0$
Sodium/Potassium	no flow	$\rho_{K^+} = 0$ mol/L
Chlorine (Cl)	no flow	$\rho_{Cl^-} = 0$ mol/L
Total mass	$P_{L(2h)} = 280$ bar	$P_L = 10^5$ Pa
Charge	$\psi = 0$	$\psi = 0$
Surrounding water (6.25 mm < r < 10 mm)		
Boundary conditions		**Initial conditions**
Balance Equation	BC right	
Carbon (C)	$P_{G(2h)} = 280$ bars	$P_G = 10^{-10}$ mol/L
Calcium (Ca)	no flow	$\zeta_{Ca} = -20$
Silicon (Si)	no flow	$\zeta_{Si} = -20$
Sodium/Potassium	no flow	$\rho_{K^+} = 0$ mol/L
Chlorine (Cl)	no flow	$\rho_{Cl^-} = 0$ mol/L
Total mass	$P_{L(2h)} = 280$ bar	$P_L = 10^5$ Pa
Charge	$\psi = 0$	$\psi = 0$

For the surrounding CO_2 (6.25 mm < r < 10 mm), there is only a gas phase, the liquid saturation degree in this region is always 0. The initial gas pressure equals to 10^{-10} Pa, and increases to 2.8×10^7 Pa in 2 hours ($P_{G(2h)} = 280$ bars in Table 7.1), to simulate the loading period of 2 hours in the experiment (Rimmelé et al., 2008). In our study, for the gas phase, we only consider CO_2 and water vapor, other gases such as N_2 and O_2 are neglected. We use a very small initial gas pressure here since initially there is no CO_2 in the system. Initial liquid pressure equals to 10^5 Pa (atmospheric pressure), and increases to

2.8×10^7 Pa in 2 hours ($P_{L(2h)} = 280$ bars in Table 7.1). Here we consider that the surrounding CO_2 phase is homogeneous, *i.e.*, the values of the main variables at each node in region 6. 25 mm $< r <$ 10 mm are the same, regardless the position. ζ_{Ca} and ζ_{Si} are set to 0 in this region, to avoid leaching of calcium and silicon through the cement paste surface since the samples are not in contact with water.

For the surrounding water (6.25 mm $< r <$ 10 mm), there is only a liquid phase, the liquid saturation degree in this region is always 1. Initial liquid pressure equals to 10^5 Pa (atmospheric pressure), and increases to 2.8×10^7 Pa in 2 hours. In order to get the same aqueous CO_2 concentration as in the experiment, the initial gas pressure equals to 10^{-10} Pa, and increases to 2.8×10^7 Pa in 2 hours. Unlike in CO_2 phase, ζ_{Ca} and ζ_{Si} in this region are set to -20 initially, thus leaching of calcium and silicon is possible. This two values are not set as constant during the simulation, ζ_{Ca} and ζ_{Si} increase as calcium and silicon flow out, the leaching stops when the surrounding water is saturated with formed calcite and silicon gel ($\zeta_{Ca} = 0$ and $\zeta_{Si} = 0$).

For the cement paste ($r <$ 6.25 mm, divided into 50 nodes), the initial gas and liquid pressures equal to 10^{-10} Pa and 10^5 Pa, respectively. Since the cement paste is initially saturated, the gas pressure is actually a "dummy" value here as there is no gas phase. This value is used to calculate the aqueous CO_2 concentration and the saturation degree. A small value of gas pressure is used here to get a small initial aqueous CO_2 concentration (about 10^{-16} mol/L). Considering the fact that in experiment cement samples were cured in pure water before carbonation, and pure water was used as external water (Rimmelé et al., 2008), no Na^+ nor Cl^- is added in the first set of simulations (the effects of alkali will be discussed later in section 7.3.3). Cement paste contains initially 5.16 mol/L of portlandite and 3.9 mol/L of C-S-H ($C_{1.7}SH_{2.1}$), the same as we used for the simulation of (Duguid and Scherer, 2010). In (Duguid and Scherer, 2010), class H cement paste was used, while in (Rimmelé et al., 2008), class G cement paste was used. The components of class G and class H cement are identical (50% C_3S, 30% C_2S, 5% C_3A and 12% C_4AF (Duguid, 2006)), and the W/C ratio is similar (0.38 for class H cement paste *vs.* 0.44 for class G cement paste). The hydration degree of cement paste is not considered in our work. With the same amount of initial hydration products, we can exclude the effects of this parameter when comparing results between different experimental works. In (Rimmelé et al., 2008), initial porosity of 33% was measured by mercury intrusion porosimetry (MIP) measurement. First, we will use 33% as initial porosity, and the influence of this value will be analyzed in the following section in the framework of a sensitivity analysis.

Rimmelé et al. estimated the dissolved CO_2 concentration in the liquid phase as 1.25 mol/L, which fits fairly well to our prediction (see Figs. 7.3). Note that in the surrounding CO_2 region, although we still get values for the concentration of aqueous species and *p*H value, they actually have no meaning due to the absence of water.

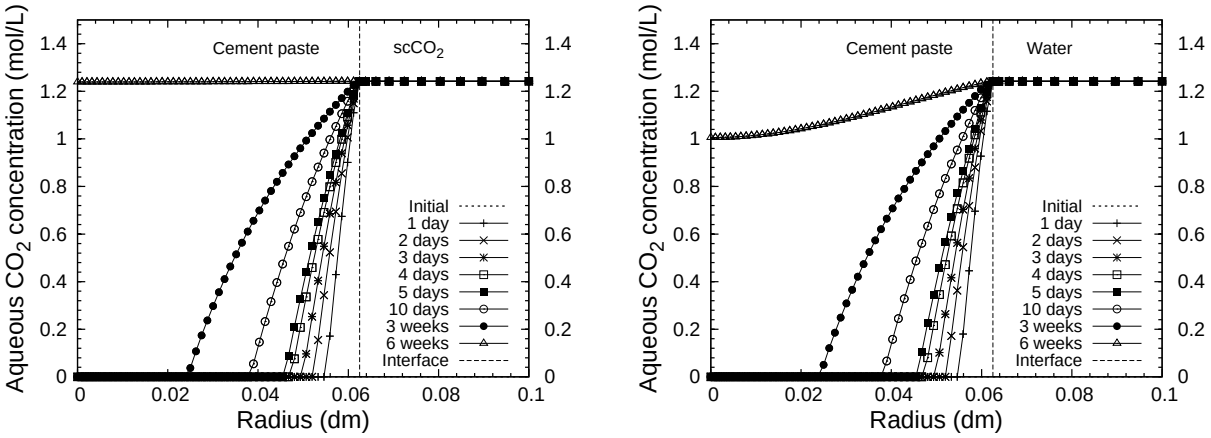

(a) Cement paste exposed to $scCO_2$

(b) Cement paste exposed to CO_2-saturated water

Figure 7.3: Calculated aqueous CO_2 concentration profiles from 1 day to 6 weeks, simulating the work of (Rimmelé et al., 2008). (a) For $scCO_2$ boundary condition. (b) For CO_2-saturated water boundary condition. Note: vertical dash line titled "Interface" indicates the interface between cement paste and $scCO_2$/water.

Rimmelé et al. observed a *p*H drop from an initial value of 13 to 6-7 after CO_2 exposure, while we predict a drop from 12 to 6.2 as shown as in Figs. 7.4a and 7.4b. The difference between our prediction and the experimental observation is probably due to the alkali remained in the pore solution, which will be discussed later.

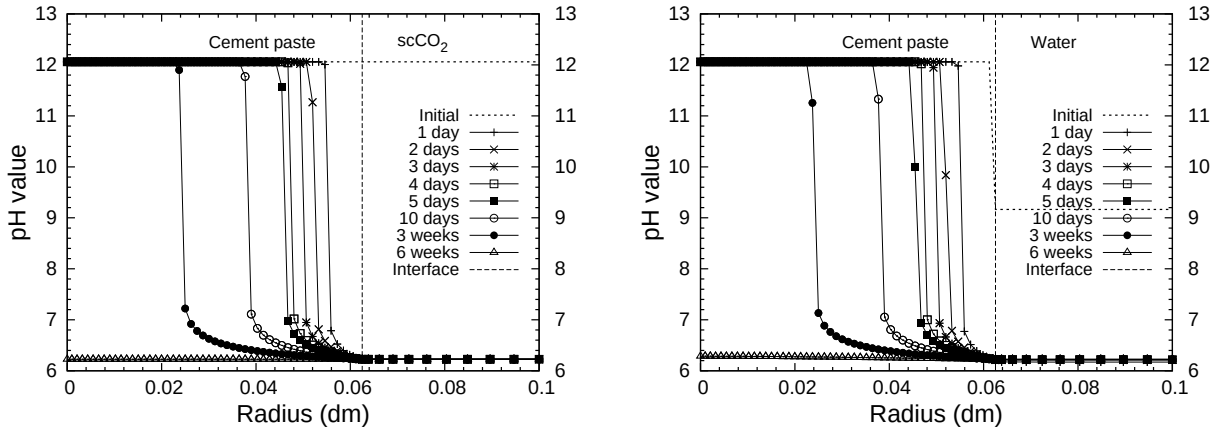

(a) Cement paste exposed to $scCO_2$

(b) Cement paste exposed to CO_2-saturated water

Figure 7.4: Calculated *p*H profiles from 1 day to 6 weeks, simulating the work of (Rimmelé et al., 2008). (a) For $scCO_2$ boundary condition. (b) For CO_2-saturated water boundary condition. Note: vertical dash line titled "Interface" indicates the interface between cement paste and $scCO_2$/water.

Cement paste remains saturated in CO_2-saturated water boundary condition (see Fig. 7.5b), which is not hard to understand. So does the sample exposed to $scCO_2$ directly (see Fig. 7.5a). This phenomena can be interpreted thanks to three aspects: first, the sample is initially saturated, second, in this set of simulation, the $scCO_2$ in the boundary is always wet, thus water can not evaporate at the sample surface,

last, carbonation reactions of CH and C-S-H release water (see Chapter 3). Since $scCO_2$ has not entered the cement paste by advection during exposure, in both conditions, CO_2 transport is controlled by diffusion, this explains the similar carbonation phenomena observed for the two different boundary conditions in the experiment of (Rimmelé et al., 2008).

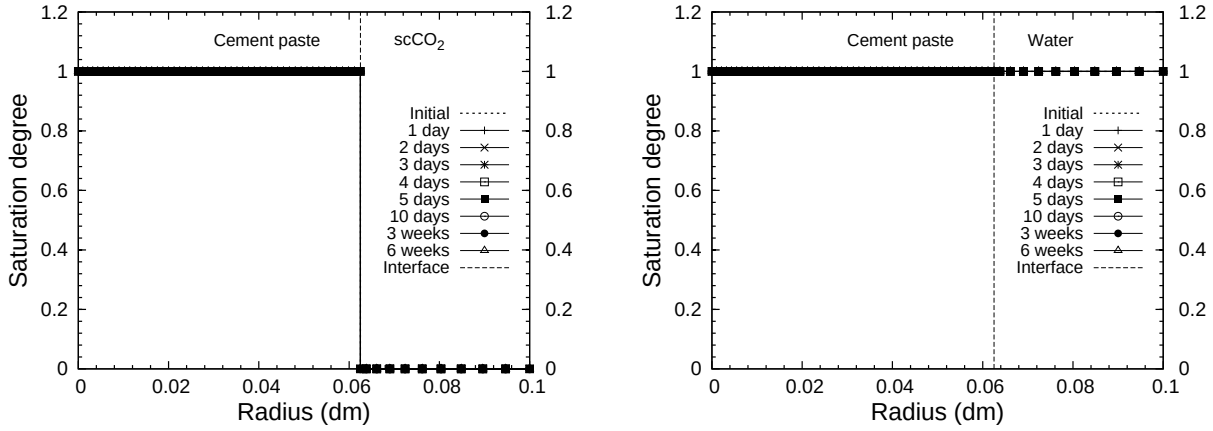

(a) Cement paste exposed to $scCO_2$

(b) Cement paste exposed to CO_2-saturated water

Figure 7.5: Calculated liquid saturation degree from 1 day to 6 weeks, simulating the work of (Rimmelé et al., 2008). (a) For $scCO_2$ boundary condition. (b) For CO_2-saturated water boundary condition. Note: vertical dash line titled "Interface" indicates the interface between cement paste and $scCO_2$/water.

In experiment (Rimmelé et al., 2008), from the rim to the center, a carbonated zone with low porosity, a carbonation front where porosity drops, a dissolution front with a higher porosity than the initial porosity and the inner healthy part were observed, see Fig. 7.6. Note that the local porosity profiles generated from SEM-BSE image only account for pore size larger than 1 μm (Rimmelé et al., 2008), thus the measured value is generally lower than values provided by other methods like MIP measurement. Nevertheless, this method could help identifying regions with different carbonation degree. A thin region with a higher porosity was observed at the sample surface, however Rimmelé et al. claimed that this region existed before CO_2 attack due to curing of cement (possible leaching).

Our predictions of the volume of solid compounds, from 2 days to 6 weeks, are presented in Figs. 7.7 to 7.9. From the surface to the inner part, we predict a region of calcite accumulation, a sharp C-S-H decalcification region, a sharp CH dissolution region and a uncarbonated region. A fully degraded region composed only of amorphous silica gel, as the one observed in sandstone-like conditions in Chapter 6, is not predicted, refers to the fact that large amount leaching of calcium does not happen. These observations are in agreement with experimental profiles shown in Fig. 7.6. Note that a porosity equals to 1 at the surface is due to the boundary condition we apply rather than carbonation reaction.

The predicted volume of solid compounds are almost identical between the two different boundary

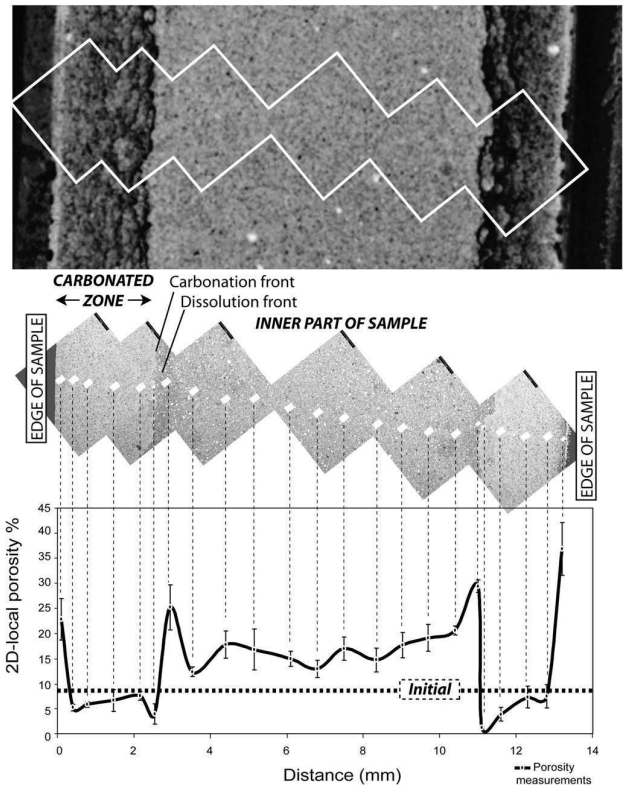

Figure 7.6: Different reaction zones observed in the cement paste after 4 days of exposure to $scCO_2$. At the top is the polished section, SEM-BSE image in the middle, and local porosity profile generated from SEM-BSE image is in the bottom. Cited from (Rimmelé et al., 2008).

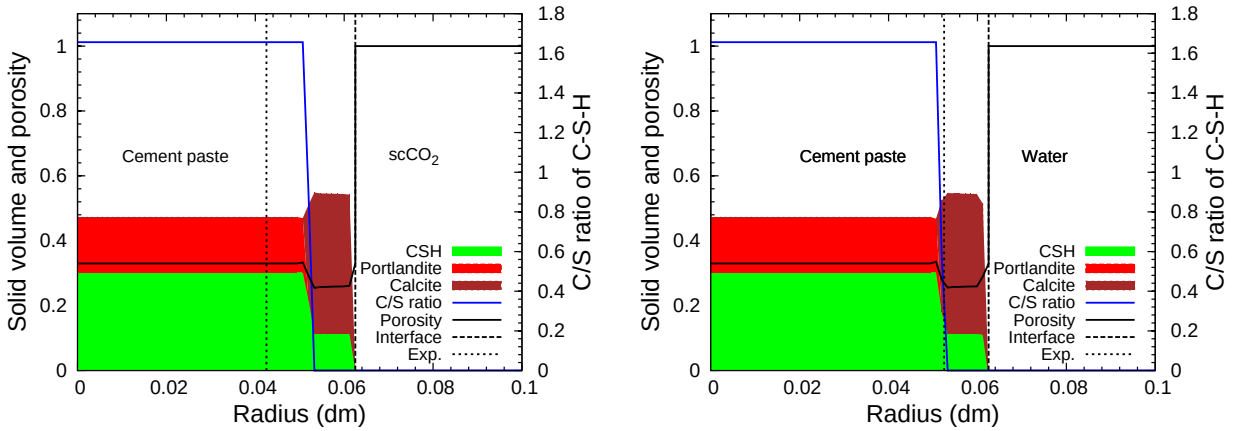

(a) Cement paste exposed to $scCO_2$

(b) Cement paste exposed to CO_2-saturated water

Figure 7.7: Calculated profiles of solid volume compounds after 2 days of exposure, simulating the work of (Rimmelé et al., 2008). (a) For $scCO_2$ boundary condition. (b) For CO_2-saturated water boundary condition. Note: dot line titled "Exp." indicates the position of the alteration front (the so-called calcite precipitation front) observed in experiment.

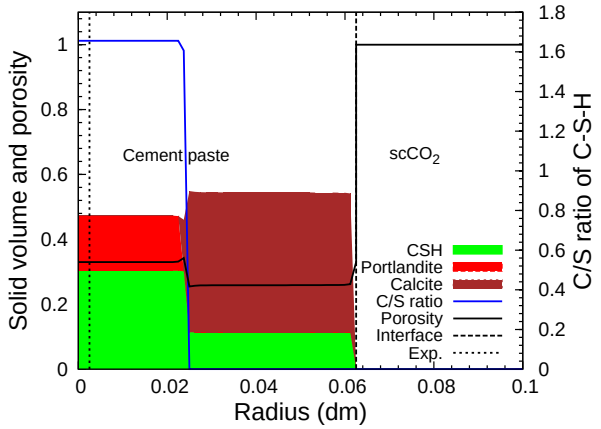

(a) Cement paste exposed to $scCO_2$

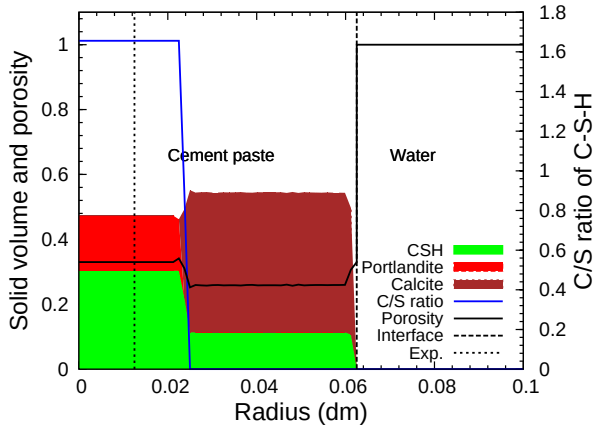

(b) Cement paste exposed to CO_2-saturated water

Figure 7.8: Calculated profiles of solid volume compounds after 3 weeks of exposure, simulating the work of (Rimmelé et al., 2008). (a) For $scCO_2$ boundary condition. (b) For CO_2-saturated water boundary condition. Note: dot line titled "Exp." indicates the position of the alteration front (the so-called calcite precipitation front) observed in experiment.

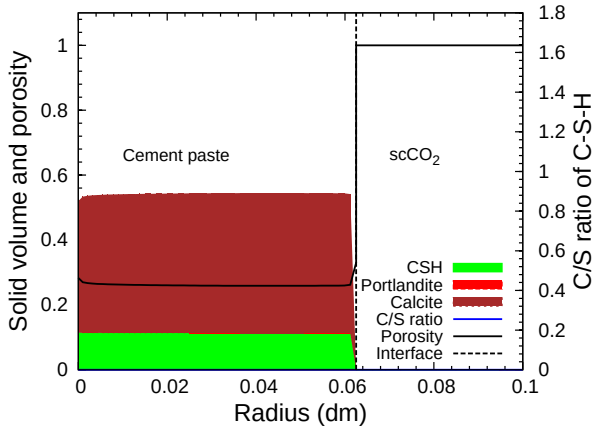

(a) Cement paste exposed to $scCO_2$

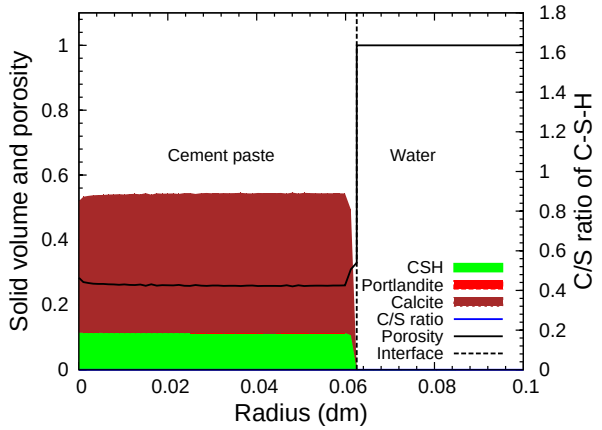

(b) Cement paste exposed to CO_2-saturated water

Figure 7.9: Calculated profiles of solid volume compounds after 6 weeks of exposure, simulating the work of (Rimmelé et al., 2008). (a) For $scCO_2$ boundary condition. (b) For CO_2-saturated water boundary condition.

conditions. One minor difference is, at the sample surface, there is slightly some dissolution of formed calcite of the sample exposed to CO_2-saturated water. We can explain that by the Ca^{2+} concentration profiles (see Figs. 7.10a and 7.10b). For $scCO_2$ boundary conditions, there is no concentration gradient of Ca^{2+} at the sample surface, since we set $\zeta_{Ca} = 0$ at the boundary. Actually, Ca^{2+} can not get out the cement paste by diffusion as there is no water at the boundary. For CO_2-saturated water boundary conditions, initially, we set ζ_{Ca} = -20 in the surrounding water (6.25 mm $< r <$ 10 mm), to simulate calcium free water, thus, there is a concentration gradient of Ca^{2+} between cement pore solution and the surrounding environment. Ca^{2+} ion can transport from cement surface to the surrounding water by diffusion. It yields leaching of calcium in the early exposure stage. Since the volume of the surrounding water is not infinity, the Ca^{2+} ion will accumulate in the surrounding water and the concentration increases rapidly as the water to sample volume ratio is quite small. The concentration gradient of Ca^{2+} at the surface quickly vanishes (from 2 days and after), and the leaching of calcium then stops.

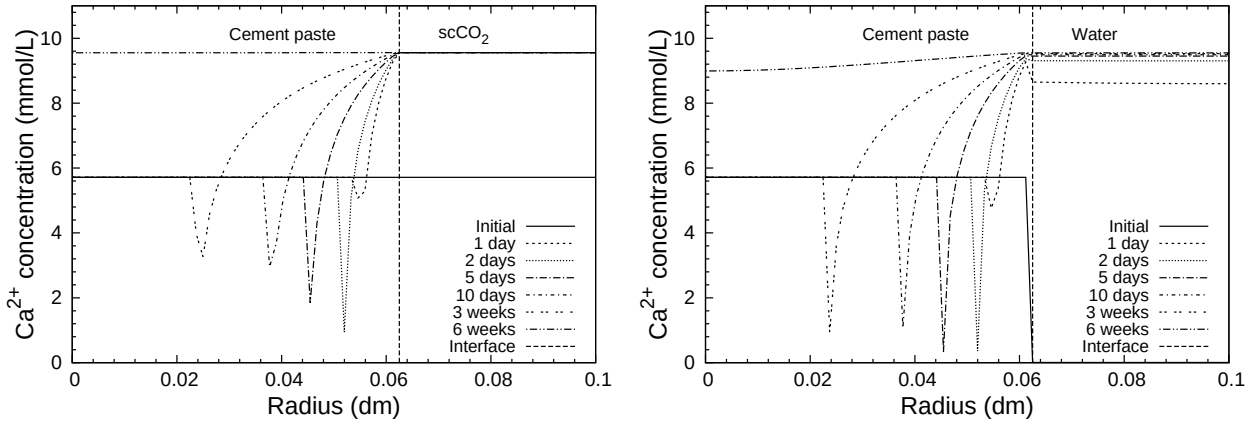

(a) Cement paste exposed to $scCO_2$

(b) Cement paste exposed to CO_2-saturated water

Figure 7.10: Calculated Ca^{2+} concentration profiles from 1 day to 6 weeks, simulating the work of (Rimmelé et al., 2008). (a) For $scCO_2$ boundary condition. (b) For CO_2-saturated water boundary condition. Note: vertical dash line titled "Interface" indicates the cement surface.

Though similar regions are predicted, the evolution kinetics of the calcite precipitation front is a little slower than experimental observations (dash line in Figs. 7.7-7.9). The measured carbonation front (the so-called calcite precipitation front) penetrated 1-2 mm into the cement paste after 2 days and 5-6 mm after three weeks of attack. After six weeks, this front has reached the central part of the cement sample. In our simulation, the calcite precipitation front penetrated about 1 mm after 2 days and 4 mm after 3 weeks. Moreover, in experimental observations, cement paste exposed to $scCO_2$ showed faster carbonation kinetics than those exposed to CO_2-saturated water, while in our simulations, a similar kinetics is predicted. We also underestimate the initial pH value (12 rather than 13 measured in experiment). These differences will be investigated and discussed in the following section.

7.3 Further investigations on the role of some parameters

7.3.1 Investigation of the porosity profiles

In (Rimmelé et al., 2008), global porosity was measured by MIP method. The maximum intrusion pressure was 2000 bars, corresponded to a minimum pore entrance size of 6.2 nm. The measured initial porosity was 33%. When fully carbonated, the global porosity decreased to 27% for the samples exposed to wet $scCO_2$ and to 30% for those exposed to CO_2-saturated water. The results of MIP method is able to investigate the volume of cavities connected to the surface through a percolative path with a diameter greater than 6.2 nm, thus, MIP method could underestimate the porosity value. In (Fabbri et al., 2009), the authors did similar experiment, with similar cement paste (ordinary portland cement, W/C = 0.44, cured for 72 hours at 207 bars and 90 ℃ in pure water), accessible to water porosity (sample mass difference between dried and saturated states) was measured before and after carbonation, it was about 41% initially and 31% after carbonation for initially saturated cement paste exposed to $scCO_2$. In our opinion, accessible to water porosity is more appropriate for simulation since MIP method neglects volumes of small pores and cavities not connected to the surface.

When we have simulated the work of (Duguid and Scherer, 2010) in Chapter 6, for the formed amorphous silica gel (SH_t), we used a stoichiometry of t = 0, with molar volume of $V_{SH_t} = 29$ cm^3/mol, following the work of (Lothenbach et al., 2008). We were not able to calibrate these values since porosity after carbonation was not provided. In the recently published works (Antoine Morandeau, 2012; Thiéry et al., 2011, 2012), authors proposed a stoichiometry of t = 2 and molar volume of $V_{SH_t} = 43$ cm^3/mol for the formed amorphous silica gel, based on their experimental measurements of the porosity and liquid saturation degree changes after carbonation. In this section, we will recalculate the same experiments than last section, with an initial porosity of 41% (accessible to water porosity) for the cement paste, and $V_{SH_t} = 43$ cm^3/mol, t = 2 for the formed amorphous silica gel. Initial and boundary conditions are the same as in Table 7.1. Simulation results of solid volume compounds from 2 days to 6 weeks, are presented in Figs. 7.11-7.13.

It's obvious that, with an initial porosity of 41%, $V_{SH_t} = 43$ cm^3/mol and t = 2, the calculated evolution kinetics of the calcite precipitation front, are quite close to experimental observations, at least for the sample exposed to CO_2-saturated water. The predicted porosity drop after carbonation, from 41% before carbonation to 28% after carbonation, is also close to the experimental measurements (Fabbri et al., 2009). Thus, hereafter, we will use $V_{SH_t} = 43$ cm^3/mol and t = 2 in simulations.

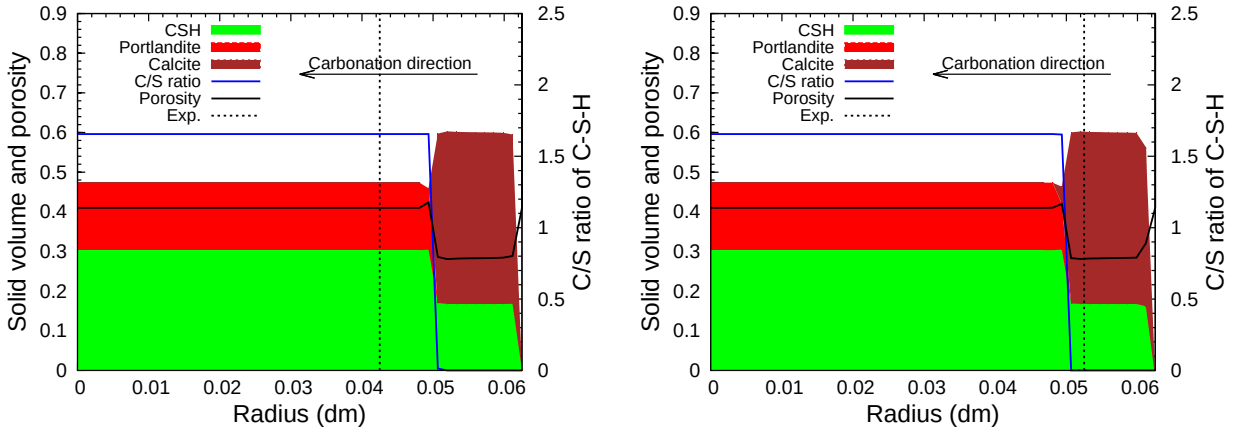

(a) Cement paste exposed to $scCO_2$

(b) Cement paste exposed to CO_2-saturated water

Figure 7.11: Calculated profiles of solid volume compounds after 2 days of exposure, simulating the work of (Rimmelé et al., 2008) with $V_{SH_t} = 43$ cm^3/mol and t = 2. (a) For $scCO_2$ boundary condition. (b) For CO_2-saturated water boundary condition. Note: dot line titled "Exp." indicates the position of the alteration front (the so-called calcite precipitation front) observed in experiment.

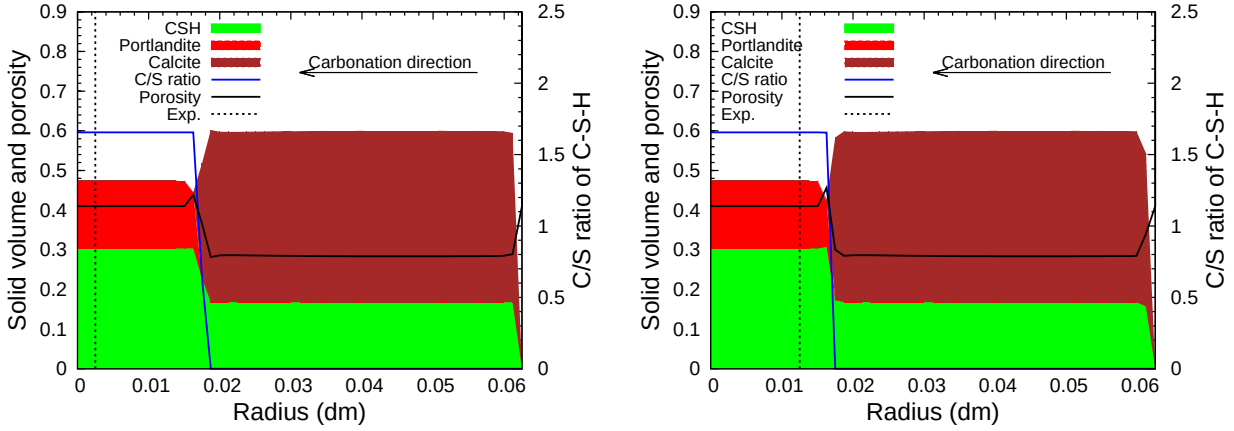

(a) Cement paste exposed to $scCO_2$

(b) Cement paste exposed to CO_2-saturated water

Figure 7.12: Calculated profiles of solid volume compounds after 3 weeks of exposure, simulating the work of (Rimmelé et al., 2008) with $V_{SH_t} = 43$ cm^3/mol and t = 2. (a) For $scCO_2$ boundary condition. (b) For CO_2-saturated water boundary condition. Note: dot line titled "Exp." indicates the position of the alteration front (the so-called calcite precipitation front) observed in experiment.

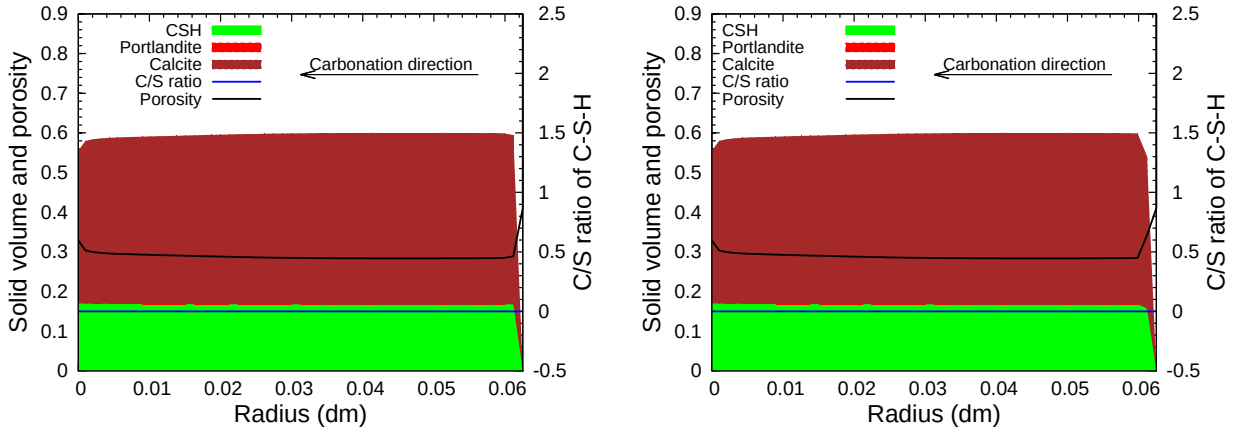

(a) Cement paste exposed to $scCO_2$

(b) Cement paste exposed to CO_2-saturated water

Figure 7.13: Calculated profiles of solid volume compounds after 6 weeks of exposure, simulating the work of (Rimmelé et al., 2008) with $V_{SH_t} = 43$ cm^3/mol and t = 2. (a) For $scCO_2$ boundary condition. (b) For CO_2-saturated water boundary condition.

7.3.2 Role of CO_2 dissolution and water evaporation kinetics

One interesting phenomena observed in experiments, which has not been predicted till now, is the difference of carbonation kinetics between $scCO_2$ and CO_2-saturated water boundary conditions. Samples exposed to $scCO_2$ experienced faster carbonation attack than those exposed to CO_2-saturated water. This difference probably comes from the CO_2 dissolution and water evaporation kinetics at the boundary. In the experiment (Rimmelé et al., 2008), after the loading period of 2 hours, although the CO_2 pressure had reached 280 bars, it should take some time for the aqueous CO_2 concentration in the water to reach the concentration corresponding to this pressure (1.25 mol/L), considering the CO_2 dissolution kinetics. As well, considering the kinetics of water evaporation, the $scCO_2$ should be initially dry, and took some time to reach 100% relative humidity HR ($y_{H_2O}/y_{H_2O(sat)}$), where y_{H_2O} is the mole fraction of H_2O in CO_2, $y_{H_2O(sat)}$ is that in saturated CO_2 (in case $P_L = P_G$).

In our previous simulations, we did not take into account these kinetics, we just considered that both P_G and P_L can reach 280 bars after 2 hours. In this section, we will analyze the effect of the dissolution/evaporation kinetics at the boundary. In our code, we use P_L to control the mole fraction of H_2O in the gas phase. In the liquid phase, we use P_G to control the aqueous CO_2 concentration (see Chapter 2 section 2.4). It's a pity that, in the studied experiment (Rimmelé et al., 2008), the relative humidity HR, as well as the aqueous CO_2 concentration versus time were not measured. We just assume that, it takes 6 hours to reach 100% of relative humidity in the wet $scCO_2$, and 6 hours to reach 1.25 mol/L for the aqueous CO_2 concentration in the water. Thus, for surrounding CO_2, P_G increases to 280 bars after a loading period of 2 hours, while P_L remains at 10^5 Pa at this time ($P_{L(2h)} = 10^5$ Pa in Table 7.2), P_L

increases to 280 bars after another 6 hours ($P_{L(8h)}$ = 280 bars in Table 7.2). For surrounding water, P_L increases to 280 bars after a loading period of 2 hours, while P_G remains at 10^{-10} Pa at this time ($P_{G(2h)}$ = 10^{-10} Pa in Table 7.2), P_G increases to 280 bars after another 6 hours ($P_{G(8h)}$ = 280 bars in Table 7.2). The procedures to introduce CO_2 dissolution and water evaporation kinetics in surrounding environments are summarized in Table 7.2. Other boundary and initial conditions are the same as in section 7.3.1.

Table 7.2: Boundary and initial conditions considering CO_2 dissolution and water evaporation kinetics at the boundary.

Surrounding CO_2 (6.25 mm $< r <$ 10 mm)		
Boundary conditions		**Initial conditions**
Balance Equation	BC right	
Carbon (C)	$P_{G(2h)}$ = 280 bars	$P_G = 10^{-10}$ Pa
Total mass	$P_{L(2h)} = 10^5$ Pa $P_{L(8h)}$ = 280 bars	$P_L = 10^5$ Pa
Surrounding water (6.25 mm $< r <$ 10 mm)		
Boundary conditions		**Initial conditions**
Balance Equation	BC right	
Carbon (C)	$P_{G(2h)} = 10^{-10}$ Pa $P_{G(8h)}$ = 280 bars	$P_G = 10^{-10}$ Pa
Total mass	$P_{L(2h)}$ = 280 bars	$P_L = 10^5$ Pa

Compared with simulations presented in section 7.3.1, where kinetics of CO_2 dissolution and water evaporation at the boundary were not considered, faster carbonation kinetics is predicted for the sample exposed to $scCO_2$ at the beginning stage (see Figs. 7.14a to 7.16a), while only slightly slower carbonation kinetics is predicted for those exposed to CO_2-saturated water (see Figs. 7.14b to 7.16b).

It's not difficult to understand the slightly slower carbonation kinetics of the sample exposed to CO_2-saturated water: the aqueous CO_2 concentration reaches 1.25 mol/L in 8 hours rather than in 2 hours. It's interesting to observe faster carbonation kinetics for the sample exposed to $scCO_2$, compared with the results without considering kinetics of water evaporation. The difference can be explained by the saturation degree of $scCO_2$ (see Fig. 7.17a). Initially, the saturation degree of $scCO_2$ (S_G) in the cement paste is 0, since the sample is initially saturated with water. After the loading period of 2 hours, the capillary pressure at the interface of the sample increases to 279 bars (P_L = 1 bar, P_G = 280 bar) due to a drying effect of the sample, as a result, S_G at the sample surface increases to 0.25. $scCO_2$ enters the cement paste during the first 8 hours by advection, thus faster carbonation kinetics is predicted (advection of $scCO_2$ is several orders of magnitude faster than CO_2 diffusion). Capillary pressure at the interface decreases down to 0 after 8 hours ($P_L = P_G$), then S_G in the cement paste has decreased to 0 since wetting happens at the surface and the carbonation reaction releases water. Actually, in the experiment of (Rimmelé et al., 2008), $scCO_2$ was initially dry, and water at the sample surface could evaporate into $scCO_2$. When the

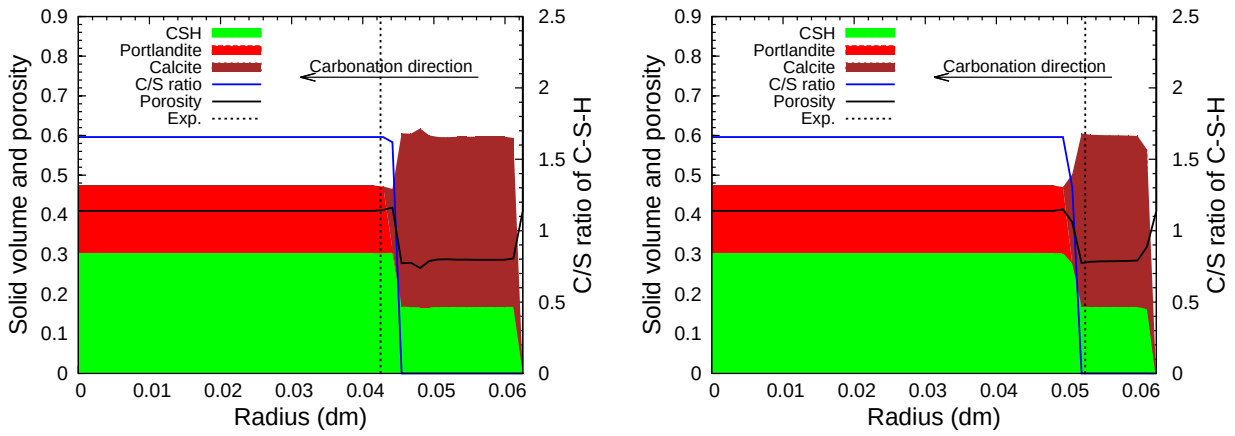

(a) Cement paste exposed to $scCO_2$ (b) Cement paste exposed to CO_2-saturated water

Figure 7.14: Calculated profiles of solid volume compounds after 2 days of exposure, simulating the work of (Rimmelé et al., 2008), considering CO_2 dissolution and water evaporation kinetics at the boundary. (a) For $scCO_2$ boundary condition. (b) For CO_2-saturated water boundary condition. Note: dot line titled "Exp." indicates the position of the alteration front (the so-called calcite precipitation front) observed in experiment.

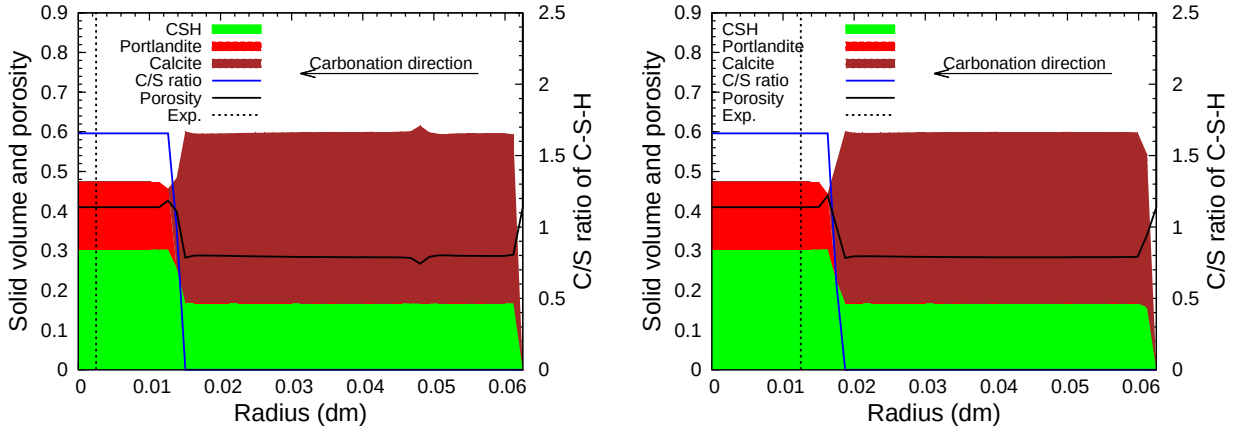

(a) Cement paste exposed to $scCO_2$ (b) Cement paste exposed to CO_2-saturated water

Figure 7.15: Calculated profiles of solid volume compounds after 3 weeks of exposure, simulating the work of (Rimmelé et al., 2008), considering CO_2 dissolution and water evaporation kinetics at the boundary. (a) For $scCO_2$ boundary condition. (b) For CO_2-saturated water boundary condition. Note: dot line titled "Exp." indicates the position of the alteration front (the so-called calcite precipitation front) observed in experiment.

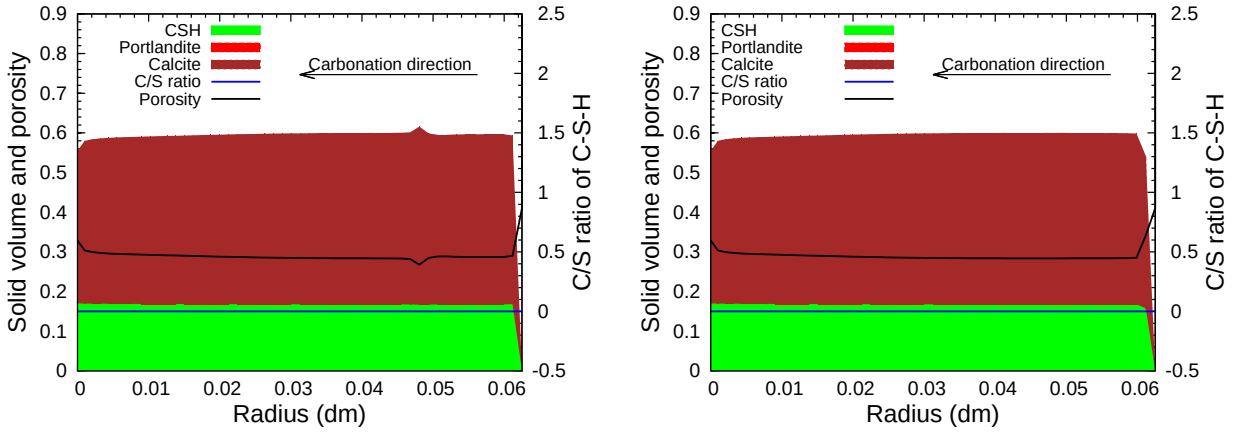

(a) Cement paste exposed to $scCO_2$

(b) Cement paste exposed to CO_2-saturated water

Figure 7.16: Calculated profiles of solid volume compounds after 6 weeks of exposure, simulating the work of (Rimmelé et al., 2008), considering CO_2 dissolution and water evaporation kinetics at the boundary. (a) For $scCO_2$ boundary condition. (b) For CO_2-saturated water boundary condition.

cement paste got unsaturated, $scCO_2$ could enter cement paste in the first few hours. This is probably the major reason of the slightly different carbonation kinetics observed between samples exposed to $scCO_2$ and CO_2-saturated water in experiment.

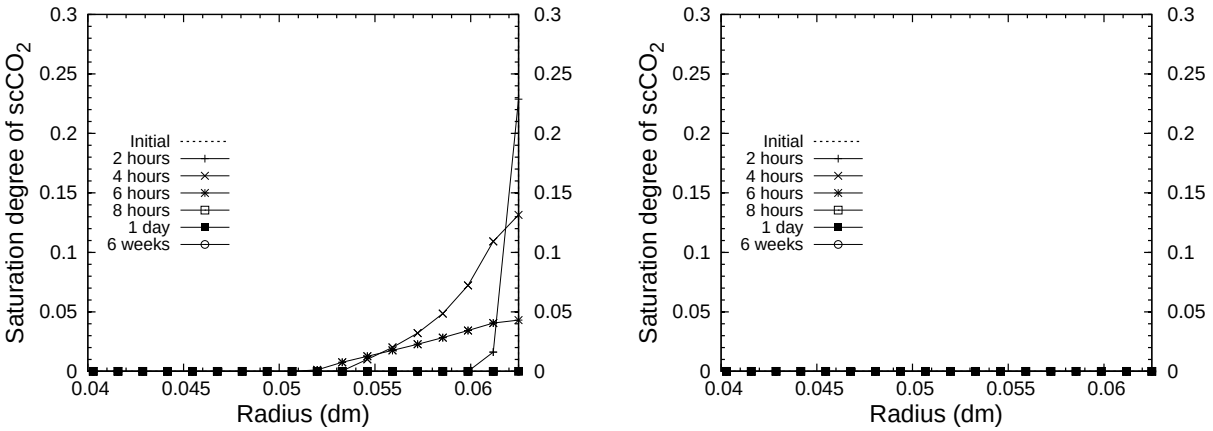

(a) Considering dissolution/evaporation kinetics

(b) Without dissolution/evaporation kinetics

Figure 7.17: Calculated $scCO_2$ saturation degree in cement paste exposed to $scCO_2$. (a) Considering kinetics of CO_2 dissolution and water evaporation at the boundary. (b) Without considering kinetics of CO_2 dissolution and water evaporation at the boundary.

7.3.3 Role of remaining alkali

It seems that, there was some remaining alkali in the cement paste, in the experiment of (Rimmelé et al., 2008), since they measured a pH value of 13 in the cement pore solution before carbonation. In this section, effects of remaining alkali will be analyzed. To achieve the same pH value before carbonation, 0.1 mol/L

K^+ is added in the pore solution of cement paste. The boundary conditions and the other initial conditions are the same as in section 7.3.2. For the surrounding water, we set initial K^+ concentration to 0 as pure water was used in experiment, thus K^+ in the pore solution of the sample can get into the surrounding water by diffusion as well as advection effect. The concentration of K^+ in the pore solution of cement paste exposed to CO_2 saturated water will decrease with time. For the samples exposed to $scCO_2$, considering that there is no diffusion at the surface of the sample, the K^+ concentration in the pore solution of the sample will not decrease. Thus we set the K^+ concentration in the pore solution constant to 0.1 mol/L in this case. The test conditions are summarized in Table 7.3.

The remaining alkali, will change the *p*H profile. For the sample exposed to $scCO_2$, *p*H value in the uncarbonated region is 13, and 6.9 in the fully carbonated region (see Fig 7.18a), higher than the value we predicted before (see section 7.3.2). For the sample exposed to CO_2-saturated water, in the uncarbonated region, the *p*H value is initially 13, and has decreased to 12.2 after 1 day. In the carbonated region, the *p*H value is 6.4. Since in the surrounding water there is no K^+ initially, the K^+ concentration in the pore solution of the sample decreases to about 0.016 mol/L after 1 day, which explains the different *p*H values predicted comparing with sample exposed to $scCO_2$.

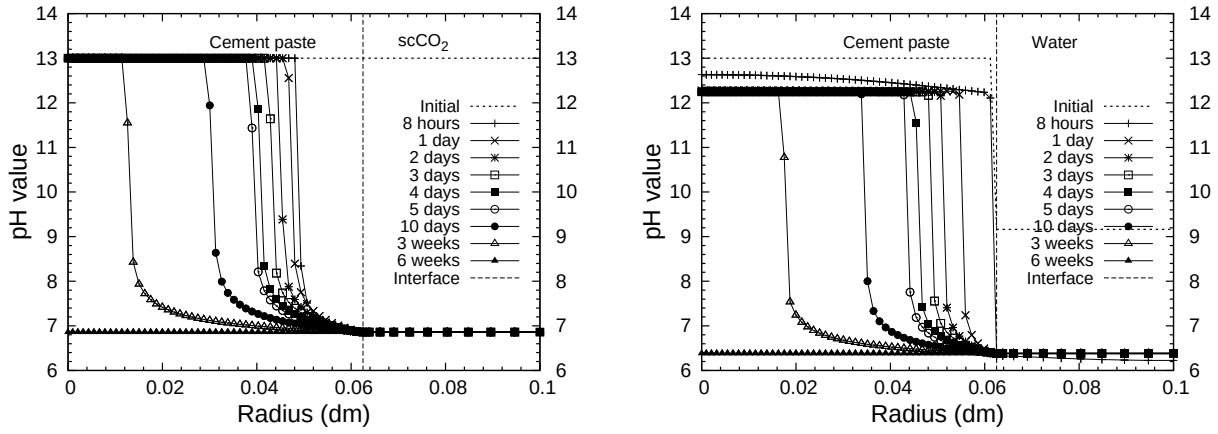

(a) Cement paste exposed to $scCO_2$

(b) Cement paste exposed to CO_2-saturated water

Figure 7.18: Calculated *p*H profiles from 1 day to 6 weeks, simulating the work of (Rimmelé et al., 2008), considering remaining alkali. (a) For $scCO_2$ boundary condition. (b) For CO_2-saturated water boundary condition.

Unlike in atmospheric carbonation experiments (Thiery, 2006; Morandeau, 2009), alkali has no obvious effects for the solid contents distribution, as well as for the carbonation kinetics in our simulations, probably due to the high CO_2 concentration. The results are almost identical with these predicted in section 7.3.2 (see Figs 7.19 to 7.21).

With the boundary and initial conditions as well as transport properties of cement paste provided in Table 7.3, we are able to perform an accurate simulation of the experiment of (Rimmelé et al., 2008). The

Table 7.3: Test conditions in simulation of the samples exposed to wet CO_2 and CO_2-saturated water, considering remaining alkali.

Transport properties of cement paste		
Temperature	Initial CH content	Initial C-S-H content
363 K	5.16 mol/L	3.9 mol/L
Initial porosity	Intrinsic liquid permeability	Intrinsic gas permeability
0.41	$K_l = 2 \times 10^{-19}$ m^2	$K_g = 14 \times 10^{-19}$ m^2
Cement paste ($r <$ 6.25 mm)		
Boundary conditions		**Initial conditions**
Balance Equation	BC left	
Carbon (C)	no flow	$P_G = 10^{-10}$ Pa
Calcium (Ca)	no flow	$\zeta_{Ca} = 1$
Silicon (Si)	no flow	$\zeta_{Si} = 1$
Sodium/Potassium	no flow	$\rho_{K^+} = 0.1$ mol/L
Chlorine (Cl)	no flow	$\rho_{Cl^-} = 0$ mol/L
Total mass	no flow	$P_L = 10^5$ Pa
Charge	no current	$\psi = 0$
The surrounding CO_2 (6.25 mm $< r <$ 10 mm)		
Boundary conditions		**Initial conditions**
Balance Equation	BC right	
Carbon (C)	$P_{G(2h)} = 280$ bars	$P_G = 10^{-10}$ Pa
Calcium (Ca)	$\zeta_{Ca} = 0$	$\zeta_{Ca} = 0$
Silicon (Si)	$\zeta_{Si} = 0$	$\zeta_{Si} = 0$
Sodium/Potassium	no flow	$\rho_{K^+} = 0$ mol/L
Chlorine (Cl)	no flow	$\rho_{Cl^-} = 0$ mol/L
Total mass	$P_{L(2h)} = 10^5$ Pa $P_{L(8h)} = 280$ bars	$P_L = 10^5$ Pa
Charge	$\psi = 0$	$\psi = 0$
The surrounding water (6.25 mm $< r <$ 10 mm)		
Boundary conditions		**Initial conditions**
Balance Equation	BC right	
Carbon (C)	$P_{G(2h)} = 10^{-10}$ Pa $P_{G(8h)} = 280$ bars	$P_G = 10^{-10}$ Pa
Calcium (Ca)	no flow	$\zeta_{Ca} =$ -20
Silicon (Si)	no flow	$\zeta_{Si} =$ -20
Sodium/Potassium	no flow	$\rho_{K^+} = 0$ mol/L
Chlorine (Cl)	no flow	$\rho_{Cl^-} = 0$ mol/L
Total mass	$P_{L(2h)} = 280$ bars	$P_L = 10^5$ Pa
Charge	$\psi = 0$	$\psi = 0$

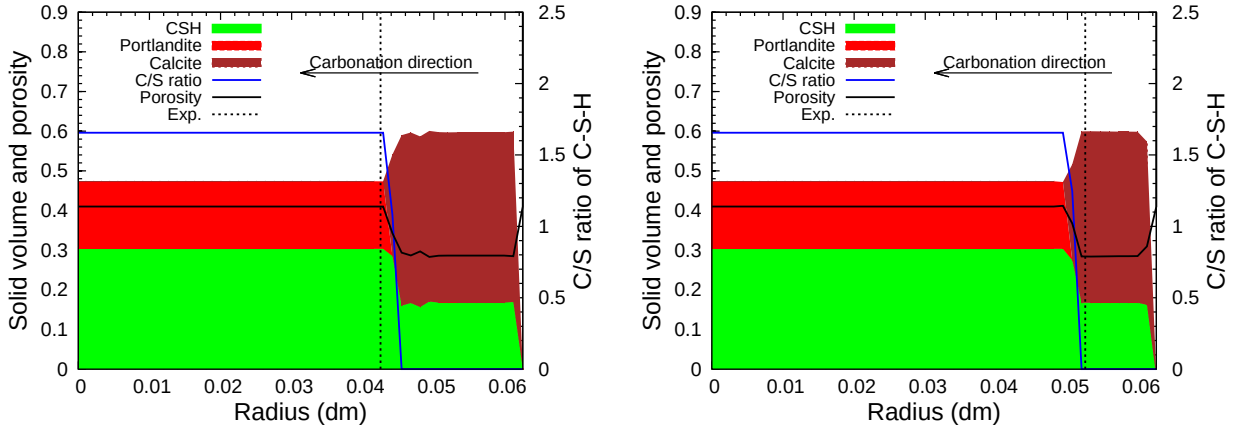

(a) Cement paste exposed to $scCO_2$ (b) Cement paste exposed to CO_2-saturated water

Figure 7.19: Calculated profiles of solid volume compounds after 2 days of exposure, simulating the work of (Rimmelé et al., 2008), considering remaining alkali. (a) For $scCO_2$ boundary condition. (b) For CO_2-saturated water boundary condition.

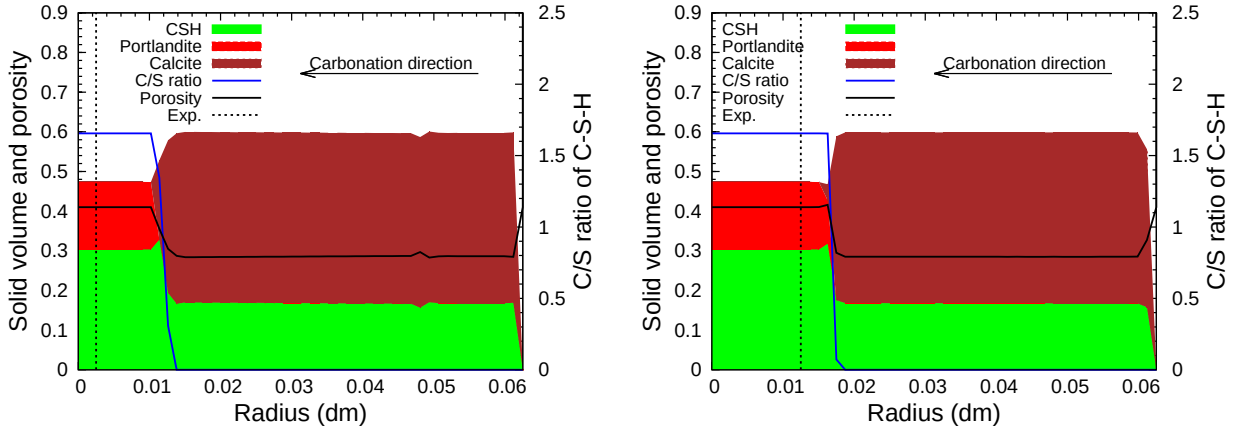

(a) Cement paste exposed to $scCO_2$ (b) Cement paste exposed to CO_2-saturated water

Figure 7.20: Calculated profiles of solid volume compounds after 3 weeks of exposure, simulating the work of (Rimmelé et al., 2008), considering remaining alkali. (a) For $scCO_2$ boundary condition. (b) For CO_2-saturated water boundary condition.

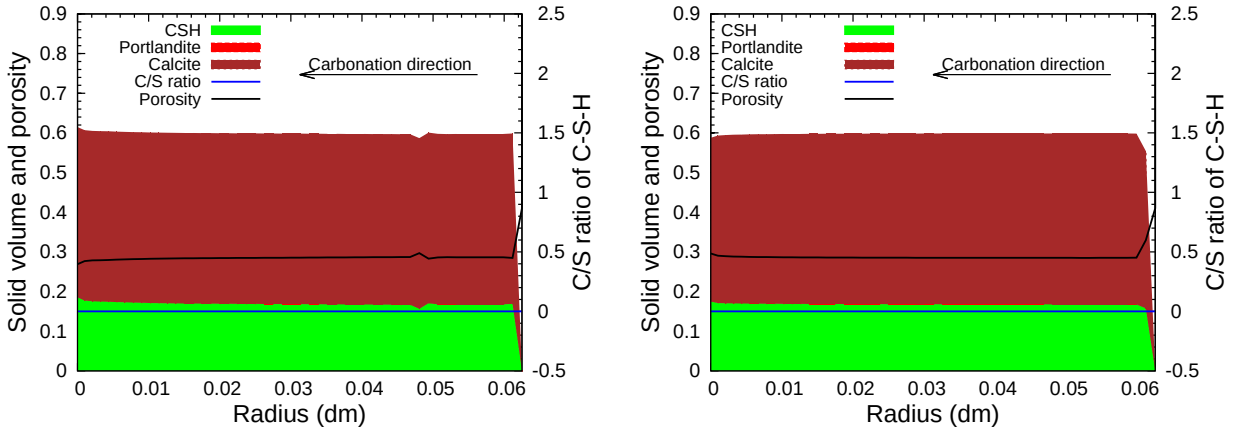

(a) Cement paste exposed to $scCO_2$

(b) Cement paste exposed to CO_2-saturated water

Figure 7.21: Calculated profiles of solid volume compounds after 6 weeks of exposure, simulating the work of (Rimmelé et al., 2008), considering remaining alkali. (a) For $scCO_2$ boundary condition. (b) For CO_2-saturated water boundary condition.

predicted *p*H value before/after carbonation and the porosity drop, are very close to the experimental results. The predicted kinetics of the penetration of the calcite precipitation front, though very close to experimental observations at 2 days and 6 weeks, is slightly underestimated at 3 weeks. The difference probably comes from the initial solid contents we use in our simulations. In the experiment of (Rimmelé et al., 2008), samples were cured for only 72 hours before carbonation, cement pastes were not well hydrated, thus, the values of 5.16 mol/L CH and 3.91 mol/L C-S-H we use for the simulations, may be overestimated.

7.4 Simulation of experiments in (Fabbri et al., 2009)

(Fabbri et al., 2009) used the same set-up as in (Rimmelé et al., 2008) and exposed both initially saturated and initially dried cement samples to $scCO_2$. Different types of carbonation features were achieved. For the initially saturated samples (wet samples), sharp carbonation fronts were observed, while for initially dried samples (dried samples), homogeneous carbonation took place. The situation of wet samples were quite similar to the results previously described, while dried samples experienced quite different carbonation patterns. In the experiment, conventional Portland cement slurry with 0.44 water/cement ratio by mass was cured for 72 hours at 21 MPa and 90 ℃. Then, the specimens were cut into cylindrical samples of 65 mm in length and 30 mm in diameter. Before exposure, half of the samples were stored in fresh water (wet samples) while the other samples were dried during a week in an oven at 85 ± 5 ℃ (dried samples). Cement samples were exposed to $scCO_2$ for the duration of 13, 35, 51 and 62 days, respectively, at 28 MPa and 90 ℃.

For dried samples, no visible carbonation front was observed. Samples showed a porosity drop from

41% before carbonation to 26% after 35 days and 24% after 62 days, and a gain of density from 1.53 g/cm^3 to 1.99 g/cm^3 after 35 days and 2.03 g/cm^3 after 62 days.

Wet samples showed a porosity drop from 41% to 31% after 62 days, and gained density from 1.53 g/cm^3 to 1.87 g/cm^3 after 62 days. Annular carbonation with a sharp carbonation front was observed. The thickness of the carbonated region increases linearly with the square root of time, which is typical for a diffusion-controlled carbonation pattern.

To simulate these experiments, we consider a cement paste cylinder of the same diameter (15 mm in radius), divided into 100 elements. As indicated before, in the case of $scCO_2$, arbitrary value of r_{CO_2} can be chosen since $scCO_2$ is homogeneous (see section 7.2). In this section, $r_{CO_2} = 15$ mm, the same value of the radius of cement paste sample used for the experiment.

For dried samples, the initial capillary pressure is 500 MPa ($S_L = 0.1$) and the gas pressure is set to 10^{-10} Pa (*i.e.*, no initial CO_2 is considered in the sample to avoid initial carbonation). At the boundary, the gas pressure rises from 0 to 28 MPa in 2 hours just the same time as in the experiment. We assume that, due to kinetics, it takes 6 hours to reach 100% of relative humidity at the boundary after the loading period. Thus we set the liquid pressure equals to -500 MPa at 2 hours and it increases it to 28 MPa at 8 hours. For the wet samples, boundary and initial conditions are the same as in section 7.3.3.

Different CO_2 transport mechanisms are predicted in our simulations. In the wet sample, CO_2 only enters the surface of the cement paste in the first few hours, and cement paste remains saturated after 8 hours (see Fig. 7.22b), thus, CO_2 moves generally by diffusion in water. In the dried sample, CO_2 moves essentially by advection of $scCO_2$ as it is unsaturated during the first 8 hours. In the pores of dried samples, liquid saturation degree gradually increases from surface to center from 7200 s (2 hours) to 14400 s (4 hours), as shown in Fig. 7.22a. Liquid saturation increase mainly comes from water released during carbonation in the first 4 hours, which is explained in Chapter 3. Liquid saturation almost remains unchanged between 14400 s and 28800 s (8 hours), since carbonation reaction stops. After 28800 s, the sample surface gets fully saturated as capillary pressure decreases to 0. Water enters the cement paste and liquid saturation degree raises to 1 gradually, from surface to center of the sample.

Compared to the wet samples, dried samples show much faster carbonation (see Figs. 7.24-7.27), as observed by Fabbri et al. (Fabbri et al., 2009). They did not observe annular carbonation during the experiment as it was observed with the wet samples. They believed that homogeneous carbonation is due to the rapid transport of wet $scCO_2$ throughout the porous network, which is confirmed by our simulation. However, instead of homogeneous carbonation, annular carbonation pattern is predicted for dried samples in our simulation. One probable explication for the homogeneous carbonation pattern observed in experiment is that due to a small liquid saturation degree in the dry cement paste, CO_2 entered the sample rapidly

Table 7.4: Test conditions in simulation the experiment of (Fabbri et al., 2009).

Temperature and transport properties of cement paste		
Temperature	Initial CH content	Initial C-S-H content
363 K	5.16 mol/L	3.9 mol/L
Initial porosity	Intrinsic liquid permeability	Intrinsic gas permeability
0.41	$K_l = 2 \times 10^{-19}$ m^2	$K_g = 14 \times 10^{-19}$ m^2

Dried sample			
Boundary conditions			**Initial conditions**
Balance Equation	BC left	BC right	
Carbon (C)	no flow	$P_{G(2h)} = 280$ bars	$P_G = 10^{-10}$ Pa
Calcium (Ca)	no flow	$\zeta_{Ca} = 0$	$\zeta_{Ca} = 1$
Silicon (Si)	no flow	$\zeta_{Si} = 0$	$\zeta_{Si} = 1$
Sodium/Potassium	no flow	$\rho_{K^+} = 0$ mol/L	$\rho_{K^+} = 0.1$ mol/L
Chlorine (Cl)	no flow	$\rho_{Cl^-} = 0$ mol/L	$\rho_{Cl^-} = 0$ mol/L
Total mass	no flow no flow	$P_{L(2h)}$ =-5000 bars $P_{L(8h)}$ =280 bars	P_L = -5000 bars
Charge	no current	$\psi = 0$	$\psi = 0$
Wet sample			
Boundary conditions			**Initial conditions**
Balance Equation	BC left	BC right	
Carbon (C)	no flow	$P_{G(2h)} = 280$ bars	$P_G = 10^{-10}$ Pa
Calcium (Ca)	no flow	$\zeta_{Ca} = 0$	$\zeta_{Ca} = 1$
Silicon (Si)	no flow	$\zeta_{Si} = 0$	$\zeta_{Si} = 1$
Sodium/Potassium	no flow	$\rho_{K^+} = 0$ mol/L	$\rho_{K^+} = 0.1$ mol/L
Chlorine (Cl)	no flow	$\rho_{Cl^-} = 0$ mol/L	$\rho_{Cl^-} = 0$ mol/L
Total mass	no flow no flow	$P_{L(2h)}$ =1 bar $P_{L(8h)}$ =280 bars	P_L = 1 bar
Charge	no current	$\psi = 0$	$\psi = 0$

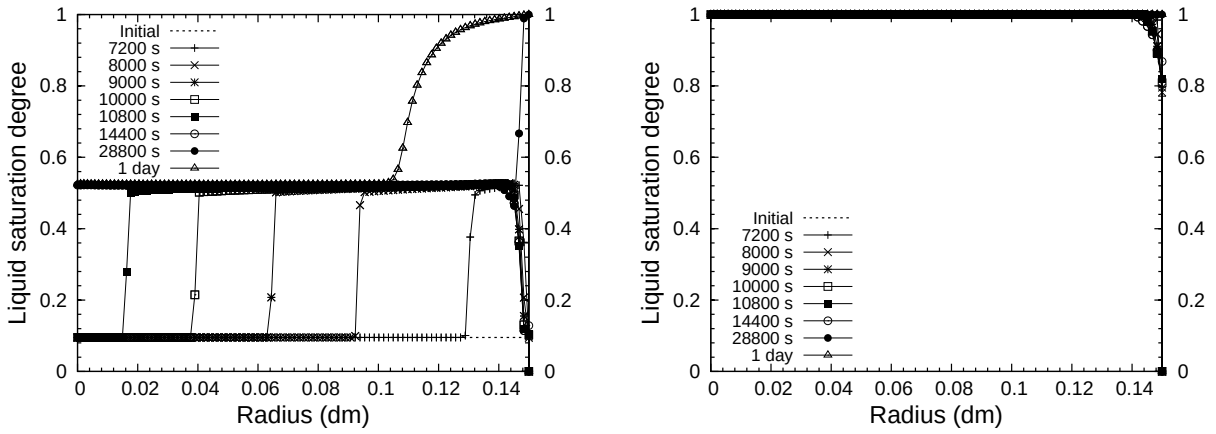

(a) Dried sample

(b) Wet sample

Figure 7.22: Calculated liquid saturation degree in cement paste exposed to scCO$_2$ in simulation of the experiment of (Fabbri et al., 2009). (a) Dried sample. (b) Wet sample.

without reaction in the first few hours, thus homogeneous carbonation took place through out the sample. Since the author did not provide any information for the first 4 hours in (Fabbri et al., 2009), it's hard to calibrate our simulation results for the carbonation pattern of dried sample. The only information provided in experiment is the measured porosity and density after 35 and 62 days of exposure for dried samples, which were almost identical in (Fabbri et al., 2009). It means that the samples were fully carbonated before 35 days. More serious study of this pattern could be done in the future, from both experimental and numerical points of view.

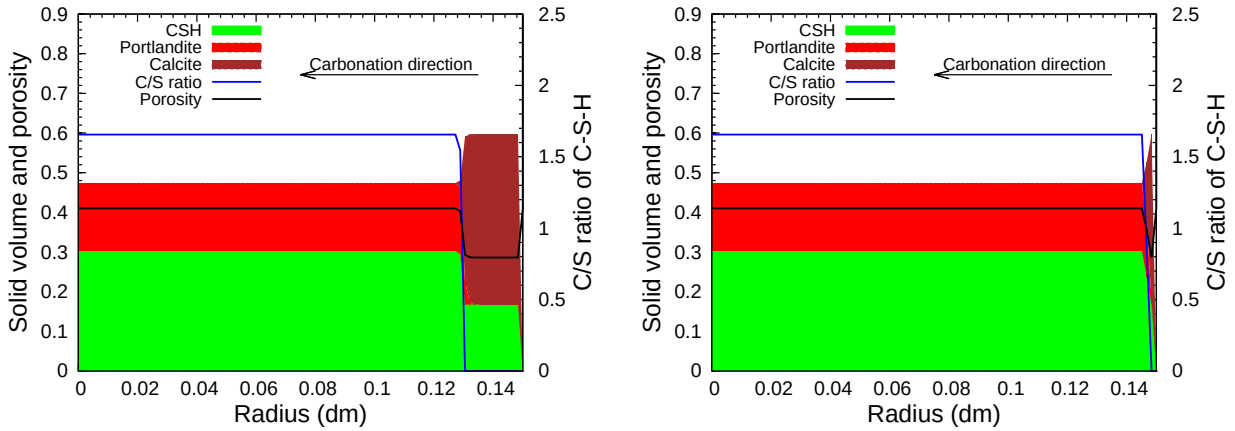

(a) Dried sample (b) Wet sample

Figure 7.23: Calculated profiles of solid volume compounds after 2 hours of exposure, simulating the work of (Fabbri et al., 2009). (a) Dried sample. (b) Wet sample.

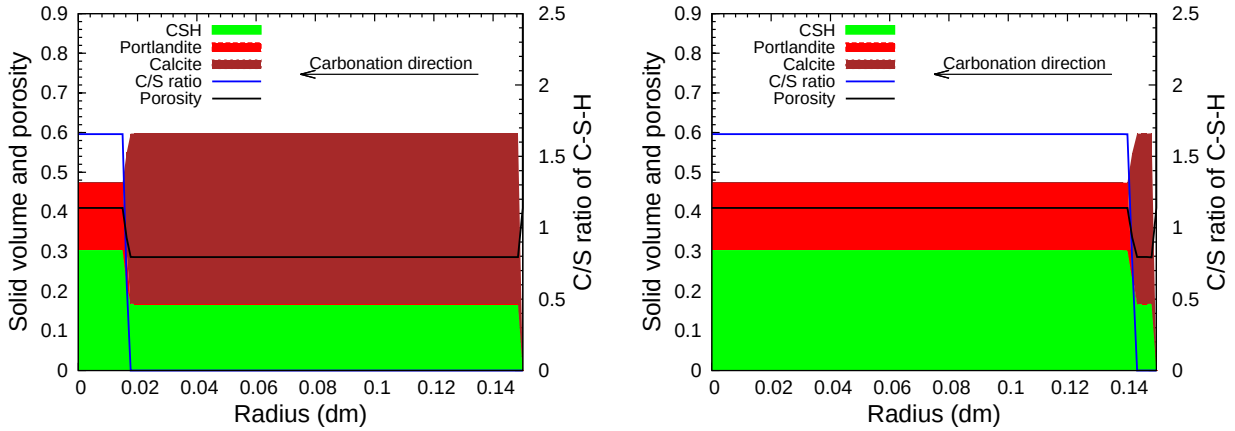

(a) Dried sample (b) Wet sample

Figure 7.24: Calculated profiles of solid volume compounds after 3 hours of exposure, simulating the work of (Fabbri et al., 2009). (a) Dried sample. (b) Wet sample.

A porosity drop from 41% to 28% and solid density increase from 1.125 to 1.536 g/cm^3 of dried samples after full carbonation are predicted by our simulation (see Figs. 7.25a and 7.26a). Here since we only

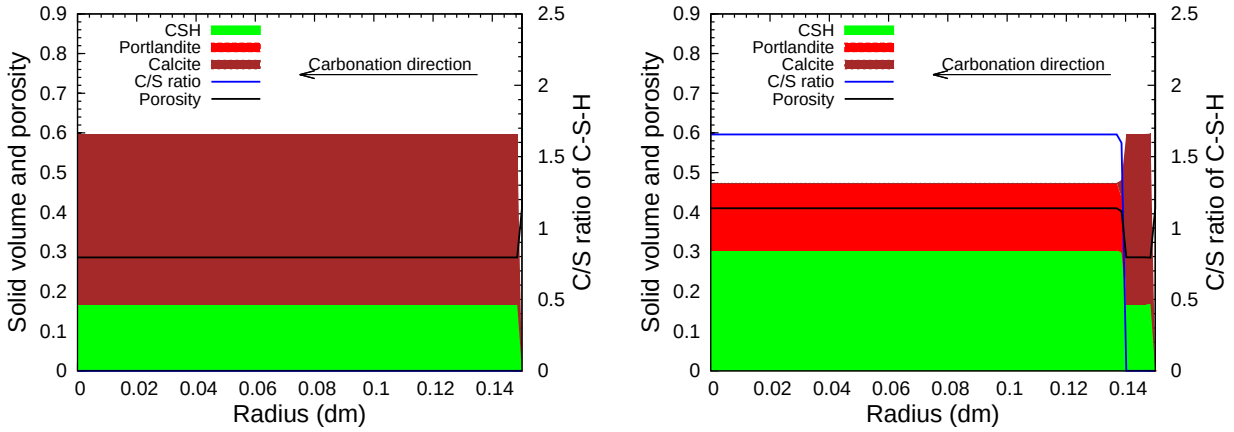

(a) Dried sample (b) Wet sample

Figure 7.25: Calculated profiles of solid volume compounds after 4 hours of exposure, simulating the work of (Fabbri et al., 2009). (a) Dried sample. (b) Wet sample.

consider CH and C-S-H as carbonatable hydration products, the calculated solid density is smaller than that measured in experiment. The predicted porosity drop and the increase of the solid density are quite close to experimental measurements.

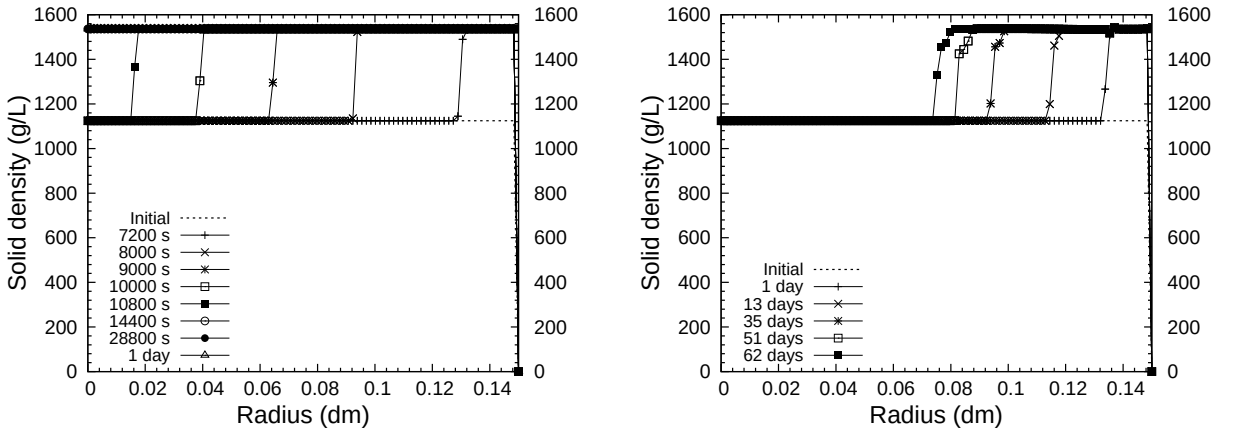

(a) Dried sample (b) Wet sample

Figure 7.26: The calculated solid density profiles, simulating the work of (Fabbri et al., 2009). (a) Dried sample. (b) Wet sample.

7.5 Comparison between experiments of (Duguid and Scherer, 2010) and (Rimmelé et al., 2008)

In the experiments of (Rimmelé et al., 2008), for the cement samples exposed to CO_2-saturated water, the surrounding water quickly got saturated with calcite. Leaching of calcium is thus very limited. As a

result, this condition is very similar to limestone-like conditions in experiments of (Duguid and Scherer, 2010) discussed in Chapter 6. Duguid et al. observed a clogging effect; it was observed that the carbonation was restricted at the sample surface for limestone-like conditions. In the work of (Rimmelé et al., 2008), clogging effect was not observed, the cement paste was fully carbonated after 6 weeks. The differences between both experiments include aqueous CO_2 concentration at the sample surface, temperature, curing time of cement paste, cement type and alkali ion concentrations. The most significant difference is the CO_2 concentration. In (Duguid and Scherer, 2010), CO_2 concentration at the boundary equals to 0.028 mol/L (1 bar, 323 K) while in (Rimmelé et al., 2008) it's 1.25 mol/L (280 bars, 363 K). In this section, we will investigate whether the clogging effect is governed by CO_2 concentration at the boundary. Simulations with different CO_2 concentrations ($\rho_{CO_2^0}$ = 0.028 mol/L corresponding to P_G = 1 bar and $\rho_{CO_2^0}$ = 1.35 mol/L corresponding to P_G = 280 bars at 323 K) are conducted, limestone boundary condition is used, temperature and cement properties are the same as in section 6.4. Boundary and initial conditions are summarized in Table 7.5.

Table 7.5: Test conditions in studying CO_2 concentration

Temperature and transport properties of cement paste		
Temperature	Initial CH content	Initial C-S-H content
323 K	5.16 mol/L	3.9 mol/L
Initial porosity	Intrinsic liquid permeability	Intrinsic gas permeability
0.4	$K_l = 2 \times 10^{-19}$ m^2	$K_g = 14 \times 10^{-19}$ m^2

At pressure of 1 bar			
Boundary conditions			**Initial conditions**
Balance Equation	BC left	BC right	
Carbon (C)	no flow	flow allowed ($\rho_{CO_2^0(2h)}$ = 0.028 mol/L)	$\rho_{CO_2^0} = 10^{-16}$ mol/L
Calcium (Ca)	no flow	$\zeta_{Ca} = 0$	$\zeta_{Ca} = 1$
Silicon (Si)	no flow	$\zeta_{Si} = 0$	$\zeta_{Si} = 1$
Sodium/Potassium	no flow	$\rho_{K^+} = 0.5$ mol/L	$\rho_{K^+} = 0.5$ mol/L
Chlorine (Cl)	no flow	$\rho_{Cl^-} = 0.5$ mol/L	$\rho_{Cl^-} = 0.5$ mol/L
Total mass	no flow	flow allowed ($P_{L(2h)} = 10^5$ Pa)	$P_L = 10^5$ Pa
Charge	no current	$\psi = 0$	$\psi = 0$
At pressure of 280 bars			
Boundary conditions			**Initial conditions**
Balance Equation	BC left	BC right	
Carbon (C)	no flow	flow allowed ($\rho_{CO_2^0(2h)}$ = 1.35 mol/L)	$\rho_{CO_2^0} = 10^{-16}$ mol/L
Calcium (Ca)	no flow	$\zeta_{Ca} = 0$	$\zeta_{Ca} = 1$
Silicon (Si)	no flow	$\zeta_{Si} = 0$	$\zeta_{Si} = 1$
Sodium/Potassium	no flow	$\rho_{K^+} = 0.5$ mol/L	$\rho_{K^+} = 0.5$ mol/L
Chlorine (Cl)	no flow	$\rho_{Cl^-} = 0.5$ mol/L	$\rho_{Cl^-} = 0.5$ mol/L
Total mass	no flow	flow allowed ($P_{L(2h)} = 280$ bars)	$P_L = 10^5$ Pa
Charge	no current	$\psi = 0$	$\psi = 0$

Calculated profiles of solid volume compounds are plotted below. A full clogging of the porosity (0 porosity) is predicted after 10 days for the sample with $\rho_{CO_2^0}$ = 0.028 mol/L at the surface (see Figs 7.27a

to 7.29a), while the porosity distribution in the fully carbonated region has been homogeneously reduced for the sample with $\rho_{CO_2^0} = 1.35$ mol/L at the surface (see Figs 7.27b to 7.29b).

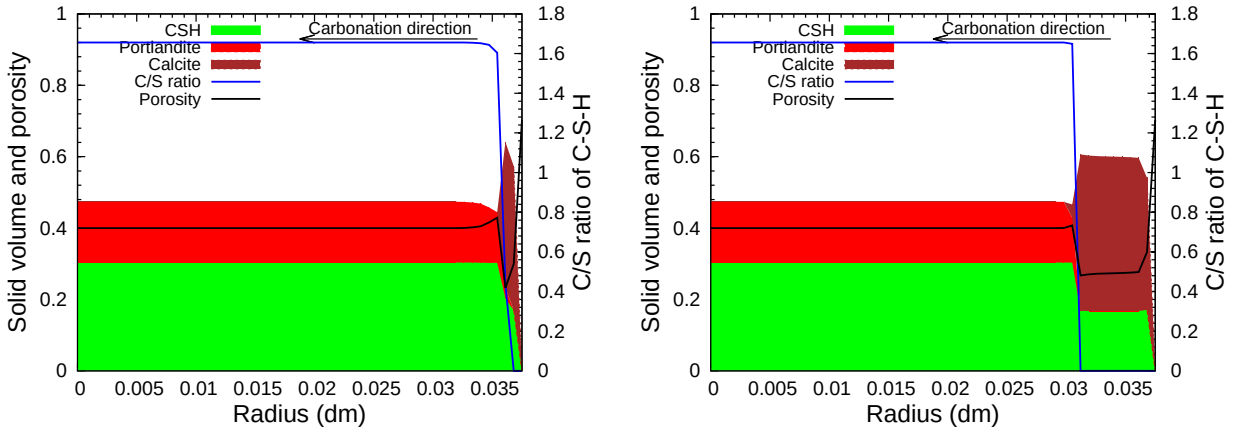

(a) $\rho_{CO_2^0} = 0.028$ mol/L (b) $\rho_{CO_2^0} = 1.35$ mol/L

Figure 7.27: Calculated profiles of solid volume compounds after 1 day of exposure. (a) With $\rho_{CO_2^0} = 0.028$ mol/L at the boundary. (b) With $\rho_{CO_2^0} = 1.35$ mol/L at the boundary.

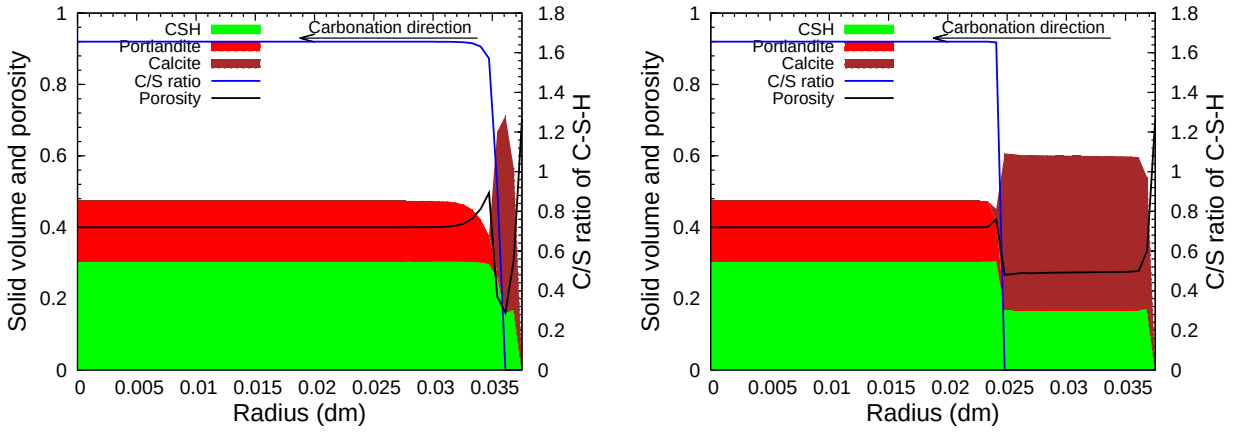

(a) $\rho_{CO_2^0} = 0.028$ mol/L (b) $\rho_{CO_2^0} = 1.35$ mol/L

Figure 7.28: Calculated profiles of solid volume compounds after 4 days of exposure. (a) With $\rho_{CO_2^0} = 0.028$ mol/L at the boundary. (b) With $\rho_{CO_2^0} = 1.35$ mol/L at the boundary.

The different porosity patterns can be interpreted by the transport of calcium and carbon. Take the flow of carbon and calcium after 4 days for example (see Fig. 7.30), it is observed that the transport of calcium is in the same order of magnitude with different CO_2 concentrations, while a difference of 10 times of carbon transport is predicted. The transport of calcium will cause extra calcite precipitation at the calcite precipitation front. In low $\rho_{CO_2^0}$ conditions, the calcite precipitation front moves slowly, and the transport of calcium from the CH dissolution region to the calcite precipitation front is very obvious. Accordingly, sufficient calcite precipitation will cause pore clogging. On the contrary, if carbon transport

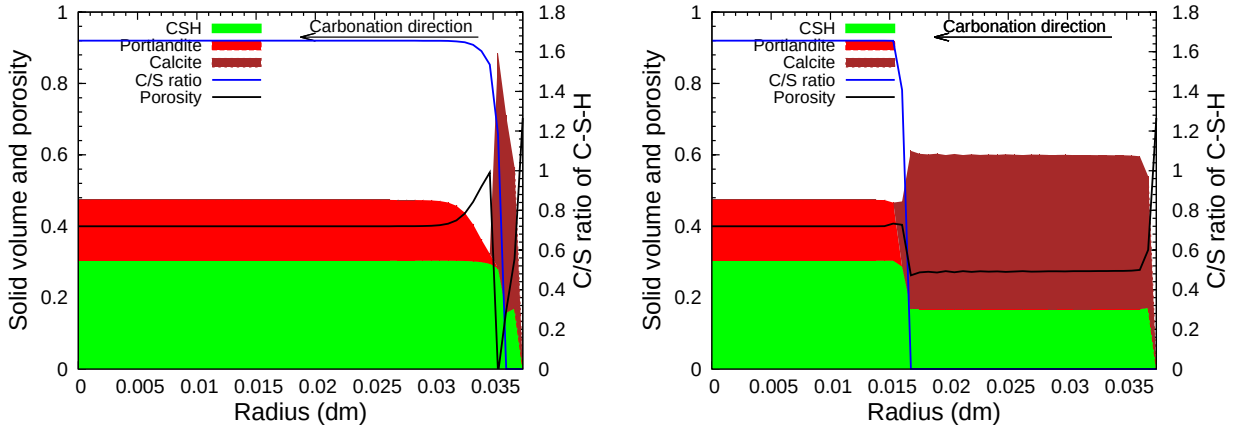

(a) $\rho_{CO_2^0} = 0.028$ mol/L (b) $\rho_{CO_2^0} = 1.35$ mol/L

Figure 7.29: Calculated profiles of solid volume compounds after 10 days of exposure. (a) With $\rho_{CO_2^0} = 0.028$ mol/L at the boundary. (b) With $\rho_{CO_2^0} = 1.35$ mol/L at the boundary.

is fast enough, the calcite precipitation fronts moves quickly and the extra calcite precipitation caused by calcium transport can be neglected.

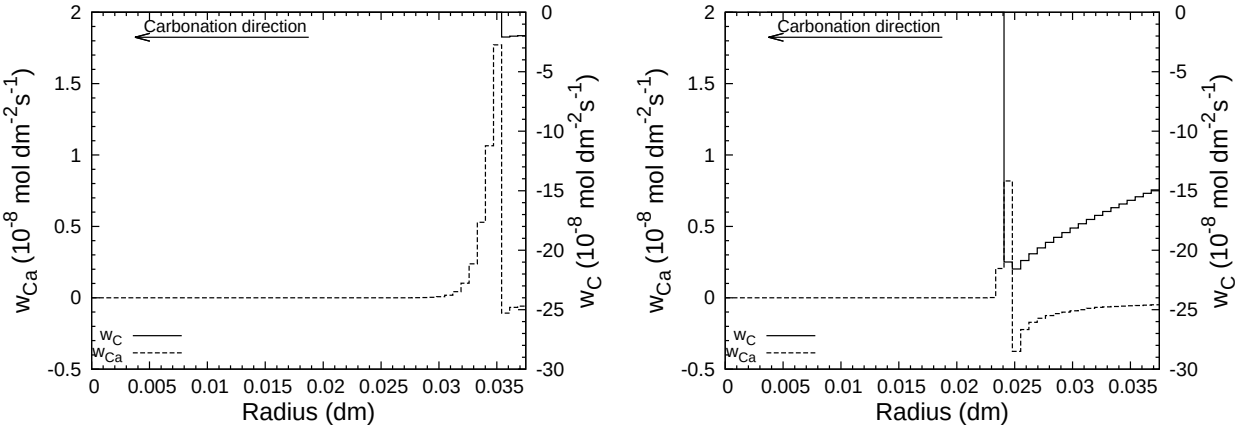

(a) $\rho_{CO_2^0} = 0.028$ mol/L (b) $\rho_{CO_2^0} = 1.35$ mol/L

Figure 7.30: Calculated flow of carbon and calcium after 4 days of exposure. (a) With $\rho_{CO_2^0} = 0.028$ mol/L at the boundary. (b) With $\rho_{CO_2^0} = 1.35$ mol/L at the boundary.

7.6 Comparison between experiments of (Kutchko et al., 2008) and (Rimmelé et al., 2008)

Kutchko et al. (Kutchko et al., 2007, 2008) conducted similar experiments as in (Rimmelé et al., 2008). In (Kutchko et al., 2007), cement paste samples made of class H cement (12 mm in diameter, W/C=0.38), cured for 28 days at 303 bars or 1 bar, and 50 or 22 ℃ in 1% NaCl solution prior to the experiments, were

Table 7.6: Curing conditions of cement paste and average depth of alteration after 9 days of exposure, cited from (Kutchko et al., 2007)

Sample	Temperature (°C)	Pressure (MPa)	Depth of carbonation (mm)
A	22	0.1	0.59 ± 0.03
B	22	30.3	0.45 ± 0.04
C	50	0.1	0.47 ± 0.19
D	50	30.3	0.22 ± 0.01

exposed to CO_2 saturated brine at 50 °C and 30.3 MPa for 9 days, in a static system. Curing conditions of cement paste and average depth of carbonation after 9 days of exposure are summarized in Table 7.6. Curing conditions played an important role on the carbonation kinetics. Sample D cured at 303 bars and 50 °C showed smallest depth of penetration, while sample A cured at 1 bar and 22 °C showed the most rapid carbonation kinetics. Kutchko et al. explained that sample D had a slightly higher degree of hydration than the other samples. A high degree of hydration decreases the permeability and thus increases the cement's resistance to attack, more hydration products to attack also slow down the penetration of carbonation. Moreover, in sample D, CH crystals are smaller and more evenly distributed throughout the solid matrix of the cement, thus, a well-defined band of calcite was formed and protected the inner part of the sample.

In (Kutchko et al., 2008), samples cured at 303 bars and 50 °C (sample D in (Kutchko et al., 2007)) were exposed to both $scCO_2$ and CO_2 saturated brine for 1 year. The measured carbonation depth didn't exceed 1 mm for samples exposed to both $scCO_2$ and CO_2-saturated brine (see Fig. 7.31). Results for cement paste in contact with $scCO_2$ was similar to that in contact with atmospheric CO_2 with a strong effect of the clogging of the microstructure able to hinder CO_2 penetration, while the one exposed to CO_2 saturated brine was typical of acid attack on cement-based materials with a significant leaching effect (both of hydration compounds and calcium carbonate).

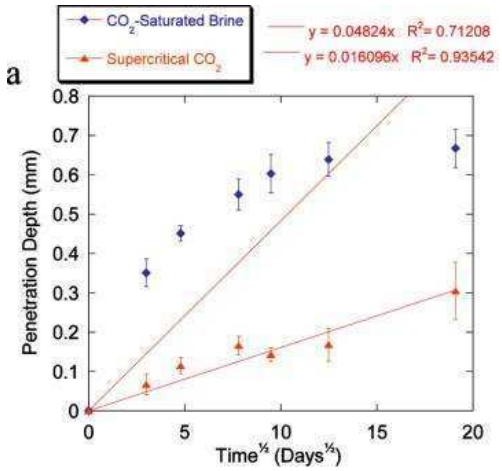

Figure 7.31: Progression of penetration depth in experiment of Kutchko et al. (Kutchko et al., 2008).

The boundary conditions of (Kutchko et al., 2008) and (Rimmelé et al., 2008) are quite similar, it's interesting that in (Kutchko et al., 2008) the measured carbonation kinetics was about 100 times lower than the one measured in (Rimmelé et al., 2008). The differences between both sets of experiments include: 1) cement type of class H *vs.* class G, 2) curing time of 28 days *vs.* 72 h, 3) temperature of 50 ℃ *vs.* 90 ℃, 4) 0.17 M NaCl in the brine *vs.* pure water used. Based on the huge difference of the measured kinetics, it seems that, the cement samples in (Kutchko et al., 2008) should have lower porosity and much lower tortuosity than in (Rimmelé et al., 2008). This is possible since samples in (Kutchko et al., 2008) had a much longer curing time, thus higher hydration degree was achieved. Though Kutchko et al. claimed that sample D had a lower porosity than other samples, due to a higher hydration degree in (Kutchko et al., 2007), and also mentioned that class H cement has very low permeability in (Kutchko et al., 2008), unfortunately, neither the porosity nor the tortuosity were quantified in (Kutchko et al., 2007, 2008). Due to the lack of data, it's hard to make a persuasive simulation. In this section, we just simulate the cement paste exposed to CO_2-saturated brine in (Kutchko et al., 2008) with different porosity (0.41 and 0.2) to illustrate how this parameter will affect the carbonation kinetics. Theoretically, with lower porosity, there will be more hydration products (CH and C-S-H). However, here we use the same initial CH and C-S-H content to exclude the influence of hydration products content. Boundary and initial conditions are listed in Table 7.7. Unlike scCO_2 boundary conditions, here we have to consider the volume ratio of brine to sample since this value will determine how much formed calcite can be dissolved into the surrounding brine (leaching of calcium). We use $r_{\text{water}} = 17$ mm to get the same volume ratio as the one provided in experiment (87%). Intrinsic permeabilities are considered as a function of porosity (van Genuchten, 1980), thus intrinsic liquid/gas permeabilities before carbonation are smaller for the sample with an initial porosity of 0.2 compared with the one with an initial porosity of 0.41.

Simulation results are presented hereafter. Much slower carbonation kinetics is predicted for the sample with an initial porosity of 0.2 (see Figs. 7.32b to 7.35b), than for the sample with an initial porosity of 0.41 (see Figs. 7.32a to 7.35a). There is some calcite dissolution at the sample surface, due to the large volume ratio of brine to sample. This region is also observed in the experiments as the degraded zone in Fig. 7.36. For the sample with an initial porosity of 0.41, porosity profiles are homogeneous in the region of calcite precipitation, while a visible porosity drop at the calcite precipitation front is observed for the sample with an initial porosity of 0.2 from 30 days and after, and note that a full clogging effect takes place after 45 days.

Again, the different porosity patterns can be explained by the flow of carbon and calcium. As discussed in section 7.5, the flow of calcium from the CH dissolution region to the calcite precipitation front can introduce extra calcite precipitation at the calcite precipitation front. This effect can be neglected when

Table 7.7: Test conditions used for the simulations of the work of (Kutchko et al., 2008).

Transport properties of cement paste		
Temperature	Initial CH content	Initial C-S-H content
323 K	5.16 mol/L	3.9 mol/L
Initial porosity	Intrinsic permeability for liquid	Intrinsic permeability for gas
0.41	$K_l = 2 \times 10^{-19}$ m^2	$K_g = 14 \times 10^{-19}$ m^2
0.2	$K_l = 0.13 \times 10^{-19}$ m^2	$K_g = 0.88 \times 10^{-19}$ m^2
Cement paste ($r <$ 6 mm)		
Boundary conditions		**Initial conditions**
Balance Equation	BC left	
Carbon (C)	no flow	$P_G = 10^{-10}$ Pa
Calcium (Ca)	no flow	$\zeta_{Ca} = 1$
Silicon (Si)	no flow	$\zeta_{Si} = 1$
Sodium/Potassium	no flow	$\rho_{K^+} = 0.17$ mol/L
Chlorine (Cl)	no flow	$\rho_{Cl^-} = 0.17$ mol/L
Total mass	no flow	$P_L = 10^5$ Pa
Charge	no current	$\psi = 0$
The surrounding water (6 mm $< r <$ 17 mm)		
Boundary conditions		**Initial conditions**
Balance Equation	BC right	
Carbon (C)	$P_{G(2h)} = 10^{-10}$ Pa $P_{G(8h)} = 303$ bar	$P_G = 10^{-10}$ Pa
Calcium (Ca)	no flow	ζ_{Ca} = -20
Silicon (Si)	no flow	ζ_{Si} = -20
Sodium/Potassium	no flow	$\rho_{K^+} = 0.17$ mol/L
Chlorine (Cl)	no flow	$\rho_{Cl^-} = 0.17$ mol/L
Total mass	$P_{L(2h)} = 303$ bar	$P_L = 10^5$ Pa
Charge	no current	$\psi = 0$

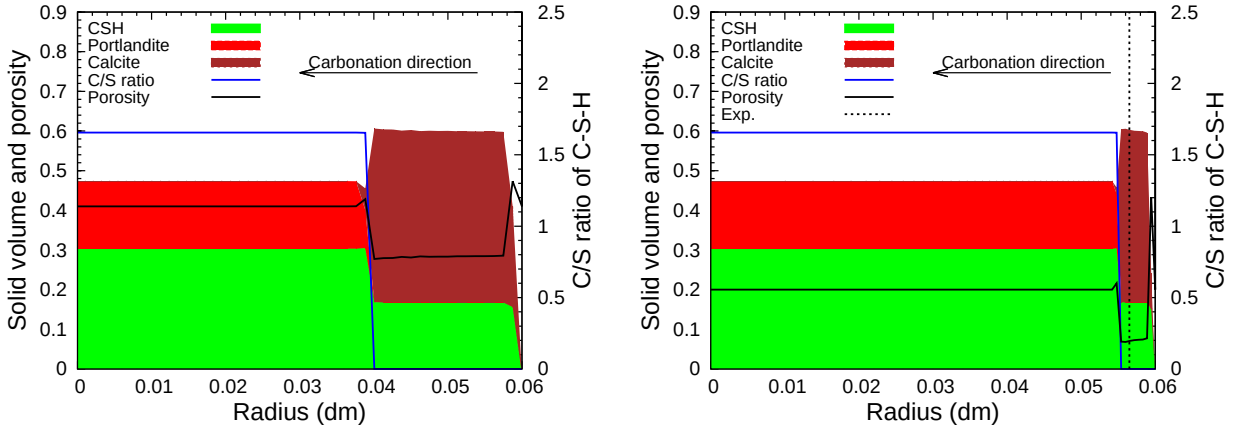

(a) With an initial porosity of 0.41

(b) With an initial porosity of 0.2

Figure 7.32: Calculated profiles of solid volume compounds after 9 days of exposure for the simulation of (Kutchko et al., 2008). (a) With an initial porosity of 0.41. (b) With an initial porosity of 0.2.

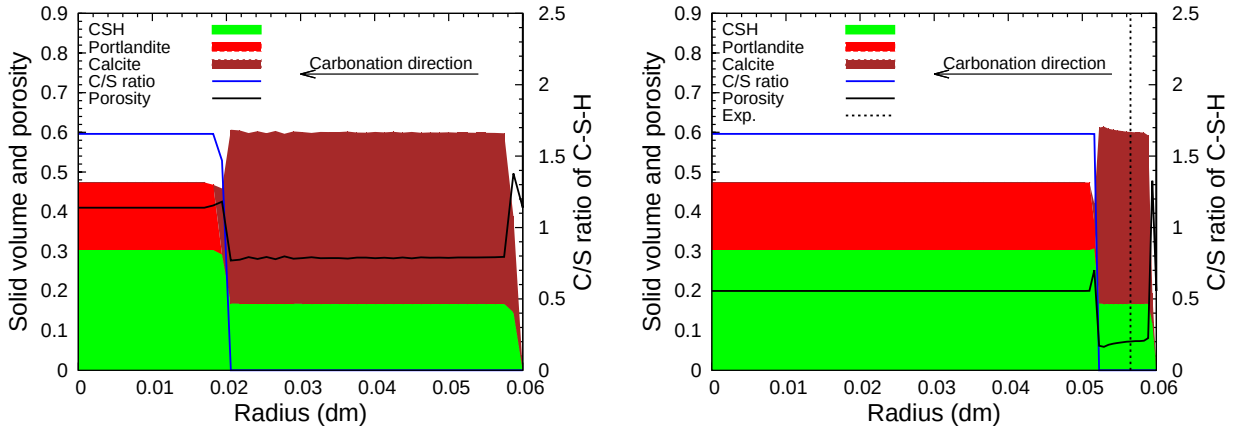

(a) With an initial porosity of 0.41

(b) With an initial porosity of 0.2

Figure 7.33: Calculated profiles of solid volume compounds after 30 days of exposure for the simulation of (Kutchko et al., 2008). (a) With an initial porosity of 0.41. (b) With an initial porosity of 0.2.

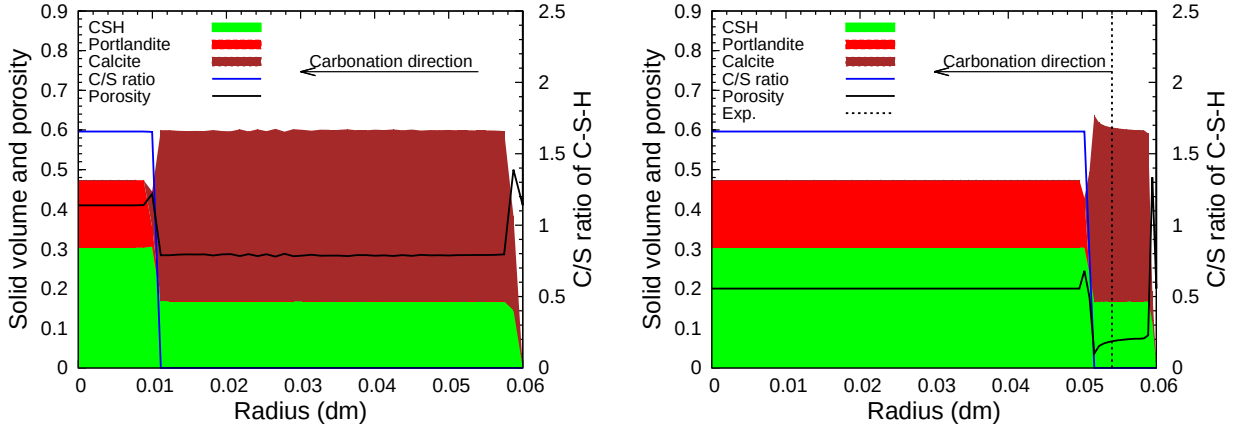

(a) With an initial porosity of 0.41

(b) With an initial porosity of 0.2

Figure 7.34: Calculated profiles of solid volume compounds after 40 days of exposure for the simulation of (Kutchko et al., 2008). (a) With an initial porosity of 0.41. (b) With an initial porosity of 0.2.

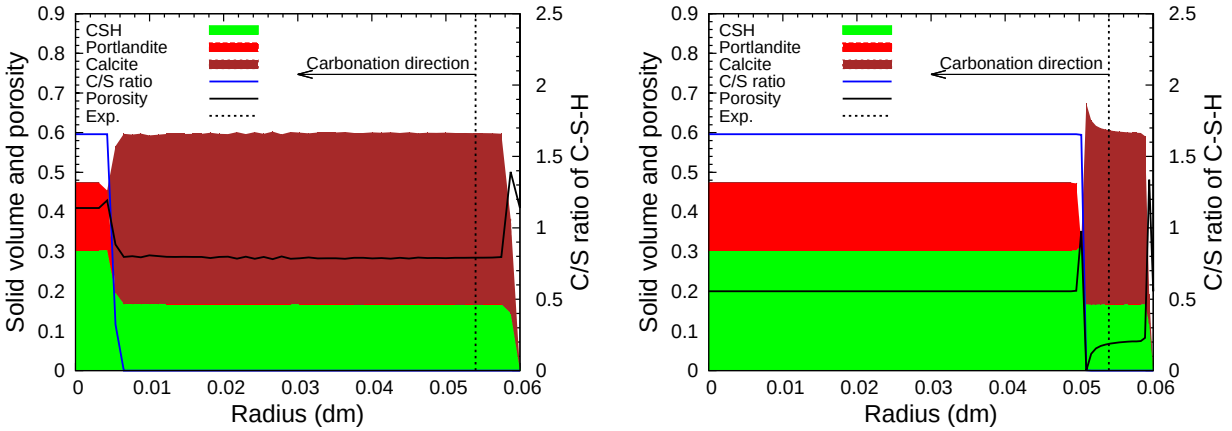

(a) With an initial porosity of 0.41

(b) With an initial porosity of 0.2

Figure 7.35: Calculated profiles of solid volume compounds after 45 days of exposure for the simulation of (Kutchko et al., 2008). (a) With an initial porosity of 0.41. (b) With an initial porosity of 0.2.

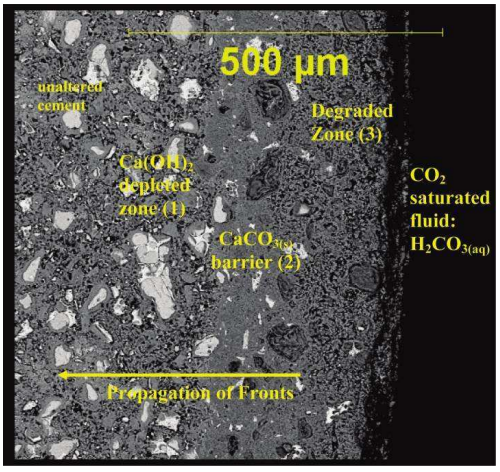

Figure 7.36: SEM-BSE image for the sample after 9 days of exposure to CO_2-saturated brine, cited from (Kutchko et al., 2008).

flow of carbon dominates the reaction since the calcite precipitation front moves fast to the cement paste center. When the flow of carbon is slow, the extra calcite formation due to calcium flow will cause a significant porosity drop at the calcite precipitation front. The clogging effect will then dominate the carbonation kinetics.

A smaller flow of both carbon and calcium is predicted for the sample with ϕ_0 (initial porosity) = 0.2 (see Figs. 7.37 to 7.40). For the sample with $\phi_0 = 0.41$, the flow of carbon and calcium does not change too much according time (see Figs. 7.37a to 7.40a), while for the sample with $\phi_0 = 0.2$, the flow of calcium increases about 10 times and the flow of carbon decreases about 3 times from 9 days to 45 days (see Figs. 7.37b to 7.40b). As the region of calcite precipitation forms, the transport of CO_2 into the cement gets slower, since CO_2 has to diffuse through this low porosity region. The calcium transport increases as it takes place in the CH dissolution region with a higher porosity. As the kinetics of penetration of the calcite precipitation front gets slower and the calcium transport increases, extra calcite precipitation due to calcium transport gets significant, and finally causes full clogging.

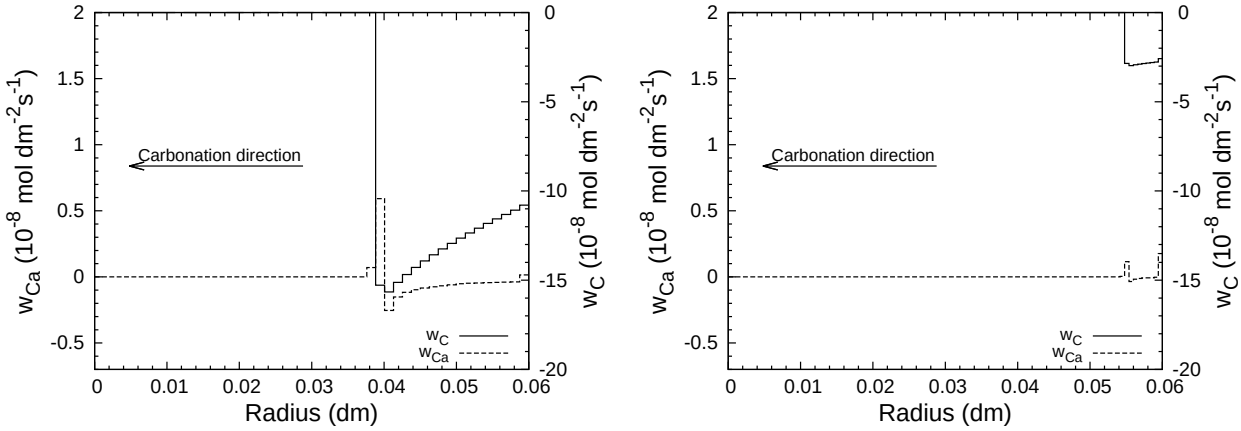

(a) With an initial porosity of 0.41

(b) With an initial porosity of 0.2

Figure 7.37: Calculated flow of carbon and calcium after 9 days of exposure for the simulation of (Kutchko et al., 2008). (a) With an initial porosity of 0.41. (b) With an initial porosity of 0.2.

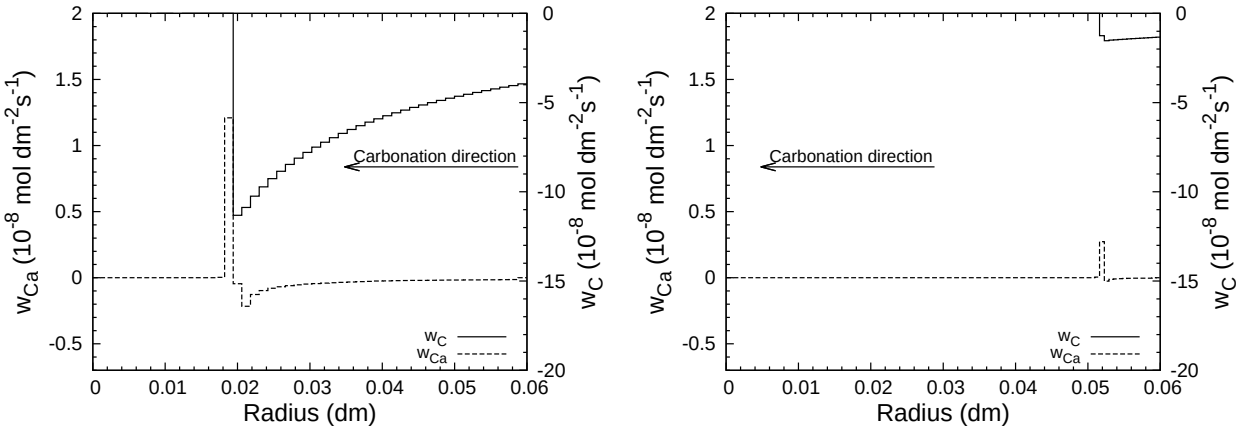

(a) With an initial porosity of 0.41

(b) With an initial porosity of 0.2

Figure 7.38: Calculated flow of carbon and calcium after 30 days of exposure for the simulation of (Kutchko et al., 2008). (a) With an initial porosity of 0.41. (b) With an initial porosity of 0.2.

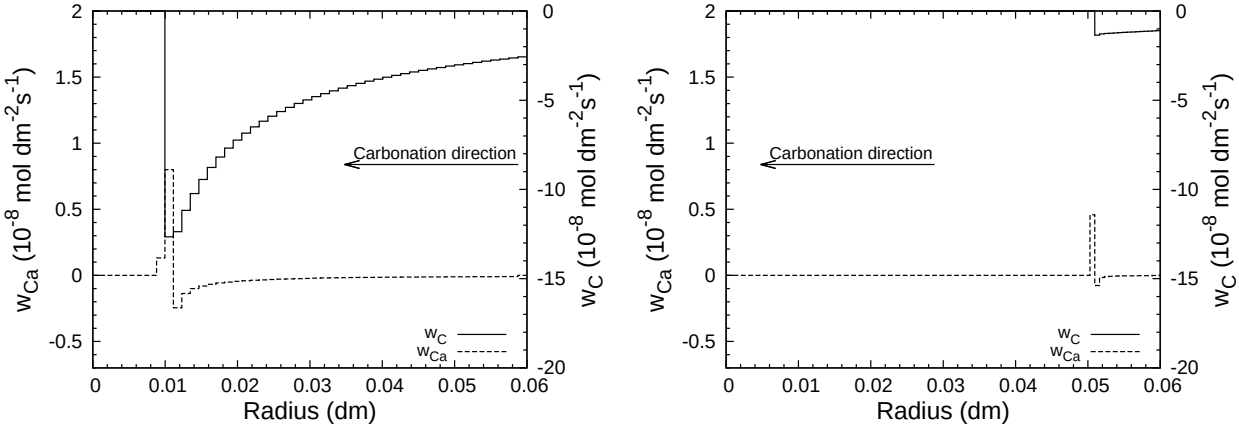

(a) With an initial porosity of 0.41

(b) With an initial porosity of 0.2

Figure 7.39: Calculated flow of carbon and calcium after 40 days of exposure for the simulation of (Kutchko et al., 2008). (a) With an initial porosity of 0.41. (b) With an initial porosity of 0.2.

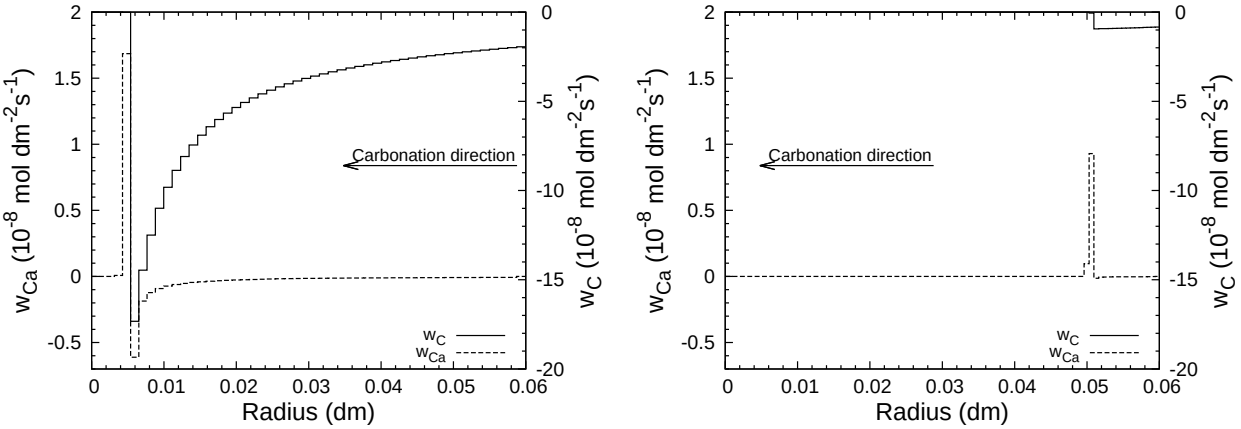

(a) With an initial porosity of 0.41

(b) With an initial porosity of 0.2

Figure 7.40: Calculated flow of carbon and calcium after 45 days of exposure for the simulation of (Kutchko et al., 2008). (a) With an initial porosity of 0.41. (b) With an initial porosity of 0.2.

7.7 Conclusion

In this chapter, first, the experiment of (Rimmelé et al., 2008) has been simulated. In the simulations without considering CO_2 dissolution and water evaporation kinetics at the boundary, carbonation patterns, as well as kinetics, were almost identical for samples exposed to CO_2 saturated water and $scCO_2$. The only difference we have observed is a very small amount of calcite dissolution for the sample exposed to CO_2-saturated water. A larger initial porosity will cause faster carbonation kinetics. Porosity drop after carbonation has been investigated. It has been found that the molar volume of $V_{SH_t} = 43$ cm^3/mol and t = 2 for the formed amorphous silica gel, proposed in (Antoine Morandeau, 2012; Thiéry et al., 2011, 2012), are more appropriate, at least to simulate the work of (Rimmelé et al., 2008). When considering water evaporation kinetics at the boundary, faster carbonation kinetics has been predicted for the sample exposed to $scCO_2$, due to the small amount of CO_2 advection into the cement paste in the first few hours. CO_2 dissolution kinetics at the boundary didn't introduce much difference in simulations, except a slightly slower carbonation kinetics. Remaining alkali affected pH value profile but didn't change carbonation patterns/kinetics.

Initial saturation degree of the cement paste is a key factor in predicting carbonation kinetics. In simulating the work of (Fabbri et al., 2009), dried samples carbonate much faster than wet samples. The difference comes from different CO_2 transport mechanisms. In wet samples, CO_2 transports generally by diffusion while in dried samples CO_2 moved essentially by advection of $scCO_2$, which is several orders of magnitude faster than diffusion.

Due to the close system used in (Rimmelé et al., 2008; Fabbri et al., 2009; Kutchko et al., 2007, 2008), the boundary condition was actually quite similar to the limestone-like conditions used in (Duguid and Scherer,

2010). Aqueous CO_2 concentration at the boundary could introduce different carbonation patterns/kinetics. With low CO_2 concentration (*e.g.*, at atmospheric pressure), clogging of the pores could take place, while with high CO_2 concentration (*e.g.*, at downhole pressures), clogging would not happen for samples with an initial porosity of 0.41 (Rimmelé et al., 2008; Fabbri et al., 2009), but would take place for samples with a small initial porosity (Kutchko et al., 2008). We can conclude that, similarly as claimed in (Huet et al., 2011), in limestone-like conditions, carbonation patterns/kinetics are either controlled by carbon transport (carbon dominated) or by the clogging caused by calcium transport (calcium dominated).

Thanks to this sensitivity analysis, this model can provide good prediction and is able to explain the different observations for experimental works in the literature. For future work, the dissolution kinetics of CO_2 in the cement pore microstructure could be introduced.

Chapter 8

Conclusion and perspectives

8.1 Summary and further discussion

A reactive transport model has been built. It aims at predicting CO_2 penetration through oil well cement, as well as understanding the behavior of cement-based materials, during long-term CO_2 geological storage conditions. The involved chemical reactions, transport properties and modeling approaches have been introduced. Simulations have been conducted and compared with experimental works from literature. Some experimental observations, as well as differences between experimental works, have been explained with the help of the model. Effects of parameters, *e.g.*, CO_2 concentration, temperature, activity product of $C\bar{C}$ at the boundary, saturation degree, also have been studied.

In this work, cement pastes or mortars are exposed to both CO_2 saturated brine or $scCO_2$. The chemistry of the CO_2-cement system involves congruent and incongruent dissolution and precipitation reactions of portlandite, calcite and C-S-H. This description of chemistry is coupled with a two-phase flow model with mass transfers of dissolved species. Temperature has been taken into account for the chemical equilibriums and the transport properties.

We consider homogeneous chemical reactions in the pore solution. A generalization of the mass action law is proposed to describe incongruent C-S-H dissolution. This theory encompasses the solid solution model and is clearly easier to implement in a transport-reaction modeling.

The changes in porosity induced by precipitation and dissolution reactions have also been taken into account by a balance of volume of the solid phases. When portlandite dissolves, the porosity will first increase, and it will then decrease as the calcite forms. The formed calcite could dissolve under peculiar boundary conditions and cause an increase in porosity. The decalcification of C-S-H could also contribute to a porosity increase or drop, due to the volume difference between C-S-H and $C\bar{C}$.

This model is able to deal with an unsaturated porous material with two immiscible fluid phases: a gas phase consisting in wet $scCO_2$ ($scCO_2$ with dissolved water) and a liquid phase. For the gas phase, we consider advection due to gas pressure gradient. For the liquid transport, we consider advection of pore solution due to liquid pressure gradient. For the dissolved aqueous species, electro-diffusion (Nernst-Plank equation) and advection have been taken into account.

Compared with other numerical models, this model considers the multiple flow of liquid and gas phase, thus is able to simulate experimental works with different test conditions, especially $scCO_2$ boundary conditions which other models are not able to simulate. This model has provided a quite good prediction of the carbonation kinetics of a cement paste exposed to a CO_2-saturated brine for sandstone-like and limestone-like conditions, as well as to $scCO_2$. Some experimentally-observed phenomena have also been explained by the model in terms of position of the calcite precipitation and hydrates dissolution fronts, the porosity profile, etc.

The originality of this work also includes solving the couplings between the chemical reactions and the transport equations in one step, as well as carefully chosen variables. These advantages make the model very efficient in calculation, thus suitable for long-term *in-situ* predictions.

Experimental works of (Duguid and Scherer, 2010; Rimmelé et al., 2008; Fabbri et al., 2009; Kutchko et al., 2008) have been simulated.

Under sandstone-like boundary conditions, successive zones have been observed, *i.e*, from the boundary to the core, the fully degraded region, the region of calcite accumulation, the C-S-H decalcification region, the CH dissolution region and the uncarbonated region. The calcite accumulation region can protect inner part of the cement paste from acid attack. The width of this region grows with time. The predominant aqueous species responsible to calcium and silicon transport have been revealed. The diffusion of Ca^{2+} ion as a result of concentration gradient causes the leaching of calcium as well as the calcium transport between different zones. The silicon transport is very limited compared with the calcium transport. Calcium is released from the calcite dissolution front and leaves the cement paste because the external solution is free of calcium. This release can be reduced or even stopped by increasing dissolved calcium in the external solution. There is also a transport of calcium from the portlandite dissolution front to the calcite precipitation front. The calcite dissolution front is the major source of carbon for the calcite precipitation.

Higher CO_2 concentration accelerates the penetration kinetics of each layer, due to a larger amount of CO_2 penetrating into the cement paste. Higher CO_2 concentration also engenders a wider calcite accumulation region. Higher temperature will enhance the diffusion of aqueous species, thus induces faster penetration kinetics of each reacted layer, with the same CO_2 concentration at the boundary. It is worthwhile noting that CO_2 solubility also depends on the temperature given that at the same pressure, CO_2

concentration decreases if temperature increases. Activity product of $C\bar{C}$ at the boundary is also an important parameter. With saturated calcium solution as boundary condition (limestone-like conditions), leaching of calcium is not possible and clogging effect due to calcite accumulation has been observed at the surface where the reaction is restricted. When calcium solution is subsaturated at the boundary, all the successive regions, *i.e.*, the fully degraded region, the region of calcite accumulation, the C-S-H decalcification region, the CH dissolution region and the uncarbonated region, have been observed, as for sandstone-like conditions. Faster penetration kinetics of the fully degraded region has been observed with smaller value of ion activity product of calcite $Q_{C\bar{C}}$ at the boundary.

For wet $scCO_2$ boundary conditions, if the cement paste is initially saturated, carbonation patterns/kinetics are identical to samples exposed to limestone-like boundary conditions, because cement paste remains saturated and there is no leaching of calcium. A larger initial porosity will cause faster carbonation kinetics. When considering water evaporation at the boundary, *i.e.*, $scCO_2$ is not saturated with water, faster carbonation kinetics has been predicted, due to CO_2 advection into the cement paste. Remaining alkalis affect *p*H value profile but do not change carbonation patterns/kinetics.

Initial saturation degree of the cement paste is a key factor in predicting carbonation kinetics. In simulating the work of (Fabbri et al., 2009), dried samples carbonate much faster than wet samples. The difference comes from different CO_2 transport mechanisms. In wet samples, CO_2 transports generally by diffusion while in dried samples CO_2 moves essentially by advection of $scCO_2$, which is several orders of magnitude faster than diffusion.

Aqueous CO_2 concentration at the boundary could introduce different carbonation patterns and kinetics. With low CO_2 concentration (*e.g.*, at atmospheric pressure), clogging of the pores could take place, while with high CO_2 concentration (*e.g.*, at downhole pressures), clogging would not happen for samples with an initial porosity of 0.41 (Rimmelé et al., 2008; Fabbri et al., 2009), but would take place for samples with a small enough initial porosity (Kutchko et al., 2008). We can conclude that, similarly as claimed in (Huet et al., 2011), in limestone-like conditions, carbonation patterns/kinetics are either controlled by carbon transport (carbon dominated) or by the clogging caused by calcium transport (calcium dominated).

Thanks to this modeling work, it is possible to specify recommendations which would be the less deleterious to preserve the integrity of the well. For long-term geological CO_2 storage, sandstone-like condition should be avoided. Indeed, the formed calcite layer could dissolve, leading to a highly porous amorphous silica gel layer, as the experiments at sandstone-like boundary conditions in (Duguid and Scherer, 2010) have shown.

Limestone-like conditions are identical to wet $scCO_2$ boundary conditions. For well hydrated cement paste with low porosity and tortuosity (*e.g.*, in the work of (Kutchko et al., 2008)), pore clogging may take

place and carbonation reactions are restricted at the sample surface. In this case, cement paste may keep its integrity for long term storage.

For cement with large initial porosity, pore clogging may not happen for downhole temperature and pressure conditions, due to high CO_2 concentration at the boundary. In this case, porosity of cement pastes decreases after carbonation, thus the resistance to acid attack may be preserved. In the work of (Fabbri et al., 2009), initially wet cement samples showed a degradation of the mechanical properties, which was probably due to the presence of micro-cracks in the vicinity of the carbonation front due to heterogeneities of mechanical properties on both sides of the carbonation front (elastic modulus). On the other hand, initially dried samples showed homogeneous carbonation through the whole sample and kept their mechanical properties. In real conditions, cement pastes are initially saturated, thus the degradation of cement mechanical properties reported in (Fabbri et al., 2009) may be a critical issue to dispose of an optimal way to plug the well with cement-based materials, and thus for the long- term well-bore casing integrity.

8.2 Future work

Future work could include improvements of the modeling to dispose of a more accurate description of supercritical carbonation of cement-based materials used to plug the well.

In this work, we assume infinite dilution approximation for aqueous species. The activity of each aqueous species is thus equal to the molar concentration expressed in mol/L, and that of each solid component equals to 1 (CH and $C\bar{C}$). This hypothesis may be criticized since the concentrations of the aqueous species could become too high in some situations like for unsaturated conditions when the concentration of the aqueous species increases. An improved model considering the effects of the chemical activity could be developed in a future work.

The reported molar volume and H/S ratio of C-S-H vary a lot according to literature. The molar volume of $C_{1.7}SH_{1.4}$ is approximately 64.5 cm^3/mol, that of $C_{1.7}SH_{2.1}$ is 78.8 cm^3/mol and that of $C_{1.7}SH_4$ is 113.6 cm^3/mol (Chen et al., 2004). For amorphous silica gel, (Lothenbach et al., 2008) proposed $t = 0$ $V_{SH_t} = 29$ cm^3/mol while experimental works of (Antoine Morandeau, 2012; Thiéry et al., 2011, 2012) suggested that $t = 2$ and $V_{SH_t} = 43$ cm^3/mol. A serious study of these values will be worthwhile in a future work.

Temperature dependence is neglected in the relative permeabilities (gas and liquid)-saturation curve and the capillary pressure-saturation curve due to a lack of experimental data. Further experimental studies could be done to get more precise values at high temperature conditions. Diffusion of water vapor in the gas phase should also be taken into account.

With well studied parameters, this code can provide good prediction and is able to explicate the different observations of experimental works from literature. However, due to a lack of some essential data (*e.g.*, initial solid contents, initial porosity), our simulations may not be precise enough. Cement used in the field of petroleum sciences are very special, in this study, as a primary work, some values (*e.g.*, transport parameters, stoichiometry of C-S-H, molar volume of solid components, etc.) are collected from OPC cement. New simulations with better studied input data could be done in the future. Long time *in situ* simulations (10 years or even more) considering different boundary conditions (*e.g.*, sandstone-like conditions, limestone-like conditions, dry or wet $scCO_2$ boundary conditions) could also be proposed.

Bibliography

P. D. Antoine Morandeau, Mickaël Thiéry. An original use of carbonation profiles to investigate kinetics, microstructurale changes and released water for type-i cement-based materials. *3rd International conference on the durability of concrete structures, Queen's University Belfast*, page INV10, 2012.

A. Atkinson, J. Hearne, and C. Knights. Aqueous chemistry and thermodynamic modelling of cao–sio2–h2o gels. *J. Chem. Soc., Dalton Trans.*, (12):2371–2379, 1989.

S. Bachu and D. Bennion. Experimental assessment of brine and/or co2 leakage through well cements at reservoir conditions. *International Journal of Greenhouse Gas Control*, 3(4):494–501, 2009.

V. Baroghel-Bouny. Water vapour sorption experiments on hardened cementitious materials. part ii: Essential tool for assessment of transport properties and for durability prediction. *Cement and Concrete Research*, 37(3):438 – 454, 2007. ISSN 0008-8846. doi: 10.1016/j.cemconres.2006.11.017.

B. Bary and A. Sellier. Coupled moisture—carbon dioxide–calcium transfer model for carbonation of concrete. *Cement and Concrete Research*, 34(10):1859 – 1872, 2004. ISSN 0008-8846. doi: 10.1016/j.cemconres.2004.01.025.

Z. Bažant and L. Najjar. Nonlinear water diffusion in nonsaturated concrete. *Materials and structures*, 5 (1):3–20, 1972.

S. Börjesson, A. Emrén, and C. Ekberg. A thermodynamic model for the calcium silicate hydrate gel, modelled as a non-ideal binary solid solution. *Cement and Concrete Research*, 27(11):1649–1657, 1997.

Ø. Brandvoll, O. Regnault, I. Munz, I. Iden, and H. Johansen. Fluid–solid interactions related to subsurface storage of co2 experimental tests of well cement. *Energy Procedia*, 1(1):3367–3374, 2009.

J. Carey and P. Lichtner. Calcium silicate hydrate (csh) solid solution model applied to cement degradation using the continuum reactive transport model flotran. *Transport properties and concrete quality: materials science of concrete, special volume; Mobasher, B*, pages 73–106, 2006.

J. Carey and P. Lichtner. Calcium silicate hydrate (csh) solid solution model applied to cement degradation using the continuum reactive transport model flotran. *Transport Properties and Concrete Quality: Materials Science of Concrete*, 62:73, 2007.

J. Carey, M. Wigand, S. Chipera, G. WoldeGabriel, R. Pawar, P. Lichtner, S. Wehner, M. Raines, G. Guthrie, et al. Analysis and performance of oil well cement with 30 years of co2 exposure from the sacroc unit, west texas, usa. *International Journal of Greenhouse Gas Control*, 1(1):75–85, 2007.

J. Chen, J. Thomas, H. Taylor, and H. Jennings. Solubility and structure of calcium silicate hydrate. *Cement and Concrete Research*, 34(9):1499–1519, 2004.

W. Crow, J. Carey, S. Gasda, D. Brian Williams, and M. Celia. Wellbore integrity analysis of a natural co2 producer. *International Journal of Greenhouse Gas Control*, 4(2):186–197, 2010.

A. Duguid. *The effect of carbonic acid on well cements*. 2006.

A. Duguid. An estimate of the time to degrade the cement sheath in a well exposed to carbonated brine. *Energy Procedia*, 1(1):3181–3188, 2009.

A. Duguid and G. Scherer. Degradation of oilwell cement due to exposure to carbonated brine. *International Journal of Greenhouse Gas Control*, 4(3):546–560, 2010.

A. Duguid, M. Raonjic, and G. Scherer. Degradation of well cements exposed to carbonated brine. In *Proceedings of Fourth Annual Conference on Carbon Capture and Sequestration*, 2005.

D. Etheridge, L. Steele, R. Langenfelds, R. Francey, J. Barnola, and V. Morgan. Natural and anthropogenic changes in atmospheric co2 over the last 1000 years from air in antarctic ice and firn. *Journal of Geophysical Research*, 101(D2):4115–4128, 1996.

D. Etheridge, L. Steele, R. Langenfelds, R. Francey, J. Barnola, and V. Morgan. Historical co2 records from the law dome de08, de08-2, and dss ice cores. *Trends: a compendium of data on global change*, pages 351–364, 1998.

R. Eymard, T. Gallouët, and R. Herbin. Finite volume methods. *Handbook of numerical analysis*, 7: 713–1018, 2000.

A. Fabbri, J. Corvisier, A. Schubnel, F. Brunet, B. Goffé, G. Rimmele, and V. Barlet-Gouédard. Effect of carbonation on the hydro-mechanical properties of portland cements. *Cement and Concrete Research*, 39(12):1156–1163, 2009.

C. Farrar, M. Sorey, W. Evans, J. Howle, B. Kerr, B. Kennedy, C. King, and J. Southon. Forest-killing diffuse co2 emission at mammoth mountain as a sign of magmatic unrest. *Nature*, 376(6542):675–678, 1995.

A. Fenghour, W. Wakeham, and V. Vesovic. The viscosity of carbon dioxide. *Journal of Physical and Chemical Reference Data*, 27(1):31–44, 1998.

K. Fujii and W. Kondo. Heterogeneous equilibrium of calcium silicate hydrate in water at 30 c. *J. Chem. Soc., Dalton Trans.*, (2):645–651, 1981.

C. García-González, N. El Grouh, A. Hidalgo, J. Fraile, A. López-Periago, C. Andrade, and C. Domingo. New insights on the use of supercritical carbon dioxide for the accelerated carbonation of cement pastes. *The Journal of Supercritical Fluids*, 43(3):500–509, 2008.

S. Gasda, S. Bachu, and M. Celia. Spatial characterization of the location of potentially leaky wells penetrating a deep saline aquifer in a mature sedimentary basin. *Environmental geology*, 46(6):707–720, 2004.

C. Geuzaine and J. Remacle. Gmsh: A 3-d finite element mesh generator with built-in pre-and post-processing facilities. *International Journal for Numerical Methods in Engineering*, 79(11):1309–1331, 2009.

P. Glynn and E. Reardon. Solid-solution aqueous-solution equilibria: thermodynamic theory and representation. *American Journal of Science*, 290(2):164–201, 1990.

S. Greenberg and T. Chang. *Investigation of Colloidal Hydrated Calcium Silicates: Pt. II. Solubility Relationships in the Calcium Oxide-silica-water System at 259*. Bulletin. 1965.

P. Hill. Possible asphyxiation from carbon dioxide of a cross-country skier in eastern california: A deadly volcanic hazard. *Wilderness & Environmental Medicine*, 11(3):192–195, 2000.

http://perso.lcpc.fr/dangla.patrick/bil/.

B. Huet, J. Prevost, and G. Scherer. Quantitative reactive transport modeling of portland cement in co2-saturated water. *International Journal of Greenhouse Gas Control*, 4(3):561–574, 2010.

B. Huet, V. Tasoti, and I. Khalfallah. A review of portland cement carbonation mechanisms in co2 rich environment. *Energy Procedia*, 4(0):5275 – 5282, 2011. ISSN 1876-6102. 10th International Conference on Greenhouse Gas Control Technologies.

N. Jacquemet, J. Pironon, and E. Caroli. A new experimental procedure for simulation of h2s+ co2 geological storage. application to well cement aging. *Oil & gas science and technology*, 60(1):193–203, 2005.

N. Jacquemet, J. Pironon, and J. Saint-Marc. Mineralogical changes of a well cement in various h2s-co2 (-brine) fluids at high pressure and temperature. *Environmental science & technology*, 42(1):282–288, 2007.

G. Kalousek. Application of differential thermal analysis in a study of the system lime–silica–water. In *Proceedings of the Third International Symposium on the Chemistry of Cement, London*, pages 296–311, 1952.

C. Keeling, S. Piper, T. Whorf, and R. Keeling. Evolution of natural and anthropogenic fluxes of atmospheric co2 from 1957 to 2003. *Tellus B*, 2011.

M. Kersten. Aqueous solubility diagrams for cementitious waste stabilization systems. 1. the csh solid-solution system. *Environmental science & technology*, 30(7):2286–2293, 1996.

E. Koenigsberger, H. Gamsjaeger, P. Glynn, and E. Reardon. Solid-solution aqueous-solution equilibria; thermodynamic theory and representation; discussion and reply. *American Journal of Science*, 292(3): 199–225, 1992.

D. Kulik and M. Kersten. Aqueous solubility diagrams for cementitious waste stabilization systems: Ii, end-member stoichiometries of ideal calcium silicate hydrate solid solutions. *Journal of the American Ceramic Society*, 84(12):3017–3026, 2001.

B. Kutchko, B. Strazisar, D. Dzombak, G. Lowry, and N. Thaulow. Degradation of well cement by co2 under geologic sequestration conditions. *Environmental science & technology*, 41(13):4787–4792, 2007.

B. G. Kutchko, B. R. Strazisar, G. V. Lowry, D. A. Dzombak, and N. Thaulow. Rate of co2 attack on hydrated class h well cement under geologic sequestration conditions. *Environmental Science & Technology*, 42(16):6237–6242, 2008. doi: 10.1021/es800049r. PMID: 18767693.

R. LeVeque. *Finite volume methods for hyperbolic problems*, volume 31. Cambridge Univ Pr, 2002.

P. Lichtner. Flotran user's manual. *Rep. LA-UR-02*, 2349, 2001.

B. Lothenbach and F. Winnefeld. Thermodynamic modelling of the hydration of portland cement. *Cement and Concrete Research*, 36(2):209 – 226, 2006. ISSN 0008-8846. doi: DOI:10.1016/j.cemconres.2005.03.001.

B. Lothenbach, T. Matschei, G. Möschner, and F. P. Glasser. Thermodynamic modelling of the effect of temperature on the hydration and porosity of portland cement. *Cement and Concrete Research*, 38(1):1 – 18, 2008. ISSN 0008-8846. doi: DOI:10.1016/j.cemconres.2007.08.017.

L. Luckner, M. Van Genuchten, and D. Nielsen. A consistent set of parametric models for the two-phase flow of immiscible fluids in the subsurface. *Water Resour. Res*, 25(10):2187–2193, 1989.

M. Mainguy, C. Tognazzi, J.-M. Torrenti, and F. Adenot. Modelling of leaching in pure cement paste and mortar. *Cement and Concrete Research*, 30(1):83 – 90, 2000. ISSN 0008-8846. doi: 10.1016/S0008-8846(99)00208-2.

L. Marini. *Geological sequestration of carbon dioxide: thermodynamics, kinetics, and reaction path modeling*, volume 11. Elsevier Science, 2007.

B. Metz. *IPCC special report on carbon dioxide capture and storage*. Cambridge University Press, 2005.

A. Morandeau. *Modélisation de la carbonatation atmosphérique : rôle des alcalins et prise en compte de la décalcification des C-S-H*. 2009.

J. Parker, R. Lenhard, and T. Kuppusamy. A parametric model for constitutive properties governing multiphase flow in porous media. *Water Resour. Res*, 23(4):618–624, 1987.

W. Pentland. The carbon conundrum, october 2008.

J. Prausnitz, R. Lichtenthaler, and E. de Azevedo. *Molecular thermodynamics of fluid-phase equilibria*. Prentice Hall, 1998.

J. Prevost. *DYNA-FLOW: a nonlinear transient finite element analysis program*. Princeton University, Department of Civil Engineering, School of Engineering and Applied Science, 2007.

J. Racine. gnuplot 4.0: a portable interactive plotting utility. *Journal of Applied Econometrics*, 21(1): 133–141, 2006.

M. Rahman, S. Nagasaki, and S. Tanaka. A model for dissolution of cao-sio2-h2o gel at ca/si> 1. *Cement and concrete research*, 29(7):1091–1097, 1999.

O. Redlich and J. Kwong. On the thermodynamics of solutions. v. an equation of state. fugacities of gaseous solutions. *Chemical Reviews*, 44(1):233–244, 1949.

O. Regnault, V. Lagneau, and H. Schneider. Experimental measurement of portlandite carbonation kinetics with supercritical co2. *Chemical Geology*, 265(1-2):113–121, 2009.

G. Rimmelé, V. Barlet-Gouédard, O. Porcherie, B. Goffé, and F. Brunet. Heterogeneous porosity distribution in portland cement exposed to co2-rich fluids. *Cement and Concrete Research*, 38(8-9):1038–1048, 2008.

J. M. Soler. Thermodynamic description of the solubility of c-s-h gels in hydrated portland cement - literature review. *Posiva working report*, 88, 2007.

N. Spycher, K. Pruess, and J. Ennis-King. Co2-h2o mixtures in the geological sequestration of co2. i. assessment and calculation of mutual solubilities from 12 to 100 c and up to 600 bar. *Geochimica et Cosmochimica Acta*, 67(16):3015–3031, 2003.

C. Steefel. Gimrt, version 1.2: Software for modeling multicomponent, multidimensional reactive transport. user's guide. Technical report, UCRL-MA-143182. Livermore, California, 2001.

P. Tans. Atmospheric co2 mauna loa observatory (scripps / noaa / esrl) monthly mean co2 concentrations (ppm) since march 1958, 2012.

M. Thiery. *Modélisation de la carbonatation atmosphérique des matériaux cimentaires:(prise en compte des effets cinétiques et des modifications microstructurales et hydriques).* Laboratoire central des ponts et chaussées, 2006.

M. Thiery, P. Belin, V. Baroghel-Bouny, et al. Modelling of isothermal drying process in cementitious materials: Analysis of the moisture transfer and proposal of simplified approaches. 2008.

M. Thiéry, P. Faure, A. Morandeau, et al. Effect of carbonation on the microstructure and the moisture properties of cement-based materials. *XII International conference on durability of building materials and components, Porto-Portugal*, 2011.

M. Thiéry, V. Baroghel-Bouny, A. Morandeau, and P. Dangla. Impact of carbonation on the microstructure and transfer properties of cement-based materials. *Tranfert 2012, Ecole Centrale de Lille*, pages 1–10, 2012.

T. Thoenen and D. Kulik. Nagra/psi chemical thermodynamic data base 01/01 for the gem-selektor (v. 2-psi) geochemical modeling code: Release 28-02-03. Technical report, PSI Technical Report TM-44-03-04 about the GEMS version of Nagra/PSI chemical thermodynamic database 01/01, 2003.

C. Tognazzi and J. Ollivier. *Couplage fissuration-dégradation chimique dans les matériaux cimentaires: caractérisation et modélisation.* 1998.

E. Toro. *Riemann solvers and numerical methods for fluid dynamics: a practical introduction.* Springer Verlag, 2009.

M. van Genuchten. A closed-form equation for predicting the hydraulic conductivity of unsaturated soils. *Soil Sci. Soc. Am. J*, 44(5):892–898, 1980.

R. Weast, M. Astle, and W. Beyer. *CRC handbook of chemistry and physics*, volume 69. CRC press Boca Raton, FL, 1988.

J. William Carey, R. Svec, R. Grigg, J. Zhang, and W. Crow. Experimental investigation of wellbore integrity and co2-brine flow along the casing-cement microannulus. *International Journal of Greenhouse Gas Control*, 4(2):272–282, 2010.

T. Xu, E. Sonnenthal, N. Spycher, and K. Pruess. Toughreact user's guide: A simulation program for non-isothermal multiphase reactive geochemical transport in variably saturated geologic media, v1. 2.1. Technical report, Ernest Orlando Lawrence Berkeley National Laboratory, Berkeley, CA (US), 2008.

Appendix A

Temperature dependence of equilibrium constants

The temperature dependence of equilibrium constants can be taken into account through the following analytical expression:

$$\log K(T) = A + BT + C/T + D \log T + E/T^2 \tag{A.1}$$

where T is the temperature in K, and values for parameters A to E can be found in (Thoenen and Kulik, 2003). Chemical equilibrium constants calculated with Eq. (A.1) at different temperatures are listed in Table A.1.

Table A.1: Chemical reactions and equilibrium constants at different temperatures, data from (Thoenen and Kulik, 2003). ρ_i prepresents the concentration of each species.

Reactions			$\log K$			
			25°C	50°C	75°C	90°C
H_2O	$\rightleftharpoons$	$H^+ + OH^-$	-14.00	-13.28	-12.71	-12.43
$CO_2^0 + H_2O$	$\rightleftharpoons$	$HCO_3^- + H^+$	-6.353	-6.286	-6.322	-6.377
HCO_3^-	$\rightleftharpoons$	$CO_3^{2-} + H^+$	-10.33	-10.17	-10.13	-10.13
$CaCO_3^0$	$\rightleftharpoons$	$Ca^{2+} + CO_3^{2-}$	-3.223	-3.510	-3.855	-4.050
$CaOH^+$	$\rightleftharpoons$	$Ca^{2+} + OH^-$	-1.224	-0.4989	0.06742	0.3471
$CaHCO_3^+$	$\rightleftharpoons$	$Ca^{2+} + HCO_3^-$	-1.105	-1.207	-1.261	-1.309
$H_4SiO_4^0$	$\rightleftharpoons$	$H_3SiO_4^- + H^+$	-9.812	-9.465	-9.168	-9.009
$H_3SiO_4^-$	$\rightleftharpoons$	$H_2SiO_4^{2-} + H^+$	-13.33	-12.66	-12.09	-11.78
$CaH_2SiO_4^0$	$\rightleftharpoons$	$Ca^{2+} + H_2SiO_4^{2-}$	-4.600	-4.600	-4.600	-4.600
$CaH_3SiO_4^+$	$\rightleftharpoons$	$Ca^{2+} + H_3SiO_4^-$	-1.200	-1.200	-1.200	-1.200
$S + 2H_2O$	$\rightleftharpoons$	$H_4SiO_4^0$	-2.715	-2.517	-2.348	-2.257
CH	$\rightleftharpoons$	$Ca^{2+} + 2OH^-$	-5.197	-5.506	-5.880	-6.125
$C\bar{C}$	$\rightleftharpoons$	$Ca^{2+} + CO_3^{2-}$	-8.479	-8.661	-8.925	-9.120

Appendix B

Dynamic viscosity of pure CO_2

Dynamic viscosity of pure CO_2, μ_G, is seen as a function of the CO_2 pressure and temperature, which is decomposed into three separate contributions as the form below, following the work of (Fenghour et al., 1998):

$$\mu_{G(\rho,T)} = \mu^0_{G(T)} + \Delta\mu_{G(\rho,T)} + \Delta\mu^c_{G(\rho,T)} \tag{B.1}$$

where $\mu^0_{G(T)}$ is the viscosity in the zero-density limit, $\Delta\mu_{G(\rho,T)}$ is the excess viscosity which represents the increase in the viscosity at elevated density over the dilute gas value at the same temperature, and $\Delta\mu^c_{G(\rho,T)}$ is the critical enhancement accounting for the increase in viscosity in the immediate vicinity of the critical point. $\Delta\mu^c_{G(\rho,T)}/\mu_{G(\rho,T)}$ is found to be less than 0.01 in most case, except in the region 300 K<T<310 K and 300 kg m^{-3}<ρ<600 kg m^{-3} which is not interested in out research. The calculation of $\mu^0_{G(T)}$ and $\Delta\mu_{G(\rho,T)}$ will be presented in the following while the influence of $\Delta\mu_c(\rho,T)$ is neglect in our work.

The viscosity of CO_2 in the zero-density limit $\mu^0_{G(T)}$ can be calculated by equation:

$$\mu^0_{G(T)} = \frac{1.00697T^{1/2}}{\delta^*_\mu(T^*)} \tag{B.2}$$

where $\mu^0_{G(T)}$ is in unit of μPa s and the temperature T in Kelvin. The reduced effective cross section $\delta^*_\mu(T^*)$ is represented by the empirical equation:

$$\ln\,\delta^*_\mu(T^*) = \sum_{i=0}^{4} a_i(\ln\,T^*)^i. \tag{B.3}$$

The coefficients a_i are listed in Table (B.1) and T^* is the reduced temperature given by

$$T^* = kT/\varepsilon \tag{B.4}$$

where ε/k is the energy scaling parameter equals to 251.196 K.

Table B.1: Coefficients for the calculation of CO_2 zero-density viscosity

a_0	a_1	a_2	a_3	a_4
0.235156	-0.491266	$5.211155\ 10^{-2}$	$5.347906\ 10^{-2}$	$-1.537012\ 10^{-2}$

The excess viscosity contribution $\Delta\mu(\rho, T)$ describes how the viscosity of the fluid behaves as a function of density outside of the critical region. A power series expansion in density for the representation of the excess viscosity is used here in the following form:

$$\Delta\mu_{G(\rho,T)} = \sum_{i=1}^{n} b_i(T)\rho^i \tag{B.5}$$

where T in K, $\Delta\mu_{G(\rho,T)}$ in μPa s and ρ in kg m^{-3}. Temperature dependence of the density coefficients, b_i, is represented by the form:

$$b_i = \sum_{j=1}^{m} d_{ij}/(T^{*j-1}) \tag{B.6}$$

the coefficients d_{ij} can be determined by fitting the experimental data, which values are listed in Table (B.2).

Table B.2: Coefficients for the calculation of CO_2 excess viscosity, the rest of d_{ij} coefficients are equal to zero

d_{11}	d_{21}	d_{64}	d_{81}	d_{82}
$0.4071119\ 10^{-2}$	$0.7198037\ 10^{-4}$	$0.2411697\ 10^{-16}$	$0.2971072\ 10^{-22}$	$-0.1627888\ 10^{-22}$

$\Delta\mu(\rho, T)$ can also be written explicitly as:

$$\Delta\mu(\rho, T) = d_{11}\rho + d_{21}\rho^2 + \frac{d_{64}\rho^6}{T^{*3}} + d_{81}\rho^8 + \frac{d_{82}\rho^8}{T^*}. \tag{B.7}$$